RICE UNIVERSITY

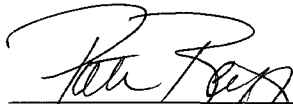# Topology and Convection of a Northward Interplanetary Magnetic Field Reconnection Event
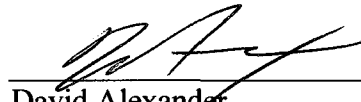
by

Deirdre E. Wendel

A THESIS SUBMITTED IN PARTIAL FULFILLMENT OF THE
REQUIREMENTS FOR THE DEGREE OF

Doctor of Philosophy

APPROVED BY THESIS COMMITTEE:

Patricia H. Reiff, Chairperson
Professor of Physics and Astronomy

David Alexander,
Andrew Hays Buchanan Associate Professor of
Astrophysics

Dale S. Sawyer
Professor of Earth Science

HOUSTON, TX

APRIL 2009

UMI Number: 3362429

UMI®

Dissertation Publishing

ProQuest®

ABSTRACT

Topology and Convection of a Northward Interplanetary Magnetic Field Reconnection
Event

by

Deirdre E. Wendel

From observations and global MHD simulations, we deduce the local and global magnetic

topology and current structure of a northward IMF reconnection event in the dayside

magnetopause. The ESA four-satellite Cluster suite crossed the magnetopause at a location

mapping along field lines to an ionospheric H-alpha emission observed by the IMAGE

spacecraft. Therefore, we seek reconnection signatures in the Cluster data. From the four-

point Cluster observations, we develop a superposed epoch method to find the

instantaneous x-line, its associated current sheet, and the nature of the reconnecting particle

flows. This method is unique in that it removes the motion of the hyperbolic structure and

the magnetopause relative to the spacecraft. We detect singular field line reconnection—

planar hyperbolic reconnecting fields superposed on an out-of-plane field. We also detect

the parallel electric field that is required to certify reconnection at locations where the

magnetic field does not vanish, and estimate a reconnection electric field of - 4 mV/m. The

current sheet appears bifurcated, embedding a 30 km current sheet of opposite polarity

within a broader current sheet about 130 km thick. Using a resistive MHD simulation and

ionospheric satellite data, we examine the same event at global length scales. This gives a

3D picture of where reconnection occurs on the magnetopause for northward IMF with B_x

and B_y components and a tilted dipole field. It also demonstrates that northward IMF 3D

reconnection couples the reconnection electric field and field-aligned currents to the

ionosphere, driving sunward convection in a manner that agrees with satellite

measurements of sunward flows. We find singular field line reconnection of the IMF with both open and closed field lines near nulls in both hemispheres. The reconnection in turn produces both open and closed field lines. We discuss for the first time how line-tying in the ionosphere and draping of open and IMF field lines produce a torsion of the reconnecting singular magnetic field lines within the magnetopause. The simulation and data show that magnetopause reconnection topology is three-dimensional in a way that challenges accepted models of neutral lines and x-lines with guide fields.

Acknowledgments

Table of Contents

List of Tables

List of Figures

Chapter 1

INTRODUCTION

1.1 Magnetic Reconnection

Collisionless magnetic reconnection is a fundamental process that is believed to occur in many natural and artificial plasmas, accounting for phenomena such as solar flares and small-scale heating of the solar corona. Magnetic reconnection is a process whereby nearby magnetic field lines with different particle populations break and connect to one another. In reconnection, particle orbits that gyrate and define one field line by the center of their orbits leave that center of gyration (or field line) and move to a center of gyration that has been defined by a different set of particles. Collisionless magnetic reconnection occurs in plasmas that are tenuous enough to have a low collision frequency. Such plasmas surround the Earth and fill the heliosphere—the interplanetary region filled by the the sun's wind and its interplanetary magnetic field. We therefore look to the boundary of the Earth's magnetosphere—the magnetic bubble defined by the boundary between the sun's and the Earth's magnetic fields—as a natural laboratory to provide us with data on the crucial process of large-scale reconnecting fields. This boundary, known as the magnetopause, is where reconnection happens at the Earth. Reconnection can occur between magnetic fields with a low shear if there is sufficient compression of the fields. However, reconnection occurs most readily between field lines with a large shear between them. The terrestrial field points northward on the sunward

side of the Earth's magnetosphere. The northward geomagnetic field at this location favors magnetic reconnection with a southward pointing interplanetary magnetic field (IMF) on a swath that stretches across the dayside of the Earth's field. However, when the IMF is northward, it drapes over the Earth's magnetopause in a roughly anti-parallel (large shear) orientation over the Earth's magnetic tail—the portion of the magnetosphere that lies away from the sun—and magnetic poles in a manner that also allows reconnection. Magnetic draping occurs as the result of an object (in this case the Earth) moving relative to a magnetized medium (in this case the solar wind). For northward IMF, the location of reconnection is generally near the magnetospheric cusp—that is, the funnel-shaped magnetic field that emanates to and from the geomagnetic poles and abuts the magnetopause. Because this configuration is somewhat less favored than that of southward IMF reconnection in that the spatial dimensions of the reconnection region are smaller and the required ram pressure larger, it has been observed less often. It is therefore less well-understood than southward IMF reconnection at the Earth. This is particularly true when the IMF is complicated by B_x and B_y components or a dipole tilt. While southward IMF reconnection can often be adequately explained by a two dimensional model, comprehension of northward IMF reconnection demands a three-dimensional analysis of the process. Moreover, the size and role of the scales over which reconnection occurs are just beginning to be understood in simulations, much less measured in the magnetosphere. The synthesis of multi-spacecraft measurements from the Cluster satellite array in orbit around the Earth's poles with dynamic atmospheric measurements and global simulations provides a unique opportunity to grapple with these issues simultaneously. In this thesis, we analyze the northward IMF reconnection event

of 18 March 2002 both on scales local to the reconnection site and on global scales encompassing the magnetophere. We draw upon *in situ* particle and field measurements from the Cluster spacecraft to explore the detailed structure of a northward IMF reconnection site in the northern cusp. We combine this with data from the ionosphere—the charged layer of the Earth's atmosphere—and theoretical magnetohydrodynamic (MHD) simulations to place constraints on the global magnetic topology and physical dimensions of the observed reconnection.

1.2 The Nature of 2D and 3D Magnetic Merging

We begin this introduction to reconnection by describing the localized physics of reconnection, first in two dimensions (2D) and then in three dimensions (3D). In an ideal plasma (a plasma in which ideal magnetohydrodynamics, or ideal MHD, holds), the particles are frozen in to the magnetic field and gyrate about and drift with the magnetic field. In this case, the electric field $\mathbf{E}$ is perpendicular to the magnetic field $\mathbf{B}$ and all of the particle species move together perpendicular to the magnetic field with a drift speed $\mathbf{v} = \mathbf{E} \times \mathbf{B}/B^2$ (though the particles may have separate velocity components along the magnetic field). Magnetic field lines are actually defined by the guiding center of the particle gyrations, and, in ideal MHD, once a particle is associated with a particular field line, it is forever associated with that field line, leading to the concept of a *flux tube*. In the plasma frame,

$$\mathbf{E}' = \mathbf{E} + \mathbf{v} \times \mathbf{B} = 0. \tag{1.1}$$

Applying Faraday's law and Stokes' theorem to this equation implies $\frac{d}{dt} \int \mathbf{B} \cdot d\mathbf{S} =$

$\int_S \frac{\partial \mathbf{B}}{\partial t} \cdot d\mathbf{S} + \int_C \mathbf{B} \cdot \mathbf{v} \times d\mathbf{S} = \int_S \left[\frac{\partial \mathbf{B}}{\partial t} - \nabla \times (\mathbf{v} \times \mathbf{B}) \right] \cdot d\mathbf{S} = 0$, where $\mathbf{S}$ is the flux tube

cross-sectional surface bounded by a curve C. Magnetic flux through a given closed fluid

element of area S is conserved.

Instabilities that create a twist of the magnetic field line and an associated

gradient in the parallel vorticity (e.g., [*Song and Lysak*, 2006]), can produce an electric

field parallel to the magnetic field. As we shall shortly demonstrate, the forces that

balance this parallel electric field also allow particles to move across field lines, thus

breaking the frozen-in, ideal condition. The responsible instability occurs when the

magnetic field varies on scales comparable to the Larmor radius or the inertial length and

when the Alfvén time is less than the collision, cyclotron, or plasma times. When this

happens, magnetic field lines once associated with one source and one topology can

connect with a magnetic field line from another topology. Some magnetic flux is

necessarily destroyed in this process, and components of the magnetic field from each of

the merging topologies oppose and cancel one another at this location. This process is

known as magnetic merging, or magnetic reconnection. The line or curve along which

this happens is known as the singular field line. In two dimensions, and sometimes in

three dimensions, the singular field line is known as the separator—the intersection

between two surfaces, known as separatrices, that separate topologically distinct

magnetic domains. The magnetic domains are defined by the location of the footpoints of

the field line, which, for example, may both lie in the sun or both lie in the Earth. In 2D,

the separator is called the 'x-line,' or 'merging line.'
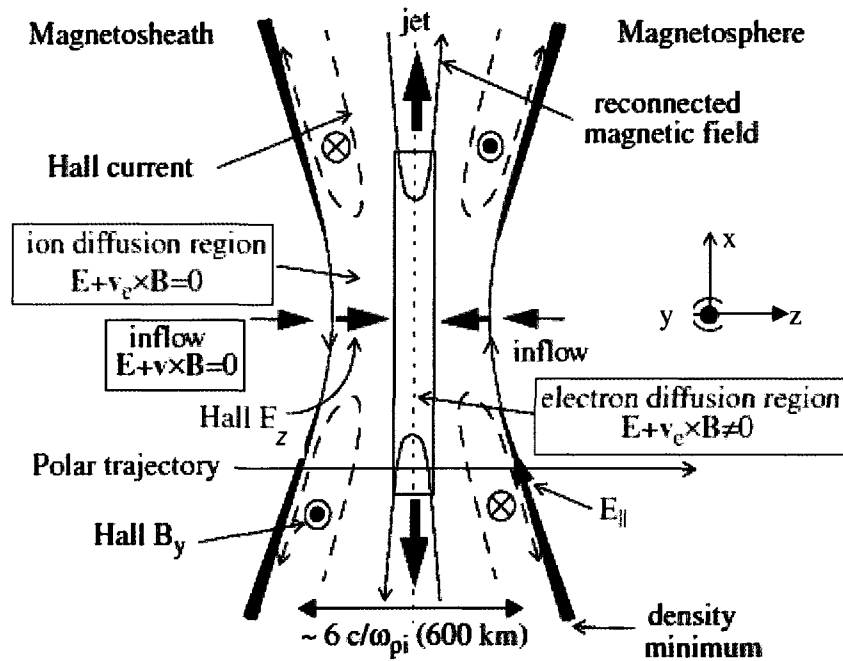
Figure 1.1 A two-dimensional cross section of an x-line. The x-line lies out of the page, and the reconnecting fields from above and below merge in a hyperbolic geometry at the x-line. The destruction of magnetic flux pulls particles in across topologies and reaccelerates them. The direction of flows are shown in blue, and the direction of the electric field in red. There is also an electric field out of the page that lies along the separator, or 'x-line' (from *Mozer et al.* [2002]).

Reconnection favors a high shear between the field lines of different topological regions, as will be discussed later at greater length, though the merging fields need not be exactly antiparallel. A current sheet forms between the sheared topologies, even without merging. It is when the compression becomes high enough that the current sheet thins to the point that the length scales approach the particle gyroradii and skin depths that merging occurs. The component of the magnetic field along the singular field line may or may not vanish (though by definition the other components do vanish). If it does, then the merging is considered antiparallel at that location. Otherwise, the field along the separator is known as the 'guide field,' and the merging is referred to as component

reconnection. Figure 1.1 (from *Mozer et al.* [2002]) illustrates the topology and geometry near a 2D x-line, located at the center of the hyperbolic reconnecting magnetic field lines. Force and energy balance at the site converts magnetic flux into the acceleration of particles from one topological region into the other. According to *Vasyliunas* [1975], this exchange of particles between magnetic topologies constitutes the definition of reconnection. Figure 1.1 also demonstrates the inflow and accelerated outflow (jets) for the 2D case.

Figure 1.1 characterizes steady two-dimensional reconnection. In a two-dimensional setting where there is time-dependence and some kind of periodicity in one spatial dimension, an instability in the growth of the ripples can give rise to a spatially patchy form of reconnection. This is known as a tearing mode, and the reconnection forms magnetic islands of plasma that are disconnected from anything else. The center of the islands are known as 'o-points,' and the junctures between islands where merging happens are the 'x-points,' as depicted in Figure 1.2 (from *Shay* [1998]). (The 'x' in this figure is horizontal, unlike Figure 1.1, where it is vertical. In both figures, the x-line is out of the page.)

The breakdown of ideal conditions necessitates the inclusion of all of the terms in the full generalized Ohm's Law to balance the electric field at the separator. Each term on the right-hand side of the generalized Ohm's Law in the ion rest frame, i.e.,

$$\mathbf{E}' = \mathbf{E} + \mathbf{v}_i \times \mathbf{B} = \frac{\mathbf{j}}{\sigma} + \frac{m_e}{ne^2}\left[\frac{\partial \mathbf{j}}{\partial t} + \nabla \cdot (\mathbf{v}\mathbf{j} + \mathbf{j}\mathbf{v})\right] + \frac{\mathbf{j} \times \mathbf{B}}{ne} - \frac{\nabla \cdot \mathbf{P}_e}{ne} \qquad (2.1)$$

$$2\,\pi/k$$
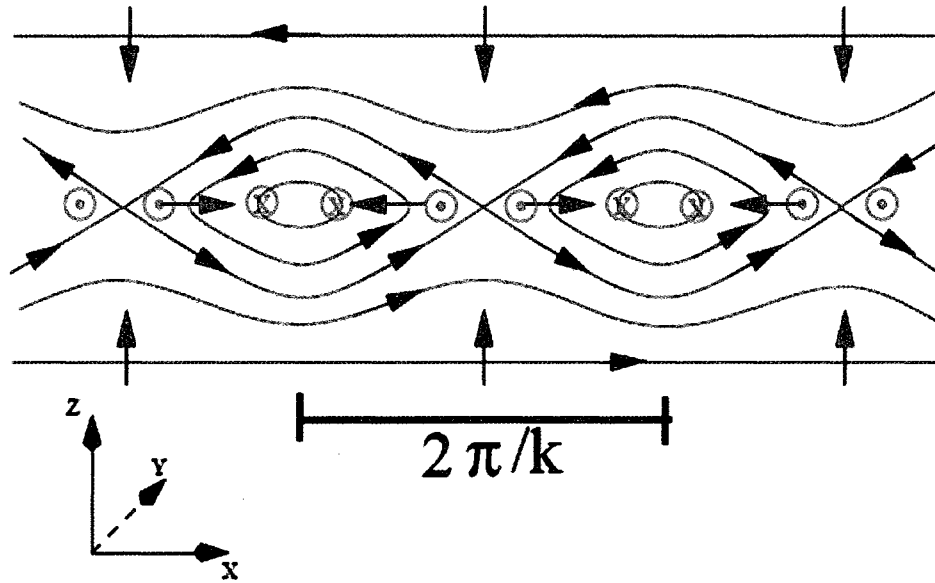
Figure 1.2 The tearing-mode geometry. Magnetic field lines are brown, flow lines blue, and the reconnection electric field purple. From *Shay* [1998].

where v_i is the ion velocity, j the current, σ the conductivity, n the density, and p_e the electron pressure tensor, acquires physical significance at a unique scale length. The first term corresponds to collisions or interactions between particles and waves. In the collisionless low densities of interest to us, this term includes only wave-particle interactions. However, MHD magnetosphere models use this term to artificially account for reconnection in what is called 'anomalous resistivity.' (see, for example, *Raeder* [2003]). Because MHD cannot, unlike smaller scale simulations, model individual particles' trajectories, or even separate species' trajectories, it cannot reproduce all the other terms in Ohm's law that account for the breakdown of MHD in a collisionless plasma. Therefore, the MHD codes insert an artificial resistivity to emulate reconnection. As might be imagined, the results are highly dependent on the resistivity model. The

second term on the right, the electron inertial term, gains importance only on the smallest scales, those comparable to the electron skin-depth. The third term represents the Hall current, relevant at the largest non-ideal scale--the ion skin-depth (the ion diffusion region). The Hall current, which arises from the differing motions of the electrons and ions, is also responsible for producing a quadrupolar magnetic field out of the page and surrounding the 2D x-line, as illustrated in Figure 1.1 The last term, significant at the intermediate scale of the ion Larmor radius, but maximum within the electron bounce width, stems from a partial electron demagnetization that produces an off-diagonal term in the electron pressure tensor [*Hesse et al.*, 2001]. Each of these terms creates a characteristic signature in some aspect of the ion and electron data. Each of these length scales are illustrated in Figure 1.1. The influence of these nonideal kinetic terms at the reconnection site accounts for an electric field along the singular field line (which in Figure 1.1 is an x-line and points in the y direction), even if the magnetic field vanishes there. This is the reconnection electric field and it is responsible for the flow of particles between topologies. This electric field gives the merging rate because, through Faraday's Law, it balances the loss of magnetic flux across the topological boundary. These nonideal terms in the generalized Ohm's Law also account for electric field components that lie parallel to the magnetic field.

Figures 1.3 and 1.4 (from [*Shay,* 1998]) describe the orbits of particles within the diffusion regions and show how particles demagnetize in a diffusion region with a nonideal electric field. In both figures, the purple lines are the electric field, the brown circles signify the direction of the magnetic field, and the blue curves are the particle orbits. Figure 1.3 is a view along the x component of the magnetic field, and Figure 1.4
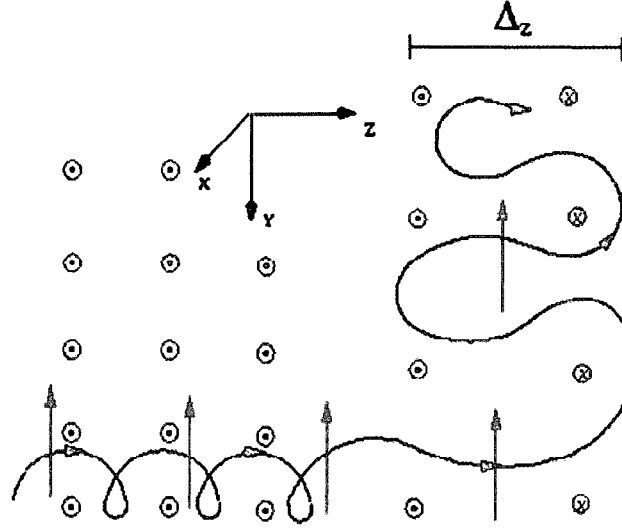
Figure 1.3 The inflowing particles become demagnetized (in blue) and meander along the reconnection line. The electric fields are in purple, and the brown circles are the direction of the magnetic field. The view is along x. From *Shay* [1998].

from along the z component. In 2D, the particles develop meandering, so-called "Speiser," orbits. Once they have crossed the layer between magnetic domains, these orbits meander between magnetic domains while traveling out of the plane of reconnection. In this layer they are demagnetized, wandering between different magnetic domains. Figure 1.4, a view along z, shows that particles remagnetize as they exit the diffusion region. Neglecting electron inertial terms, the electric field along the separator, $E_y = - (\partial P_{xy}/\partial x + \partial P_{zy}/\partial z + \partial P_{yy}/\partial y)$. In 2D, the last term vanishes. As demonstrated by *Vasyliunas* [1975], symmetry of the velocity distributions about the merging site makes P_{xy} vanish at an x-line, though it acquires a nonzero value on either side of the x-line within the diffusion region. P_{xy} approaches zero at the edge of the diffusion region because the growing gyromotion about a larger B_z essentially magnetizes the electrons
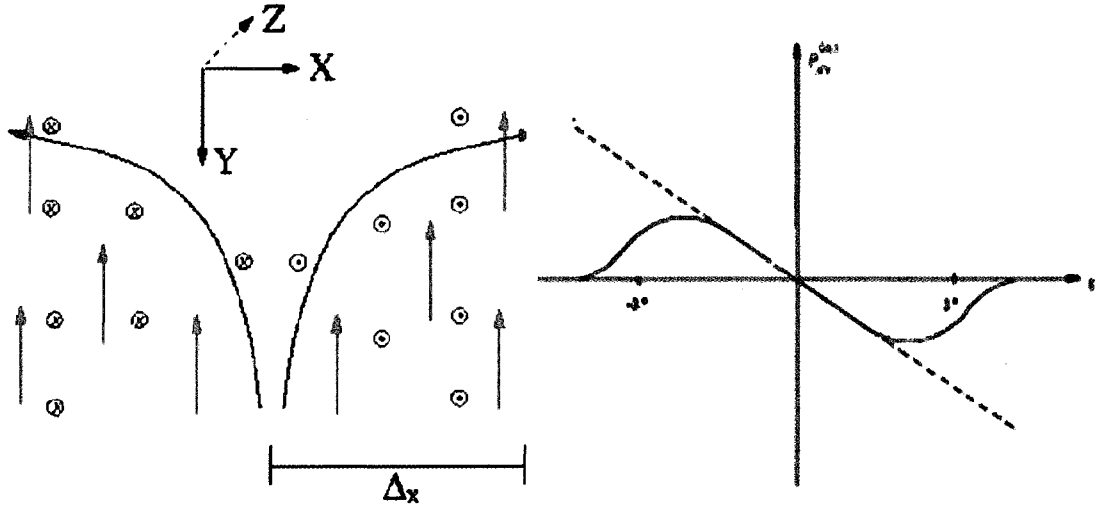
Figure 1.4 (a) Left. As it leaves the vicinity of the x-line, the particle becomes remagnetized. The view is along z. From *Shay* [1998]. **(b) Right.** For 2D reconnection at a null line, the variation of the pressure shear term P_{xy} with x along the midplane of the field reversal region. From *Vasyliunas* [1975].

and increases axial symmetry about the z-direction. Thus, far enough away from the x-line, the off-diagonal terms P_{xy} diminish and the particles are remagnetized. Figure 1.4b illustrates the resulting asymmetric variation of P_{xy} with x at $z = 0$.

Modeling reconnection in three dimensions requires magnetic gradients in three spatial dimensions. An ambiguity arises, however, in how to define reconnection in three dimensions. The classic Vasyliunas definition [*Vasyliunas, 1975*] of reconnection as a process whereby plasma flows between distinct magnetic topologies falters in three dimensions. *Hesse and Schindler* [1988] give the field $(B_x, B_y, B_z) = (y, x, 1)$ as an example. For a suitable choice of coordinate axes, any given point is an x-point (with a guide field) and, thus, any field line is a reconnection line. Though there are no topologically distinct field regions and thus no real separatrices, it can appear that plasma flows across apparent separatrices. This example proves that in general one cannot

identify a reconnection line based solely on the local magnetic field geometry and plasma flow. Furthermore, unlike two-dimensional x-lines, three-dimensional magnetic neutral lines are unstable to general perturbations. This means that the associated separatrix surfaces fail to provide a stable topology with respect to which one can define plasma flows [*Schindler and Hesse,* 1988; *Hesse and Schindler,* 1988]. Small perturbations to the magnetic field may result in very large topological changes, meaning there isn't a stable separatrix with which to define particle flows. At the Earth's magnetopause, for example, in the vacuum superposition of a purely northward IMF and an untilted Earth dipole field [*Dungey,* 1961; 1963], a single, spherical separatrix surface divides the two magnetic domains of the IMF and the Earth's dipole (for example, in Figure 1.5b, from *Dorelli et al.,* [2007]). In this setting, reconnection takes place simultaneously at two null points, shown as a red and blue sphere in the northern and southern hemispheres, and there is no separator line. The separatrix surface, defined for a zero dipole tilt, is unstable to general perturbations, however. Once a dipole tilt is added, for example, there are three magnetic domains (IMF field lines, so-called 'open' field lines that are reconnected field lines with one end in the Earth and one end in the sun, and closed Earth field lines). In this case, the single separatrix surface is replaced by two spherical separatrix surfaces that intersect along a field line. In this scenario, insofar as the magnetic topology alone can tell us, reconnection could occur anywhere along this field line. Thus, to identify precise locations of reconnection, either in satellite data or global simulation output, we need to supplement the magnetic topology with both necessary and sufficient conditions.

In order to address this deficiency, a number of alternative definitions have been proposed: *Schindler and Hesse* [1988] and *Hesse and Schindler* [1988] suggest defining
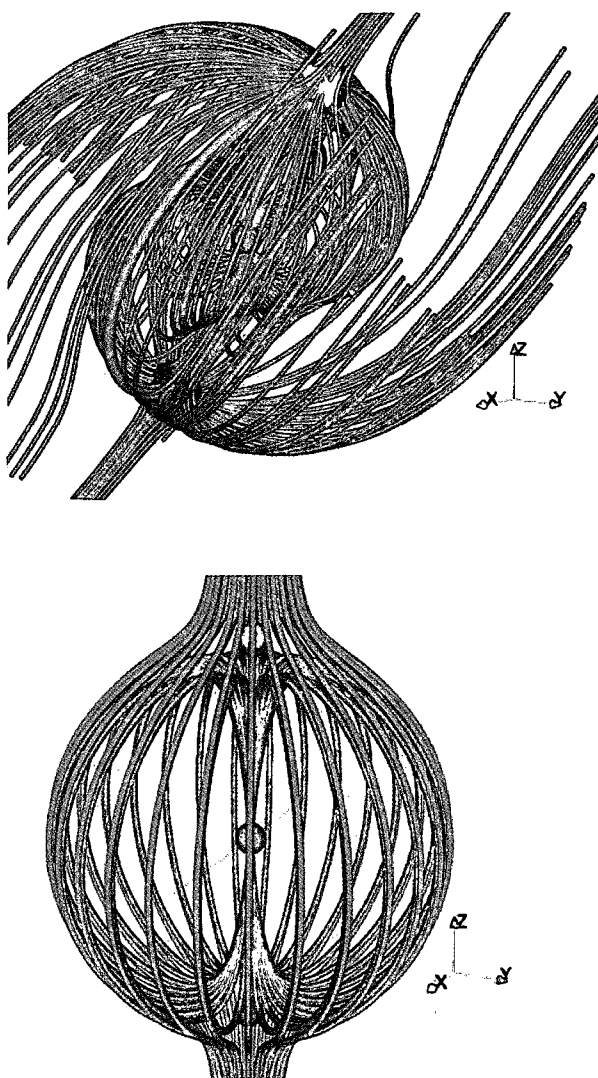
Figure 1.5a-1.5b **(a) Top:** The intersection of the two separatrix surfaces forms a single separator line linking the two cusp nulls in each hemisphere. Figure 1.5a is an example of such a model with a dipole tilt. The red lines go through the northern hemisphere null (red sphere), the blue lines through the southern hemisphere null (blue sphere), while the yellow line is a closed field line that approximates the location of the separator line. **(b)Bottom:** With zero dipole tilt, the northward IMF merges at two null points, one the northern and one in the southern cusp. A single, spherical separatrix surface divides the two magnetic topologies. Both figures are from *Dorelli et al.* [2007].

reconnection by the presence of a parallel electric field that causes field lines from distinct topologies to exchange plasma. For the reasons cited above, they avoid invoking separatrices and null points in their definition, and prove that a nonvanishing parallel electric field along a field line, i.e., $\int E_{\parallel} \, ds \neq 0$, is a necessary and sufficient condition for reconnection. As Priest and Forbes [2000] point out, however, this definition is perhaps overly general in that it includes diffusion and double layers, which characterize processes such as turbulent (viscous) magnetic fields and the Aurora. At the other extreme, *Boozer* [2002] adopts a stringent definition of reconnection that equates steady state magnetic flux with ideal field line evolution—i.e., field lines for which $\frac{\partial \mathbf{B}}{\partial t} = 0$. His arguments pertain to field lines that close on themselves and therefore define reconnection as the breakdown of the constraint $\oint \mathbf{E} \cdot \mathbf{dl} = 0$. This definition therefore excludes reconnection at steady state magnetic fields (even if the plasma is nonideal). Others have claimed such a definition is too restrictive, citing as an example the occurrence of reconnection at the Earth's magnetopause with no change in polar cap flux [*Dorelli et al.,* 2007], and Boozer himself makes an exception for the case of astrophysical and space plasmas where field lines rarely close on themselves. Because here we are interested in processes whereby solar wind mass and energy transit into the magnetosphere, in this work we adopt the definition put forward by Priest and Forbes [2000], i.e., that of singular field line reconnection. In addition to a nonvanishing $E_{\parallel}$ along a field line—the singular line, singular field line reconnection stipulates a nearby "X-type topology in a plane perpendicular to the field line" [*Priest and Forbes,* 1989]. (This definition does not mean we are excluding component reconnection. In component reconnection, the fields need not be completely antiparallel. Only the components of the

fields that are antiparallel reconnect. This means that the components of the fields that are perpendicular to the x-line (or singular field line) reconnect and the component that does not reconnect *becomes* the singular field line.) The nature of the topology is shown in Figure 1.6. The presence of a nonvanishing parallel electric field signifies global magnetic reconnection, in which case effects are felt outside of the diffusion region. If the electric field is non-ideal, but not parallel, then effects are not felt outside the diffusion region, and reconnection is local in nature only [*Priest and Forbes*,2000; *Hesse and Schindler*, 1988].
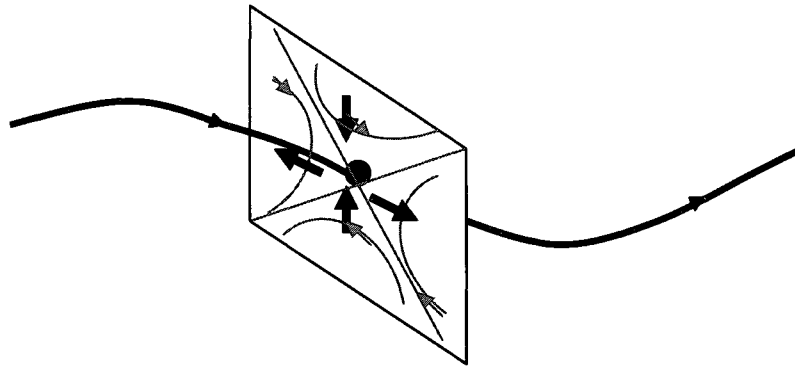
Figure 1.6 An illustration of singular field line reconnection, defined by a singular field line perpendicular to which the field vanishes to form an x-type topology. The singular field line must carry a parallel electric field.

Three-dimensional reconnection at the Earth involves magnetic nulls and separatrices. The magnetic field structure found around a three dimensional reconnection null can be found by expanding the (sufficiently well-behaved) field in a Taylor expansion about the null: $B(r) = r \cdot \nabla B$. The topological degree, or the net difference

between positive and negative nulls, of the domain determines the nature of the field in the domain. The topological degree is given by $deg = \sum_{nulls} sgn[det\,(\nabla B)]$ [*Greene*, 1992; *Kronecker*, 1869]. The sign and type of the eigenvalues of ∇B determine the type of null: if one eigenvalue vanishes and the other two are real, then the reconnection is two-dimensional and the null is an x-line; if one eigenvalue vanishes and the other two are complex, reconnection is two-dimensional and the null is an o-line; if all eigenvalues are real and one is positive, the null is a type A (i.e., bundles of field lines, known as the the spines, flow away from the null); if all eigenvalues are real and one is negative, the null is type B (the spines flow into the null); if one eigenvalue is real and positive and the other two complex conjugates, the null is type A_S; finally, if one eigenvalue is real and negative and the other two are complex conjugates, the null is type B_s. The field lines associated with type A_s and B_s nulls spiral into or out of the null, the direction depending on the sign of the real part of the complex eigenvalues [*Priest and Forbes*, 2000; *Dorelli et al.*, 2007; *Greene*, 1992]. The topological degree of a domain is defined as the difference between the number of type A and the number of type B (or the number of type A_s and the number of type B_s) nulls in the domain. Because the nulls are created in pairs, the topological degree of the global system must identically vanish at all times [*Dorelli et al*, 2007]. As demonstrated in Figure 1.7 (from *Dorelli et al.*, [2007]), at a three dimensional reconnection null the field lines flowing into (or away from) the null form what are called spines (sometimes referred to as γ lines). The field lines fan out in the plane containing the null and perpendicular to the spine in what is referred to as the Σ surface, or the fan plane. Therefore, $\nabla \cdot B = 0$ is always satisfied: the spine field lines flowing away from (toward) a type A (type B) null spread out over the fan plane where
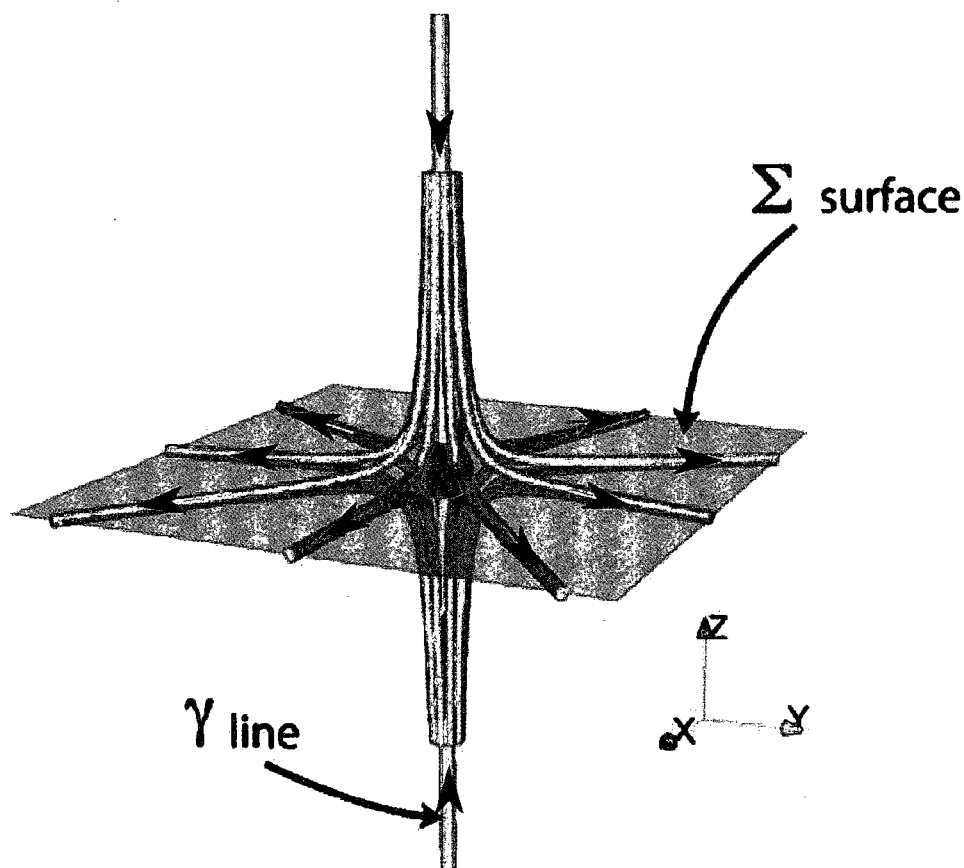
Figure 1.7 At a three dimensional reconnection null, the field lines flowing into (or away from) the null form what are called spines (sometimes referred to as γ lines). The field lines fan out in the plane containing the null and perpendicular to the spine in what is referred to as the Σ surface, or the fan plane. In three-dimensional reconnection, this surface serves as the separatrix surface. The example shown in the figure is for a type B null with **B** = (-2x, y, z). The large black arrows indicate the direction of the field lines.Figure is based on Figure 4. from *Dorelli et al.,* [2007].

they converge toward (diverge from) the null. In three-dimensional reconnection, this surface is the separatrix surface. The example shown in the figure is for a type B null with **B** = (-2x, y, z). At a pair of nulls, one type A and one type B, the two Σ surfaces usually intersect along a line that joins the two nulls, as depicted in Figure 1.8 (from *Dorelli et al.,* [2007]). The intersection is therefore a separator line, along which the magnetic field is nonvanishing: the field lines flowing along the fan plane away from the
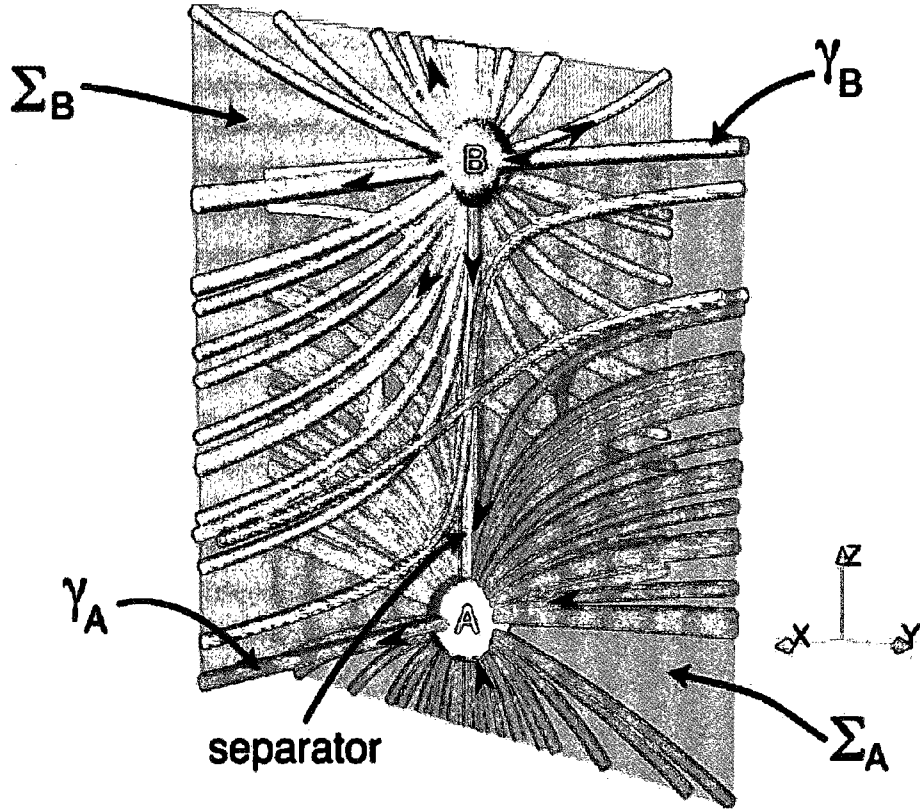
Figure 1.8 At a pair of nulls, one type A and one type B, the two Σ surfaces usually intersect along a line that joins the two nulls. The intersection is therefore a separator line, but one along which the magnetic field is nonvanishing: the field lines flowing along the fan plane away from the type A null head along the separator into the type B null, along its fan plane. The black arrows indicate direcions of sample field lines. This figure is adapted from Figure 5 in *Dorelli et al.*, [2007].

type A null head along the separator into the type B null, along its fan plane [*Priest and Forbes,* 2000; *Dorelli et al,* 2007]. A separator line is a type of a singular field line [*Priest and Forbes,* 2000]. Viewed along the separator, as in Figure 1.9a (from *Dorelli et al.,* [2007]), we see that in a plane perpendicular to the separator at any point along the separator, the field lines form a hyperbolic geometry visually indistinguishable from that of a two-dimensional x-line [*Dorelli et al,* 2007]. A pair of nulls is required for this geometry. However, any of the field lines feeding into the null, including those spanning the fan plane and the spine, can play the role of the singular field line. Reconnection can
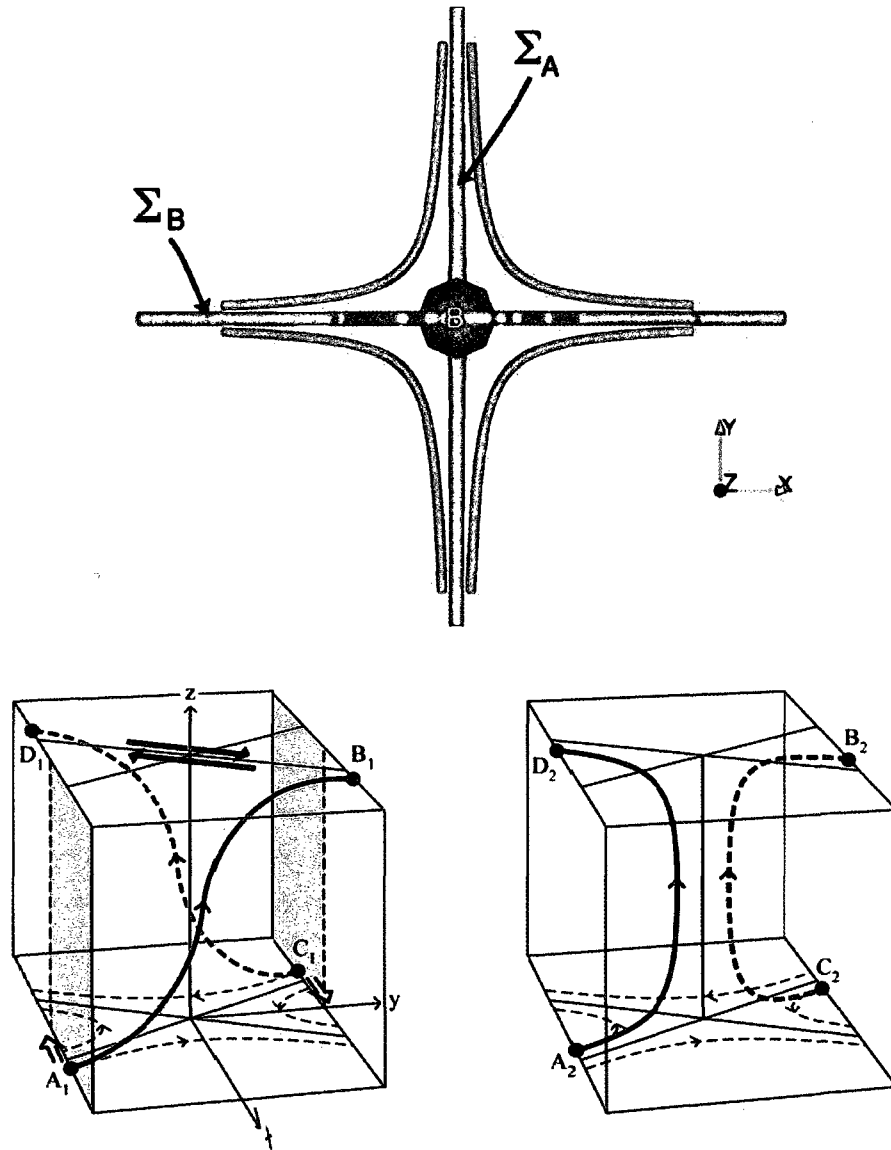
Figure 1.9a-1.9b **(a) Top:** Viewed along the separator, we see that in a plane perpendicular to the separator at any point along the separator, the field lines form a hyperbolic geometry visually indistinguishable from that of a two-dimensional x-line. Figure is from *Dorelli et al.*, [2007]. **(b) Bottom:** Figure 1.9b (from [*Priest et al.*, 2003]), depicting more general singular field line reconnection, would also appear hyperbolic when viewed along the singular field line.

Interplanetary Field Southward
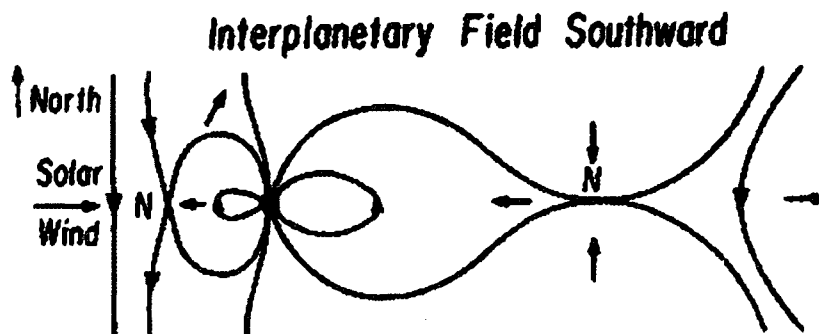
Figure 1.10 The Dungey model of southward IMF reconnection at the subsolar point. The opened field lines convect antisunward and reconnect at the neutral point in the tail. From *Dungey* [1961].

also occur along these lines under the right conditions, i.e., a parallel electric field and a

nearby hyperbolic topology in a plane perpendicular to the field line. Figure 1.9b (from

[*Priest et al.,* 2003]), depicting more general singular field line reconnection, would also

appear hyperbolic when viewed along the singular field line.

1.3 Reconnection at the Magnetopause

Reconnection at the magnetopause was first proposed by *Dungey* [1961] for a

southward IMF. For a perfectly southward IMF, reconnection with closed Earth field

lines happens at the subsolar point (the nose of the magnetopause on the Earth-Sun line),

as pictured in Figure 1.10. In the two-dimensional case of Figure 1.10, reconnection

occurs along a line perpendicular to the neutral point at left marked by an *N*. The merged

(now open) field lines convect antisunward across the polar cap, as shown in Figure 1.11.

The polar cap is the area in the ionosphere occupied by open field lines. The open field

lines from the northern and southern hemisphere now meet in the tail and reconnect at the
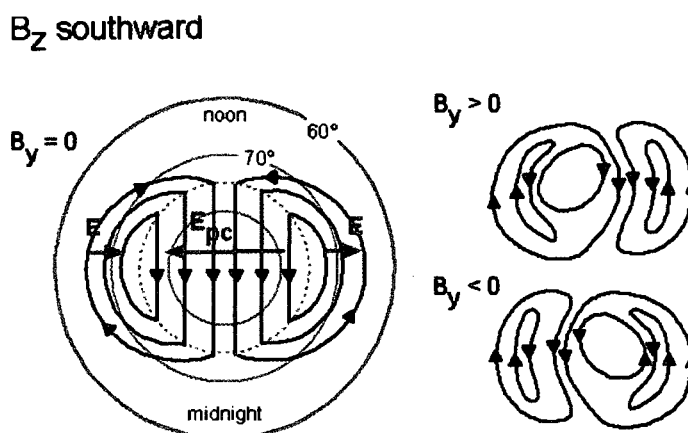
Figure 1.11 A view of two-cell polar cap convection flows for southward IMF. For southward IMF, the electric field from the magnetopause reconnection site maps to the ionosphere to produce antisunward motion of open field lines across the open polar cap (> 80° latitude) . After reconnecting in the tail, the closed field lines return to the dayside along the flanks. Figure from the University of Oulu space physics textbook, http://www.oulu.fi/~spaceweb/textbook/convect.html.

tail neutral point (marked N to the right of Figure 1.11) to reclose and convect sunward along the flanks. Figure 1.11 also shows the electric potential that gets mapped from the magnetopause to the ionosphere to produce antisunward convection there. This process creates a steady-state convection pattern for southward IMF. The reconnection location changes if the IMF has other components, but it still occurs on dayside Earth field lines and the steady-state convection process remains essentially the same. The reconnection may not necessarily be steady state, but it is nevertheless possible to explain the convection as mapping from the solar wind to the ionosphere on open field lines.

For northward IMF, the observed steady-state convection patterns are more difficult to explain, and reconnection requires draping. For purely northward IMF and no dipole tilt, reconnection is expected to proceed as depicted in Figure 1.5b: reconnection occurs simultaneously at the neutral points defined by the locations on the northern and
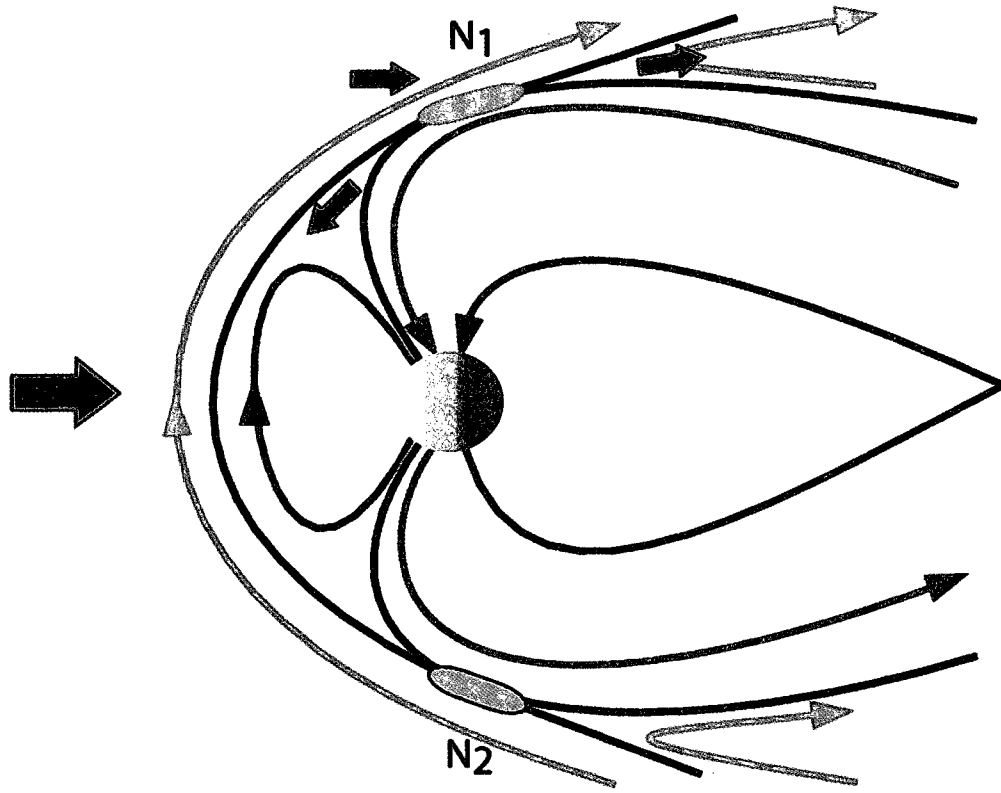
Figure 1.12 In two dimensions, northward IMF reconnection occurs at the neutral points defined by the locations on the northern and southern tail lobes where the earth and draped interplanetary fields are antiparallel. The separators lie at the intersection of the two separatrix surfaces (black curves) that are infinite in the out-of-plane direction. Three topologically distinct regions emerge: IMF field lines (red), open field lines with one foot in the earth and one in the heliosphere (green), and closed earth field lines (blue). This figure represents a configuration with open field lines that corresponds to non-steady convection. Figure is adopted from *Dorelli et al.* [2007].

southern tail lobes where the earth and draped interplanetary fields are antiparallel. However, this does not produce any ionospheric convection on open field lines, does not model solar wind pressure asymmetry, and is not very realistic.

A more general case of northward IMF reconnection is that shown in Figure 1.12 (from *Dorelli et al.* [2007]), where reconnection occurs in both hemispheres, but has produced open field lines (which, for northward IMF violates steady-state conditions, as

we'll discuss). This figure represents an inherently two-dimensional perspective, where the reconnection separators are defined by the intersection of the two separatrix surfaces (black curves) that extend infinitely in the out-of-plane direction. Three topologically distinct regions emerge, one comprising closed Earth field lines (blue), another comprising open field lines with one foot in the earth and one in the heliosphere (green), and closed IMF field lines (red).

The corresponding ionospheric convection involves sunward flows across the center of the open polar cap. *Maezawa* [1976], the first to observe this pattern in the polar cap data, proposed reconnection of northward IMF with antiparallel open tail lobe field lines that convect toward dawn and dusk and then tailward. Previously opened tail lobe field lines then convect sunward to fill the vacated region. This model involves steady state circulation of open field lines only. Other models, as we describe below, involve tailward circulation on closed field lines. In any event, two polar cap convection cells form on open field lines, with the central flow directed sunward. The inclusion of viscous interactions at the magnetopause adds two more convection cells on closed field lines (see Figure 1.13a, for example) (*Reiff and Burch* [1985]). Figure 1.13a displays four-cell convection patterns that hold sway for three different values of B_y (but $B_y < B_z$) [*Potemra et al.*, 1984].

Magnetospheric convection from reconnection can be understood by regarding field lines as equipotentials. Except where reconnection is occurring or there is a parallel electric field, the field lines can be regarded as equipotentials. This means the potential drop between any two field lines is fixed, producing the electric fields between field lines as shown in Figure 1.13b. The dashed lines with arrows represent the direction of the
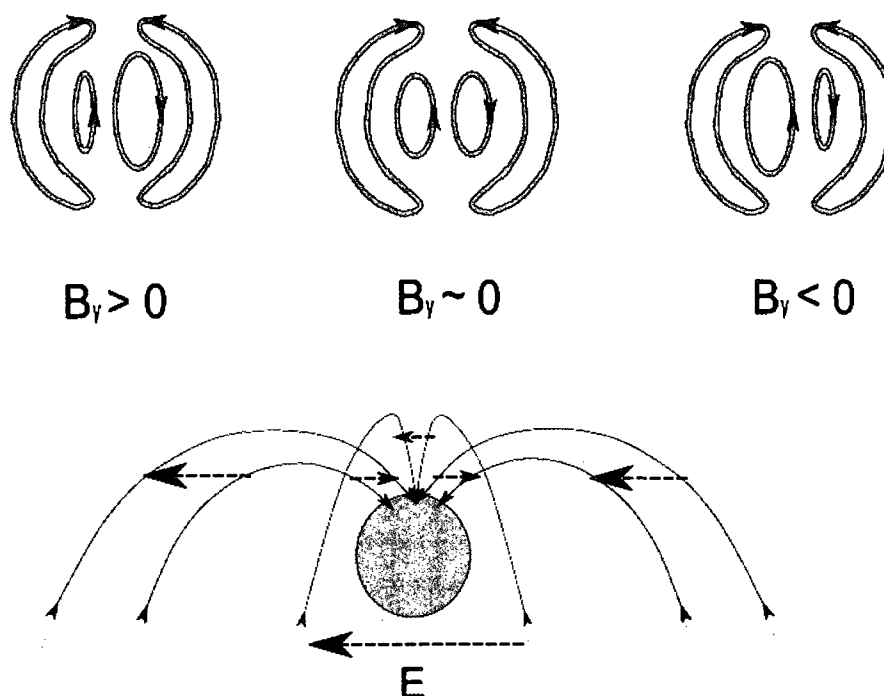
Figure 1.13a-1.13b. (a) The polar cap convection cells associated with northward IMF reconnection for three values of $B_y < B_z$. **(b)** The dashed lines with arrows represent the electric field directions. If regarded as equipotentials, reconnected field lines along the sun-earth line map a dusk-to-dawn electric field in the solar wind to a dusk-to-dawn electric field in the ionosphere, creating a sunward convection in the ionosphere. However, peripheral equipotential field lines map a solar wind dusk-to-dawn electric field to a dawn-to-dusk electric field in the ionosphere—convecting the field lines tailward.

convection electric field between field lines. Reconnected field lines, regarded as equipotentials, map the dusk-to-dawn electric field in the solar wind to the ionosphere. IMF field lines along the Sun-Earth line map a dusk-to-dawn electric field in the solar wind to a dusk-to-dawn electric field in the ionosphere, creating a sunward convection in the ionosphere. However, the peripheral field lines map a solar wind dusk-to-dawn electric field to a dawn-to-dusk electric field in the ionosphere—convecting the field lines tailward. According to current models of reverse convection, once northward IMF reconnection is established, the convection process starts with newly reconnected field
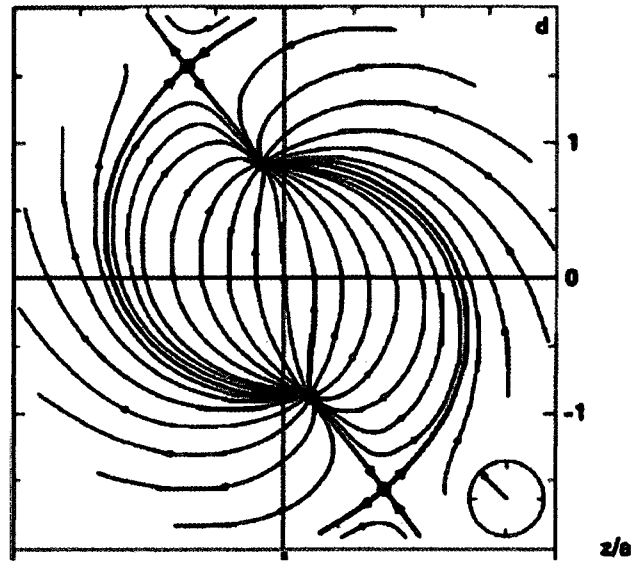
Figure 1.14 The antiparallel merging lines between a northward IMF with a negative y component and an Earth field with zero dipole tilt, from *Crooker* [1985].

lines that drape over the dayside separator, moving sunward for a distance, but soon turning either duskward or dawnward. These field lines head tailward, while new magnetic flux moves forward from the tail lobes to take the place of that which has moved to the tail. If the process is quasi-steady, then the width of the forward moving flux tubes should roughly match the width of the cusp reconnection region. This type of electric field pattern with sunward flows requires current to flow downward between the duskward $E_y > 0$ and $E_y < 0$, and upward between the dawnward $E_y > 0$ and $E_y < 0$, forming cells of downward and upward field-aligned current (FAC) in the dusk and dawn sectors respectively. Models explain sunward flows by way of the $E_y < 0$ at the magnetopause that has now effectively coupled along field lines to the ionosphere (*[Burke et al., 1979; Reiff and Burch,* 1985]*).

More realistic geometries allow for x and y components of the IMF, draping, and dipole tilt. The IMF B_x and B_y and dipole tilt influence the x and y locations of the

reconnection sites and the type of ionospheric convection [*Russell*, 1972; *Cowley*, 1973; *Reiff and Burch*, 1985; *Crooker*, 1979; *Song et al.*, 1999; *Tanaka*, 1999; *Watanabe et al.*, 2004]. For example, Figure 1.14, from *Crooker* [1985], models the locations on the cusps where the IMF and Earth field lines are antiparallel for a northward IMF with negative B_y and zero dipole tilt. For a significant B_y, *Reiff and Burch* [1985] propose the sunward convection of field lines that have reclosed in the the tail as a way of explaining the theta Aurora (an Aurora that is characterized by Auroral emissions along the sun-Earth line to form a shape resembling the Greek letter θ). A strongly negative IMF B_x component, or a dipole tilt, favors reconnection in the summer hemisphere, and a sunward dipole tilt also tends to preclude simultaneous reconnection.

A IMF x component, IMF draping, and dipole tilt can in fact account for steady-state northward IMF convection on open field lines. These factors are important to this work, as our event includes a significant IMF B_x of approximately -10 nT, and a sunward dipole tilt of 9.4° in GSE. (The IMF clock angle is 15° in GSE, and the y-z GSE dipole tilt is 18.2°.) *Crooker* [1992], after *Cowley* [1981,1983], summarizes the possible modes of northward IMF reconnection at the magnetopause, as shown in Figure 1.15. Figure 1.15a and 1.15c depict the case of no dipole or IMF tilt, in which case reconnection is expected to occur simultaneously at the northern and southern cusps to form new closed field lines and new IMF field lines. Simultaneous merging on closed field lines, as in Figure 1.15a, after Dungey's original 1963 model [*Dungey*, 1963], conserves flux, but it doesn't explain sunward convection on the open polar cap. Flux that has transferred from closed night-side to closed dayside field lines must make its way tailward on closed field lines by a viscous interaction. Simultaneous reconnection on open field lines, as in Figure
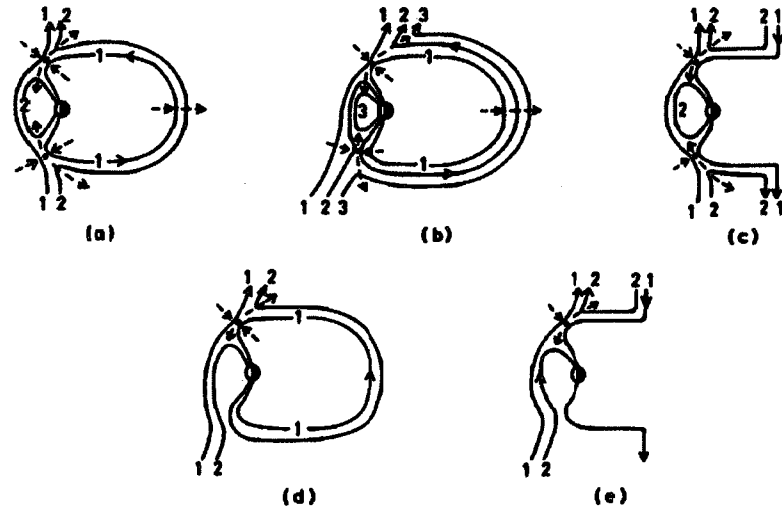
Figure 1.15. From *Crooker* [2005], after *Cowley* [1981, 1983], a catalog of northward IMF merging topologies. The numbers indicate the sequence of field line merging.

1.15c, does not conserve flux. Figure 1.15c therefore represents a nonsteady case. One way to circumvent this and allow steady northward IMF reconnection on open field lines is to add an IMF or dipole tilt, as in Figure 1.15e, because now reconnection occurs in only one hemisphere on the same field line, to form a new open and new IMF field lines. IMF or dipole tilts also produce steady state reconnection onto closed field lines if the reconnection occurs at both the northern and southern hemispheres, as in Figure 1.15b. (*Kan and Burke* [1985] describe the presence of plasma sheet particles in the theta bar of the so-called theta aurora by northward IMF reconnection onto closed field lines in one hemisphere, as in Figure 1.15d, but this model is intrinsically nonsteady.)

However, Figure 1.15d, where tilted IMF field lines reconnect in only one hemisphere onto closed field lines, to produce two new open field lines, is not steady

state. And even if (or, perhaps, especially if) the reconnection occurs in one of the steady state modes, theoretical models initially failed to explain the sunward ionospheric convection observed by *Maezawa* [1976] and others. *Vasyliunas* [1988] and *Hill* [1992] both made arguments finding steady state sunward convection on open field lines unphysical, since the sunward convection on part of the field lines accompanied by antisunward convection on the other part should produce a time-dependent change in **B**.

Crooker [1992] resolves both of the above mentioned obstacles by introducing a model with a sunward dipole tilt. It explains quasi-steady state sunward convection on newly-opened field lines. She proposes that the magnetosheath portion of the reconnected lobe that has reconnected first with a closed field line in the summer hemisphere over-drapes the dayside. In this configuration, it feels a tug in the antisunward direction, transmitted as a sunward tug onto the ionsopheric end of the field line. This mechanism allows the geomagnetic portion of the field line to convect sunward and the IMF portion to convect antisunward without any change of shape in the field line. The nonsteady feature of her model involves the sunward convection of open field lines in the tail to fill the vacancy left by newly reconnected flux tubes that have moved sunward. Because the ionosphere is incompressible ($\nabla \cdot \mathbf{v} = 0$), the tail flux tubes must replace the footpoints of the flux tubes that have been driven sunward by the merging potential. In this case, since the IMF portion is dragged antisunward while the geomagnetic portion ploughs sunward, the field line changes shape in time. Figure 1.16 displays the merging pattern and convection cells her model yields for varying values of IMF B_x and dipolt tilt. *Watanabe et al.* [2004; 2005] extends Crooker's exploration of dipole tilts in vacuum superposition topologies to an MHD simulation. In an MHD simulation of the magnetosphere with a
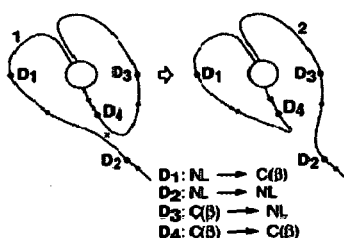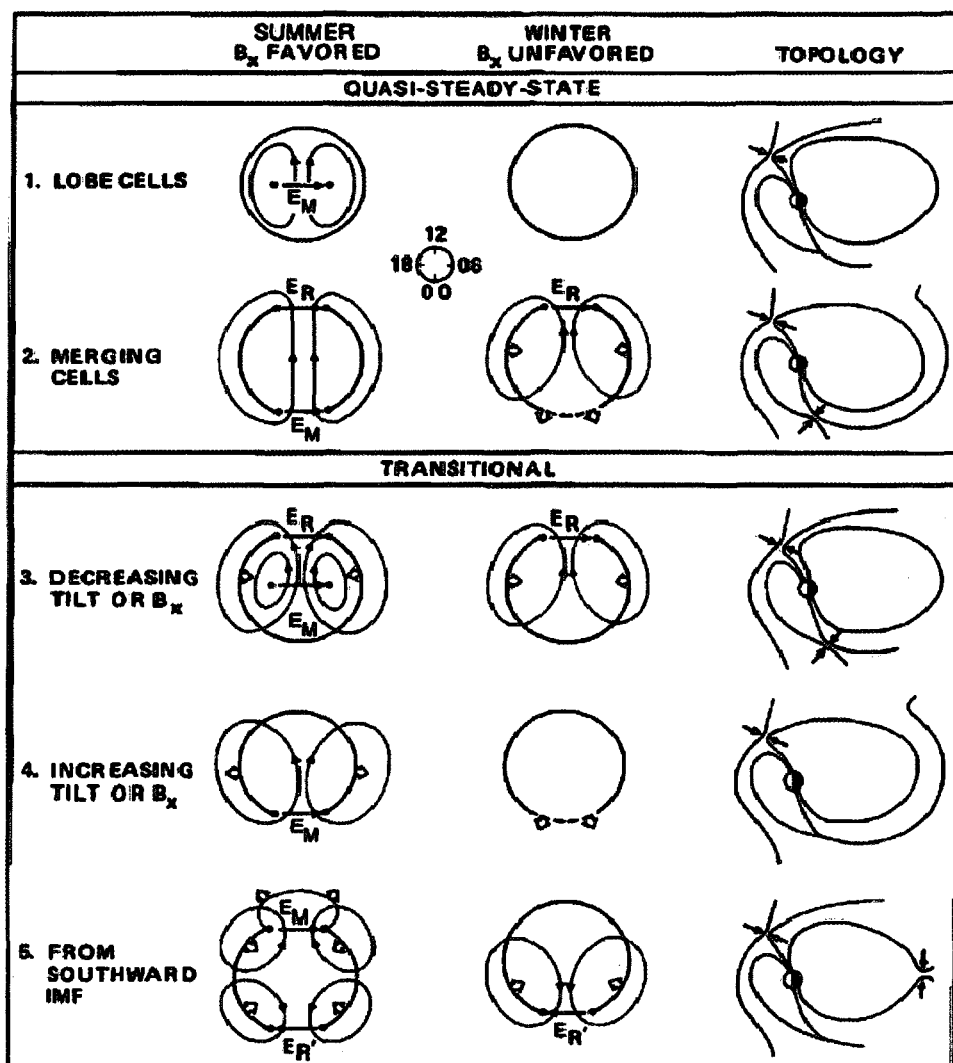
Figure 1.16a - 1.16b **(a)** Reverse ionospheric convection and magnetic topology for several IMF B_x and dipole tilts in the *Crooker* [1992] model. E_R is the electric field from what the author called the 'internal' reconnection site (the reconnection site in the winter hemisphere—the southern hemisphere in this figure.) E_M is the electric field mapped from the merging site on the magnetopause (the northern hemisphere in this figure). **(b)** The *Watanabe et al.* [2005] developement of the Crooker model includes reconnection between an overdraped field line and a closed tail field line. The overdraped field lines has first reconnected to a closed summer hemisphere field line.

dipole tilt, so as to include the effects of realistic features such as current sheets, he also finds reconnection in the winter hemisphere between an overdraped field line and a closed field line that lies on the nightside (or the flanks). The overdraped field line must have first reconnected to an open field line in the summer hemisphere. In other words, a field line that has opened and overdraped by way of reconnection as in Figure 1.15e then reconnects to a closed tail field line to form a new open and closed field line. The process is demonstrated in Figure 1.16b. He finds that the effect of a $|B_y| \sim B_z$ is to force the overdraping onto the flanks so that reconnection with the winter hemisphere closed field line is flankward of the tail [*Watanabe et al.,* 2004].

In terms of separatrix/separator/null topology, reconnection that occurs on already opened Earth field lines lies on the separatrix surface between open and IMF field lines. Reconnection that occurs between an IMF and a closed Earth field line must occur along the separator, because an IMF field line is making its way all the way to the closed field line boundary. If an open and closed field line merge, as in *Watanabe et al.* [2005], then the merging lies on the inner separatrix boundary between open and closed field lines. Reconnection between two open field lines—i.e., two lobe field lines, as in the second half of the process portrayed in Figure 1.15b, occurs inside the magnetopause, somewhere between the inner and outer separatrices. In fact, *Crooker* [1992] coined this process *internal reconnection*. Where exactly on the separator or on or between the separatrices the reconnection occurs depends on where the parallel electric field and perpendicular vanishing field lie. From the simulation study in Chapter 4, we will determine which mode of reconnection occurs on which of these topological boundaries for this real event.

The relative importance of component versus anti-parallel magnetopause reconnection is of longstanding debate (e.g., *Sonnerup* [1974], *Crooker* [1979], *Sonnerup* [1974], *Cowley* [1976], *Gosling,* [1991; *Fuselier et a.,* [2000a], *Fuselier et al.* [2000b], and *Karimabadi* [2005]). Component reconnection is associated with the concept of driven reconnection with a guide field, while the physics of anti-parallel reconnection is more in keeping with the theory of tearing. This can occur under sufficient compression of the fields. Simulations, models, and observations have alternatively favored both models (e.g., on the component reconnection side, see *Sonnerup* [1974], *Gosling et al.* [1990], *Paschmann et al.* [1993], *Fuselier et al.* [2000a], *Swisdak et al.* [*2003*], *Karimabadi et al.* [2005], and on the antiparallel reconnection side, see *Crooker* [1979], *Quest and Coroniti* [1981], *Gosling et al.* [1991], *Kessel et al.* [1996], *Russell et al.* [1998], *Fuselier et al.* [2000b], and *Onsager and Fuselier* [1994]), though it was not clear whether component reconnection could occur for arbitrary clock angles and what constraints the guide field must satisfy [*Sonnerup, 1974; Cowley,* 1976]. The recent statistical analyses of *Fuselier et al.* [2000b] and *Trattner et al.* [2004] for cases of northward IMF reconnection observed that both forms occurred simultaneously at different locations. *Trattner et al.* [2004] found that the type of merging depended only on the location along the magnetopause and not on solar wind conditions. Later work with Polar spacecraft ion measurements for southward IMF events revealed reconnection occurring at the cusps and across the dayside magnetopause wherever the magnetic shear maximizes, whether it be 180° (antiparallel reconnection) or less (component reconnection) [*Trattner et al.,* 2007].

Both component and antiparallel merging have their roots in two-dimensional models that, for northward IMF, place two separate x-lines in each hemisphere at the intersection of infinitely out-of-plane separatrix surfaces. The parallel electric field and current sheets are localized at the x-lines thus defined. Once one allows for three-dimensional field dependence, a very different picture—in a vacuum, that of Dungey's vacuum superposition topology—emerges [*Dorelli et al.*, 2007]. In this model a *spherical* separatrix surface demarcates regions of open and closed field lines, while another spherical separatrix surface separates open from IMF field lines. A single IMF field line passes through both nulls simultaneously. In contrast to the two-dimensional view, the intersection of these surfaces forms a single separator line linking the two cusp nulls in each hemisphere. Figure 1.5a (from *Dorelli et al.* [2007]) is an example of such a model with a dipole tilt. The red lines go through the northern hemisphere null (red sphere), the blue lines through the southern hemisphere null (blue sphere), while the yellow line is a closed field line that approximates the location of the separator line. For the case of a zero-dipole tilt, there is no separator: there is *one* spherical separatrix surface that separates closed from IMF field lines, for the IMF and the Earth dipole field merge only at two nulls, one over each of the Earth's poles. Figure 1.5b portrays this case. Even once a three-dimensional model is adopted, there is the further question of how the parallel electric field and particle diffusion arising from reconnection are distributed on the magnetopause. As *Hesse and Schindler* [1988] demonstrate, since there is no longer a concurrence of the singular field line with a null line (antiparallel reconnection), the magnetic topology alone is insufficient to identify the location of reconnection.

1.4 Background and How Our Work Contributes to Studies of Northward IMF Reconnection

Researchers have established an increasing number of observations of reconnection under a northward IMF (e. g., *Kessel et al.*, [1996]; *Fuselier et al.*, [2000a]; *Fuselier et al.*, [2000b]; *Onsager et al.*, [2001]; *Mozer et al.*, [2002]; *Scudder et al.*, [2002]; *Frey et al.*, [2003]; *Mozer et al.*, [2005]). These have included *in situ* multi-spacecraft observations of reconnection in the tail [*Runov, et al.*, 2003; *Borg et al.*, 2005; *Wygant et al.*, 2005; *Eastwood et al.*, 2007], multiple and single spacecraft remote sensing of cusp reconnection [*Fuselier et al.*, 2000; *Onsager et al.*, 2001; *Pitout et al.*, 2001; *Vontrat-Rebec et al.*, 2003], and single spacecraft *in situ* detection in the cusp and dayside regions [*Mozer et al.*, 2002; *Scudder et al.*, 2002; *Mozer et al.*, 2005]. One recent investigation using data from the Polar spacecraft placed the spacecraft within the electron demagnetization region of a northward IMF reconnection line [*Scudder et al.*, 2002].

Recent simulations have documented the micro-structure of two and three dimensional reconnection, with and without a guide field [*Hesse et al.*, 1991; *Shay et al.*, 1991; *Xie et al.*, 2000; *Birn et al.*, 2001; *Hesse et al.*, 2001; *Pritchett*, 2001;*Wiegelmann and Buchner*, 2001; *Yin et al.*, 2001; *Craig et al.*, 2003; *Rogers et al.*, 2003; *Hesse et al.*, 2004; *Ricci et al.*, 2004], locating the sizes and locations of regions where the various terms in the generalized Ohm's law hold sway. While theoretical simulations have been working to discern the micro-scale physics and the dimensions of the diffusion regions where particles become demagnetized, recent magnetopause observations claim to have detected signatures of these spatial scales surrounding an x-line. At the same time, others

have been exploring the global structure of magnetopause reconnection through improved satellite data and MHD simulations: the degree of the magnetic shear involved, the scale of the separators, and possible three-dimensional dependence of the magnetic topology (e.g., *Onsager and Fuselier* [1994], *Song et al.* [1999], *Crooker et al.* [1998], *Raeder et al.* [2001], *Dorelli et al.* [2007], *Phan et al.* [2006], and *Trattner et al.* [2006]).

Recently, some MHD models have associated parallel potential drops with the length of the separator between the cusps, thus removing the association of northern and southern nulls with localized regions of parallel electric fields and diffusion regions [*Dorelli et al* 2007; *Crooker et al.*, 1998]. In a simulation of a purely duskward IMF, for example, *Siscoe et al.* [2001] find that the parallel electric field is in fact stronger at the subsolar point than at the two magnetic nulls. For a northward IMF at a 45° clock angle, zero dipole or IMF tilt, and a uniform resistive MHD model, *Dorelli et al.* [2007] find a parallel electric field distributed across the dayside separator. Using a Gumics-4 global MHD simulation of an artificial event, *Laitinen et al.* [2006] find the global separator that stretches across the dayside and the nightside. Based on where the separator intersects the Poynting vector divergence, they find large diffusions regions in the tail and on the dayside magnetopause.

However, as far as we are aware, this study is the first to address *in situ* multi-point observations and a global 3D resistive MHD simulation of a real northward IMF cusp reconnection event on the dayside. Also, this thesis presents the first attempt to compare the *in situ* local and the global perspectives of the same event. Previous observations differ in that they involve remote detection, a single spacecraft, the magnetotail, or a southward IMF. Previous simulations of even northward IMF events

differ in that they either do not model a real event, they make simplifying assumptions such as zero tilt, or they interpret the topology in terms of 2D magnetic field x-lines. First, we take advantage of the Cluster multi-point measurements to directly evaluate the length and time scales of a northward IMF reconnection current sheet and its associated demagnetization regions. Furthermore, we determine an x-line centered coordinate system that removes the motion of the site relative to the spacecraft. Thus we can configure all of the data in this coordinate system for comparison to simulation models, creating a two dimensional spatially superposed epoch analysis. As far as we are aware, this is the first time experimental data, and in particular multiple-spacecraft data, have been analyzed in this coordinate system. Moreover, we extend this type of analysis to extract not just the current sheet thickness but the spatial distribution of most of the available data, including particle moments, currents, electric and magnetic fields, and temperature. We compare the details of our results to other experimental observations and to simulations. Next, on larger scales, DMSP and Iridium ionospheric measurements and the Open Global Geospace Circulation Model (GGCM) resistive MHD simulation provide a point of comparison to the Cluster and IMAGE observations. When synthesized, these tools yield new insights into the nature of global 3D reconnection and what we can expect spacecraft to observe for northward IMF magnetopause reconnection. Iridium measures the magnetic field and infers the field-aligned currents (FACs). DMSP measures the polar cap potential drop, convection flows and magnetic fields that correspond to this northward IMF reconnection. The simulation reveals the separator and magnetic nulls and the distribution of the parallel electric field. We compare the reconnection topology derived from the simulation to that inferred from Cluster data. We

also make connections between simulations and observations that demonstrate how the three-dimensional global picture of northward IMF reconnection couples the IMF to earth field lines in such a way as to create polar cap potential drops and reverse convection in the ionosphere. Comparing the size, location, and magnitude of the GGCM simulation's separator electric field that couples to the ionosphere with the size of sunward flows measured by DMSP in the ionosphere links convection observations with 3D reconnection. The global MHD simulation also yields insight into where, with what topology, and on what type of field lines, merging occurs. The satellite and simulation data together create a picture of northward IMF magnetopause merging that is a far cry from the simplicity of the two-dimensional neutral line with or without a guide field. The picture that emerges impacts what observers can expect to look for in magnetopause reconnection data.

In the next chapter of this thesis, we will briefly discuss the data and software tools required for this study, including a discussion of the relevant spacecraft instruments. In Chapter 3, we present a detailed study of the local scale magnetic, electric, and flow properties of the event based entirely on *in situ* Cluster measurements. Chapter 4 covers the global properties of the reconnection event, as inferred from synthesizing Cluster data, two sets of ionospheric satellite data, and a global resistive MHD simulation of the actual event. Finally, in Chapter 5 we will summarize the major conclusions. Except where noted in the text, throughout we will work in SI units.

Chapter 2

SATELLITE INSTRUMENTATION AND NUMERICAL TOOLS

2.1 The Satellites

The IMAGE spacecraft provided the first data signaling the reconnection event of 18 March, 2002 [*Frey et al.*, 2003]. The FUV SI-12 instrument, one of several UV imaging instruments on board, observed the auroral Lyman α emission produced by charge exchange with the outflow of protons from the magnetopause reconnection site. The instrument measures the Doppler-shifted Lyman α emission from charge exchange between precipitating protons and neutral atmospheric atoms or molecules. The emission wavelength depends on the line-of-sight velocity of the resulting hydrogen. The instrument, highly-transmitting at the Doppler-shifted Lyman α wavelengths of 121.8 nm and 122.1 nm, detects emissions from proton with energies that exceed 1 keV and filters out the background glow of the stationary geocoronal hydrogen at 121.6 nm [*Mende et al.*, 2003]. The instrument has a spatial resolution of less than 100 km at apogee distances and a temporal resolution of 120s (Harald Frey, personal communication).

The Cluster mission, launched in 2000, consists of four spacecraft that fly in close formation to investigate the size and structure of boundaries in the Earth's vicinity. The spacecraft fly in a tetrahedral formation of varying size and planarity—ranging from sizes on the order of 100 km to on the order of 10,000 km, adapted to best resolve the dimensions of interest at a particular location. The spacecraft positions in the tetrahedron are specified at two places within the orbit and at other times simply follow the
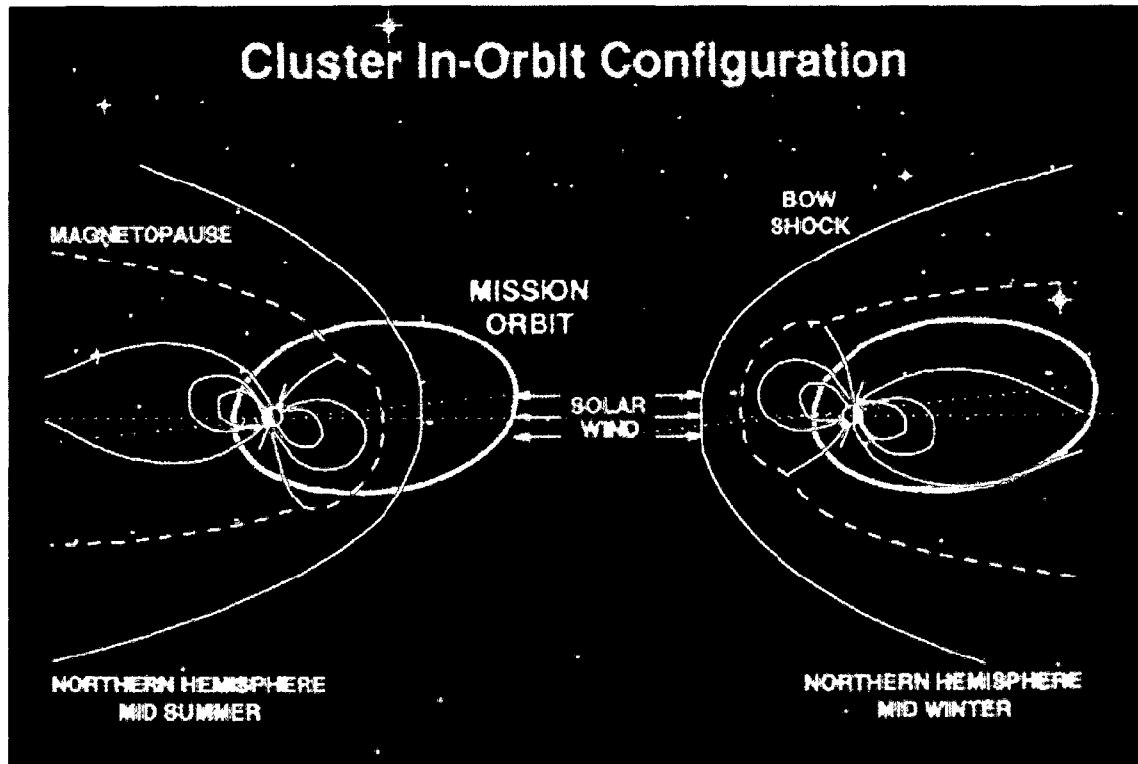
Figure 2.1 The Cluster orbit. From *Credland et al.* [1997].

gravitational dynamics. Thus, the shape of the tetrahedron ranges from very flat and pancake-like, through knife-blade-like, sphere-like, cigar-like, to potato-like. The shape of the tetrahedron has a large impact on the resolution of observed structures. The spacecrafts' highly-elliptical orbit, with an apogee on the order of 20 R_E, where R_E designates Earth radius, is inertially fixed. This means the apogee moves from the tail region to the solar-wind region and back over the course of a year [*Credland et al.,* 1997]. The orbit includes the polar cusp regions. Typical mid-summer and mid-winter orbits are shown in Figure 2.1 (from *Credland et al.* [1997]).

The instruments onboard Cluster that are relevant to this thesis are the ion and electron spectrometers (referred to as CIS and PEACE, respectively), the Electric Field and Wave instrument (EFW), and the magnetometer (FGM). The particle spectrometers
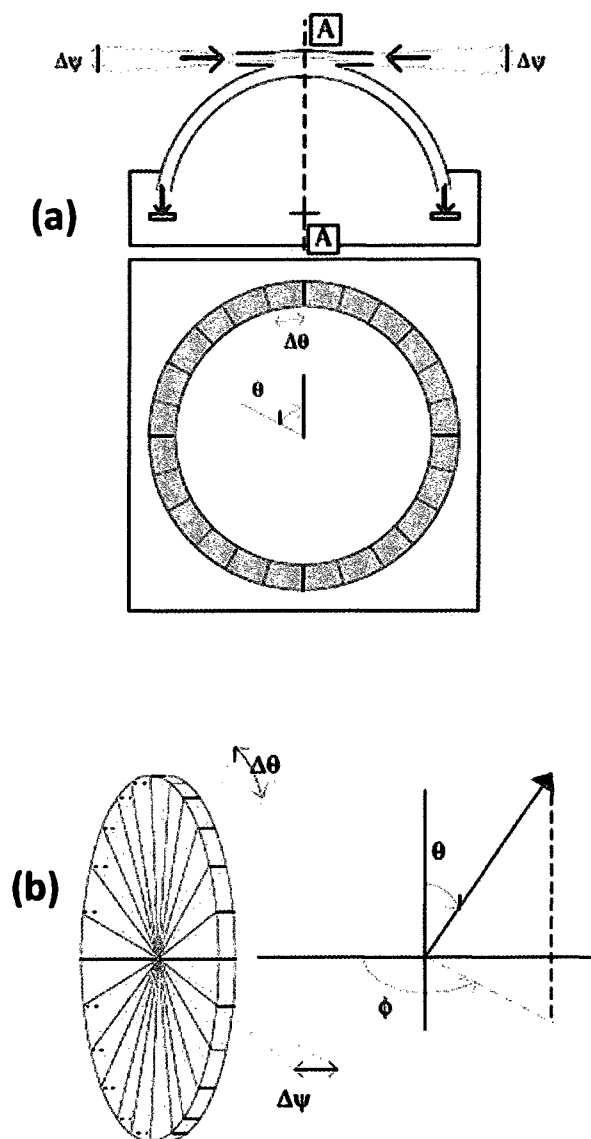
Figure 2.2 (a) Top: Side and top views of a quadrispherical top-hat analyzer. The aperture accepts particles within $\Delta\psi$. The aperture is circular, so that all polar angles θ are accepted for a given azimuth φ. **(b) Bottom:** The spacecraft spin axis is along θ = 0 and 180°. The azimuthal angles φ is covered by the spacecraft's spin. From *Fazakerley et al.* [1997].

measure the ion and electron moments (e.g., density, velocity, pressure tensor, heat flux tensor) by determining the three-dimensional particle distributions during a complete (~ 4 s) spin of the spacecraft.

The CIS instrument includes a time-of-flight ion composition and distribution function analyzer (CODIF) and a Hot Ion Analyzer (HIA). CODIF measures the distributions of H^+, He^+, He^{++}, and O^+ with energies from 0 to 40 keV with a 22.5° polar angular resolution. The CODIF instrument has an instantaneous 360° × 8° (polar by azimuthal) field-of-view that covers 4π steradians after a full spin. The ion energies are measured by an energy-per-charge electrostatic analyzer (ESA), and subsequently processed by a time-of-flight analyzer to discriminate the mass-to-charge ratio. Figure 2.2a is a side and top view of the ESA, a so-called quadrispherical (or top-hat) analyzer. The top-hat consists of three hemispheres, an inner, an outer, and a small circular top cap which creates the entrance aperture. The aperture's circular symmetry allows detection of all polar angles θ, and as in Figure 2.2b, all azimuthal angles φ are swept out by the spacecraft's spin. A voltage applied between the inner and outer hemispheres deflects incoming particles by an angle ψ_n such that only particles within a given velocity v_s and azimuthal angular range $\Delta\psi$ make it down to the exit aperture. Thus the applied voltage drop selects only values of $v_s\sin\Delta\psi + v_s\sin\psi_n$ such that the particle makes it to the exit without striking the shell wall. At the exit the particles are accelerated through a potential V and then directed into the TOF analyzer. They first strike a thin foil, from which secondary electrons signal the start time and also give the angular position of the ions. When the particles strike a microchannel plate (MCP) the stop time is measured [*Rème et al.*, 1997] and a count is produced. Since the distance d between the MCP and the foil is known, the time-of-flight τ measured, the velocity v_f can be found from $v_f = d/\tau$. Conservation of energy gives the mass to charge number Z ratio, i.e.,

$$\frac{m}{Z} = \frac{2\left(\frac{\frac{1}{2}mv_s^2}{Z} + eV\right)}{v_f^2} \tag{2.1}$$

Though HIA does not resolve mass, it provides higher angular resolution velocity measurements. Like CODIF it has two different sensitivies and also boasts a larger dynamic range and an angular resolution of $5.6° \times 5.6°$. It has two $180°$ field-of-view sections parallel to the spin axis, one with high gain, one with low gain. The high gain section is divided into 16 anodes of $11.25°$ each, and the low gain section has 8 anodes of $11.25°$ each and 9 anodes of $5.6°$ (the full $180°$ is not used). A full 2D distribution is measured every high voltage sweep period (62.5 ms), while the full 4π steradians is accumulated over each spin [*Rème et al.*, 1997]. The velocities are determined by the TOF method.

The Plasma Electron and Current Experiment (PEACE) measures the electron moments in the energy range 0.59 eV to 26.4 keV also by way of a pair of hemispherical electrostatic analyzers of the same principle used in the CIS experiment. The voltage across the detector heads sweeps through a range of values to selectively admit electrons of a range of particular energies and thus construct a picture of the electron velocity distribution. Two hemispherical sensors on opposite sides of the spacecraft each give a snapshot of $180°$ polar angles, as in Figure 2.3. Each sensor records in one of two partially overlapping energy ranges: the Low Energy Electron Analyzer (LEEA) from 0.59 to 9.45 eV, and the High Energy Electron Analyzer (HEEA) measures the higher energies (though the range of overlap can be specified). The azimuthal angles are swept out during a spin to give the full 4π steradians of coverage. Thus in the overlap energy
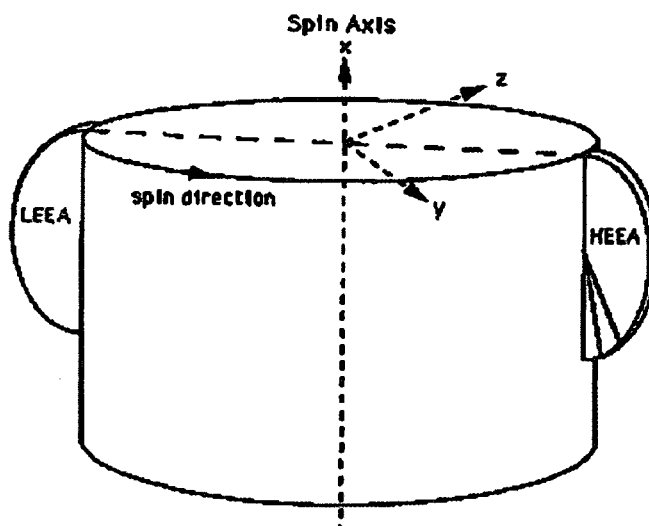
Figure 2.3 The HEEA and LEEA electrostatic analyzers of the Cluster PEACE instrument as they are mounted on the spacecraft body.

range, the complete angular range of data is collected in a spacecraft half-spin, and all other energies in a full spin. Each hemispherical sensor is divided into anodes with 15° polar resolution. In one of the hemispherical sensors, the coarser angular resolutions anodes are further subdivided into finer angular resolution zones of 3.75°. The anodes in one hemispherical sensor subtend 2.8° azimuthal resolution, and those in the other sensor subtend 5.3° angular resolution. The energy range is covered in 88 bins, linearly spaced up to 9.45 eV, logarithmically spaced thereafter. There are four energy sweep modes (Low Angular Resolution, or LAR, Medium Angular Resolution, or MAR, and High Angular Resolution, or HAR) that vary the azimuthal angular resolution from 5.625° to 22.5° by varying the number of energy sweeps per spin [*Johnstone et al.*, 1997].

One of the PEACE data products, the 3DF particle distribution, is of particular relevance to this thesis. It contains both LEEA and HEEA coarse zone data at the highest resolution possible. No assumptions about particle gyrotropy need to be made in this

case. In general, because of telemetry limitations, this form of the data is saved and telemetered to the ground only when the instrument is in burst mode. The one exception is Cluster 2, for which this form of the data is always available, owing to the fact that the failure of its CIS instrument renders more telemetry and storage capability available to PEACE. All other moments are calculated assuming gyrotropic electrons. When 3DF distributions are telemetered to the ground in burst mode, the moments they produce are then subjected to the best and most up-to-date calibrations and post-processing available. Otherwise, the moments are calculated onboard and no post-processing or improved calibrations are possible. For this study, the 3DF distribution is only available from Cluster 2.

The electrostatic analyzers record counts per energy per steradian. To convert these to particle moments such as velocity, pressure, temperature, etc., entails summations over the energies and polar and azimuthal angles of the counts. These summations take the place of integrations of weighted particle distribution functions $f(v)$ over phase space volumes d^3v, i. e., $\int_0^\infty v^n f(v) d^3 v$, where v^n is an n-fold dyadic product. In spherical polar velocity space coordinates, the infinitesimal volume element is $d^3v = v^2 dv \sin\theta d\theta d\varphi$. It can be shown that, for this kind of analyzer, $\Delta E/E = dv/v = $ constant, where E is the energy [Fazakerley et al., 1997]. Thus, $d^3v = v^2 dv = v^3 dv/v = $ constant $\cdot v^3$, meaning d^3v is directly proportional to v^3. Since the number flux varies as v, the count rate varies as the phase space density times v^4. The exact relation between the mean phase space density f_{ijk} in the acceptance volume d^3v and the counts C_{ijk} detected in the accumulation time t_{acc} is $f_{ijk} = C_{ijk}/(t_{acc} v^4_k G_i)$, where v_k is the velocity corresponding to the center energy of the accumulation time interval, and the indices i, j, k refer to θ, φ,

Density:

$$N = \sum_k \frac{1}{V(E)} \sum_\phi \sum_\theta C(\theta, \phi, E)$$

Number flux density vector:

$$NV_x = \sum_E \sum_\phi \cos\phi \sum_\theta \cos\theta \, C(\theta, \phi, E)$$

$$NV_y = \sum_E \sum_\phi \sin\phi \sum_\theta \cos\theta \, C(\theta, \phi, E)$$

$$NV_z = \sum_E \sum_\phi \sum_\theta \sin\theta \, C(\theta, \phi, E)$$

Momentum flux density tensor:

$$P_{xx} = \sum_E V(E) \sum_\phi \cos^2\phi \sum_\theta \cos^2\theta \, C(\theta, \phi, E)$$

$$P_{yy} = \sum_E V(E) \sum_\phi \sin^2\phi \sum_\theta \cos^2\theta \, C(\theta, \phi, E)$$

$$P_{zz} = \sum_E V(E) \sum_\phi \sum_\theta \sin^2\theta \, C(\theta, \phi, E)$$

$$P_{xy} = \sum_E V(E) \sum_\phi \cos\phi \sin\phi \sum_\theta \cos^2\theta \, C(\theta, \phi, E)$$

$$P_{xz} = \sum_E V(E) \sum_\phi \cos\phi \sum_\theta \cos\theta \sin\theta \, C(\theta, \phi, E)$$

$$P_{yz} = \sum_E V(E) \sum_\phi \sin\phi \sum_\theta \cos\theta \sin\theta \, C(\theta, \phi, E)$$

Energy flux density vector:

$$H_x = \sum_E V^2(E) \sum_\phi \cos\phi \sum_\theta \cos\theta \, C(\theta, \phi, E)$$

$$H_y = \sum_E V^2(E) \sum_\phi \sin\phi \sum_\theta \cos\theta \, C(\theta, \phi, E)$$

$$H_z = \sum_E V^2(E) \sum_\phi \sum_\theta \sin\theta \, C(\theta, \phi, E)$$

Table 2.1 The moments sums performed onboard the spacecraft before accounting for calibration factors, particle mass, and detector response. N is density, V velocity, P pressure, and H heat flux. From *Paschmann et al* [1997].

and E. G_i is the analyzer response function integrated over the range of velocities accepted by the aperture. G is independent of the energy of the measurement, but it could vary with polar zone [*Fazakerley et al.*, 1997]. Table 2.1 shows the onboard summations for all moments, where E is the energy and $V(E)$ the velocity per energy bin and θ and φ the polar and azimuthal angles measured by the analyzer. The counts C_{ijk} have already

been corrected for detector dead time and the energy-dependent detection efficiency, and a factor cosθ has been applied that removes the over-sampling at high elevation angles [*Paschmann et al.,* 1997]. The table does not include a detector response function factor, calibration factors, particle mass, or integration volume elements, which can be applied later. These moments are calculated for separate particle species and can be summed over species for single fluid quantities. Errors involved in all moments calculations are discussed fully in the next chapter.

To measure the electric field, the Electric Fields and Waves (EFW) instrument uses four spherical sensors at the ends of 50 m perpendicular and externally nonconducting booms that lie in the spin plane of the spacecraft. The double spherical probes are 8 cm aluminum spheres coated with a graphite conducting paint [*Gustafsson et al.,* 1997]. Assuming the Debye length (the length over which mobile charged particles shield potentials from the rest of the plasma) is less than the antenna length, spherical probes couple to the surrounding plasma sheath either resistively for frequencies < $(RC)^{-1}$, and capacitively for frequencies > $(RC)^{-1}$, where R is the resistance and C the capacity of the plasma sheath surrounding the probe. (The sheath is a polarized layer surrounding an object inserted within a plasma that largely excludes electrons. This is because the object collects electrons, due to their higher thermal speeds and hence higher collision rates. The resulting negatively charged surface tends to repel other electrons and attract ions.) The resistance of the preamp is made much less than R when coupling is resistive, and the capacity of the preamp made much larger than C for capacitive coupling. The electric field is then found from the potential drop between the probes after correcting for the effective length. For wavelengths longer than the antenna length,

which is usually the case, the effective length of the antenna is the measured voltage divided by an applied electric field [*Russell*, 2008]. The probe can sample up to 36,000 times per second, though the sampling period in this work is 0.04 s. The instrument is capable of measuring quasi-static electric fields up to 700 mV/m and electric waves of bandwidth 4 kHz [*Gustafsson et al.*, 1997]. The third component of the electric field is calculated from the assumption that $\mathbf{E \cdot B} = 0$, which is generally valid unless there are parallel electric fields, as at an x-line. However, the discrepancy between perpendicular particle velocities and $\mathbf{E \times B}/B^2$ gives some insight into any breakdowns in the ideal MHD assumption. During the mission and preceding the event discussed here, one of the probes on Cluster 1 failed. Therefore we will not use electric field data from Cluster 1. As for accuracies, there is an offset in E_i which is at maximum 1mV/m, and the amplitude of the electric field can be underestimated by at most 10%. Usually the data for a particular event can be calibrated and these errors can be significantly reduced (Yuri Khotyaintsev, personal communication). One problem is that an artificial $\mathbf{E}$ may be created by a wake of supersonic ions streaming around the charged spacecraft. Although this problem was discovered in the Earth's tail lobes (see *Engwall et al.* [2006]), the same phenomenon may occur near the magnetopause when cool (few eV) ionospheric ions are present (Mats André, EFW PI, personal communication). However, in order for this wake to form, the plasma must be tenuous enough that the ion flow energy is less than the spacecraft potential [*Engwall et al.*, 2006]. Since our data is characterized by very high densities, the contamination by a wake is not a source of concern to this study.

The Cluster FGM experiment consists of a pair of triaxial fluxgate magnetometers, one outboard, mounted on the end of a 5 m boom, and the other onboard.

The instruments are located to minimize contamination from magnetic fields from the spacecraft. The fluxgate magnetometers consist of a magnetically susceptible core wrapped by two coils of wire. An alternating current through one wire drives the core through the hysteresis cycle, which in turn induces an electric current in the other coil. The input and output currents will match in the absence of an external magnetic flux. However, in an external magnetic flux, the core will be more easily saturated along that field. The induced output current will be out of phase with the input current. The current difference integrated for voltage V is proportional to the external magnetic field by $V = -N_l \frac{d(\mathbf{B} \cdot d\mathbf{A})}{dt}$, where N_l is the number of loops and $\mathbf{A}$ is the cross-sectional coil area. The operating ranges of the Cluster magnetometers are chosen to accommodate a dynamic range from a few to 1000 nT. Sampling intervals as low as 0.044 s are available for the interval in our study, but we primarily use the 0.25 s resolution data for reasons that we will make clear later. For this work we have used the best calibrations available. The largest relative error in the FGM measurements is the uncertainty in the spin axis offset (essentially the error in B_z, where z is the spin axis direction). The error in the spin axis offset is generally less than 0.5 nT, and during the dayside season where one can do intercalibration in the solar wind, it is even smaller, but still on the order of tenths of a nT. The offset errors are smaller in the spin plane components. Ongoing comparisons of FGM $|\mathbf{B}|$ with the magnetic field magnitude $|\mathbf{B}|$ calculated from two other experiments on board Cluster suggest that there is a systematic difference between FGM and the other two instruments of ~0.2% across all ranges. In small fields the impact of this uncertainty is much smaller than that of the uncertainty in the spin axis offset (Elizabeth Lucek, FGM PI, personal communication).

The Iridium and DMSP satellites provide *in situ* ionospheric measurements. The Iridum array is a constellation of 66 communications satellites in polar orbit at about 756 km altitude. The constellation gives comprehensive coverage of the polar cap region. Onboard magnetometers form the basis of scientific ionospheric magnetic field and currents studies. A least-squares spherical harmonic fit to the magnetometer data provides a model for upward and downward field-aligned currents. The DMSP spacecraft are in near-polar and circular orbits at an altitude of 835 to 850 km. The orbital inclination of these spacecraft is such that the orbit stays roughly fixed in local time throughout the year. The onboard space environment sensors of interest to this study include a Retarding Potential Analyzer (RPA), Ion Drift Meter (IDM), and vector fluxgate magnetometer. Every 4 s, the RPA measures the component of the ion velocity along the direction of spacecraft motion and the IDM measures the ion velocity in the two directions perpendicular to the spacecraft motion. The RPA is a device that collects particles of different energies. It consists of a grid with a square wave voltage that steps between V_1 and V_2 on collectors at the rear of the instrument. Ions with energy less than qV_1 get reflected by the potential, while more energetic ions pass through to the collector. Likewise, when the grid potential is modulated with potential V_2, ions with energy less than V_2 are reflected. The difference in particle flux collected when the grid lies at V_1 and when it lies at V_2 measures the flux of particles in the energy range between qV_1 and qV_2. Likewise, the difference in flux at V_2 and at V_3 measures particle flux in the range from qV_2 to qV_3, and so on. The IDM determines the trajectories of particles by measuring the currents produced by impacts of ions in different locations on a collector. Knowledge of the trajectories combined with knowledge (from the RPA) of the ion speed along the

direction of spacecraft motion gives the ion velocity components in the two directions perpendicular to the spacecraft motion. The DMSP flow data has been corrected for corotation. The potential drop along the trajectory is found from inserting the particle velocities in the frozen-in drift condition. The magnetic field in the drift formula is calculated from the empirical International Geomagnetic Reference Field. For the time interval of this event, F13, F14, and F15 are operational, but only F13 and F15 provide reliable and uncorrupted data.

2.2 Cluster Analysis Software

The software tools we use to analyze the Cluster data consist of a set of Matlab programs. Important algorithms are discussed either in the main text or in the appendix.

2.3 Geospace General Circulation Model (OpenGGCM)

The coupled Geospace General Circulation Model (OpenGGCM) is a parallelized code that models the global coupling between the Earth's magnetosphere and the solar wind and between the magnetosphere and the ionosphere. The MHD equations are solved on a nonuniform rectilinear grid, or a 'stretched Cartesian' grid, with a minimum grid spacing of 0.1 R_E at the subsolar point and a maximum of 0.5 R_E at $y = z = \pm 40R_E$. In the x direction the grid extends from 24 R_E to –200 R_E. For this run we chose 6.5 million cells with greatest resolution (grid spacing as small as ~ 0.016 R_E) on the dayside. OpenGGCM models the magnetosphere reliably down to altitudes of only about 5 R_E [*Raeder et al.*, 1998; *Raeder*, 2003; *http://ccmc.gsfc.nasa.gov/models*].

The code solves the (normalized) MHD single-fluid continuity, momentum, energy, Maxwell, and state equations :

$$\frac{\partial \rho}{\partial t} = -\nabla \cdot (\rho \mathbf{v}) \tag{2.2}$$

$$\frac{\partial \rho \mathbf{v}}{\partial t} = -\nabla \cdot \left(\rho \mathbf{vv} + p\overleftrightarrow{\mathbf{I}}\right) + \mathbf{j} \times \mathbf{B} \tag{2.3}$$

$$\frac{\partial e}{\partial t} = -\nabla \cdot \left(e + p\overleftrightarrow{\mathbf{I}}\right) + \mathbf{j} \cdot \mathbf{E} \tag{2.4}$$

$$\frac{\partial \mathbf{B}}{\partial t} = -\nabla \times \mathbf{E} \tag{2.5}$$

$$\nabla \cdot \mathbf{B} = 0 \tag{2.6}$$

$$\mathbf{E} = -\mathbf{v} \times \mathbf{B} + \eta \mathbf{j} \tag{2.7}$$

$$\mathbf{j} = \nabla \times \mathbf{B} \tag{2.8}$$

$$e = \frac{\rho v^2}{2} + \frac{p}{\gamma - 1}, \tag{2.9}$$

where $\mathbf{B}$ and $\mathbf{E}$ are the magnetic and electric fields, $\mathbf{v}$ is the plasma velocity, ρ is the density, p the particle pressure, $\mathbf{j}$ the current density, η the anomalous resistivity, and γ the ratio of specific heats. The equations formulated in this way embody what is known as a gas dynamic semi-conservative formalism, because while they conserve mass, momentum, and plasma energy, they allow a switch-off of energy conservation in low β regimes (where $\beta = \frac{p}{B^2/2\mu_0}$), the ratio of plasma pressure to magnetic pressure). Conservation of energy in low β regions can create numerical errors that result in non-physical negative pressures [*Raeder*, 2003]. Because the simulation is large scale, it is

limited to MHD modeling of the non-ideal terms in the generalized Ohm's law through an anomalous resistivity. More realistic modeling that includes the Hall term, electron inertial terms and pressure divergence term involves a degree of resolution that is prohibitive for large scale systems.

The CCMC implementation of GGCM uses a current-dependent non-linear anomalous resistivity, a model based on the assumption that anomalous resistivity is a function of the local current density [*Raeder*, 2003]. Thus the nonideal electric field $\mathbf{E}_{NI}$ is modeled by the term $\mathbf{E}_{NI} = \eta \mathbf{j}$, where the anomalous resistivity, η, is given by

$$\eta = \alpha j'^2 \text{ if } j' \geq \delta,$$

$$\eta = 0 \text{ otherwise.} \tag{2.10}$$

The normalized current density j' is given by

$$j' = |j|\Delta/(|B|+\varepsilon), \tag{2.11}$$

where Δ is the grid spacing, B the magnetic field magnitude, and ε a small constant to prevent division by zero [*Raeder et al.*, 2003]. α and δ are empirical constants [*Raeder et al.*, 1996]. The resistivity model in this study differs from *Dorelli et al.* [2007], where the resistivity was uniform and equal to the reciprocal of the Lundquist number.

As for the boundary conditions, $\nabla \cdot \mathbf{B} = 0$ must be applied at all boundaries. On the sides, the free flow conditions apply, i.e., $\partial \psi / \partial n = 0$ for all parameters ψ other than $\mathbf{B}$, and on the solar wind side the time-dependent boundary conditions are propagated from ACE measurements (ACE is a solar wind monitoring satellite located at the Lagrangian point between the earth and the sun), where B_x is held fixed in time.

The Earth's magnetic field is approximated by a fixed dipole tilt, whose orientation is not updated during the simulation run. At the approximately 5 R_E inner magnetosphere boundary, the MHD calculation stops. There the code maps the FAC's along polar cap dipole field lines to the ionosphere and solves a potential equation on a 1 R_E spherical section to find the ionospheric convection potential from $\nabla \cdot \Sigma \cdot \nabla \Phi = - J_{\parallel} \sin(I)$, where Σ is the ionospheric conductivity tensor, $J_{\parallel}$ the FAC, and I is the inclination of the dipole in the ionosphere. The solver then maps the potential back to the magnetosphere inner boundary, where the potential Φ serves as the boundary condition for the flow and field integration ($v = -\nabla \Phi \times B/|B|^2$). Our simulation computes the electron precipitation parameters and the ionospheric Hall and Pedersen conductances from empirical relations. The model uses a solar EUV ionization empirical model that depends on solar 10.7 cm radio flux and the solar zenith angle, a model for the mean energy and energy flux of precipitating magntospheric electrons, and an empirical relationship between electron precipitation parameters and local conductance (equations 38 through 45 of *Raeder* [2003]). The model assumes no corotation velocity at the inner boundary of the magnetosphere. The magnetospheric plasma initial conditions are given by a cold (5000 °K), low density (0.1 cm^{-3}), uniform plasma [*Raeder*, 2003].

The MHD equations are solved with a second-order explicit time integration and with conservative and flux-limited spatial finite differences. The conservative finite differences approach aims to discretize the spatial grid to globally conserve variables. The solver also implements a flux-limiting hybridization scheme that uses first-order conservative Rusanov fluxes (equation 22, *Raeder* [2003]) where gradients are large, and a fourth-order scheme everywhere else. The fourth-order scheme minimizes numerical

diffusion (error terms), which works well in the absence of sharp gradients and discontinuities. However, at discontinuities it yields gross dispersion errors (ripples, undershoots, and overshoots). At these locations, the first-order scheme kicks in to control the solution [*Raeder*, 2003].

2.4 Null and Separatrix Finders

In this section we discuss the algorithms written by John Dorelli of the University of New Hampshire (now at Goddard) and by Asher Pembroke of Rice University for numerically locating the magnetic nulls and separatrices in the MHD field model output. The null finding algorithm tracks nulls based on the topological degree of the magnetic field using a method first proposed by *Greene* [1992]. The algorithm depends on a mapping between a three-dimensional configuration space and a three-dimensional magnetic field space, such that locations where the magnetic field vanishes in configuration space correspond to origins $\mathbf{B} = \mathbf{0}$ in magnetic field space. The matrix $\nabla \mathbf{B}$ is the Jacobian of this mapping in the original, most general derivation of topological degree by Kronecker [1869], i.e., $deg = \sum_{x \in f^{-1}(0)} sgn[det\,(\mathbf{J}_f)]$, where x is on the configuration space domain, f is the mapping, and $\mathbf{J}$ is the Jacobian [*Dorelli et al.*, 2007]. The Kronecker integral for the topological degree over a domain D in an n dimensional space $\{x_1, x_2, ..., x_n\}$ (e.g., [*Polymilis et al.*, 2003]), is defined as

$$\deg(f, D) = \frac{\Gamma(n/2)}{2\pi^{n/2}} \int_{\partial D} \frac{\sum_{i=1}^{n} A_i\, dx_1 dx_{i-1} dx_{i+1} dx_n}{(f_1^2 + f_2^2 + \cdots f_n^2)^{n/2}} \qquad (2.12)$$

where Γ is the gamma function. $A_i = (-1)^{n(i-1)} det(\mathbf{M})$, with $\mathbf{M}$ an $n \times n$ matrix with $M_{i1} = f_i$ and $M_{ij+1} = \partial f_i / \partial x_j$ for j on $\{1,...,i-1,i+1,...,n\}$. If the magnetic field $\mathbf{B}$ is the map, then replacing f with $\mathbf{B}$ in (2.12) and replacing the configuration space integral with an integral over the corresponding magnetic field space domain ∂D_B, turns (2.12) into

$$\deg(\mathbf{B}, D) = \frac{1}{4\pi} \int_{\partial D_B} \frac{\mathbf{B} \cdot d\boldsymbol{\sigma}}{B^3} \tag{2.13}$$

[*Dorelli et al.*, 2007].

Greene [1992] discretizes the function in (2.13) in a way to make it numerically solvable. He evaluates $\mathbf{B}$ on the eight corners of a rectangular box in configuration space. Each side of the box is divided into triangles, onto which $\mathbf{B}$ is linearly interpolated from its value on the vertices. These values are then mapped to magnetic field space, producing a dodecahedron with triangular faces. The solid angle subtended by this object onto a unit sphere that contains the origin $\mathbf{B} = \mathbf{0}$ determines whether this object contains the origin. He then projects the triangular faces onto the unit sphere, and calculates the area of the triangles on that sphere. This area is essentially the solid angle subtended by three magnetic field vectors, denoted as $\mathbf{B}_1, \mathbf{B}_2$, and $\mathbf{B}_3$. Then the area S of these spherical triangles are given by

$$S = 4 \tan^{-1} \left\{ \left[\frac{tan(\theta_1 + \theta_2 + \theta_3)}{4} \right. \right.$$

$$\times \frac{tan(\theta_1 + \theta_2 - \theta_3)}{4} \times tan \frac{(\theta_2 + \theta_3 - \theta_1)}{4}$$

$$\left. \left. \times \frac{tan(\theta_3 + \theta_1 - \theta_2)}{4} \right]^{\frac{1}{2}} \right\}, \tag{2.14}$$
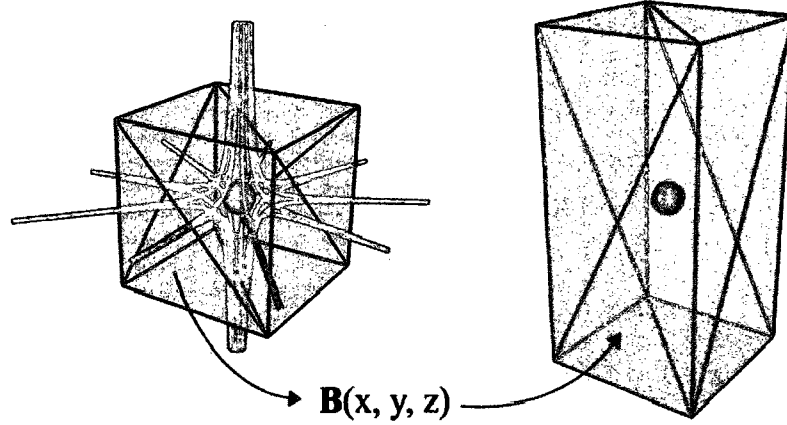
Figure 2.4 This figure illustrates the calculation of the topological degree of a discretized magnetic field relative to an OpenGGCM finite difference cell. Each computational cell is decomposed into 12 triangles (green cube), each of which is mapped (using the values of the magnetic field at the eight vertices of the cell) to a corresponding triangle in magnetic field space (blue cube). In this example there is a single linear null (red sphere) such that $B_x = x$, $B_y = y$ and $B_z = -2z$. (from *Dorelli et al.* [2007]).

where θ_1 (and similarly θ_2 and θ_3 by cyclic permutation) is given by

$$\cos(\theta_1) = \mathbf{B}_2 \cdot \mathbf{B}_3 / |\mathbf{B}_2||\mathbf{B}_3| \qquad (2.15)$$

The sign of the area of the triangle S_i is the same as the sign of $\mathbf{B}_1 \cdot \mathbf{B}_2 \times \mathbf{B}_3$. All the spherical triangle areas S_i on the dodecahedron object are then summed. The result is the number of times the projected dodecahedron covers the unit sphere, divided by 4π. The sign of the result depends on the type of null enclosed. If there is more than one null in the box, the topological degree can be > 1 or < -1. Figure 2.4 serves to illustrate how this mapping and discretization process works with regard to the GGCM grid.

The algorithm for the open/closed separatrix surface works by performing a search on a 2D grid above the northern ionosphere. The search uses a crude iterative cell splitting method: at each iteration, field lines are traced from each vertex in the current mesh, which are then declared open or closed based on the field line trace; all the cells that are on the open/closed boundary are split with an isocontour that represents an

approximation to the separatrix (halfway between open/closed). A new mesh is created from the split cells and the process repeats. The 2D search returns a multi-resolution grid, with the highest resolution right next to the boundary. At each iteration, the field lines are stored in low resolution. Then, the field lines are converted into a separate 3-D volumetric grid, using the connections of the 2D grid to build the 3D volume elements. This last step finds the open/closed surface by interpolating from the 3D grid. Starting on a mesh in the equatorial plane that spans from the solar wind across the magnetopause to the magnetosphere, the algorithm uses the same search method to find the open/IMF separatrix surface (Asher Pembroke, personal communication).

2.5 The Tsyganenko 2004 Model

In Chapter 4 we use the Tsyganenko 2004 model to trace magnetospheric field lines from the ionosphere to the magnetopause. Since its genesis in 1982, the Tsyganenko (TS) model has provided an empirically based model of the Earth's magnetic field. It has since then undergone many iterations and improvements, the latest version being the 2004 model (TS04, also sometimes called TS05). (As of the completion of this thesis, work has been performed on a yet higher spatial resolution model.) The earliest models used data from spacecraft such as IMP and ISEE 1 and 2, while the later models avail themselves of Polar, Geotail, Equator-S, and GOES measurements, progressively incorporating higher spatial resolution, storm-time data and more distant magnetospheric fields. The newer models include a more realistic magnetopause, shielding of the magnetic field by magnetospheric current systems, tail and ring currents [*Tsyganenko* 1995], and solar wind effects, such as solar wind dynamic pressure, IMF direction, and

reconnection [*Tsyganenko*, 1996]. The TS04 model attempts to derive from the data the time dependence of the major current systems. The authors assigned each source an individual relaxation timescale, quiet-time strength and external driving history. In addition, the magnitudes of the principal field sources were assumed to saturate during extremely large storms with abnormally strong external driving. All the parameters of the model field sources are treated as free variables. The expected Dst variation based on the model output at Earth's surface compares well with the actual observed Dst [*Tsyganenko and Sitnov*, 2005]. The inputs to the model include the date, the solar wind ram pressure, the Dst index, the IMF B_y and B_z, and the start position of the field line tracing. (The Dst index (Disturbance Storm Time index) is a measure of the degree of change in the Earth's dipole field induced by a magnetic storm time ring current.) However, this model shuts off the effects of the IMF for northward IMF, a caveat we will take into account when considering the code's output in this work. Essentially it severely limits the radial range over which the Earth's dipole model is valid for our scenario.

Chapter 3

CLUSTER'S ENCOUNTER WITH THE RECONNECTION SITE

3.1 Observation of a Northward IMF Reconnection Event

In this chapter we will discuss the topology and scales associated with a Cluster observation of a northward IMF reconnection event. During this long-lived event of 18 March 2002, the Cluster four-satellite suite crossed the magnetopause at a location mapping along field lines to an ionospheric H-alpha emission caused by proton precipitation from reconnection at the magnetopause [*Phan et al.*, 2003; *Frey et al.*, 2003]. From 14:54 to 15:03 UT, Cluster passed from the northern tail lobe through the magnetopause, at 77.8° magnetic latitude and 12.2 MLT (Magnetic Local Time), into the magnetosheath, moving primarily along the noon-midnight meridian northward and towards the sun (see Figure 3.1a). Figure 3.1b shows the red-shifted H-alpha light caused by protons precipitating from the reconnection site as they strike the ionosphere. The image, taken by the IMAGE FUV SI-12 instrument, demonstrates the position of an auroral emission from the reconnection site that is centered near 80° on the dayside and between about 9 and 15 MLT. The spot is usually at noon MLT, but moves somewhat in time along with the IMF B_y component. The auroral arcs are also visible on the flanks of the polar cap. The long-lived reconnection emission was observed by IMAGE for about four hours. During this interval, between 14:54 and 15:03 UT, Cluster passed through the northern cusp magnetopause. Using Tsyganenko '89, '96, and '01 model field lines, *Phan*
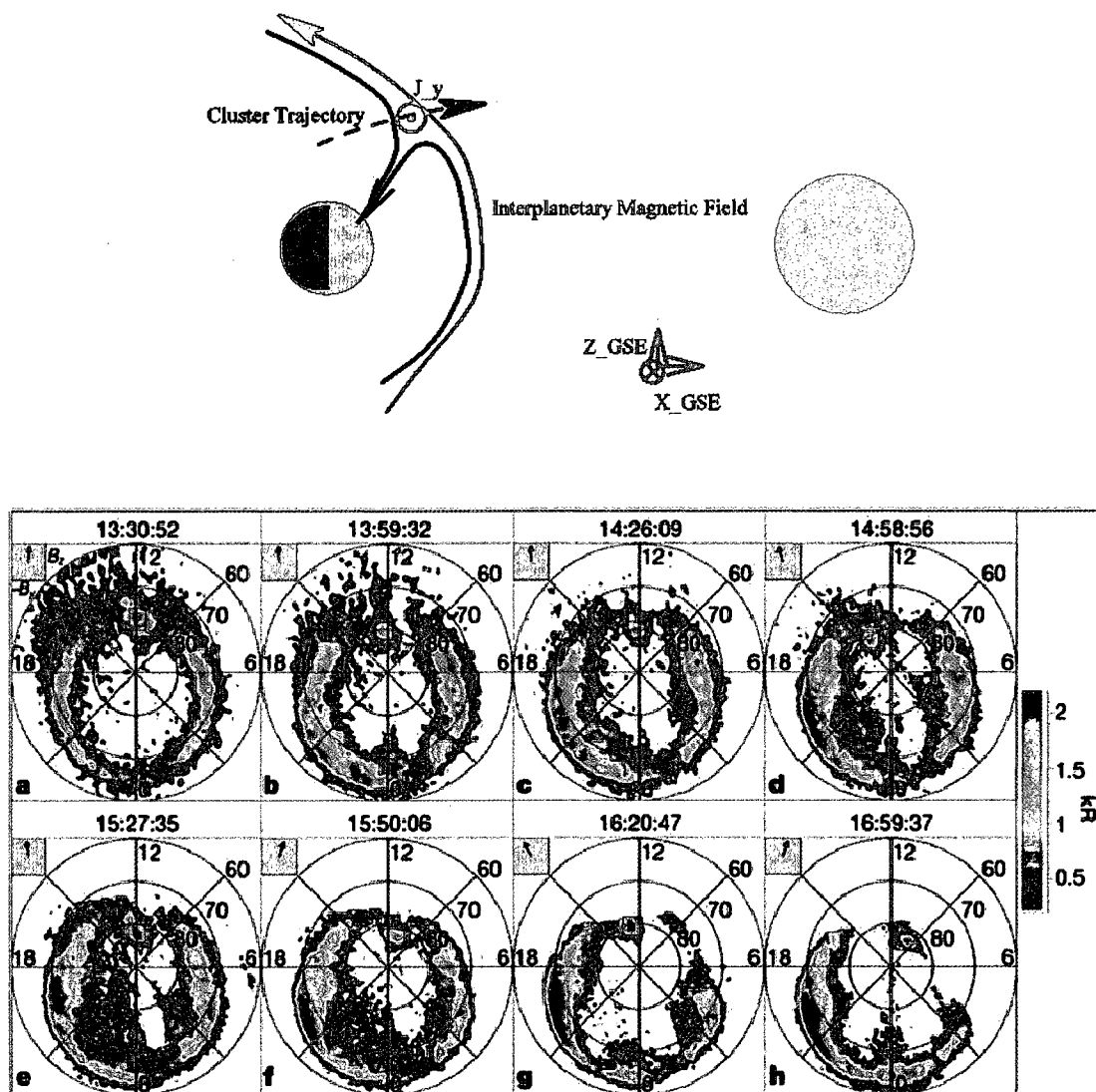
Figure 3.1a-3.1b. (a) Top: Cluster passes from the northern tail lobe through the magnetopause and into the magnetosheath, moving primarily along the noon-midnight meridian toward the sun. **(b) Bottom:** The IMAGE FUV detects an auroral H-alpha spot from precipitating reconnection protons over an extended period of time. The spot comes from northward IMF reconnection at the cusp, and can be seen on the dayside near noon. The position of the spot varies with the IMF B_y. The green inset shows the IMF clock angle.

et al. [2003] mapped the Cluster position at about 15:00 UT to within error of the ionospheric proton spot observed at the same time at about 80° latitude and 2:30 MLT (in apex geomagnetic coordinates) by the IMAGE FUV SI-12 instrument. This implies that Cluster was in the vicinity of the reconnection site at the magnetopause at the time the reconnection footprint was observed at the ionosphere by IMAGE. From the four-point Cluster magnetopause observations of this event, we develop a superposed epoch portrait of the instantaneous magnetic x-line, the current sheet, the particle flows, and the diffusion scales.

3.2 Local Magnetic and Current Sheet Structure

In their analysis of the Cluster magnetopause crossing on March 18, 2002, *Phan et al.* [2003] present evidence of an ion moment reversal detected by Cluster at approximately 14:56 UT. In addition to the reversing proton jets, they measure ion velocities throughout the magnetopause crossing that meet the Walèn criterion for reconnection (defined in the Appendix), thus arguing that Cluster had encountered a reconnection jet at 14:56 UT. Based on the magnetic field data, we argue that they observed an encounter with reconnection jets at the sunward separatrix and that the magnetic field observed at later times is more consistent with proximity to an active reconnection site. In this paper we will examine this event using Cluster's instantaneous multi-point magnetic field measurements to locate the reconnection site. By doing so, we will determine a coordinate system centered on the x-line and describe the reconnection site's particle properties, motion, and magnetic structure in that system. Our goal, therefore will be to seek within the data a magnetic topology consistent with singular

field line reconnection, 3D reconnection in its most general form, and a corresponding parallel electric field.

We begin by describing the magnetic data in Section 3, where we delineate the features in the fields that indicate the presence of reconnection. The physical basis for the coordinate system we adopt lies in the location of the satellites and the characteristics of the fields. Here we describe the coordinate system we adopt for further analyses. In section 3.4, we derive the spatial gradients of the magnetic field, which are necessary for all our subsequent work. These quantities allow us to develop the x-line centered coordinate system and infer the shape and dimensions of the current layer, which we do in Section 3.5. Section 3.6 presents the electron and ion flows near the x-line, affirming the x-line geometry discussed in Section 3.4. In section 3.7, we extract evidence for nonideal and parallel electric field and discuss the location and size of diffusion regions inferred from higher-order electron and ion moments. Section 3.8 is a summary.

3.3 Magnetic Field Data: Features Characteristic of Reconnection

During the magnetopause crossing, Cluster observed a series of nulls in the GSE x and z components of the magnetic field (Figure 3.2a). (The magnetopause lies roughly between the dotted lines. In the Appendix we define the GSE and other coordinate systems that appear throughout this thesis.) To properly analyze this data, however, we must first rotate it from the GSE system to one aligned with the local magnetopause—and preferably one where the only component that exists on each side of the magnetopause is the new x component. Qualitatively, we wish to align ourselves with the magnetopause and with the current sheet in the magnetopause, so that our new z direction lies along the
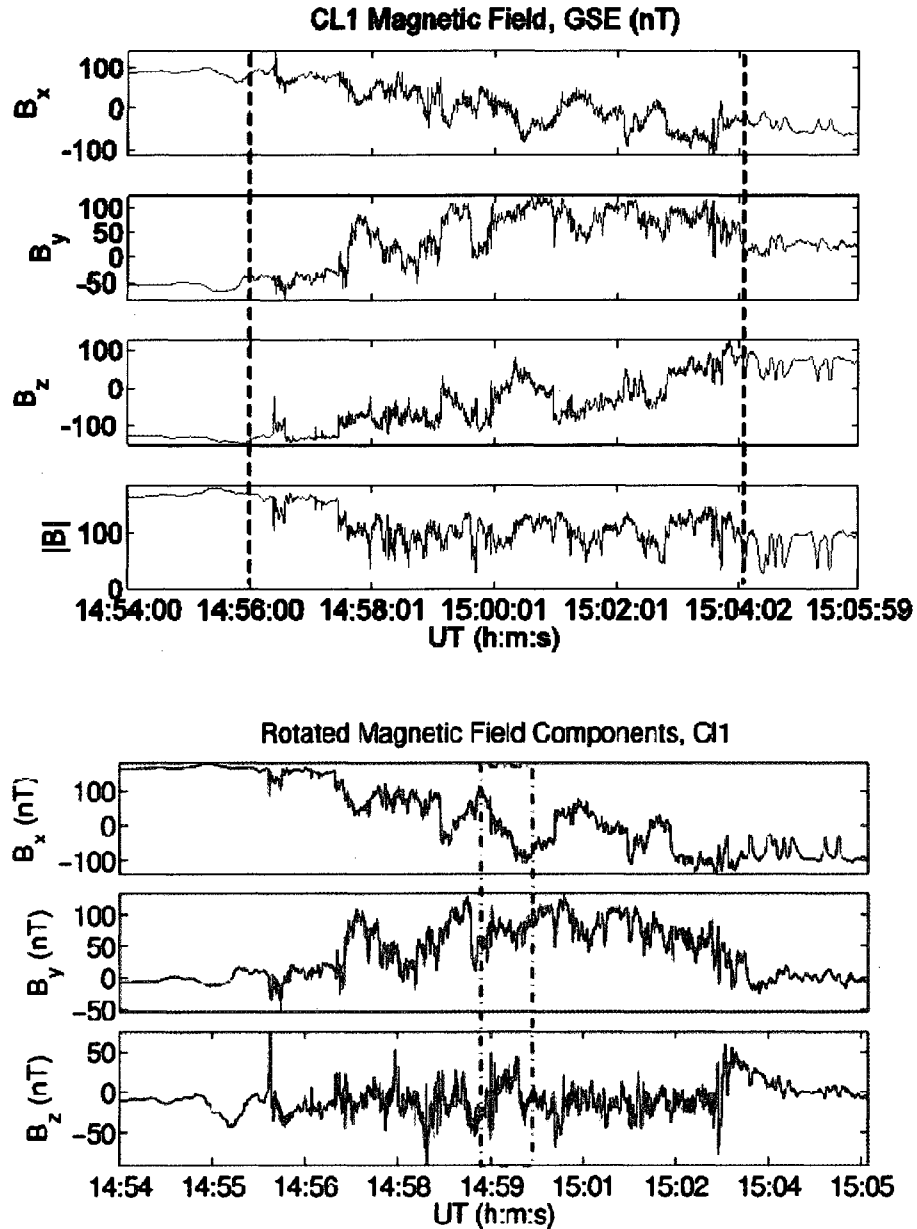
Figure 3.2a-3.2b. (a) Top: The FGM magnetic field data from Cluster 1, in GSE coordinates, for the duration of the magnetopause crossing. The top three panels show the x, y, and z components, and the bottom panel the total magnitude. There are no nulls (i.e., $\mathbf{B} \equiv 0$). in all three components. **(b) Bottom:** Cluster-1 FGM magnetic field data for the interval during Cluster's magnetopause crossing in a boundary normal coordinate system. The data has been rotated into a magnetopause-aligned coordinate system according to a minimum variance analysis.

normal to the magnetopause and the new y direction is parallel to the magnetopause current. In other words, we are seeking the large-scale coordinate system for anti-parallel reconnection—one in which only a B_x component exists on either side of the magnetopause. This new coordinate system would then be aligned with the plane of two-dimensional reconnection, with x pointing along the field on either side of the discontinuity, y pointing out of the plane, and z oriented perpendicular to the discontinuity but within the plane (as in Figure 1.1). We can then identify the true current sheet crossings as those locations where the new B_x component changes sign. If, within this coordinate system, we can identify a singular field line topology with either an x-type null or an x-type hyperbolic geometry perpendicular to a magnetic field component along the current sheet, then we have established to first step in satisfying the necessary and sufficient conditions for reconnection (the second and final step being the detection of a parallel electric field along the singular field line near the x).

To establish the best rotation angles to accomplish this, we use a Minimum Variance Analysis (MVA) (outlined in the Appendix). The MVA requires at least three magnetic field values—one before, one during, and one after the boundary crossing. We first rotate the data by different sets of Euler angles, testing each set of rotation angles by a MVA to determine which set is best. The set of data input to the MVA consists of a region on each side of the magnetopause (the "before" and "after" inputs to the MVA) and the region of the width of the magnetopause (the "intermediate" input to the MVA). The angles that minimize the variance along the normal to the boundary and maximize it along the boundary in the MVA comprise the best set of rotation angles. We apply the test to all four spacecraft. A rotation of 52° about the GSE y-axis, 20° about the new z

axis, and, finally, 10° about the newest x axis gives the best normal in the final z direction and the best alignment of the current sheet with the y direction. (The best rotation angle about the z-axis was found to range between about 17° and 30°, depending on the spacecraft. An angle of 20° was the average that worked best for all spacecraft.) With these rotation angles, the MVA gives a maximum eigenvalue in the new x direction, an intermediate value in the y direction, and a minimum value in the new z direction, as desired. These angles coincide very closely with the angles that best remove the average B_z and B_y fields on either side of the boundary. In the appendix we discuss the errors in the MVA and the robustness of the estimates. To test the stability of the MVA to averaging over varying interval lengths, we also apply the MVA to a range of sub-interval sizes in the magnetopause. We find the method to perform well on this data.

Figure 3.2b shows the rotated data from Figure 3.2a. As desired, only the B_x component remains on either side of the magnetopause after rotating the coordinates. We note that all references to the magnetic field henceforth refer to the rotated coordinates, though we will continue to designate them by unprimed variables B_i. The bottom panel of Figure 3.2a displays the magnitude of the magnetic field. Though there is a minimum of about 30 nT in the magnitude, there are no true nulls (i.e., $\mathbf{B} \equiv 0$). As Figure 3.2b demonstrates, however, there are nulls in the B_x-B_z components. These are the components we would expect to exist and to reconnect at Cluster's location near the noon-midnight meridian. (As we will discuss, there is also a B_y component that exists only within the magnetopause.) The rotated fields show that they are very nearly antiparallel on either side of the magnetopause (a rotation angle of about 175°), with a positive B_y associated with the current sheet crossings throughout the magnetopause.

From Figure 3.2 it can be seen that there are multiple current sheet crossings in the magnetopause, identified by those locations where B_x changes sign. At most of these instances there is a normal B_z component that simultaneously changes sign. This pattern suggests Cluster either touches or crosses a single magnetic reconnection site moving with the magnetopause, or traverses multiple current sheets associated with a tearing mode. The B_x-B_z null near 15:00 UT presents the smallest values observed and thus the closest possible approach to a reconnection site. In addition, Cluster traverses this null the most slowly, minimizing temporal aliasing of the moment calculations. As we will see shortly, it also corresponds to the maximum current sheet. Therefore this study will focus on that interval.

After the rotation, B_y vanishes on both sides of the magnetopause. However, a purely positive B_y manifests itself exclusively inside the magnetopause. Because the local B_y does not change sign when B_z changes sign through the x-line, as we will show in this chapter, it is not a quadrupolar field. However, it is consistent with a singular field line. Thus we have established a singular field line topology within our desired magnetopause-aligned coordinate system. We will show in the subsequent chapter that we can attribute this singular field line component of the magnetic field along the current sheet to IMF draping and magnetospheric convection—though it is also consistent in principle with separator reconnection.

Magnetic reconnection creates a rotational discontinuity (RD) in the magnetic field. Therefore, detection of a RD is a necessary condition in the magnetic field for reconnection. A magnetic field component and velocity component normal to the plane of the discontinuity signify a rotational discontinuity (see the appendix and [*Landau and*

Lifshitz, 1960]) and an open magnetopause. The direction of the tangential magnetic field and the tangential velocity are discontinuous across the boundary, but the magnitudes of both the normal and tangential magnetic field components and the normal velocity component are continuous. The value of the normal velocity component is the Alfvén speed from the normal component of the magnetic field, or $v_n = B_n / \sqrt{4\pi\rho}$, where ρ is the plasma density. On MHD scales, the current sheet of an open magnetopause is a standing steepened Alfvén wave (or rotational discontinuity) on either side of the merging region [*Sonnerup and Cahill,* 1968]. Though not a sufficient condition for reconnection, a RD is a necessary condition for reconnection. As a formal check for RDs in the magnetic field data, we apply an algorithm, developed by *Hausman and Michel* [2004], that picks out field rotations while remaining blind to tangential discontinuities, i.e.,

$$\rho = (\mathbf{B_1} \times \mathbf{B_2}) \cdot \mathbf{B_3} \tag{3.1}$$

where ρ (not to be confused in this context with the particle gyroradius or density), identifies the RD, and B_1, B_2, and B_3 are sequential measurements of the magnetic field. (In our case the FGM data has 0.25 second resolution and we have smoothed it by a running 1.25 second average.) Figure 3.3a depicts two components of the magnetic field along with the quantity ρ. The small oscillations in ρ are noise, but the large spikes signify RDs. Note that these occur where the B_x component approaches zero, B_y experiences a sudden enhancement, and B_z develops a normal component. The x-line at 15:00 UT lies between two RDs, a large one on the magnetosphere side (the large spike between 14:58:59 and 15:00:39), and a much smaller one on the magnetosheath side,

Cluster 2 ρ

ρ/|B(i)×B(i+1)|
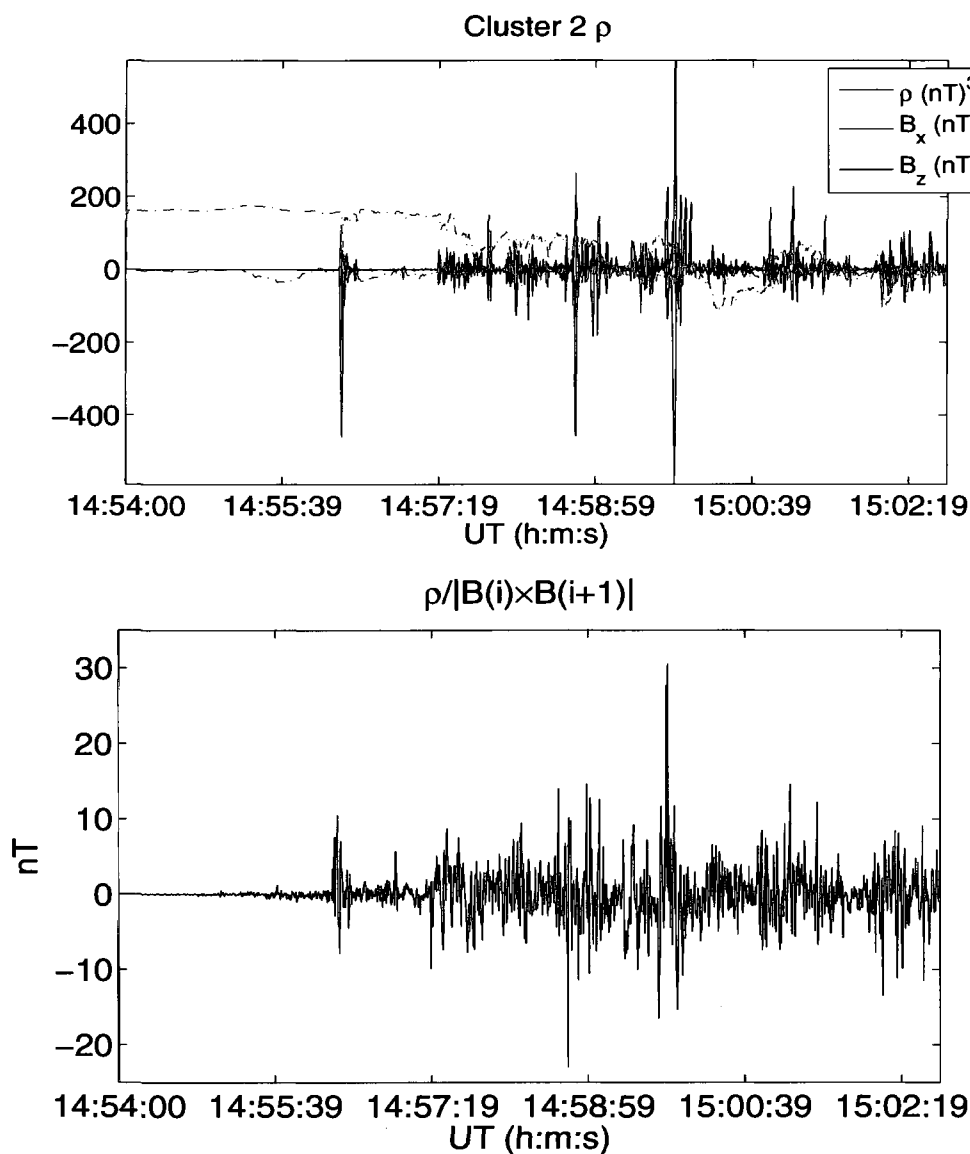
Figure 3.3a - 3.3b. (a) Top: The x and z components of the magnetic field along with the measure of rotational discontinuity (RD finder), ρ, from Cluster 2. **(b) Bottom:** ρ normalized by $|B_1 \times B_2|$ gives a measure of the noise and the normal component of the discontinuity, which is here about 30 nT, the largest spike.

such as observed in simulations and previous data [*Xie and Lin,* 2000]. This timing lends support to the hypothesis that Cluster is traveling through a reconnection site lying between a pair of RDs. In fact, the repeated appearance of normal B_z along with a RD

suggests the presence of either a tearing-mode structure or a suite of encounters with one reconnection site. Figure 3.3b normalizes ρ by $|\mathbf{B}_1 \times \mathbf{B}_2|$, putting it in units of nT. In this normalization, ρ not only effectively measures the noise in the measurements, but also the discontinuity's normal component—here roughly 30 nT, the largest spike in the figure.

Before proceeding further, we mention that we have time synchronized all magnetic and electric field data, because different Cluster instruments take measurements at different times, as do the same instruments on different spacecraft. We have accomplished this by interpolating all data to match the time tags of the FGM instrument from Cluster 1, and then reducing the sampling rate once again to match the instruments' authentic sampling rate.

3.4 Instantaneous Reconnection Magnetic Field Derivatives: Curlometer Current and Prologue to Superposed Epoch Analysis

To investigate the structure, size, and motion of the current sheet, we first need to calculate the spatial derivatives of the magnetic field. The error in relative spacecraft positions is a maximum of 10 km (and a minimum of 150 m) for inter-spacecraft distances less than 1000 km [*ESA/ESOC*, 2000]. Indeed, during this magnetopause crossing, a 10 km error bar exceeds the inter-spacecraft distance in the y-direction for most spacecraft pairs and forms a huge fraction of it for the others. We therefore treat the problem as a two-dimensional geometry with an out-of-plane field. We can justify this treatment by a lack of dependence of B_x and B_z on y, as will be shown in the next section. To derive the current in the y direction, and for a two-dimensional treatment of the

reconnection line, we need to estimate the spatial derivatives $\partial B_x/\partial z$, $\partial B_z/\partial x$, $\partial B_x/\partial x$ and

$\partial B_z/\partial z$ at the x-line.

The four Cluster spacecraft lie on the corners of a tetrahedron, which allows

instantaneous measurement of the magnetic field spatial gradients by way of the

curlometer method [*Dunlop et al.*, 2002; *Chanteur*, 1998]. We initially attempt to use this

method and establish whether it is sufficiently robust. In using this method, our criterion

for the site of the x-line is a minimum of $\sqrt{B_x^2 + B_z^2}$. Thus we choose times when the

centroid (average) field exhibits a minimum $\sqrt{B_x^2 + B_z^2}$ to determine the instantaneous

spatial gradients of the fields at a reconnection site. We choose the centroid values

because the magnetic field derivatives derived from the curlometer method lie at the

location of the centroid. Though the spacecraft are at most roughly 180 km apart, the

assumption of spatial linearity is questionable in this data. Therefore we determine the

magnetic spatial gradients by way of an estimated multi-spacecraft quadratic interpolated

fit to $\partial B_i / \partial x_j$. This approach, described in detail in the Appendix, follows the same

principle as the curlometer method [*Dunlop et al.*, 2002], a linear estimate, but makes use

of the spacecraft motion to approximate intermediate grid points. Hence it permits

quadratic instead of linear fits (*Chanteur* [1998]). These intermediate grid points can be

exploited to perform a best quadratic fit. For the highest fidelity, for this task we use the

highest resolution (0.045 s) magnetic field data.

The quantity $\nabla \cdot \mathbf{B}/|\nabla \times \mathbf{B}|$ provides a quality estimate for the spatial gradients at

any given time [*Dunlop et al.*, 2002]. Where it becomes large, it indicates that even the

quadratic assumption is of insufficient order to capture the nonlinearities present. It will

rarely vanish (to numerical accuracy) using the curlometer method, unless an additional

constraint that requires $\nabla \cdot \mathbf{B} = 0$ is applied to the fit (using a Lagrange multiplier, as

explained in the appendix). First and foremost we must take into account the role the

shape of the tetrahedron plays in the quality of the estimates. The tetrahedral elongation

has a value of about 0.58, and a planarity of 0.76, which places the tetrahedron in the

range of a potato or a pancake [*Robert et al.,* 1998b], where the tetrahedral geometry

contributes up to a 50% error to the quality estimate [*Robert et al.,* 1998a]. The smallest

dimension has also been shown to provide the least reliable gradients [*Robert et al.,*

1998a], and in our case this lies along the y direction.

In the Appendix, we plot the quality factor against the spatial gradients and the

magnitude of $\sqrt{B_x^2 + B_z^2}$ in the interval around 15:00 UT (see Figures A2a-A2c). We

find there that, in the current sheet, the quality factor varies considerably, from values

near zero up to 1 (and even larger at one location at the end of the interval). Therefore,

the accuracy of the curlometer current within the current sheet will vary. Further into the

current sheet (minima in $\sqrt{B_x^2 + B_z^2}$ and in $(\nabla \times \mathbf{B})_y$), for example between the dashed

lines in the figure, the quality factor is smaller, ranging from zero to 0.5. The

corresponding spatial gradients are $\partial B_x / \partial z \sim -0.5$nT/km and $\partial B_z / \partial x \sim -0.2$ nT/km. But

because of these accuracy issues, we consider it prudent to supplement the curlometer

calculations with an alternative method that is less prone to errors. The alternative

method depends on a superposed epoch of the four spacecrafts' magnetic field

measurements near the x-line, and we will describe it in section 3.4. The propagation of

errors involved in the calculation of the gradients (not related to the errors arising from

tetrahedral geometry) is discussed in the appendix, and is no worse than 0.09 nT/km.

In Figure 3.4, the resulting y-direction curlometer current density reveals a steady, and possibly bifurcated, current sheet. The superposed heavy curve attempts to delineate this structure in the data. A bifurcated current sheet presents itself as a local current positive sandwiched between two minima, which are roughly -1.6 $\mu A/m^2$. Two-dimensional kinetic simulations with a guide field yield such a bifurcated current sheet [*Hesse et al.*, 2001; *Singh et al.*, 2006]. We will revisit this issue later when we address the particle flows and currents in a coordinate system centered around the x-line.

3.5 Structure of Reconnecting Magnetic Fields: A Superposed Epoch Analysis

In the rotated, boundary-normal coordinate system, we treat the reconnection region as a two dimensional structure extended in the (new) y direction. As we will discuss further in the subsequent chapter, a three-dimensional topology may provide the most accurate description of this event. As we will show in Chapter 4, global resistive MHD simulations of our event exhibit nearby three-dimensional magnetic nulls connected by x-lines. For a position on a singular field line, this kind of a null system reproduces our observation of two-component reconnection with a locally enhanced out-of-plane magnetic component. Such a system has a non-vanishing magnetic component along the x-line along with locally hyperbolic magnetic field components perpendicular to the x-line. Moreover, the simulations display an enhanced B_y component in the location of Cluster in the northern hemisphere and in the southern hemisphere that exists only within the magnetopause. However, we proceed from a two-dimensional projection of such a model as a starting point, especially considering the large uncertainties in the y
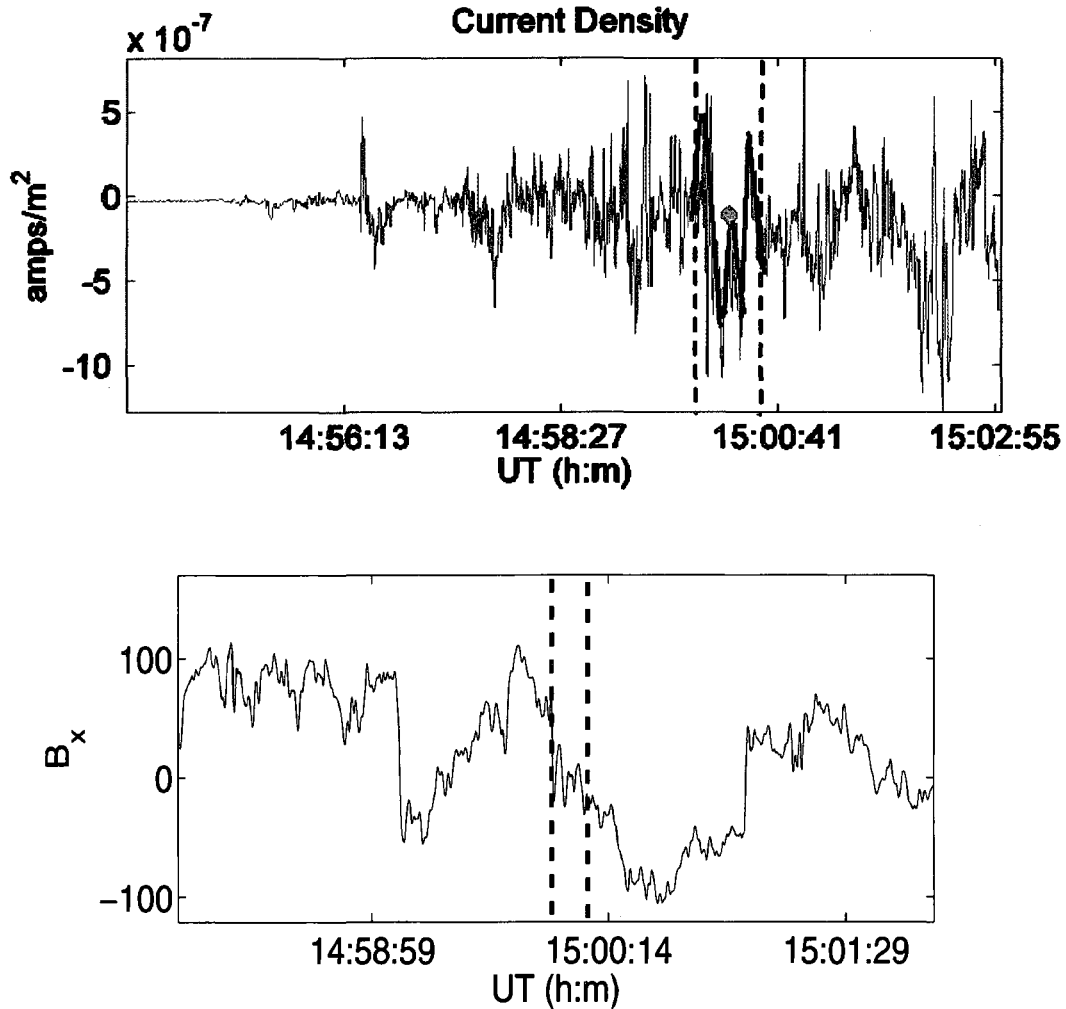
Figure 3.4a-3.4b (a) **Top:** The shape of the current sheet J_y is somewhat extended but possibly bifurcated in both the x and z coordinates. It is shown between the dotted lines in the figure, and we have limned the bifurcated structure in the data in a darker color. This feature is observed in the x direction in fully kinetic reconnection simulations and attributed to details of particle orbits on electron diffusion scales that are not observed in fluid or Hall MHD simulations. It is observed in the z direction after current sheet thinning evolves into a bifurcation. **(b) Bottom:** The x component of the magnetic field, which has a flattening at the center of the current sheet (between dashed lines) that is characteristic of bifurcation.

gradient.

Our goal is to derive a superposed epoch coordinate system centered on the x-line. What we will accomplish is based entirely on the magnetic field data. Therefore, no other effects, such as pressure or density gradients, can play a role in the interpretation of the resulting topology. Indeed, these effects are completely removed by placing all the data in a superposed epoch coordinate system fixed in the 'x-line' reference frame. We create the superposed epoch in three steps: we first identify the location of the x-line by the minima in B_x-B_z; we then compute the distance of the spacecraft from the x-line by using the linear gradients of **B** and inverting the corresponding Taylor expansion; finally, we place the spacecraft in a coordinate system with the x-line at the center, using the distances we calculate in the second step.

A superposed epoch that exploits minima of the quantity $\sqrt{B_x^2 + B_z^2}$ provides another way to estimate the gradients that govern the fields near the x-line. The linear gradients $\partial B_x/\partial z$ and $\partial B_z/\partial x$ are prerequisites for the later stages of the full superposed epoch analysis. However, it is possible to derive rough but robust estimates of these gradients from a primitive superposed epoch of the spacecraft magnetic fields at only those points where each spacecraft passes closest to the B_x-B_z null. Though its general utility is limited, this method doesn't suffer from the errors of the curlometer method. First we filter the magnetic field data using a zero-phase forward and reverse digital filter, which results in zero phase distortion. We filter in the frequency range 0.1 to 1.3 Hz, where waves have a dominating effect on the lower frequency trends apparent in the data, particularly on the B_z trend. These lower frequency trends represent the x-line crossing, and so we want to keep these trends and find their slopes. All spacecraft that

measure a value of the quantity $\sqrt{B_x^2 + B_z^2}$ that is less than 7 nT are placed at (0,0) in the relative coordinate system, assuming that the spacecraft is essentially at the location of the x-line. (We choose 7 nT, because it is the smallest value for which we retain enough values from which to derive significant fits.) The other three spacecraft fall into place surrounding the x-line, based on their instantaneous location relative to the spacecraft that measures the minimum $\sqrt{B_x^2 + B_z^2}$. The values used for the fit include data only from these other three spacecraft; the spacecraft observing the minimum value is excluded from the fit. Each one of the spacecraft takes its turn at various times in being closest to the x-line. The pattern that evolves reveals the instantaneous large-scale slope of $B_x(z)$ and of $B_z(x)$ from a best linear fit. (The points are clustered at discrete values of z (in 3.5a) and x (in 3.5b), as a result of the nearly fixed spacing of the spacecraft. Thus, when spacecraft 2 measures minimum $\sqrt{B_x^2 + B_z^2}$ and is thus assigned to $x = z = 0$, for example, spacecraft 3 is always found at $(x, z) = (-18.4, -64.8)$, spacecraft 4 at (23.5, 69.5), and spacecraft 1 at (-44, 69.8).) The fits shown in Figure 3.5a-5b as red curves give the slopes $\partial B_x/\partial z \sim -.56$ nT/km $\pm$ 0.04 nT/km and $\partial B_z/\partial x \sim -.11$ nT/km $\pm$ 0.04 nT/km. The R^2 goodness of fit for $\partial B_x/\partial z$ is $\sim .92$, and for $\partial B_z/\partial x$ it is ~ 0.5. These values agree quite well with those derived from the curlometer method in the previous section. Note that this method gives an instantaneous gradient derived without any assumptions about the motion of the x-line relative to the spacecraft. Because there is some low frequency curvature to B_z even after filtering, $B_z(x)$ has some small nonlinearity away from $x = 0$. This nonlinearity will have a small impact on the accuracy of x-line position estimations from data at these x distances, but is accounted for in the statistical error
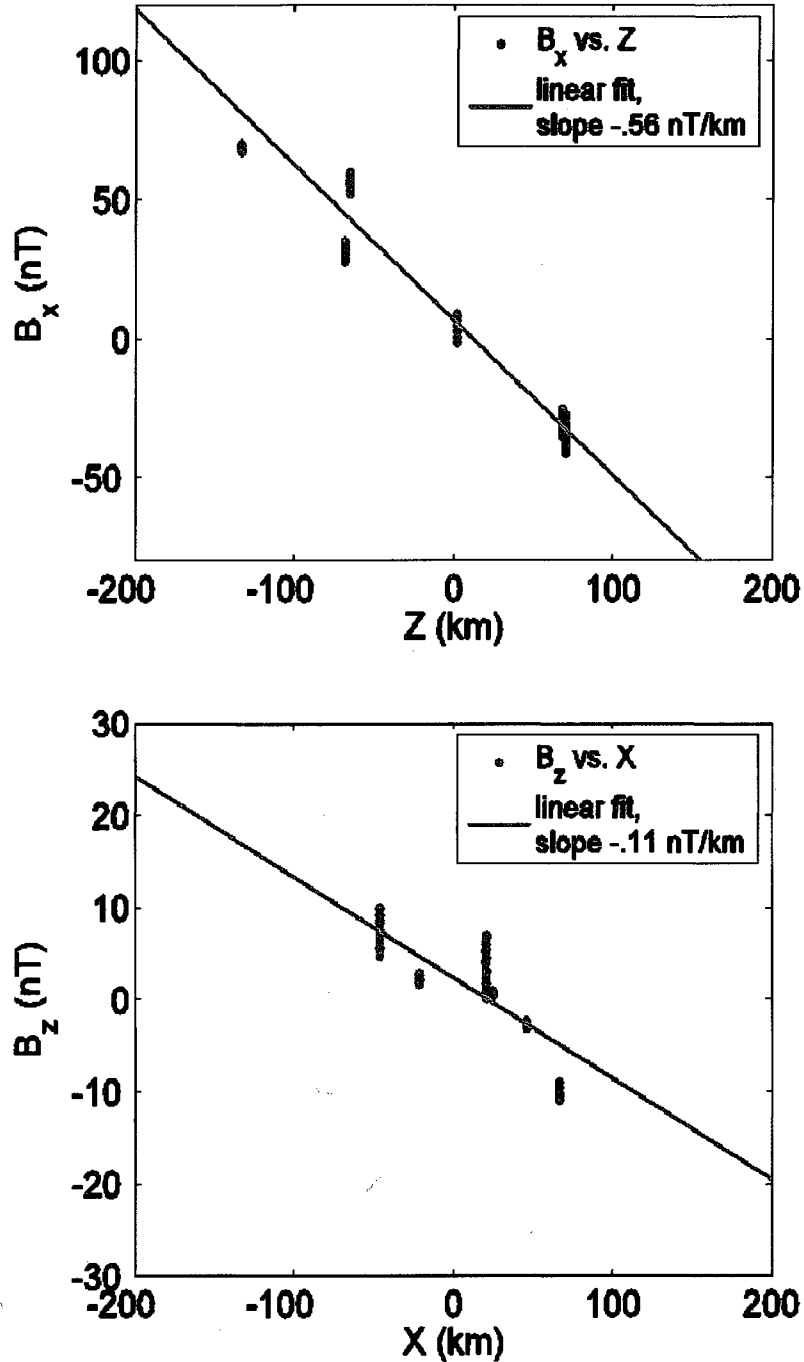
Figure 3.5a-3.5b. A portrait of the magnetic field $B_x(z)$ (top) and $B_z(x)$ (bottom) surrounding the x-line at (0,0). Any spacecraft detecting $(B_x{}^2 + B_z{}^2)^{1/2} < 7$ nT is placed at (0,0). The position values appear discretized because of the fixed spacing of the spacecraft. This rough superposed epoch portrait serves as a mechanism to detect the spatial gradients that will be used in the more precise superposed epoch portraits that follow.

analysis that we discuss in section **A.4** of the Appendix.

In order to find the distances of the spacecraft from the x-line, we equate the measured magnetic field values near the x-line with a Taylor expansion for the difference between the measured magnetic field at the known location of the spacecraft and the magnetic null in B_x and B_z expected at the x-line (Equation (3.2)). The expansion is roughly valid (i.e., the data are roughly linear) over the roughly 50 s time window about the x-line crossing between dashed lines in Figure 3.2b. At each of the measurement times during this 50 s interval, we place the position and magnetic field values of the spacecraft with the smallest value of B_x and B_z in the Taylor expansion. The positions of the spacecraft (x, z), the magnetic field measurements at those locations (B_x and B_z), and the magnetic spatial gradients are known. We then invert the resulting equations below for the unknown positions of the x-line, i.e., x_{xl} and z_{xl}, relative to the defining spacecraft:

$$B_x = \left(\frac{\partial B_x}{\partial x}\right)\Big|_{xl}(x - x_l) + \left(\frac{\partial B_x}{\partial z}\right)\Big|_{xl}(z - z_l)$$

$$B_z = \left(\frac{\partial B_z}{\partial x}\right)\Big|_{xl}(x - x_l) + \left(\frac{\partial B_z}{\partial z}\right)\Big|_{xl}(z - z_l) \tag{3.2}$$

The result is an x-line position as a function of time during a 50 s interval about the x-line crossing. Once we have defined the position of the x-line, we make this position the center of the coordinate system and place the spacecraft relative to it.

The curves in Figures 3.6a and 3.6b show the tanh functions that are the best fits to the data, namely,

$$B_x(z) = B_{0x}\tanh(z/z_0)$$

$$B_z(x) = B_{0z}\tanh(x/x_0). \tag{3.3}$$

The use of the tanh function is justified by the roughly linear nature of the magnetic field

time series data in this region, and by the general shape of the B_x and B_z data presented in the superposed epoch graphs. We will see later that aspects of the electron pressure and density data also justify this step. The prediction bound curves signify the likelihood a new observation lies within the bounds at the 95% confidence level. The value of the adjusted R-square statistic for the fit to B_x is 0.9 (a value closer to 1 being better), meaning that the fit explains 90% of the variance of the data, assuming the error is random and Gaussian. For the fit to B_z, R^2 is 0.5. The smaller value of B_z makes it much more susceptible to the wave-like fluctuations observed in the data.

The propagation of errors in the inversion for the x-line position arises from the known errors in the spacecraft relative positions, in the linear assumption, and in the estimates of the magnetic spatial gradients. The farther from the minimum in B_x and B_z, the larger the error gets, naturally. At the farthest edges of the curves in Figures 3.6a and 3.6b, the error in the x position of the x-line is at most about 80 km, and in the z position, about 60 km. However, closer to the central, linear region of the curves, the error in the x position oscillates between 3 and 16 km, while that of the z position between 3 and 8 km. For a more descriptive view of the x-line position errors, Figures A3a and A3b in the Appendix map the error sizes (by color) of the x and z coordinates of the x-line at the positions of the centroid throughout the layer.

The assumption of a tanh function form does not rule out the presence of higher-order complexities to the curve, such as an embedded thin or bifurcated current sheet. In fact, there is evidence for the latter, in this and in other aspects of the data. There is a possible signature of bifurcation—a flattening of the tanh curve near the origin—in Figure 3.6a. This is difficult to resolve from Figure 3.6a, but is more obvious in the raw
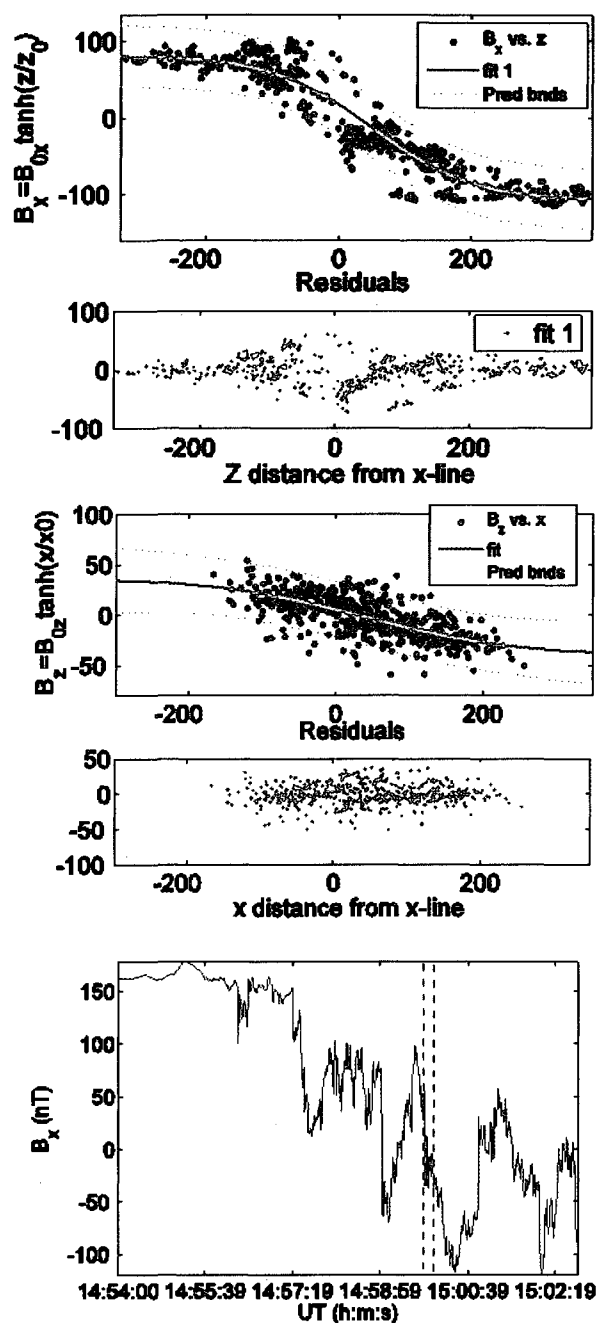
Figure 3.6a - 3.6c. A statistical map of B_x as a function of z (above) and B_z as a function of x (middle). The figures include all times in a 50 s interval around 15:00 UT. The area between dotted lines is a thin area of flattening of B_x (here from Cluster 1) that characterizes current sheet bifurcation.

time series signature, as shown in Figure 3.6c. The area between dotted lines is a thin

area of flattening of B_x (here from Cluster 1) that characterizes current sheet bifurcation.

This can be seen in this section of the magnetic field data from all four spacecraft.

Interestingly, the residuals of the tanh fits are largest in a region near the origin. This is not caused by larger position errors near the origin, as in fact these are smallest at the origin (see Figures A3a and A3b in the appendix). Therefore, the larger residuals are caused by a poorer fit to the tanh function near the origin, not by propagation of errors. This is consistent with the area where an embedded thin or bifurcated current sheet would show itself.

The fit to B_x gives an absolute current sheet thickness, since we have derived it in a coordinate system centered on the reconnection site. If the operational definition of the current sheet thickness is full-width at half-maximum, from Figure 3.6a, the current sheet thickness is approximately 130 km. The fit to the $B_z(x)$ data in Figure 3.6b yields a significant asymptotic reconnection B_{0z} of approximately 20 nT, which would produce a reconnection electric field of roughly $E_y = -4$ mV/m and a polar cap potential drop of about 26 kV, given a reconnection width of 1 Earth radius and the perpendicular solar wind speed (measured by the ACE spacecraft) in the rotated coordinate system of roughly -200 km/s. $B_z = 20$ nT is also in reasonably good agreement with $B_z \sim 30$ nT as derived from the normalized value of the RD finder, ρ, at the discontinuity.

A superposed epoch portrait of B_x, B_y, and B_z as functions of the y distance from the spacecraft that is closest to the x-line (Figure 3.7a-3.7c) reveals that all components of **B** are invariant with y, at least within the distance spanned by the spacecraft in the y direction. All three components take on their full range of values for all values of y. Therefore, we can argue that over the length in y encompassed by the spacecraft, the observed structures in **B** are not a function of y, but rather of x and z. This provides support for the two-dimensional treatment of the current layer. The components appear to
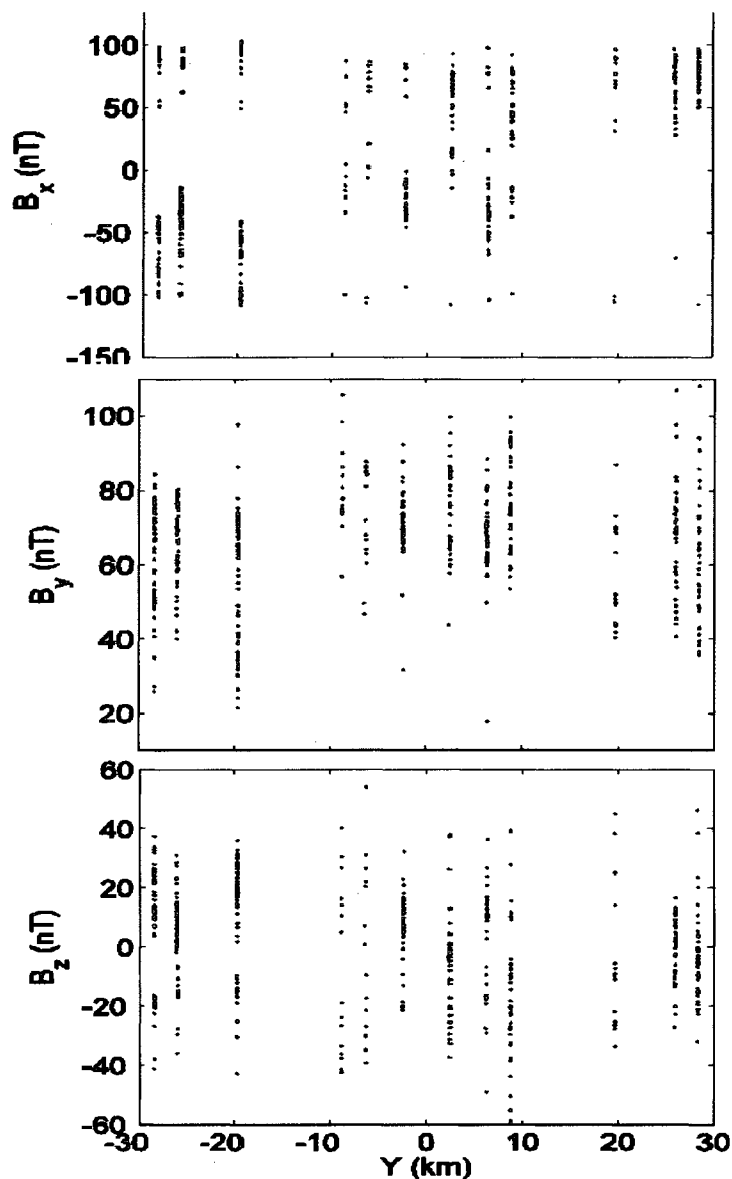
Figure 3.7a - 3.7c. Top to bottom: B_x, B_y, and B_z do not show any dependence on the y coordinate. The y positions are shown relative to that of the spacecraft that observes the minimum planar magnetic field. Since B_x, B_y, and B_z take on all observed values for all values of y, this is an argument for the invariance in the y direction and the two-dimensional treatment. The components appear to take on multiple values for discrete positions because their position coordinates are found from the respective distances from the spacecraft at the minimum B_x and B_z.

take on multiple values for discrete positions because their position coordinates are found

from the respective distances from the spacecraft at the minimum B_x and B_z. There is no

way to find a y distance from an x-line that is defined to lie in the y direction.

We advance the analysis further by placing data within two dimensions surrounding the x-line at the spacecraft positions defined from the inversion of Equation (3.2). In Figure 3.8 and in all the superposed epoch portraits to follow, the red and blue curves are sample field lines derived from the tanh fits, chosen to be at $x = x_0$ and $z = z_0$, one "scale height" in current away from the separatrix. They are derived by integrating the differential equations $dz/dx = B_z/B_x$, where B_x and B_z are replaced by their tanh functions. We use the superposed epoch technique to place all four spacecraft based on the derived position of the spacecraft with the smallest measured $\sqrt{B_x^2 + B_z^2}$. Figure 3.8a represents the measured B_y values by color. In this and all subsequent superposed epoch plots, the sun and lower latitudes are toward the left. It is clear that B_y maximizes near the x-line, a geometry which is consistent with a 3D x-line, or a singular field line, as discussed in the introduction. Figure 3.8b depicts the individual 0.25 s B_x-B_z vectors, revealing a statistically good fit to the model, as expected, in terms of both field magnitude and direction.

When placed in the x-line-centered coordinate system, the magnetopause-aligned current components derived from the magnetic field spatial gradients capture the expected structure of an out-of-plane current sheet in the $- y$ direction near the central region of the x-line. Figure 3.9 displays the superposed epoch x, y, and z curlometer current components, respectively, from top to bottom (the location of the current is set at the centroid of the four spacecraft tetrahedron, yielding only ¼ the number of data points in Figure 3.8). Note that cool shades signify negative current, and warm shades positive. There is also some current along the x-lines in the x-z-plane.

The curlometer current (Figure 3.10a) has a peak current in the $- y$ direction near
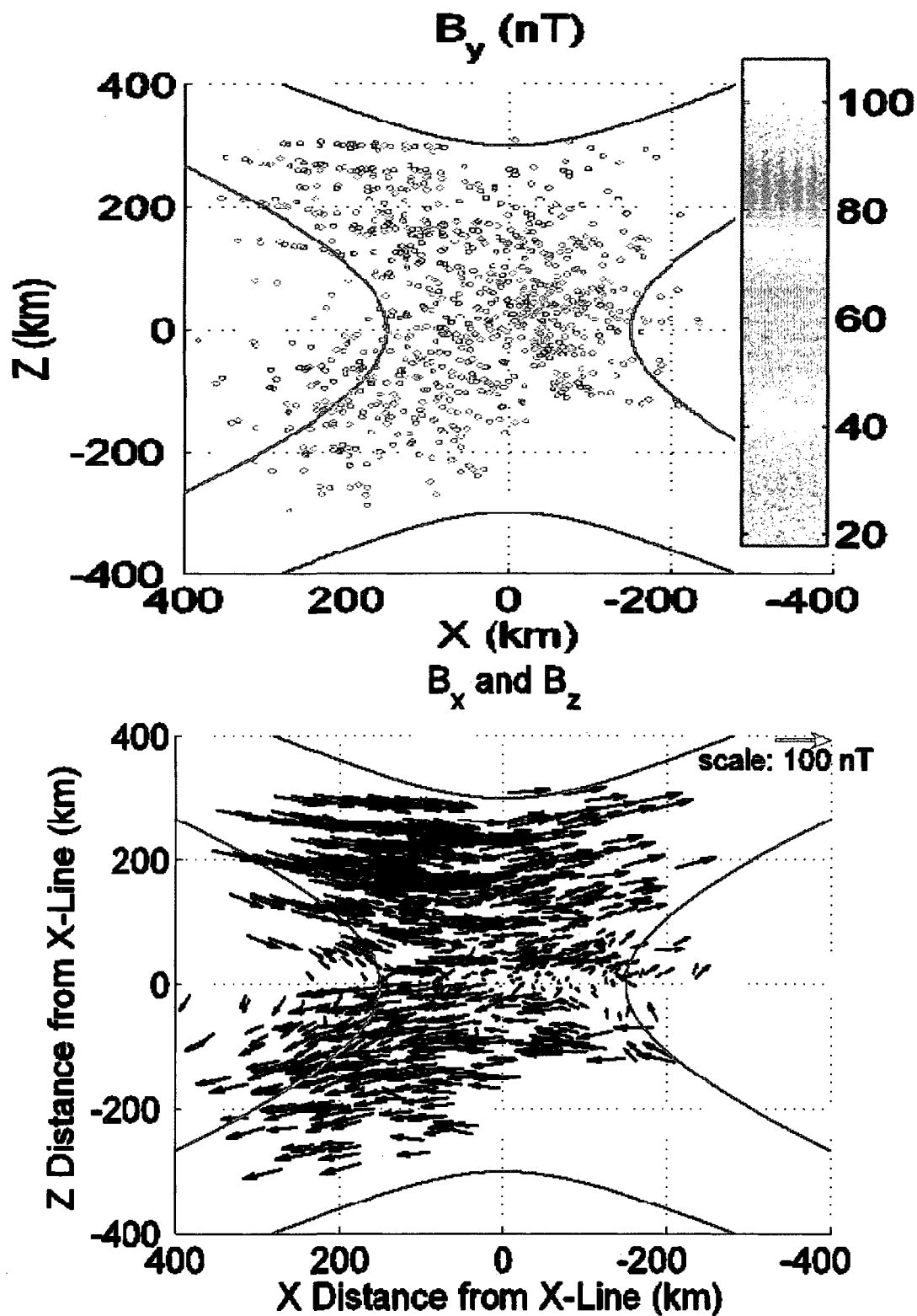
Figure 3.8a - 3.8b. Superposed epoch of B_y (top) and of B_x-B_z (bottom). The magnitude of B_y is shown by color, and that of B_x-B_z by the size of the arrows.
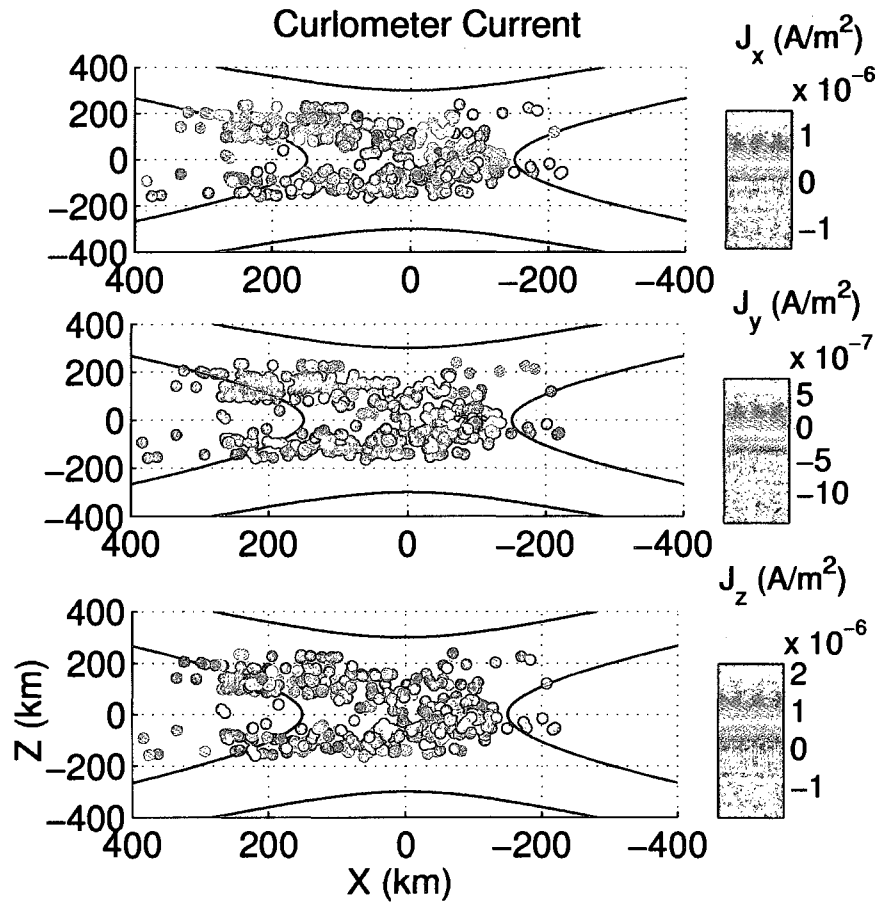
Figure 3.9a-3.9c. The three components J_x, J_y, J_z (top to bottom) of the superposed epoch curlometer current sheet at the x-line. Cooler colors indicate a negative current. J_y appears bifurcated at the current sheet.

the x-line in the superposed epoch. But it also suggests a filamentary structure, wherein a zero or even positive current breaks into the negative y current near the center of the z axis. The dotted lines in Figure 3.10a mark the approximate perimeter of the innermost negative current on both sides of the x-line. Because of the large variance in the data, the filamentation is not conclusive but rather suggestive. The flattening of B_x near the current sheet crossing in the time series magnetic field data presented in Figure 3.6b is consistent

Curlometer Current Density J_y

$\times 10^{-6}$

Z distance from x−line

Ion Temperature Anisotropy

$\times 10^7$

UT (h:m:s)
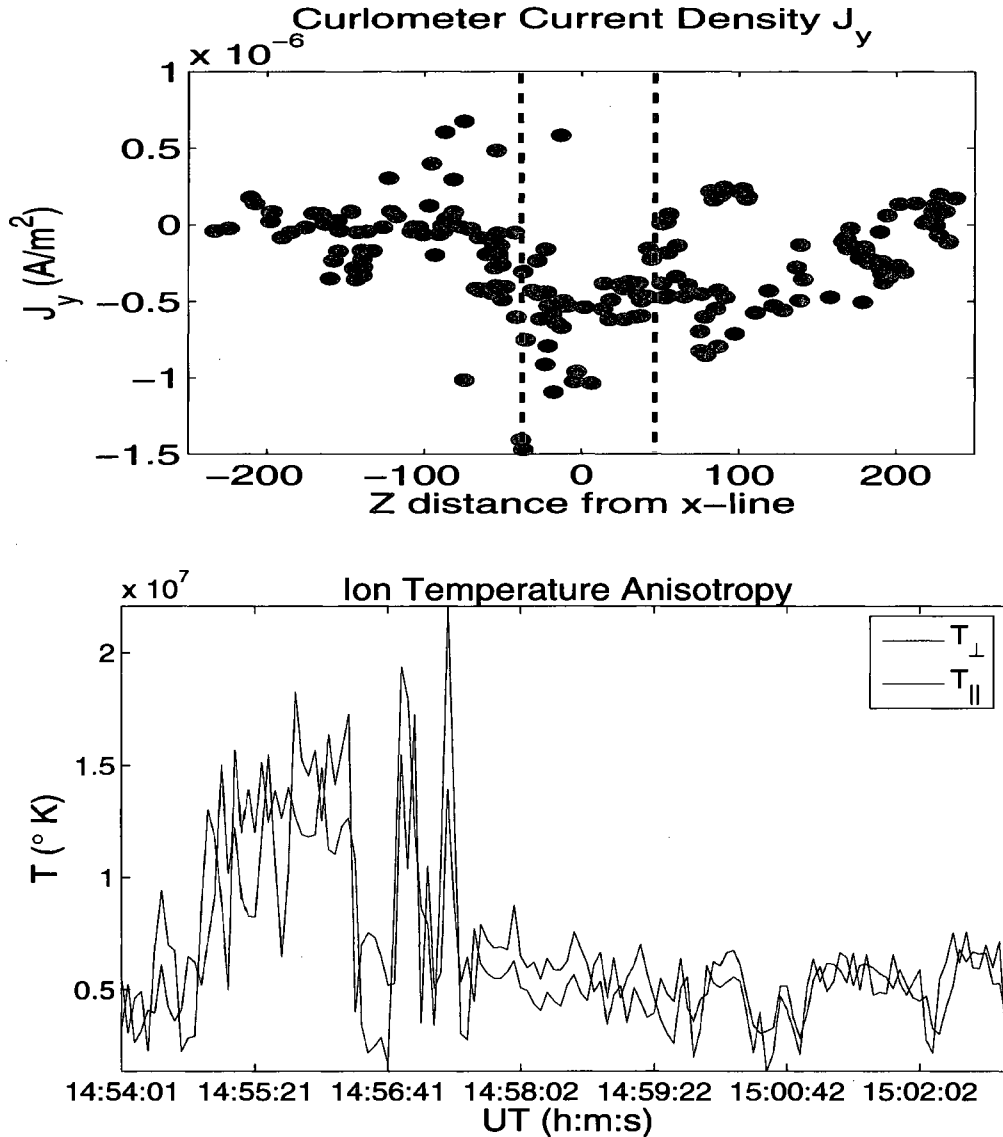
Figure 3.10a-3.10b. (a) **Top:** Though not conclusive owing to the variance in the data, evidence for a filamentary current sheet is reflected in the superposed epoch portrait of the curlometer current profile J_y as a function of z. (b) **Bottom:** The ion temperature anisotropy near 15:00 UT provides the conditions for the development of a bifurcated current sheet.

with bifurcation, which may actually be associated with the apparent lessening of the negative current right at the x-line. (The particle current values will not provide a good source of comparison, as the electron moments are highly aliased.) This filamentary or bifurcated structure has been observed in kinetic simulations [*Hesse et al.*, 1999, *Sitnov et*

al., 2003 and *Singh et al., 2006*], and frequently in data [*Runov et al.,* 2003]. It is associated with a thin current sheet embedded in a thicker sheet and associated with fast reconnection, where it represents a later stage of development of a thin current sheet [*Singh et al.,* 2006]. All these studies find the electrons to be the primary current carriers. The current profile is also somewhat asymmetric in the z direction, with a somewhat higher value on the magnetosheath side. Again, this has been observed previously in data [*Singh et al.,* 2006 and *Runov et al.,* 2006]. We find that the thickness of the local minimum, i.e., $\sim \pm 30$ km north and south of the x-line, corresponds to the proton Larmor scale others have associated with such structures [*Birn et al.,* 2004]. *Sitnov et al.* [2003] attribute a thin current sheet of this size to anisotropies in the ion temperature. In their theoretical studies, *Sitnov et al.* [2003] have demonstrated the development of the thin current sheet in layers with as small as 10% ion temperature anisotropy, $T_{\perp i} > T_{\parallel i}$. *Singh et al.* [2006] also find that this ion temperature anisotropy plays a role in the formation of the thin, bifurcated current sheet. Figure 3.10b reveals that, at the location surrounding the current sheet, $T_{\perp i}$ is roughly 21% larger than $T_{\parallel i}$. The data therefore satisfies the conditions required by some simulations to generate the bifurcated current sheet.

Figures 3.11a and 3.11b depict the motion of the x and z position of the x-line during the 50s interval surrounding the main x-line crossing at 15:00 UT. The positions are in km altitude from the Earth. With regards to the motion of the x-line, the x position initially appears to oscillate by about 350 km back and forth across the spacecraft, at about 14:59:58 UT (Figure 3.11a). The z position (Figure 3.11b) is fairly steady. The curlometer spatial gradients at this time are $\partial B_x/\partial z \sim -1.2$ nT/km, and $\partial B_z/\partial x \sim 0.5$nT/km, while the gradients used to place the x-line are both negative and correspond to the more
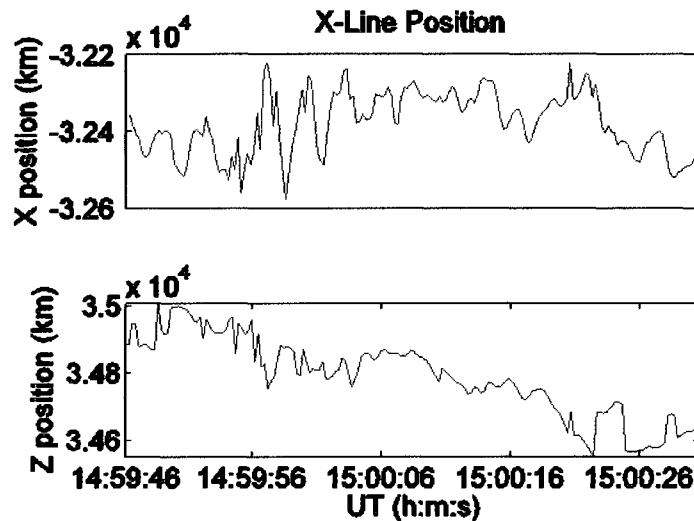
Figure 3.11 (a) (top) The x coordinate and (b) (bottom) the z coordinate of the x-line. Initially there are large oscillations in the x direction superposed on an otherwise steady position. The coordinate system is the rotated magnetopause-aligned.

general trend into the center of the current sheet (persisting starting at 15:00:07). The former gradient correspond to an o-line structure, while the latter to an x-line. Thus it is possible that a tearing mode structure is oscillating across the spacecraft, or that a rotating wave sweeps past. It is also possible that it is part of a series of x and o's that sweep past the spacecraft. In fact, this same type of search unearths a total of nine encounters with such structures that have normal magnetic fields of at least 5 nT. Four occur before the x-line of our study, and 5 later, placing them both tailward and sunward of the x-line of interest. Furthermore, they occur at locations adjacent to where the steepened Alfvén waves are seen.

A movie of the spacecrafts' passage through the site reveals the x-line oscillates relative to the spacecraft. Figures 3.12a-3.12d are frames selected from the movie modeling the spacecraft motion relative to the reconnection site near 15:00 UT. (Cluster '0' marks the centroid position of the spacecraft and the corresponding average values of **B**.) Since the successive frames represent increasing time from top to bottom, it is clear

14:59.59.648 UT

15:00.01.878 UT

15:00.04.152 UT

15:00.19.896 UT

X Distance from X-Line (km)
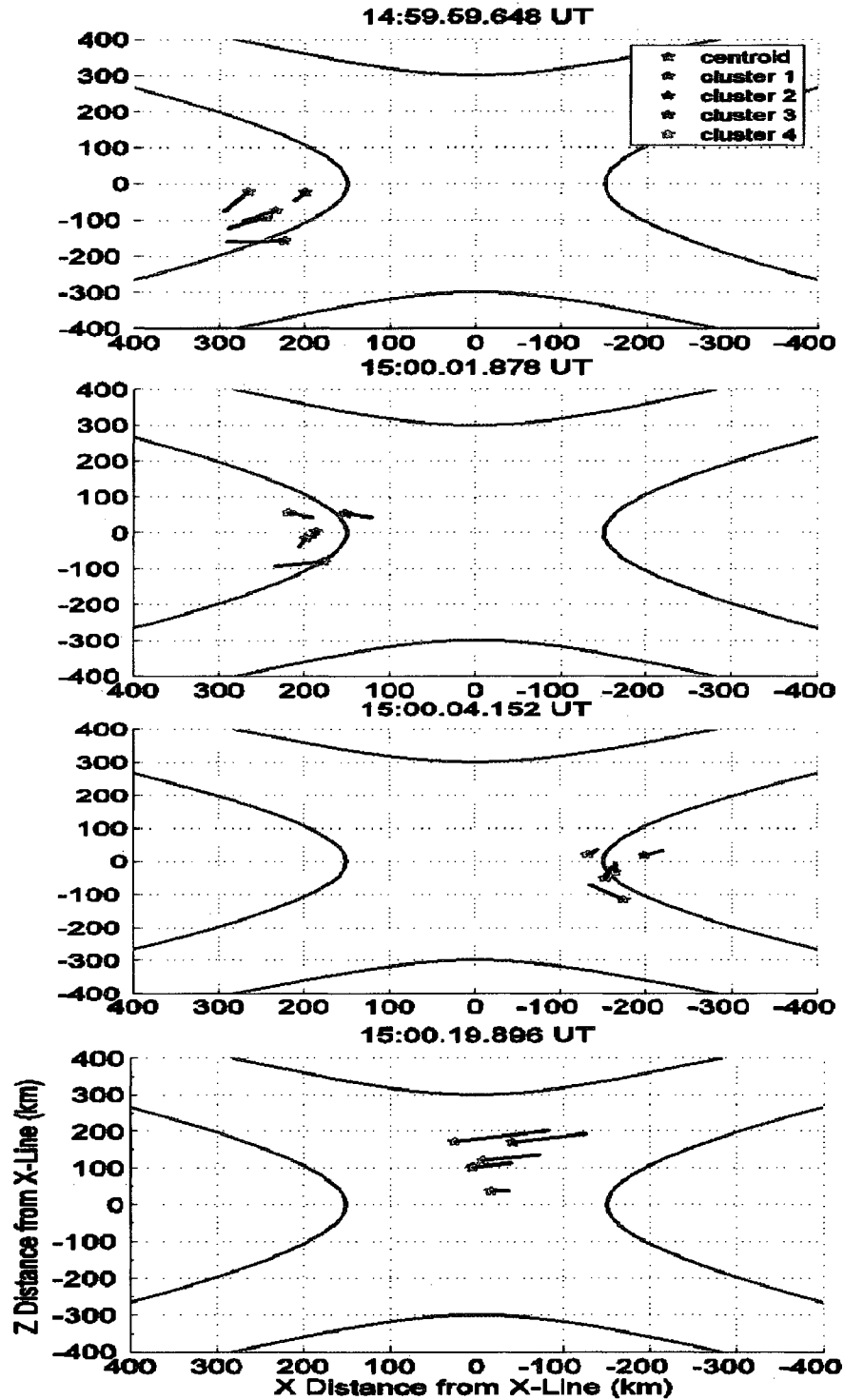
Figure 3.12a-3.12d Top to Bottom: Frames from a movie modeling the spacecraft motion relative to the reconnection site near 15:00 UT, in the reconnection site coordinate system. We include a model of the zeroth-order reconnection site magnetic fields. The arrows at each spacecraft represent the local magnetic field vectors. Cluster '0' marks the centroid position of the spacecraft and the corresponding average values of **B**.

that the position of the x-line bounces with respect to the spacecraft. Arrows represent 0.25 s magnetic field vectors at each spacecraft. In two of the frames shown, the spacecraft instantaneously capture three tangent directions to the curved normal field, proving that the observed normal field does not arise simply from an oscillation of the magnetopause about the y axis.

3.6 Superposed Epoch Particle Flows

The HIA and CODIF instruments (subsets of the CIS instrument) capture the Cluster ion distributions (the number of particles at different energies), while the PEACE instrument measures electron distributions. The HIA instrument sorts the incoming ions according to energy per charge ratio. The CODIF instrument includes a mass spectrometer, permitting calculation of the distribution functions of component ion species. The measurements of the ion and electron distributions are completed at a four s rate, corresponding to the spacecraft spin. Cluster 1 and Cluster 3 provide the only HIA data available for this interval, and Cluster 4 the only O^+ data (Cluster 1 and Cluster 3 were operating in a mode that telemetered the HIA data, and Cluster 4 in a mode that telemetered the CODIF data). The PEACE data are available from all four spacecraft. Moments are calculated on-board, and, where the full three-dimensional raw data are available, again on the ground using the most up-to-date calibrations. For our event, the Cluster 1, Cluster 3, and Cluster 4 PEACE moments are available from onboard calculations only, so that they cannot been recalibrated on the ground. However, Cluster 2 telemeters full three-dimensional raw data to the ground, where recalibrations have been made for known offsets in the GSE v_z component and for sensor degradations.

Moreover, we have applied existing software (available to co-investigators at http://www.mssl.ucl.ac.uk/missions/peace/) that corrects for known geometric and inter-anode calibration changes in some of the sensors and for the spacecraft potential. The onboard moments have only the inter-anode and geometric factor calibrations available in 2002 when the data was taken. The newest calibrations available on ground produce more accurate densities and velocities, more consistency between HEEA and LEEA measurements, and much improved corrections for the velocity v_z component offset the results from inter-anode calibration errors (Andrew Lahiff, personal communication).

Aside from the calibration issues mentioned above, there are several other sources of error in the computations of the moments of the distributions. Because Cluster 2 has been calibrated to correct for the v_z offset, the largest statistical instrumental errors for Cluster 2 PEACE particle moments are very small (less than 10%). Assuming calibrations are good, the main source of statistical instrumental error lies in the summation of counts at various energies to get the distribution function. These errors come from random counting errors that follow Poisson statistics. Based on previous estimates from similar counts as seen here and because the counting error scales as $\sqrt{\delta N}/N$, where N is the number of counts, these will be about 10% for densities, velocities, pressures, and temperatures [*Paschmann et al.*, 1998; George Parks, personal communication, 2007]. However, aliasing errors can become quite serious in regions where temperature, density, or magnetic field gradients vary significantly over a spin period. The instantaneous densities and temperatures directly affect the measured distributions, and the summations of the moments components are evaluated based on the instantaneous magnetic field direction. One of these parameters changing at a faster rate

than the spin period may masquerade as a bulk moment. Electrons with their larger thermal speeds are more susceptible to time-aliasing of the moments than the ions are. During the interval of interest here, the largest aliasing errors occur where the magnetic field changes rapidly during a spin or where the particle densities vary over a spin, while the temperature variations over a spin have a much smaller effect. The electron moments suffer some magnetic field direction aliasing effects during spins during our interval of interest, and a great deal of aliasing from density gradients. The error in the electron moments measured by Cluster 1, 3 and 4 must also include the inter-anode calibration issue that gives rise to the erroneous offset in GSE v_z. The statistical averages of this offset have been calculated for each spacecraft. For Cluster 1, it is 50 km/s, for Cluster 3, 70 km/s, and, for Cluster 4, 100 km/s. Rotating the 100 km/s GSE v_z error into our magnetopause-aligned coordinate system generates electron velocity errors of [-68, -50, 54] km/s, respectively, due to the average errors in GSE v_z measurements. In the following discussion, we will estimate the contribution of aliasing and other errors to the velocities, and in section 3.6, to the pressure tensor.

The velocity moment errors are first calculated in the GSE coordinate system and then rotated into the new magnetopause aligned coordinate system. We use the GSE coordinate system because it is very close (differing by at most 7°) to the spacecraft spin-axis centered ISR2 coordinate system, a natural coordinate system in which to estimate the moments errors due to aliasing. We model the density and temperature aliasing by assuming a difference in density and temperature during one-half of the spin. We choose the fraction of ½ because it is for this value that the aliased moment is the largest. We are therefore being conservative in that this target produces the worst case. Aliasing

effectively alters the estimation of the ISR2 x or y velocity components, since they lie perpendicular to the spin axis, but not the ISR2 z component, which lies along the spin axis. We assume a Maxwellian velocity distribution with a uniformly larger density or temperature during the first half of the spin. Though there are some highly accelerated particles that form high energy tails to the distribution, as can be seen from the electron distributions discussed in section **3.6**, the assumption of a Maxwellian distribution provides an upper limit to the model of aliasing errors. For the density, integration of the measured particle distribution which would result from this model yields an artificial bulk moment nv_y, in the ISR2 x or y directions, where

$$nv_y = \delta n (\frac{m}{2\pi kT})^{3/2} \int_0^\infty \int_0^\pi \int_0^\pi v^3 \sin^2\theta \sin\varphi\, e^{-\frac{mv^2}{2kT}} d\varphi\, d\theta\, dv \qquad (3.4)$$

$$\Rightarrow v_y = \frac{\delta n}{n} \left(\frac{\pi kT}{2m}\right)^{1/2} = \frac{\delta n}{n} \sqrt{\pi} v_T, \qquad (3.5)$$

where v_y is the spurious velocity moment, n is the particle density measured during the spin, δn is the excess in density during the first half of the spin, k is Boltzmann's constant, T is the temperature, m the particle mass, and v_T the thermal speed. Thus, density aliasing contaminates more strongly at high thermal speeds, and the artificial moment scales as the relative difference in density during the spin. From azimuthal symmetry, the spurious moment in the x direction will be the same. Whether the false moment shows up as an x or a y component depends on which azimuthal (spin) angular dependence of the density jump. For a temperature gradient, the mathematics is similar, except now the difference goes as the square root of the temperature, so that the spurious

contribution to the velocity moment is

$$v_y = \left(\frac{\pi k}{2m}\right)^{1/2} \left[(T + \delta T)^{1/2} - (T)^{1/2}\right],$$

(3.6)

where $T + \delta T$ is the temperature during the first half of the spin, and T is the temperature during the second half. In the case of the ions, we simulate δn and δT by the difference in n and T between each spin, since half-spin data are not available. Hence the errors shown for the ions are truly a worst case scenario. In the case of the Cluster 2 electron data, however, δn and δT during a spin are directly available from half-spin summations. Thus the errors we calculate for the electrons will be more in line with the actual errors.

We produce the superposed epoch portrait of the particle flows by first performing a Galilean transformation to the moving x-line coordinates. The x and z velocity of the x-line is estimated by time differencing the estimated x-line x and z position coordinates. This transformation can be safely ignored in the case of all higher-order electron moments and quantities derived from them, and in fact have a very small effect (well below 10%) on even the first-order electron moments. Only the O^+ speeds are significantly affected by the x-line motion. The spacecraft speeds have also been removed, though their speeds (< 10 km/s) are relatively insignificant.

The superposed-epoch electron moments in the reconnection site coordinates in Figure 3.13 have strong components normal to the magnetopause, one of Vasyliunas' defining conditions of two-dimensional reconnection [*Vasyliunas*, 1975]. (Note that purple indicates vectors with a negative y-component, and black indicates vectors with a positive y-component). There is something of a pattern of inflow (for example the
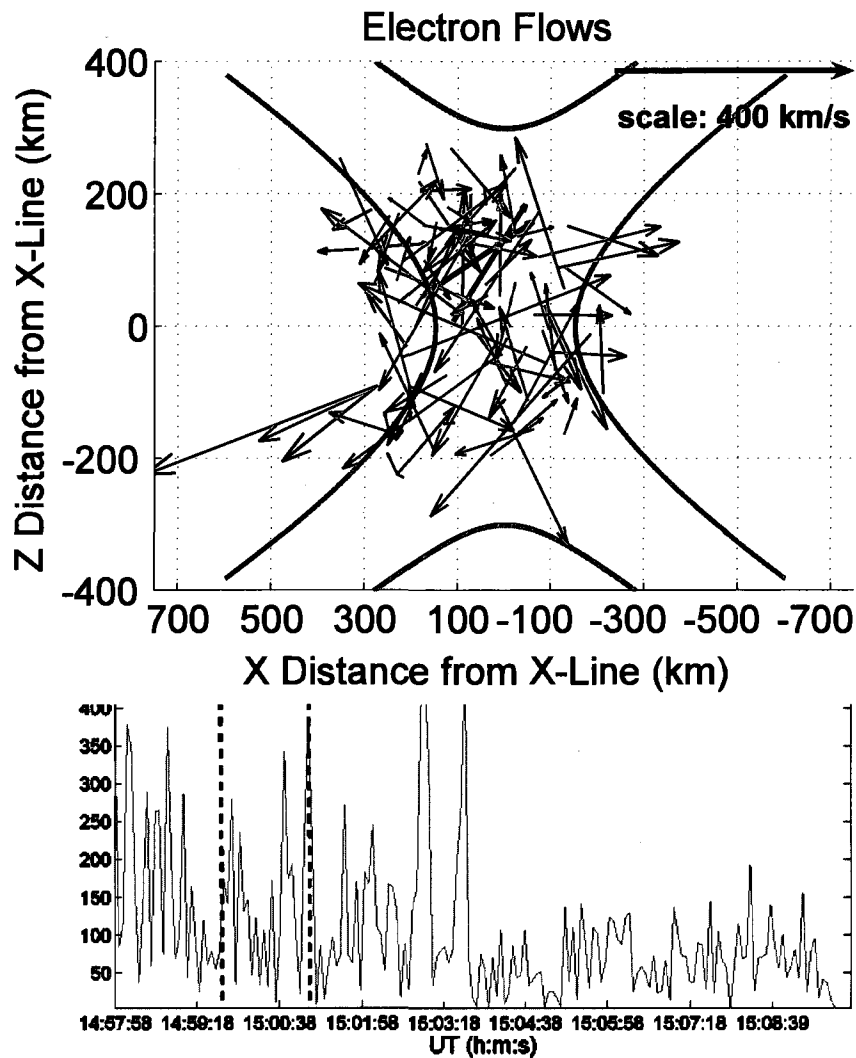
Figure 3.13a - 3.13b. (a) Top: Superposed epoch electron flow vectors with y-component < 0 (purple) and y-component > 0 (black) near the reconnection site at 15:00 UT. **(b) Bottom:** The total rms velocity moment error from all contributions except magnetic field aliasing. The dotted lines mark the region included in the superposed epoch plot. The density and temperature aliasing errors are included by way of inserting the density and temperature differences from one half-spin to the next in a Maxwellian velocity distribution.

downward pointing arrows into the center of the x from above and the upward pointing

arrows into the center of the x from below) and accelerated outflow (for example along

the lower portion of the left red magnetic field line or close to the upper portion of the

right red magnetic field line) at the reconnection site in the x-z plane, in agreement with the x-line electron flows in the presence of an out-of-plane field that *Hesse et al.* [2001] obtain in their kinetic simulations with a guide field. The first-order electron moments in the vicinity of the reconnection appear to be in concert with smaller, normal inflows converting to higher, tangential outflows.

These electrons, however, often suffer significant aliasing, as Figures 3.13b and 3.14a-3.14c from Cluster 2 data, attest. It is best to appraise aliasing errors on Cluster 2, since it has the best calibrations and the full spin distribution calculations (the other spacecrafts' moment calculations reduce memory requirements by measuring a half spin of data and exploiting a gyrotropic assumption to produce the balance). Figure 3.13b plots the total rms magnitude of the potential false bulk velocity moment along one component direction for the entire magnetopause crossing. The error includes contributions from density and temperature aliasing along either the ISR2 x or the ISR2 y directions, and 10% Poisson statistics fluctuations along all three components. The density and the temperature aliasing are calculated from the actual differences in density and temperature between half-spins assuming a Maxwellian distribution. (Magnetic field aliasing is not included, but will be examined later in the context of spins of particular interest. There is also inevitably some error introduced into the positions by reducing the 0.25s position calculations to 4s resolution.) The time interval is that of the superposed epoch in Figure 3.13a. Figure 3.14a shows the magnitude of v_x (blue) in the rotated magnetopause-aligned coordinate system as well as the error contribution to v_x from the ISR2 errors δv_x (red) and from δv_y (green) after having been rotated into the magnetopause-aligned coordinate system. The components of these errors in the rotated
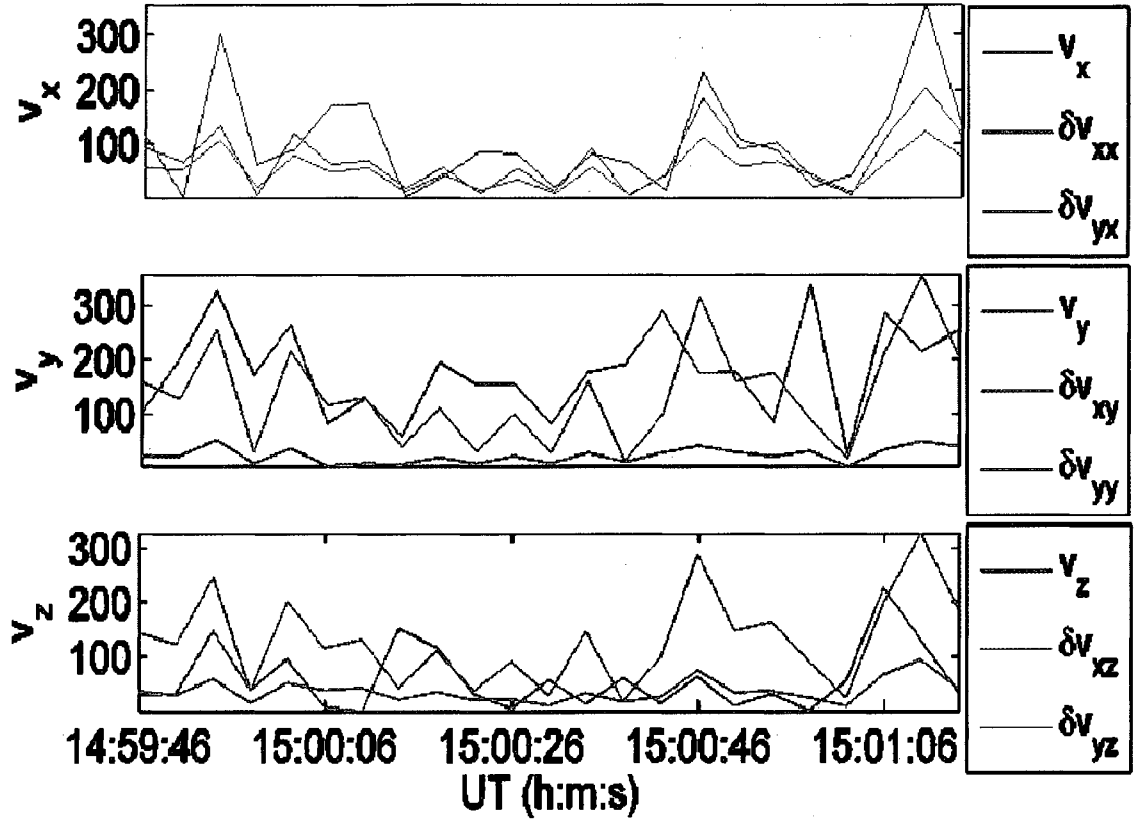
Figure 3.14a-3.14c. The flow speeds (blue) from Cluster 2, and the corresponding error vectors assuming a density and temperature aliasing error in either the x (red) or y (green) directions of the ISR2 coordinate system. Here the errors from density and temperature aliasing are calculated from the actual differences in density and temperature between half-spins assuming a Maxwellian distribution. The time interval is that of the superposed epoch in Figure 3.13a. **(a) Top:** The magnitude of v_x (blue) in the rotated magnetopause-aligned coordinate system and the error contribution to v_x from the ISR2 errors δv_x (red) and δv_y (green) after having been rotated into the magnetopause aligned coordinate system. The components of these errors in the rotated coordinate system are denoted by δv_{xx} and δv_{yx}, etc. **(b) Bottom:** The same as (a), but for the speed and errors in the magnetopause aligned y direction. (c) The same as (a) and (b) for the magnetopause aligned z direction.

coordinate system are denoted by δv_{xx} and δv_{yx}, etc. Figure 3.14b is the counterpart to (a) for the speed and errors in the magnetopause-aligned y direction. Figure 3.14c is the analog of (a) and (b) for the magnetopause aligned z direction. There is still a small ISR2 v_y component in the magnetopause aligned x-z plane because the rotation to the
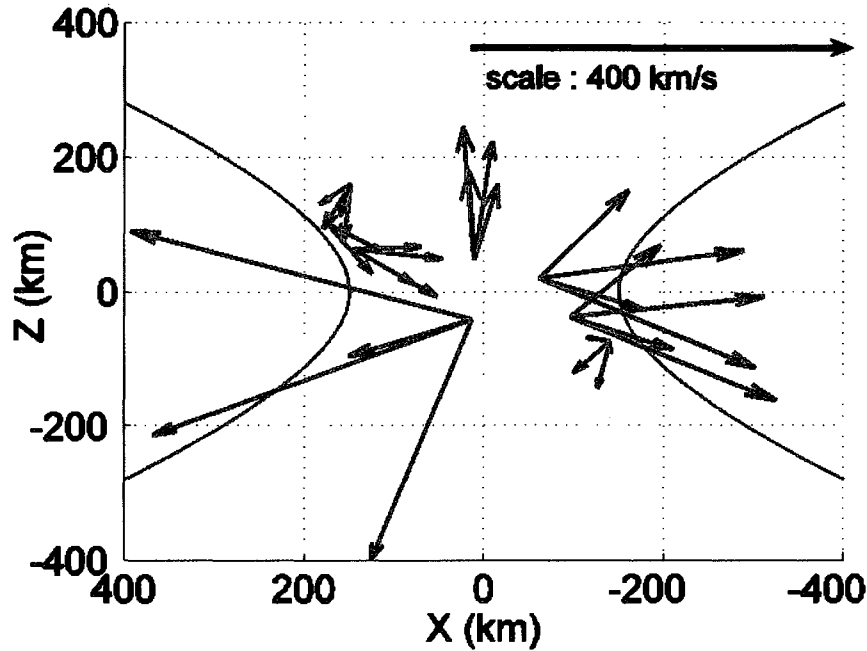
Figure 3.15 Aliasing contributes significant errors for most data points, though a few can still be shown to contribute strongly normal velocity components regardless of the error bar, as shown in this figure. In this figure, we include only data points where the measured flow exceeds the magnitude of the errors projected on to the x-z plane. The pairs of blue arrows represent the measured flow vectors "+" or "-" the rms ISR2 error δv_x, and the pairs of red arrows represent the measured flows "+" or "-" the rms ISR2 error δv_y. Thus the set of four arrows at each data point span the cone of possible corrected flow vectors.

magnetopause-aligned coordinate system includes a small rotation about the GSE z direction (as discussed earlier). The aliasing errors probably account for the electron velocities largely flowing in the 'wrong' direction along y: we expect predominantly positive electron flows in the y direction, but there are many in the negative y direction. The errors in the magnetopause-aligned x-z plane are also significant. Since the errors are further compounded on Cluster 1, 3, and 4 by the v_z offsets mentioned above, it is difficult to come to a definitive conclusion about the overall flow pattern.

However, we can retain certain inferences about at least some of the data points,

Ion Flows, CL 1 and CL3
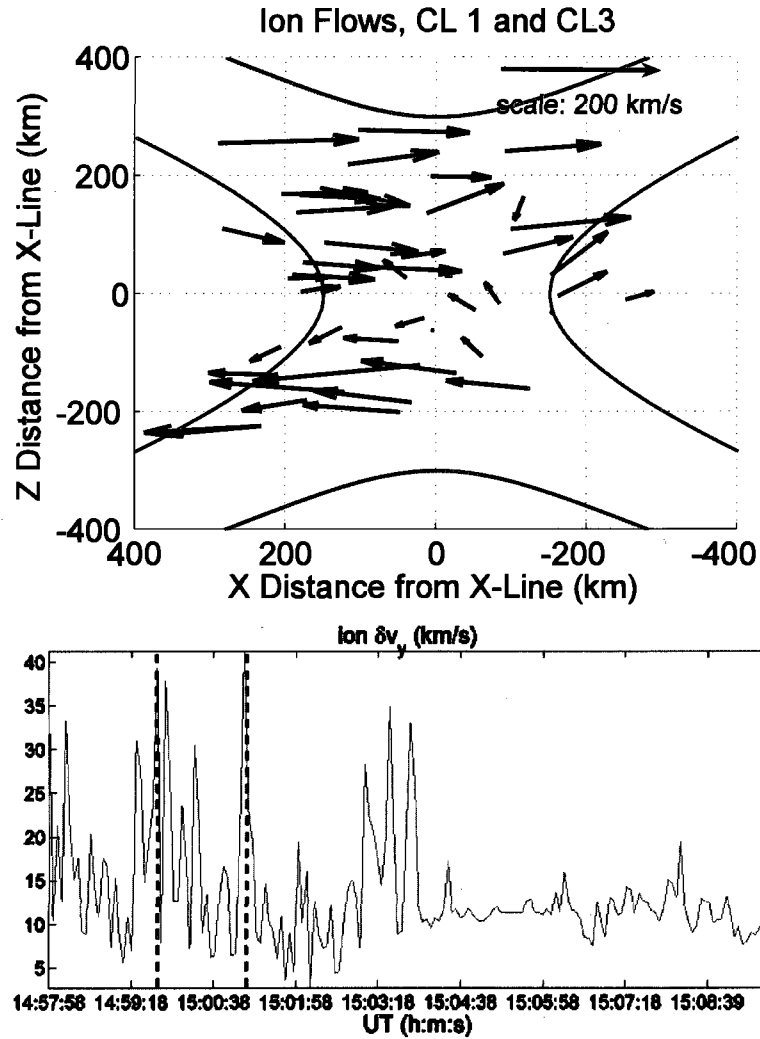
igure 3.16a-3.16b. (a) Top: Superposed epoch ion moments from Cluster 1 near the reconnection geometry. These ion velocities are not mass differentiated. **(b) Bottom:** The total rms error for ion velocity moments.

as we demonstrate in Figure 3.15. In this figure, we include only data points where the measured flow exceeds the magnitude of the errors projected on to the x-z plane. The pairs of blue arrows represent the measured flow vectors "+" or "-" the rms ISR2 error δv_x, and the pairs of red arrows represent the measured flows "+" or "-" the rms ISR2

error δv_y. Thus the set of four arrows at each data point span the cone of possible corrected flow vectors. There are clearly a number of data points that retain a normal component to the magnetopause even after accounting for the errors in the moments summations. Some even retain a large magnitude. The highest, and supra-Alfvènic, electron flows lie roughly along the x-line with a magnitude in the x-z plane of 300 to 400 km/s, and an Alfvén Mach number $M_{Ae} > 1$. This implies that the high flows are not merely supporting the current sheet. (The Alfvén speed is roughly 218 km/s for the asymptotic ion density ($\sim 100/cm^3$, as in Figure A5a), using an asymptotic magnetic field of 100 nT. This electron Mach number is equivalent to v_e/v_A, where v_A is calculated from the ion density.)

The Cluster 1 and Cluster 3 ion moments from the CIS particle analyzer (Figure 3.16a) flow predominantly sunward in the magnetosphere, and tailward in the magnetosheath. However, over a narrow width in the z-direction, within $\sim \pm 75$ km of the x-line, the ions' velocities in the x-direction oppose the standard flow. As expected in reconnection, they turn in x and follow the field lines away from the x-line in that region. The ion velocities also exhibit a significant normal component in some of this region, within roughly ± 100 km from it in the z direction, and within ± 200 km along it.

The CIS ion moments experience the same order of magnitude and source of statistical Poisson error as the PEACE moments. But unlike PEACE onboard moments, they do not suffer from the spurious offsets in v_z, and, unlike any of the PEACE moments, they are much more invulnerable to aliasing, since the ions have much smaller thermal speeds. (Prior to 2001, the Cluster 3 CODIF instrument suffered degradation of its v_z measurements, but this was improved by onboard software patches. There are
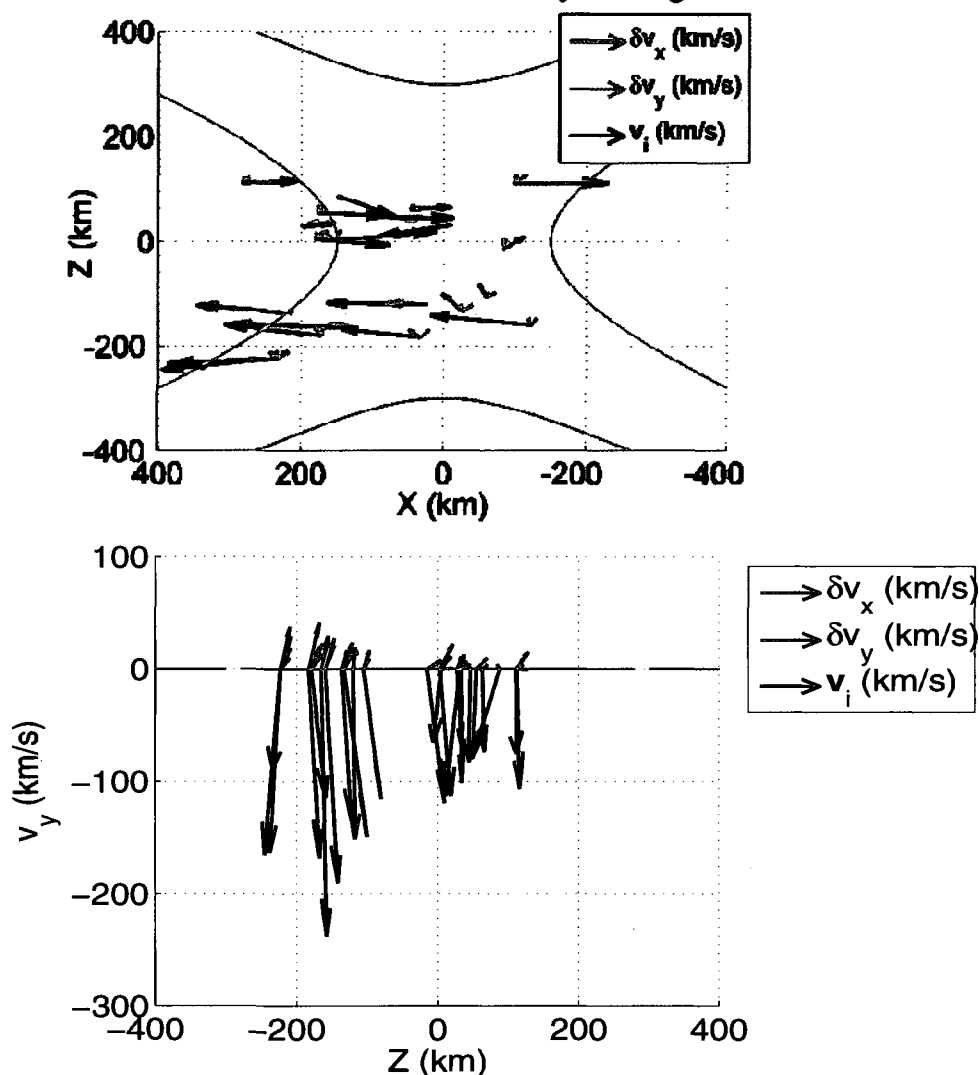
Figure 3.17a-3.17b. (a) **Top:** The ion flow vectors (black) from Cluster 3, and associated error bars (blue for δv_x and red for δv_y). The ions are not strongly affected by density and temperature aliasing errors. (b) **Bottom:** A view of the out-of-plane flows v_y.

several known caveats regarding CIS data in the "solar wind mode", but these do not apply to our data which was obtained in the "magnetosphere mode." CIS data caveats are available at http://cluster.cesr.fr:8000/.) Figure 3.17a-3.17b displays the ion velocities from Cluster 3 (black arrows), and the rms velocity errors from ISR2 x and y directions

(red and blue arrows). the blue arrows correspond to the rms error that arises when the density and temperature aliasing error affects the ISR2 v_x component, and the red arrow to that which arises when the density and temperature aliasing affects the ISR2 v_y (thus the error bars point along these two directions). The sense of the red and blue arrows may be opposite to what is shown, since what is plotted is the positive rms value along the ISR2 x and y directions. The errors clearly do not significantly alter the interpretation of the overall ion flow pattern and the presence of velocity components normal to the magnetopause. The CIS data does not differentiate ions by mass, though we assume a proton mass to calculate the aliasing errors. However, this assumption produces a worst case estimate, because the density and temperature aliasing errors scale inversely with mass.

The much slower O^+ ions, measured by Cluster 4 (Figure 3.18), show a similar pattern of flow normal to the magnetopause in a narrow region surrounding the x-line in the z-direction. The sheer presence of anti-sunward flowing O^+ in the magnetosheath implies reconnection somewhere else on this field line upstream of the spacecraft and shows that field lines in the magnetosheath carry particles accelerated from the ionosphere. Generally one would not expect to see terrestrial O+ outside of the magnetopause unless there is a field line that connects those fluxes to the Earth (or at least did, at an earlier time). This fact suggests that Cluster encounters either (a) a tearing mode, and thus exhaust flows from more sunward, lower latitude reconnection sites on the magnetopause, or (b) a field line that has already reconnected in the southern hemisphere, creating a layer of open flux overdraping the dayside magnetopause [*Lavraud et al.*, 2005; *Onsager et al.*, 2001].
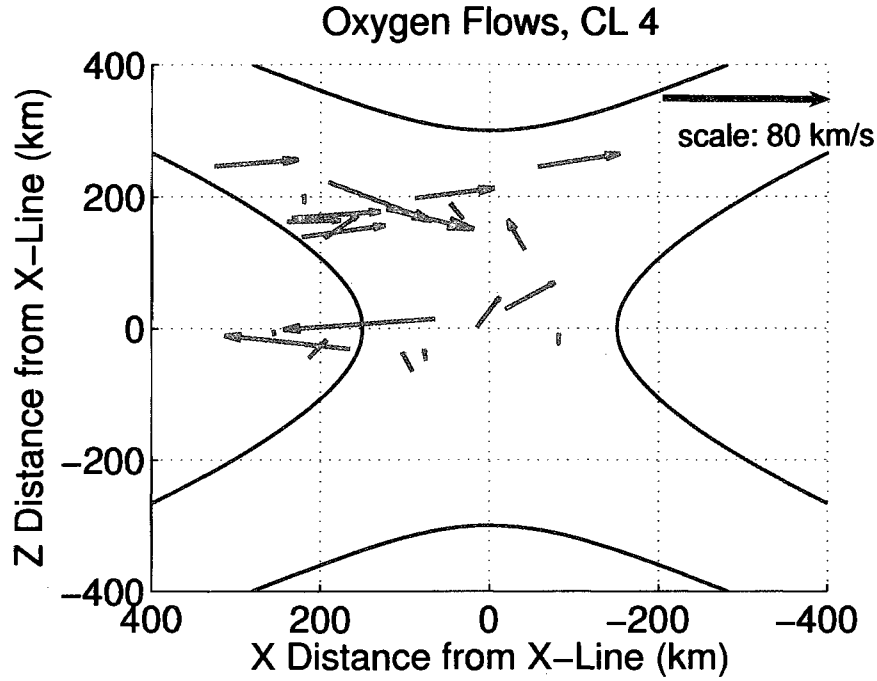
Figure 3.18. The O$^+$ flows near the x-line are streaming along the magnetosheath, as well as across the magnetopause. The magnetosheath O$^+$ is traveling either from a downstream cusp x-line or from the southern hemisphere.

Both the ion and the O$^+$ flows are largest in the y, out-of-plane, direction, closer to the x-line. Coming up, we will show evidence that Cluster moves through the ion diffusion region, where the magnetic field gradients vary on a scale smaller than the ion inertial length. The ion first moments further support this in Figure 3.19, where we plot the superposed epoch of the magnitude of the out-of-plane ion Alfvén Mach number, M_{Ai}. We calculated M_{Ai} from the y component of the ion moments as a function of position in the reconnection plane, where the values are color-coded. The maximum value (~ 0.75) occurs at the x-line crossing, and the average value is highest at the x-line. We will discuss the diffusion regions at greater length in the following sections.
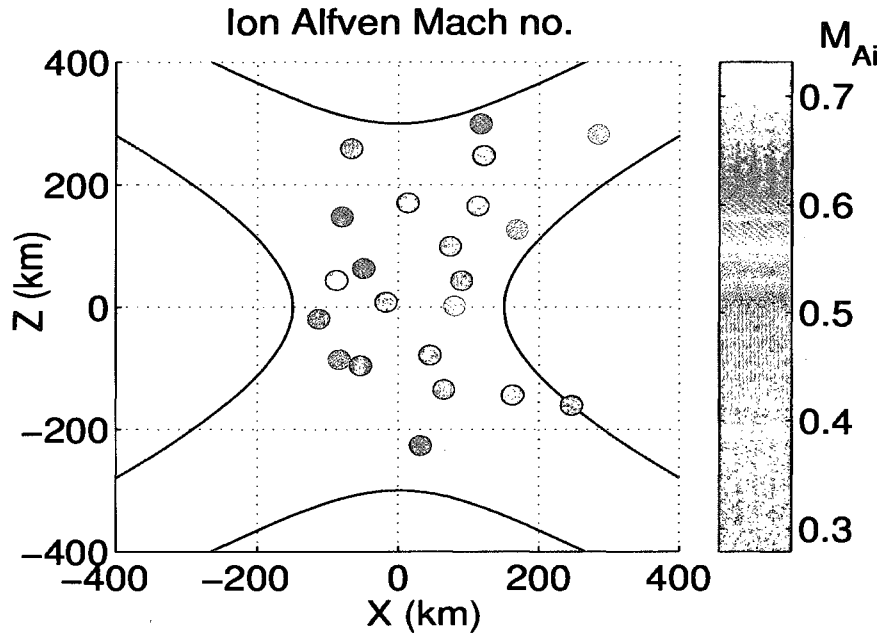
Figure 3.19. The out-of-plane (y) component of the ion Alfvén Mach number M_{Ai} is maximum near the x-line.

3.7 Non-Ideal Electric Field, Higher-Order Moments, and Particle Diffusion Regions

Even though the EFW instrument measures only two components of the electric field, it is still possible, in theory, to identify the presence of a non-ideal electric field by comparing the two measured components to the corresponding components of $v \times B$, where v is the ion or electron velocity. In practice this is fraught with difficulty, for the velocities, magnetic field, and electric field are all measured at a different cadence, and the measured velocities are potentially beset with errors, as discussed above. However, we proceed mindful of the error sources and also compare the drift electric field to the

measured electric field in the ISR2 coordinate system in which the electric field is measured. Any rotation of the measured electric field requires knowledge of the third component. This requires assuming $\mathbf{E\cdot B} = 0$, an assumption we do not wish to make. The magnetic field data is available at the spin resolution (the resolution of the particle data), but the electric field data is only available at that resolution in rotated coordinates. So first the data must be resampled and interpolated onto common time tags. The best calibrated particle data and the magnetic field data are available in GSE coordinates, which differs at most by 7° from the ISR2 coordinate system. This difference between the $\mathbf{v \times B}$ coordinate system (GSE) and the electric field coordinate system (ISR2) contributes a very small error that we will account for in the final tallying of errors. Any verifiable differences we can discover between the measured and drift electric fields will include perpendicular and parallel components, but they will nevertheless all be non-ideal. A parallel electric field is required to certify global x-line reconnection. We do not have sufficient information to find the parallel electric field since we only know two of the electric field components. A non-ideal electric field constitutes a sufficient condition for local reconnection at the very least. However, as we shall show, since we find a nonideal electric field in the direction along B_y, we can infer that it is a parallel electric field.

First we find that there are differences between the ion drift electric field and the measured electric field at certain locations. The difference will include the Hall term, $\frac{\mathbf{J \times B}}{n_e e}$, the pressure divergence term $-\frac{\mathbf{\nabla \cdot P}_e}{n_e e}$, and the electron inertial term. Thus we can expect a non-ideal electric field to have components directed both towards (Hall term) and away from (pressure divergence term) the x-line. The pressure tends to bulge at the x-line,

producing a negative divergence there. Figure 3.20a plots the total absolute difference between the Cluster 3 drift electric field and the measured electric field in the ISR2 x and y directions in blue, and the total calculated rms electric field errors in red. (Only Cluster 3 data are available, because the CIS instrument onboard Cluster 2 is nonoperational, HIA moments are not available from Cluster 4, and the EFW instrument onboard Cluster 1 is damaged.) We call this difference the non-ideal electric field, or E_{NI}. The components of E_{NI} are plotted as absolute values. The dashed lines mark the region around the x-line that is used in all the superposed epoch portraits. The error curve includes contributions from the density and aliasing errors in the particle moments, the maximum 10% Poisson error in the particle moments, the maximum 1mV/m electric field measurement offset, and the ~12% error in the components E_{NIi} from the maximum 7° offset between ISR2 and GSE coordinate systems. The magnetic field measurements contribute errors that are negligible (< 0.2% in B_i). The density and temperature aliasing effects are derived from the Maxwellian model with the density differences between spins, as discussed above in the context of particle flows. Thus this error represents the worst-possible case scenario. This is particularly the case since we assumed a proton mass in the aliasing errors. Some of the ions are heavier, which would actually make the error smaller. Also, no doubt the actual density aliasing errors are smaller than we calculated, because we had to assume the density differences during the spin were the same as those between spins. As we will see with the electrons, the actual density changes during the spin are smaller than those between spins. Nevertheless, there are several regions where the E_{NIi} derived from measurements clearly exceeds the worst-case errors. Most of them, and the largest, lie within the region spanning the x-line at 15:00
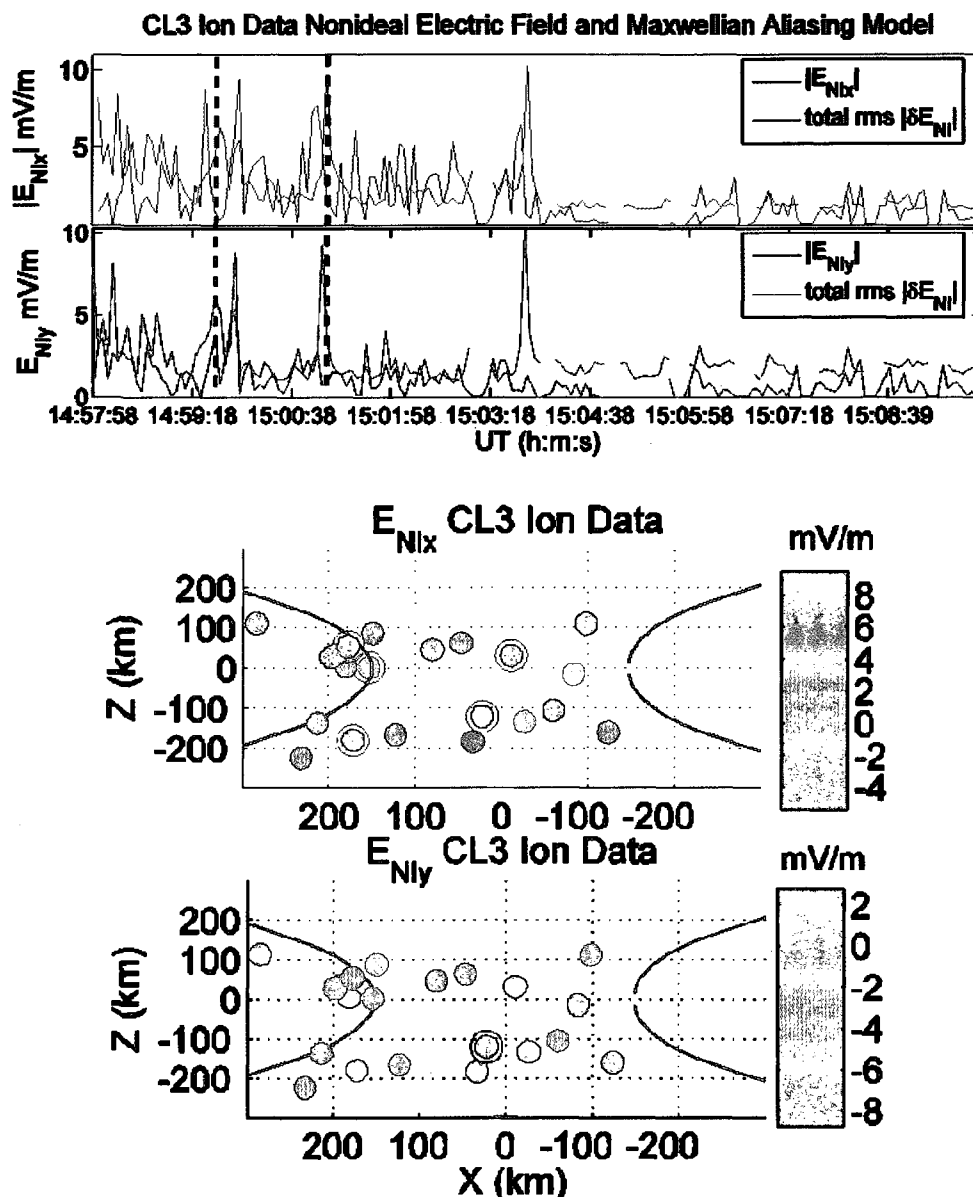
Figure 3.20a-3.20b. **(a) Top:** A plot of the total absolute difference between the Cluster 3 drift electric field and the measured electric field in the ISR2 x and y directions in blue, and the total calculated rms electric field errors in red. The density and temperature aliasing effects are derived from the Maxwellian model with the density differences between spins. The dashed lines mark the region around the x-line that is used in all the superposed epoch portraits. **(b) Bottom:** The superposed epoch of both of the E_{NI} components. Here we are showing the sign of E_{NIi} so we can see where the values are negative and positive. The x and y components of E are in the ISR2 coordinate system, which is about 52° clockwise from the superposed epoch coordinate system. The data points with blue circles denote the times where the inferred E_{NIi} exceed the error floor.

UT that we have included in all the superposed epochs. In contrast to select locations within the magnetopause, the calculated E_{NI} always falls at or below the δE_{NI} within the magnetosheath (which the spacecraft enters after the final spike of $\delta E_{NI} = 10$ mV/m), where we do not expect to see any non-ideal electric fields. (The error spike occurs there because it is the boundary of the magnetosheath, which undergoes a large jump in density. Other nonideal regions within the magnetopause are other approaches to an x-line.) This fact lends weight to the error we have calculated.

In order to get a sense of the location and direction of the resulting E_{NIi}, Figure 3.20b shows the superposed epoch of both of the E_{NI} components. Here we are showing the sign of E_{NIi} so we can see where the values are negative and positive. It must be borne in mind, however, that the x and y components of E that are presented here are those of the ISR2 coordinate system, almost the same as GSE, which is oriented about 52° clockwise from the x-line centered coordinate system. The data points with blue circles denote the times where the inferred E_{NIi} exceed the error floor. We are defining the error floor to be the magnitude of the rms error at any given instant. The x component of E_{NI} has maximum values of about 4 mV/m above the error floor, and the y component of about 4 mV/m above the error floor in the negative direction. The largest E_{Nix} fall within about a 150 km thick layer about the x-line, and the peak E_{NIy} lies at about $x = 0$ and 100 km below the x-line. The $E_{NIy} < 0$ is in keeping with a reconnection electric field along the x-line of - 4 mV/m. The large distance scales of these nonideal values can be attributed to two factors. One is that these ion flows include much heavier particles, such as O^+, which have much larger ion gyroradii and skin depths than protons—on the order of 100 km for the relevant densities and magnetic fields. These are the scale lengths over

which we expect to see particle demagnetization. The second reason is that the association of values with positions gets somewhat smeared in the low time resolution fitting of particle data to the x-line coordinate system, since the positions of the spacecraft relative to the x-line were initially performed using the .25s resolution data of the magnetic field. The positions at the spin resolution must be found from the 0.25s resolution time tags that best match the spin resolution time tags, which correspond to the center of the spin interval).

Figure 3.21a-3.21b, displays the same results for the electrons. Of course we now use Cluster 2 because it has the best electron moments. Because aliasing is so much worse for the electrons than for ions, the error floor is much higher, even though the density differences used in the electron aliasing calculations are the actual differences between half-spins. There are a few locations within the magnetopause near the x-line crossing where E_{NIx} exceeds δE_{NI}—by about 10 mV/m at one location. There are no locations where E_{NIy} exceeds δE_{NI}. In the superposed epoch, the values that exceed the error floor (marked by blue circles) are all positive and on the sun side of the x-line. This is consistent with an electric field pointing away from the x-line in that quadrant. Because the nonideal electric field includes only the divergence and inertial terms, and the divergence term dominates, we expect to see a non-ideal electric field that points away from the x-line.

The source of error that remains to be addressed is the electron moment aliasing from a rapidly changing magnetic field. To this end, for the spins with $E_{NIx} > \delta E_{NI}$, we present the full-spin electron velocity distribution functions in Figure 3.22. Each row of Figure 3.22 displays the distribution function (as in the number of particles per velocity

CL2 Electron Data Nonideal Electric Field and Data Density Aliasing

E$_{Nlx}$ CL2 Electron Data

E$_{Nly}$ CL2 Electron Data
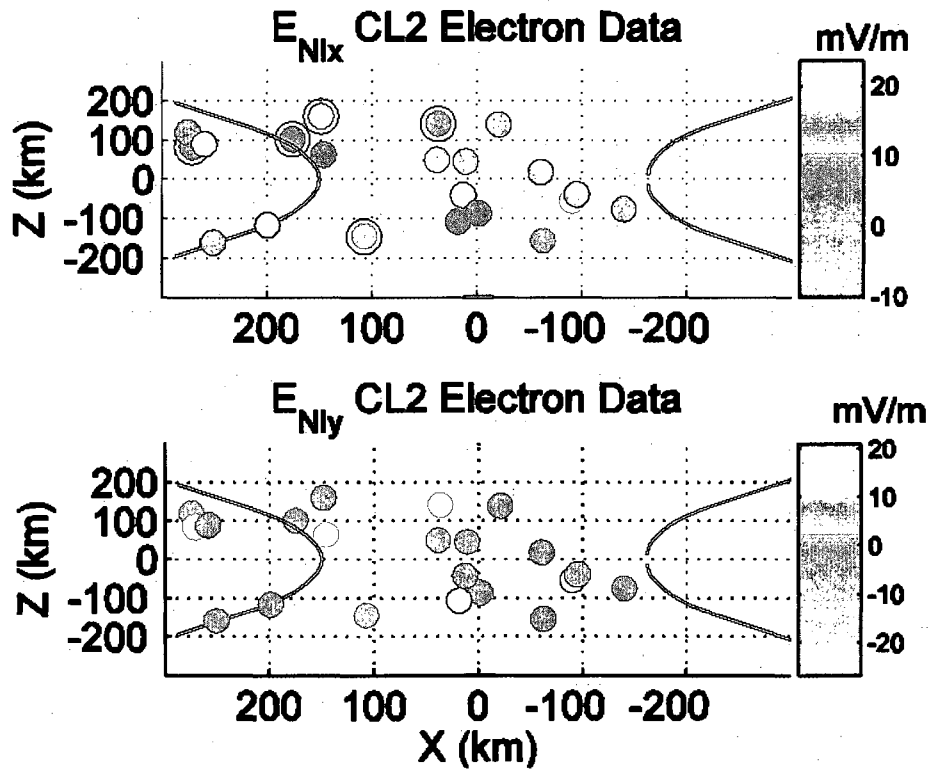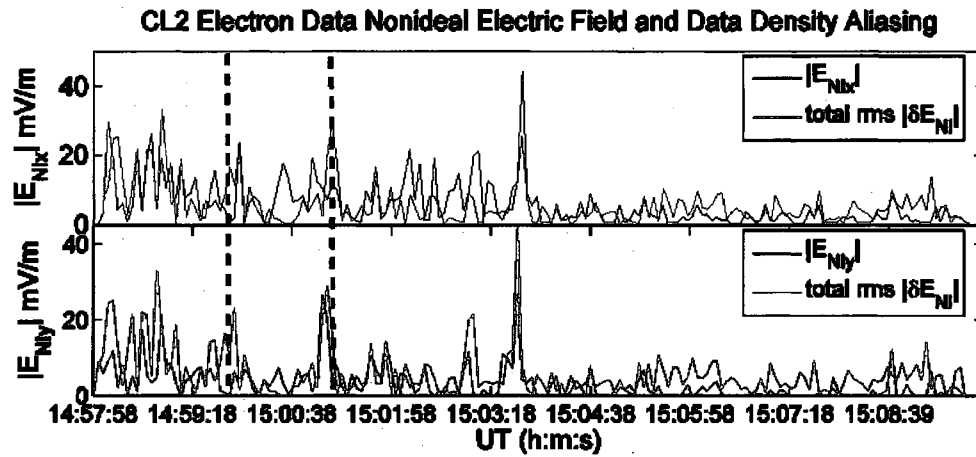
Figure 3.21a-3.21b The figures analagous to Figures 3.20a and 3.20b for the electron measurements on Cluster 2.

space per position space corresponding to a given energy) by color (we describe the smoothing method in the appendix). We have included only those energies that lie above the spacecraft potential and for which there are significant fluxes. The numbers above each subplot denote the range of phase space densities in units of s^3/km^6. The vertical
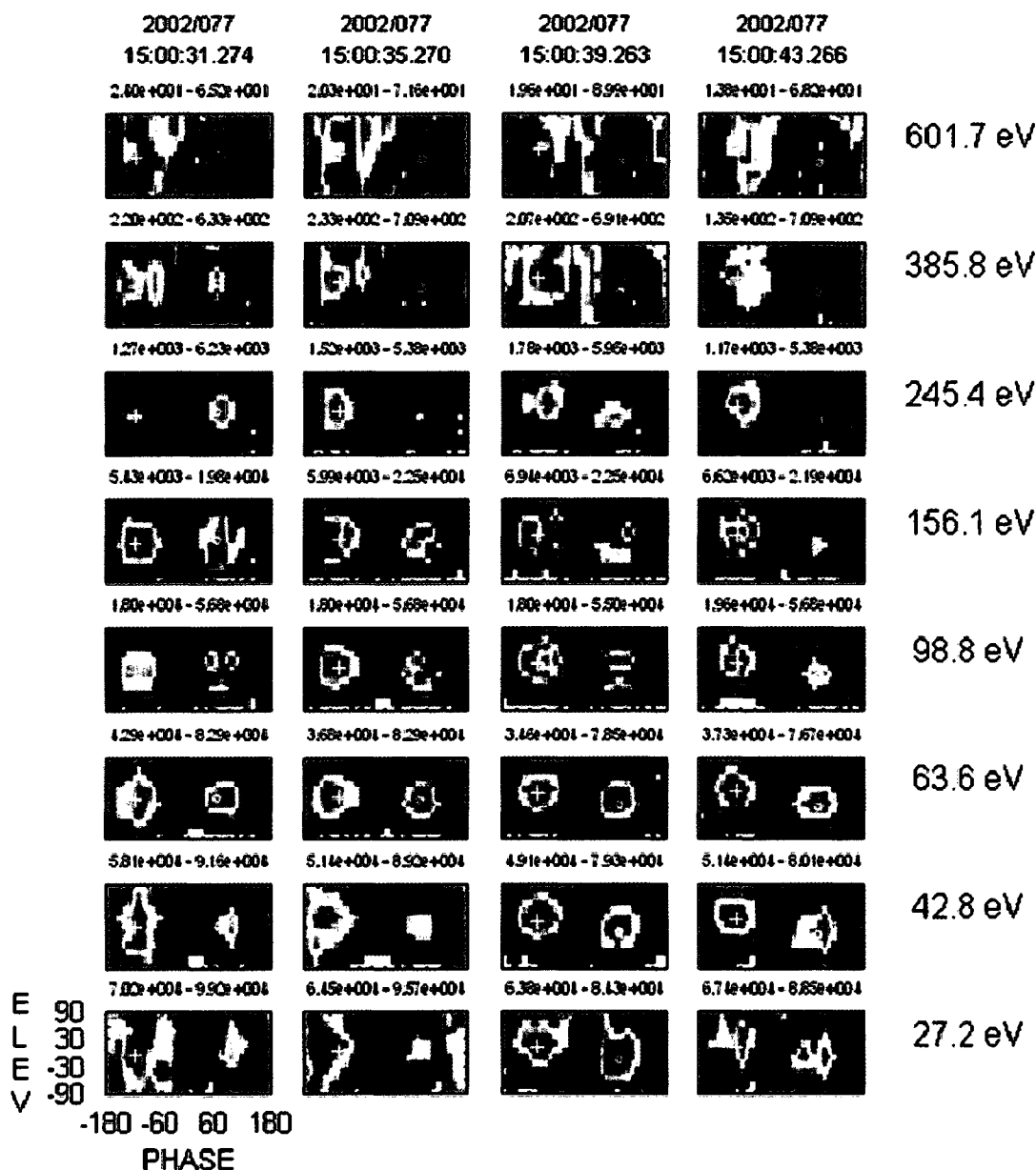
Figure 3.22 Each row displays by color the number of particles per velocity space per position space corresponding to a given energy (see the appendix for a description of the smoothing method). We have included only those energies that lie above the spacecraft potential and for which there are significant fluxes. The numbers above each subplot denote the range of these values in units of s^3/km^6. The vertical axis of each subplot represents elevation angle and the horizontal axis the phase, or azimuth, of the spin in a GSE coordinate system. The white cross designates the head of the magnetic field, and the white circle the tail (this software does it opposite to the convention). The second column is the spin with the first peak in E_{NIx} during the x-line crossing.
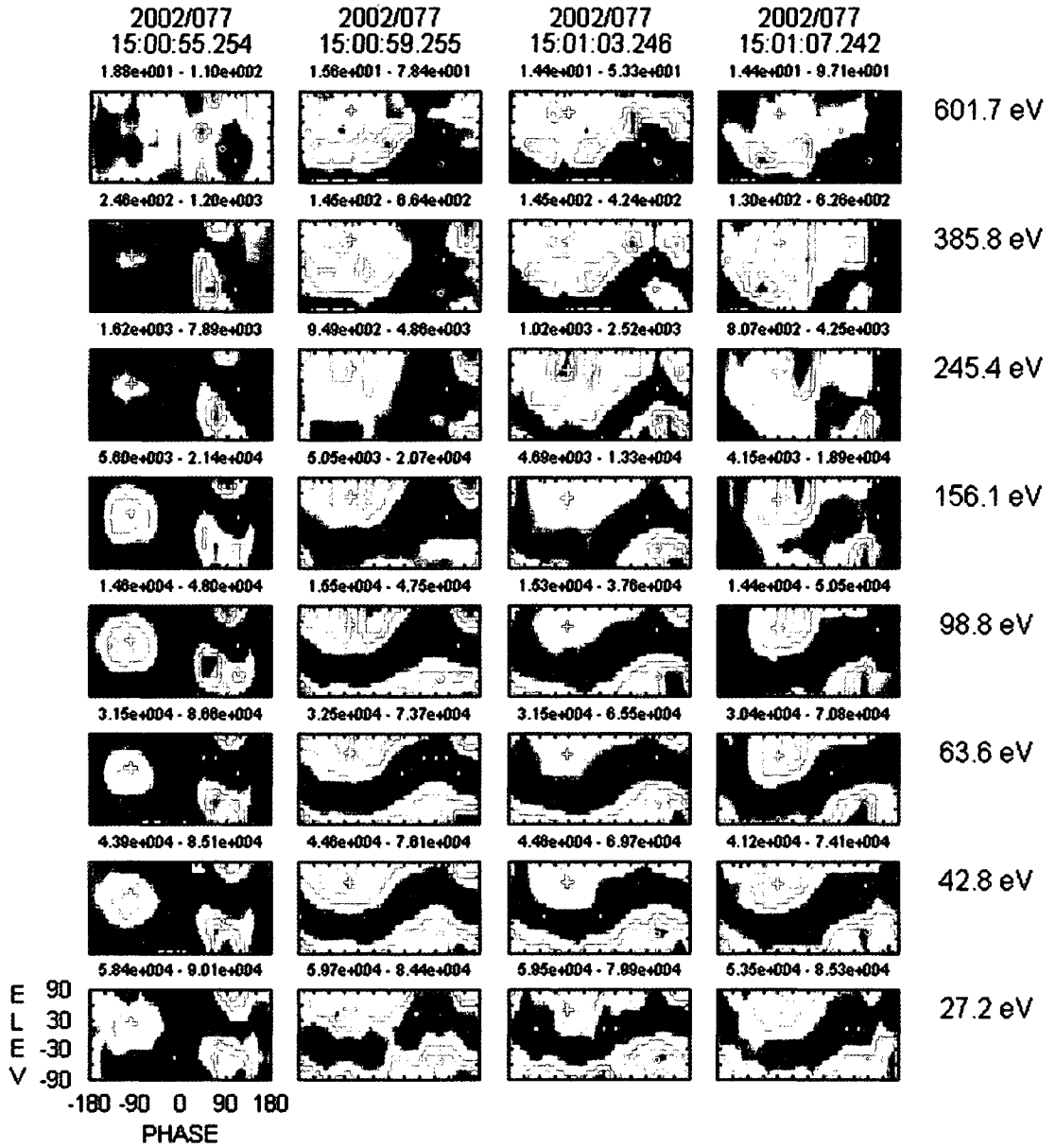
Figure 3.23 The electron distributions as in Figure 3.22 at later spins. The second column is the second peak in E_{Nix} between the dotted lines.

axis of each subplot represents elevation angle and the horizontal axis the phase, or azimuth, of the spin in a GSE coordinate system. The white cross designates the head of the magnetic field, and the white circle the tail (this software does it opposite to the convention). The second column of Figure 3.22 is the spin with the first peak in E_{Nix}

during the x-line crossing, and the second column of Figure 3.23 is the second peak in E_{NIx} between the dotted lines. In both cases, the magnetic field direction remains quite steady—it moves slightly from the first to second spins shown, but is very steady thereafter. Examination of the magnetic field during these spins also shows it varies very little during the spin. Moreover, the nature of the distributions remains largely similar over these spins, with bi-streaming electrons and ring distributions at certain energies. Thus we conclude that, at these spins of interest, magnetic field variations are not producing aliased moments. At a later point we shall return to address the most salient features in the electron distributions.

The order of magnitude of the inferred electric field along the x-line can also be compared to the value of the particle drift electric field E_y far away from, and on either side of, the x-line. Steady state reconnection and Faraday's law requires the same E_y from the pressure divergence and electron inertial terms along the x-line as that further away arising from particle drift motion. In Figure 3.24, the measured y-component of the Cluster 3 ion drift electric field is superposed over the x-line. In this case we plot the component after rotating the data into the magnetopause-aligned coordinate system. It plays a progressively dominant role at increasing distance from the x-line. The scale on the y-axis gives the value of E_y. The ideal MHD electric field far away from the x-line reaches roughly -2 to - 6 mV/m (somewhat asymmetric across the boundary), in close agreement with the value of -4 mV/m derived from the normal magnetic field component in Section 4 and with the discrepancy between drift and measured electric fields as discussed above. The terms that ought to sustain the electric field near the x-line arise from the Hall term, the pressure divergence, and the electron inertial terms in Equation
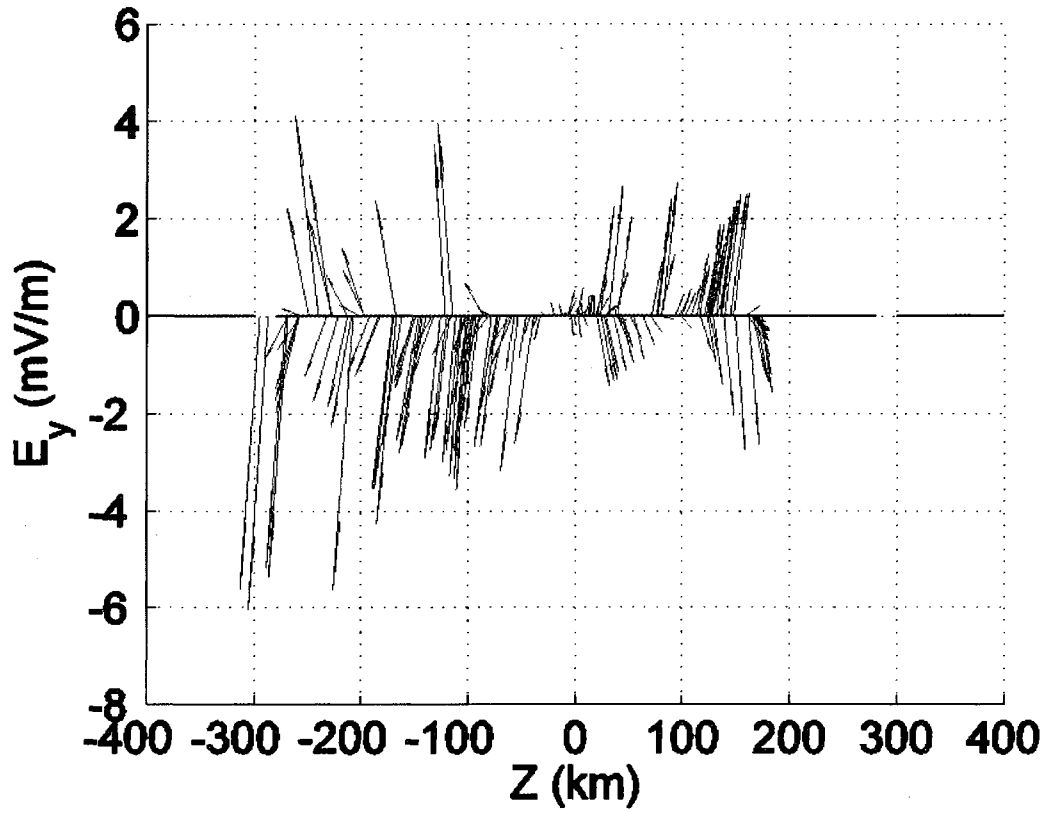
Figure 3.24. The superposed epoch showing the y component of the Cluster 3 ion drift electric field. The electric field E_y should be continuous from Faraday's law, so that the hole around the x-line would be filled by the non-ideal terms to remain continuous with the values of E_y on either side. The view is in the y-z plane, although the scale along the y-axis is that of the electric field.

(1.1), and would be of this magnitude as well. *Hesse et al.* [2001] achieve a steady state reconnection E_y of $0.1v_A B_0$, where v_A and B_0 are the asymptotic Alfvén speed and magnetic field, respectively. For our asymptotic field of $B_0 \approx 100$ nT and an Alfvén speed of ≈ 218 km/s, $0.1v_A B_0 \approx 2$ mV/m. This value roughly agrees at least in order of magnitude with that estimated from the electric field measurements discussed above. In the Appendix, we describe why, though theoretically feasible from multiple spacecraft measurements, a direct calculation of $\nabla \cdot \mathbf{P}_e$ fails with this data set. The spacecraft spatial separations exceed the scale lengths expected of the electron demagnetization region, and
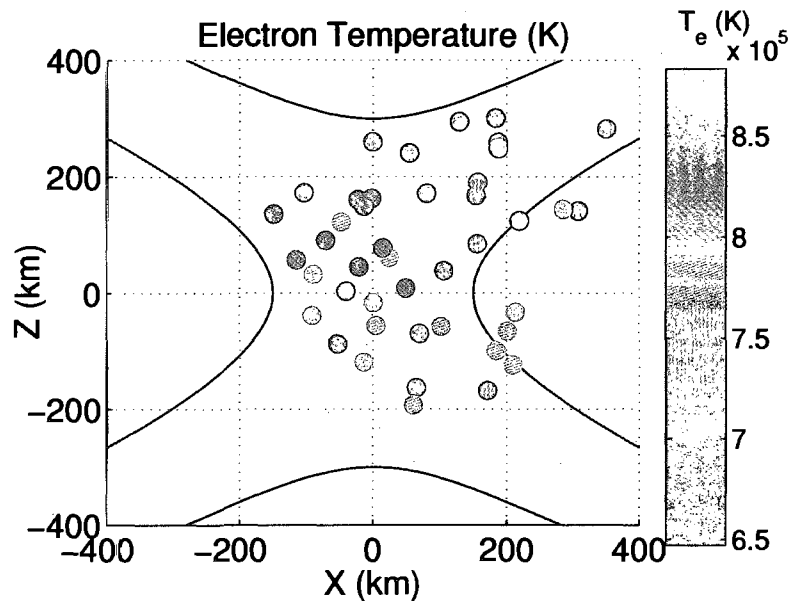
Figure 3.25. The electron temperature in the x-line coordinate system shows the electrons are heated in the area surrounding the x-line relative to surrounding areas.

the propagation of errors going into the calculation swamp the resulting values for $\nabla \cdot \mathbf{P_e}$.

The higher order electron moments also bear signatures of heating and partial demagnetization, through the pressure moments. The electrons are considerably heated, as shown in Figure 3.25, with temperatures elevated by about 20-30% relative to the surrounding temperature in a region of about 200-300 km centered on the x-line. The electron pressures also experience periods of pressure agyrotropy—a sign of partial demagnetization. Figure 3.26 reveals augmented off-diagonal pressure values that persist for a number of spin periods near the reconnection location (just before 15:00 UT) on Cluster 2. The shears reach values up to 25% of the gyrotropic pressure term. The dashed lines are intended to mark the two times corresponding to the largest pressure shears, not to bound a region of interest. (The large increase in the diagonal and off-diagonal terms at
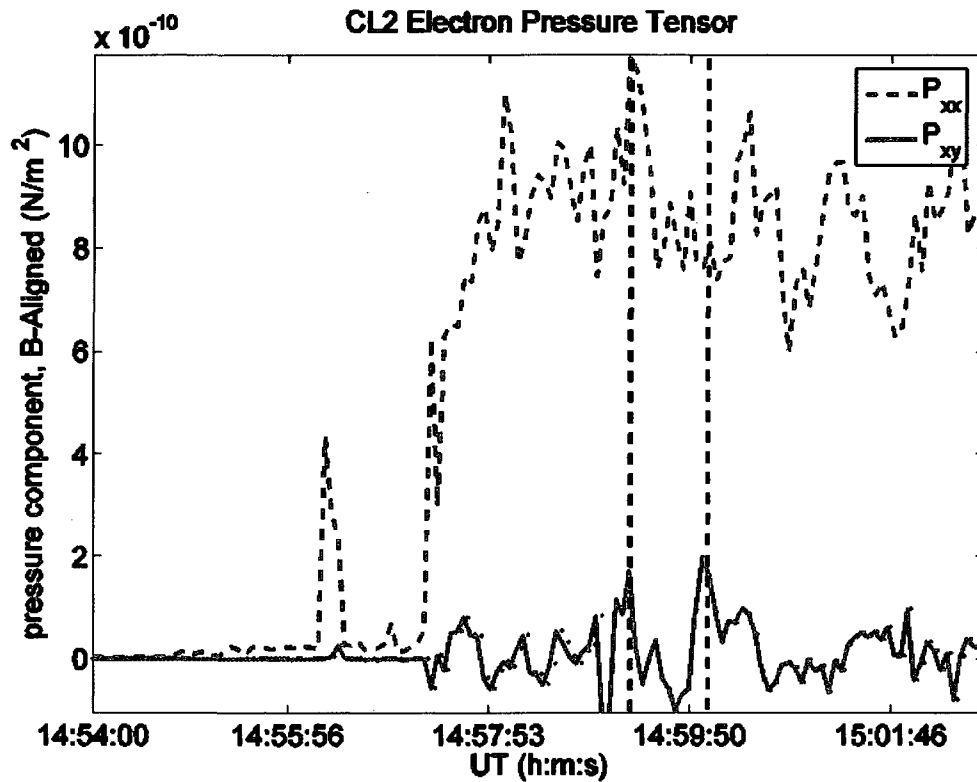
Figure 3.26. One diagonal (P_{xx}) pressure and one off-diagonal (P_{xy}) pressure in a field-aligned coordinate system (other off-diagonal components are similar). The diagonal term P_{xx} is included for comparison, where the subscript x designates the magnetic field direction. The shear term reaches up to 25% of the diagonal term (marked by dotted lines). The shear near the x-line at 15:00 UT is at the second dotted line. All spacecraft saw similar variations.

about 14:57:30 UT marks the entrance into the magnetopause.) These values are plotted in the magnetic field aligned coordinates so as to eliminate spurious off-diagonal components from the coordinate system, where the subscript x designates the magnetic field direction. This structure endures for roughly 11 spin periods, suggesting it is experimentally robust. However, once again we have to face the difficulties presented by aliasing, which we will describe below. But, if genuine, the off-diagonal components of the electron pressure tensor in a field-aligned coordinate system arise from electrons departing from field-aligned gyrotropy. An earlier observation of a northward IMF

reconnection null by the Polar spacecraft also observed such electron pressure shears (off-diagonal components in the pressure tensor), which indicated Polar was in the electron demagnetization region [*Scudder et al.,* 2002].

We apply several tests to the full 3-D spin-resolution pressure tensor data from Cluster 2 to rule out spurious signatures from either residuals from the bulk flow removal, from aliasing rapid time variations of the magnetic field, or from aliasing gradients in the density or temperature. Though the time resolution of the Cluster 2 data is the same as that for all other spacecraft (every 4 s spin), Cluster 2 is the only spacecraft that provides down-linked full 3D data for this time interval. The other spacecraft calculate the moments from their full spin complement of data but downlink only a reduced data set that assumes gyrotropy. Full 3-D data is required if we are to look for true asymmetries in the electron distribution function, since in this case no gyrotropic assumption is made to complete the distribution function. The first test involves calculating the two pressure eigenvalues perpendicular to the magnetic field over the full interval of the magnetopause crossing. If the bulk flows are routinely removed accurately enough to avoid contamination by residuals, then the difference of these eigenvalues divided by their average should be generally centered about zero. Then if there are intervals where they are not, we have some guarantee that these instances are genuine agyrotropies. Figure 3.27a displays the results. Besides the point of entry into the magnetopause, it reveals that there is a significant difference from zero only in the two intervals where the shears are present in the data, and where Cluster nears a current sheet. One advantage is that the electron thermal speeds far exceed even the largest bulk flows observed, which diminishes the influence of residuals from bulk flow removal.
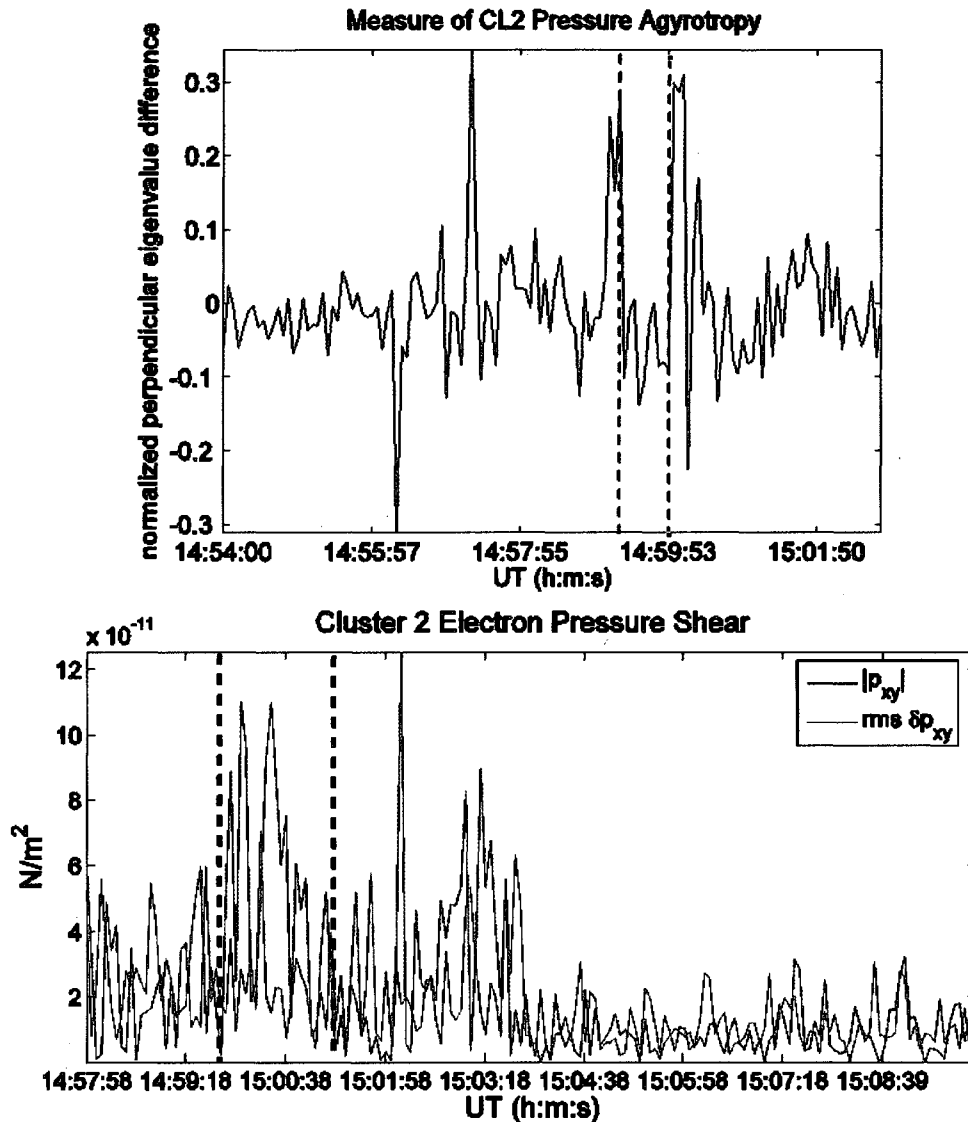
Figure 3.27a-3.27b. (a) Top: In the B field-aligned coordinate system, the difference between the two perpendicular pressure components (normalized by their average sum) generally fluctuates about zero. The two exceptions are at times where the current sheet is crossed and the difference is significant. The second set of large values is near the x-line of this study. **(b) Bottom:** Figure 3.24b plots the absolute value of the GSE pressure shear P_{xy} in blue along with the total calculated rms error of P_{xy} in red.

The second test involves estimating the influence of the magnetic field motion during the spins where we see significant shears and estimating the error that results from the given variation of **B**. We start with the equation for a pressure tensor, which we

assume to be gyrotropic, in terms of its components $p_\perp$ and $p_{/\!/}$ perpendicular and parallel to **B**, respectively, i. e.,

$$\mathbf{P} = p_\perp \mathbf{I} + (p_{\|} - p_\perp)\frac{\mathbf{BB}^{\mathbf{T}}}{B^2} \tag{3.7}$$

The extent to which rapid fluctuations in the magnetic field **B** engenders false off-diagonal terms in the pressure during a spin interval would come into the second term. We then calculate the amount of deviation of the resulting off-diagonal terms $(p_{\|}-p_\perp)\mathbf{BB}^{\mathbf{T}}/B^2$ during a spin by taking the standard deviation of $\mathbf{BB}^{\mathbf{T}}/B^2$ during a spin. This tells us by how much the direction of **B** calculated from the spin mean value of the direction of **B** differs from the actual value of the direction of **B** during a spin. The result reveals how much the corresponding off-diagonal terms in **P** result from this direction error rather than from a real shear. As discussed more fully in the appendix, for spins with the largest agyrotropy, the shears exceed the timing induced errors significantly.

The third test demonstrates the robustness of the agyrotropy presented in Figure 3.27a against aliasing from gradients of the parameters that factor into the pressure moments. Figure 3.27b plots the absolute value of the GSE pressure shear P_{xy} in blue along with the total calculated rms error of P_{xy} in red. In this case we plot the shear P_{xy} in GSE coordinates, because the errors include aliasing errors that we calculated in the spacecraft ISR2 coordinates using the assumption of a Maxwellian velocity distribution, as explained in the section on velocity moments. The GSE coordinate system differs from the ISR2 coordinate system by no more than 7°. The density aliasing errors contribute

$$\delta p_{xy} = \delta(nv_x v_y) = m\delta n(\frac{m}{2\pi kT})^{3/2} \int_0^\infty \int_0^\pi \int_0^\psi v^4 \sin^3\theta \cos\varphi \sin\varphi e^{-\frac{mv^2}{2kT}} d\varphi \, d\theta \, dv \quad \textbf{(3.8)}$$

$$= \frac{1}{\pi} g(\psi)\delta nkT_e,$$

where $g(\psi) = \frac{1}{2}(1 - \cos^2(\psi))$ is a geometric factor from the integration over ϕ and that

depends on ψ (the integral vanishes if ψ is $\frac{\pi}{2}$), and δn is the difference in density during

the spin. For temperature aliasing, the error is

$$\delta p_{xy_e} = \frac{1}{\pi} g(\psi)nk\delta T_e,$$

$$\textbf{(3.9)}$$

where δT_e is the difference in temperature during the spin. The factor $g(\psi)$ is a maximum

(worst case) when ψ is a multiple of $\frac{\pi}{2}$, and in this case is ½. This is the value we used in

our calculations. We have also included a 10% error from Poisson counting statistics. The

effect of the magnetic field aliasing as calculated in the previous paragraph (and in the

appendix) is to add an error of only about 0.5×10^{-11} N/m^2 to the first large peak in P_{xy}

between the dashed lines in Figure 3.27b, and about 0.15×10^{-11} N/m^2 to the second

largest peak in P_{xy} between the dashed lines. Two intervals where P_{xy} clearly exceeds the

errors lie between the dashed lines and correspond to the two peaks discussed in Figure

3.27a.

We inspect the distributions of these particular spins to see if there are signatures

of agyrotropy and also to rule out aliasing, even though the effect of magnetic

fluctuations was already shown to be insignificant. The Cluster 2 velocity distribution

functions from four spins with the largest agyrotropy in the pressure moments (15:00:07
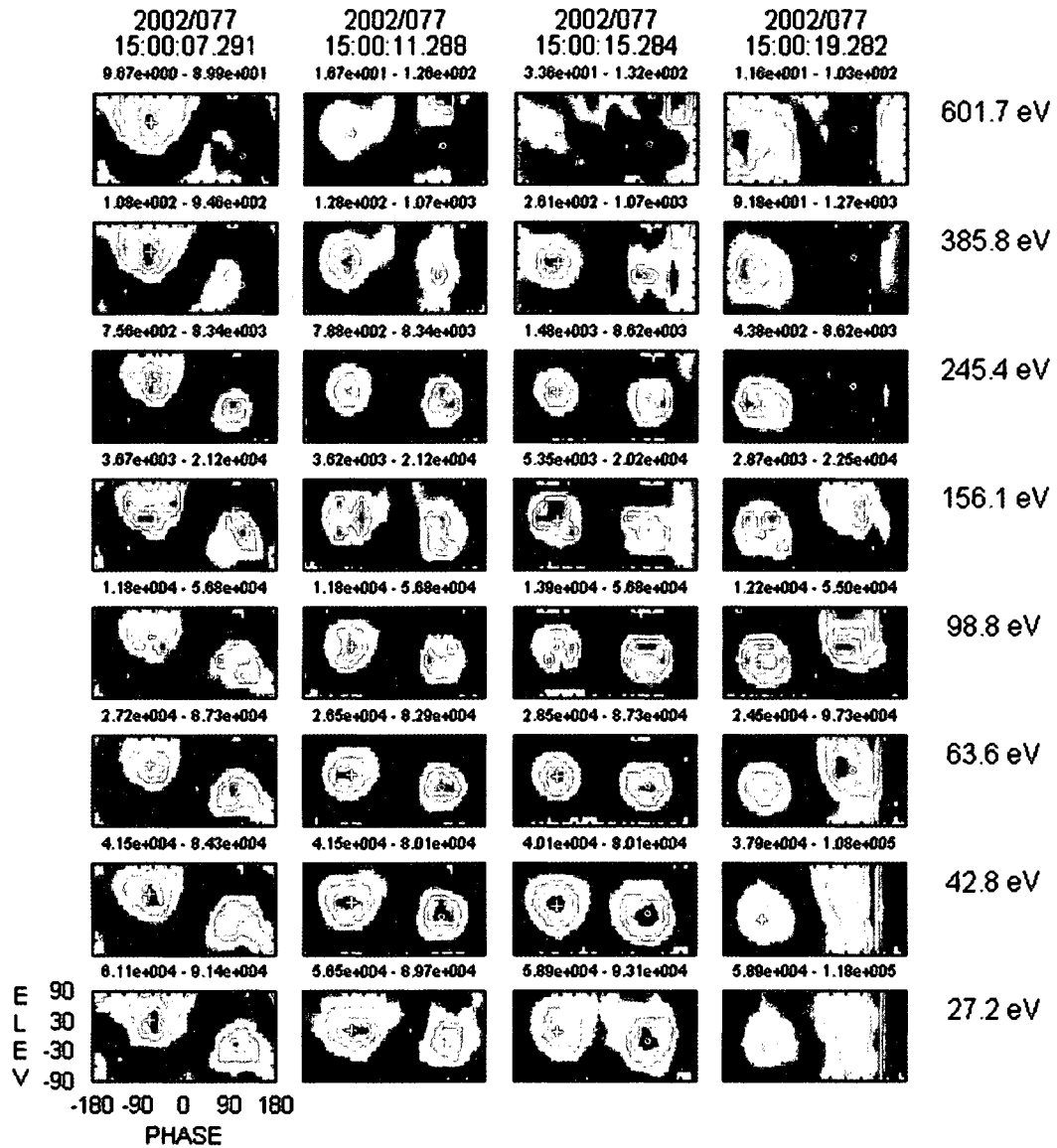
Figure 3.28. Four spins of data from Cluster 2 are shown for the period of agyrotropy surrounding the x-line crossing. Each column corresponds to a spin, and each row an energy level. The vertical axis of each subplot is the elevation, and the horizontal axis the phase of the spin, in GSE coordinates. The numbers above each sub-plot are the number of phase-space particles (s^3/km^6). White cross-hairs denote the head of the magnetic field, and white circles the tail. The loss of cylindrical symmetry in the distributions reflects the agyrotropy observed in the pressure. The first and last columns may be aliased.

through 15:00:23) are shown in the four columns of Figure 3.28. The distributions are shown from Cluster 2 in the same form as discussed for Figures 3.22 and 3.23. Cluster 2 is suited to agyrotropy studies, as its angular distributions do not rely upon symmetry assumptions. Moreover, the extremely high densities in this region place the data well above the agyrotropic "noise" known to issue from poor counting statistics even in the absence of reconnection. Besides revealing field-aligned counter-streaming beams at low energies, loss cones (field-aligned ring distributions) at middle energies, and field-aligned beams at high energies, the distribution function regularly deviates from cylindrical symmetry about the magnetic field. In the first and last of the spins, the magnetic field direction clearly changes significantly (the last spin) or has ring distributions that are misaligned with the magnetic field (the first spin). But in the other two spins the magnetic field direction does not change significantly and rings are centered about the magnetic field direction, ruling out aliasing. However, the distributions lack cylindrical symmetry about the magnetic field, indicating the detection of genuine agyrotropy.

Since these agyrotropic peaks in the pressure pass all of our tests of significance, we conclude that they are valid pressure shears. From Figure 3.29, displaying the position of Cluster 2 at the beginning and end times of one of the spins where the agyrotropy is observed, we can see that the spacecraft straddles the x-line at these times. (Cluster '0' marks the centroid position of the spacecraft and the corresponding average values of **B**.) The spins with the large pressure shears directly follow the spins where we observe the non-ideal electric field. This may be because the pressure divergence electric field is actually a response to the spatial gradient in the pressure shear, as we discuss further, below.

15:00.11.154 UT

15:00.15.124 UT
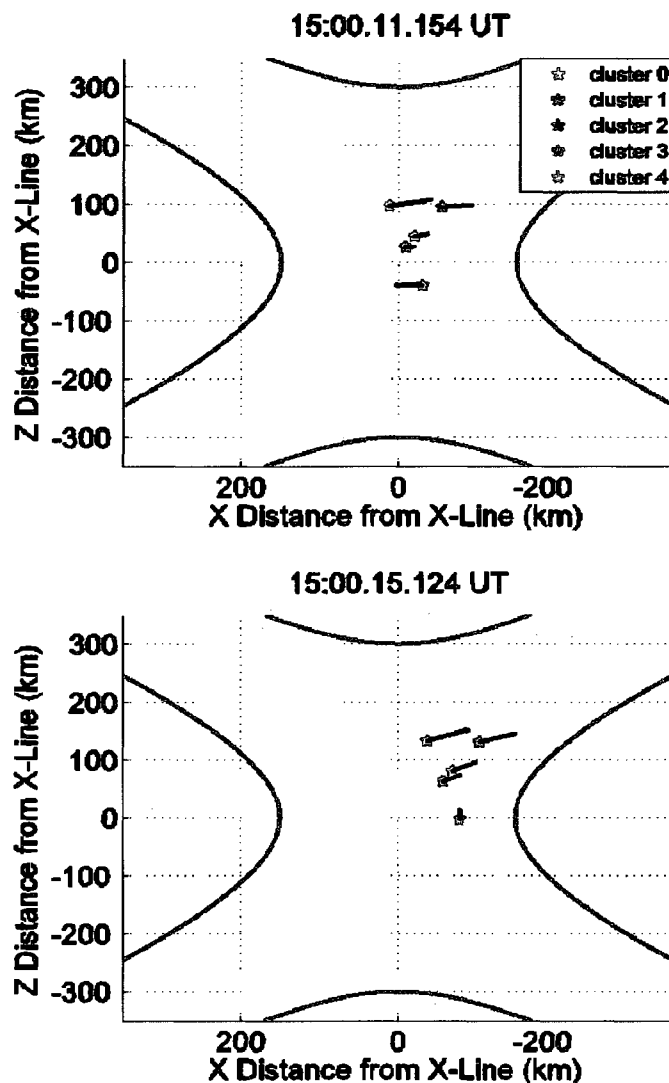
Figure 3.29a-3.29b. The position of Cluster 2 at the two time intervals when agyrotropy appears (see Figure 3.27). The spacecraft straddles the current sheet at these times. Cluster '0' simply represents the centroid position of the spacecraft, and the average values of B.

The anisotropies in the electron distributions give us the opportunity to make some inferences about the local magnetic topology. These observations apply also to the distributions of Figure 3.22 and 3.23. The distributions at higher energies (386 and 602 eV center energies) show a strong field-aligned asymmetry, with almost no returning fluxes. The distribution at middle energies (99 and 156 eV) show bi-directional

streaming but with an interesting conical distribution, which is often interpreted as a time-of-flight parallel velocity selection effect. Because of the very fast motion of electrons, such dispersions can only be observed very close to the X-line. The fluxes at 245 eV show an effect that might be bouncing of the fluxes off an ionospheric mirror or circulating around an O-line. Since a 245 eV electron has a velocity of about 1.5 R_E per second, having a bounce time of around 2-6 seconds implies a reflection point about 1.5 - 4 R_E away. Looking again carefully at the 386 eV electrons in Figure 3.22, we can infer a burst of fluxes roughly every 0.8 seconds, which could be either the circulation time around an o-line, or a cadence of reconnection bursts. If it is circulation, it makes the circulation path around 1.5 R_E, which is reasonable for a tearing mode.

As described in the introduction, in the absence of a guide field, symmetry of the velocity distributions about the merging site gives P_{xy} an asymmetric variation with respect to x, with vanishing values at the x-line and at the edges of the diffusion region (Figure 1.4b). A similar gradient in the P_{zy} term is expected in the z-direction. These are the structures that give rise to the pressure divergence reconnection electric field $E_y = -(\partial P_{xy}/\partial x + \partial P_{zy}/\partial z)/en_e$. However, in the absence of a guide field, it is not obvious that the electron pressure shear would still play a role in electron demagnetization, since symmetric gyromotion could still occur around the guide field. *Hesse et al.* [1999] and *Hesse et al.* [2004] nevertheless observe electron pressure shears near the x-line in their simulations of guide field reconnection. They argue that the increased electron heating in a guide field contributes to the higher off-diagonal pressure terms and that the Hall electric field from charge separations deflects the electron orbits in a manner to cancel the symmetric gyromotion caused by the guide field. It is clear from the measured

distribution functions from Cluster that significant kinetic effects are observed in the electron distributions during the times of greatest pressure anisotropies. However, the presence of an out-of-plane field modifies the expected pressure symmetries somewhat from the case of zero guide field reconnection. P_{xy} and P_{zy} develop somewhat more asymmetry with the z direction. Though populating the region rather sparsely, off-diagonal terms in our data coordinate with those observed for reconnection studies performed with a significant guide field [*Hesse, et al.*, 2002, *Hesse et al.*, 2004]. Figures 3.30a and 3.30b superpose the values of P_{xy} and P_{zy} from all the spacecraft in the x-line coordinate system. They display a general asymmetry in the x and z directions and a tradeoff between P_{xy} and P_{zy} in concert with simulations, which are shown in Figure 3.30c to 3.30d from *Hesse et al.* [2004]. The *Hesse et al* [2004] axes are in units of the proton skin depth c/ω_p and the x-line is centered at $z = 0$ and $x = 13.2$. Their pressure is in units of B_0^2/μ_0, where B_0 is the asymptotic magnetic field. The sign of P_{xy} and P_{zy} in our data differs from that in the *Hesse et al.* [2004] simulations because the orientation of the magnetic field in our data is the reverse of that in their simulation. The unconventional "flipped" orientation of our x axis also accounts for the difference in the symmetry of our and the *Hesse et al.* [2004] simulation's P_{zy}. The sign of $\partial P_{zy}/\partial z$ across the z boundary and of $\partial P_{xy}/\partial x$ across the x boundary are both consistent with generating a negative reconnection E_y. Moreover, the data shows that the largest gradient that contributes to E_y is $\partial P_{zy}/\partial z$, in agreement with the observation from simulations by *Hesse et al.* [2004].

In the presence of a guide field, the electron Larmor radius, ρ_e, defines the region of maximum electron diffusion effects [*Hesse et al.*, 2004]. In the absence of a guide
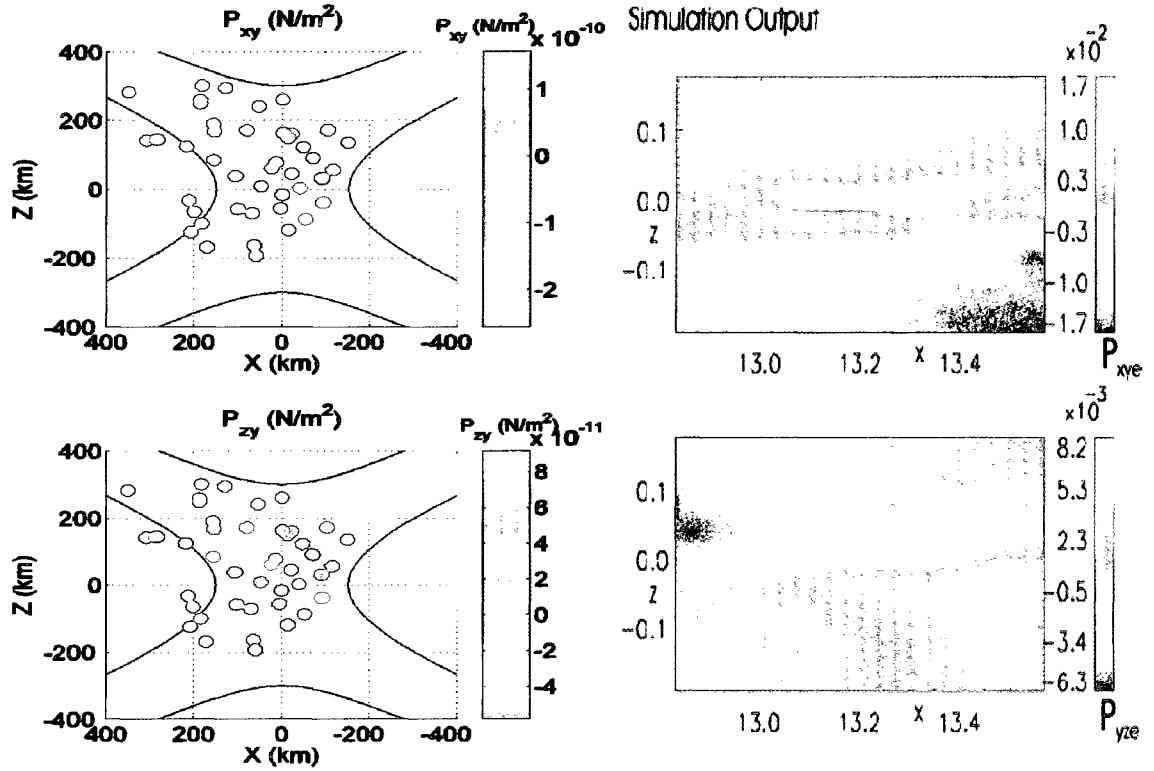
Figure 3.30a-3.30d. (a)-(b) Left, top and bottom: The superposed epoch off-diagonal pressure terms, P_{xy} (Figure 3.30a) and P_{zy} (Figure 3.30b), have similar symmetries to those observed in guide-field reconnection simulations. **(c)-(d) Right, top and bottom:** The equivalent quantities from the *Hesse et al.* [2004] simulation with a guide field. Their axes are in units of the proton skin depth c/ω_p and their x-line is centered at $z = 0$ and $x = 13.2$. Their pressure shears, in units of the asymptotic magnetic pressure, have the opposite sign to ours because their magnetic field orientation is the reverse of ours. The unconventional "flipped" orientation of our x axis also accounts for the difference in the symmetry between our P_{zy} and the *Hesse et al.* [2004] simulation's P_{zy}. Right figure from *Hesse et al.* [2004]

field, the region is generally associated with the electron skin depth (see, for example, *Hesse at al.* [2001]). For our data the electron Larmor radius in the guide field, $\rho_e = 0.3$ km, is less than the electron skin depth $d_e = 0.7$ km. While ρ_e may well define the region of maximum dissipation in a guide field, we lack the resolution to uncover the electron diffusion governed by these kinds of length scales. Our observations of agyrotropy are,

however, in keeping with the intermediate scales associated with the electron pressure tensor divergence. *Scudder et al.* [2002] see agyrotropic effects on the scale of $\rho_s = \beta_e^{1/2} c/\omega_i$, a scale length intermediate between the electron and ion skin depths when $1/1836 \; (m_e/m_i) < \beta_e < 1$, and the length scale on which the electron pressure divergence in the generalized Ohm's law becomes significant. The latter scale serves to intensify current on a tighter scale length than the ion skin depth [*Scudder et al.*, 2002]. We see agyrotropies in the pressure data on the order of ρ_s from the central current sheet given an ion mass that includes the heavier particles such as O^+ and He^+. For protons, ρ_s is only about 15 km. But for He^+ it is about 30 km, and for O^+ it is 60 km—about the length scale on which we observe electron pressure shears.

3.8 Summary

In this chapter we have presented data from the Cluster suite of spacecraft that captures the instantaneous structure of reconnecting magnetic fields in the magnetopause. The magnetopause reconnection site maps to the location on the ionosphere where emission is induced by protons accelerated downward by the reconnection. The magnetic topology at the site has the form of singular field line reconnection, a general form of reconnection in three dimensions. Though the reconnection is between almost antiparallel IMF and magnetosphere fields, there is layer between the antiparallel fields with a singular field line—a field line along the current sheet and perpendicular to hyperbolic reconnecting magnetic field components. This field line acts like a guide field, but exists only within the magnetopause. We observe strong evidence for a parallel electric field

along this field line. This set of observations therefore satisfies the necessary and sufficient conditions for singular field line reconnection. The spacecraft also come close enough to the reconnection line to observe signatures of ion and electron demagnetization, not only in the form of nonideal electric fields, but also by way of strong agyrotropic electron pressure shears. In the next chapter, we will show that the global MHD simulation of the event also produces a singular field line reconnection topology, consistent with the location and observations of Cluster.

Chapter 4

GLOBAL RECONNECTION TOPOLOGY AND CONVECTION:

SYNTHESIZING AN MHD SIMULATION AND DATA FROM THE

MAGNETOPAUSE AND IONOSPHERE

4.1 Looking at the Event from a Magnetospheric Perspective

Using OpenGGCM, with real solar wind data measured by ACE as inputs, and satellite data to validate the model at the magnetopause and the ionosphere, we develop a global picture of the reconnection event of March 18, 2002. This gives a 3D picture of where reconnection occurs on the magnetopause for northward IMF with B_x and B_y components and a tilted dipole field. The satellite data and the model agree well where they intersect. OpenGGCM demonstrates the important role played by the IMF and dipole tilts in producing reconnection away from the separator and in overdraping field lines that reconnect and convect sunward. It also shows that line-tying in the ionosphere and draping of open and IMF field lines over the dusk and dawn flanks of the magnetopause produce torsion of the reconnected magnetic field lines within the magnetopause. These field lines are associated with parallel electric fields and feed into a tearing mode series of nulls in the antiparallel regions of the cusps. The model shows that, consistent with Cluster observations, the reconnection geometry is not a simple two-dimensional hyperbolic structure, but rather in the nature of singular field line reconnection.

In section 4.2, we will introduce the ionospheric data from the Iridium and DMSP satellites. This data includes the polar cap field aligned current patterns, the ionospheric convection flows, and the polar cap potential drop. We will then present the GGCM simulation's global magnetic topology and parallel electric fields in sections 4.3 and 4.4, establishing the location and types of magnetic reconnection at the dayside magnetopause. Finally, in section 4.5, we synthesize and compare the various satellite data and the simulation results to derive the M-I coupling scales and the magnetospheric convection pattern.
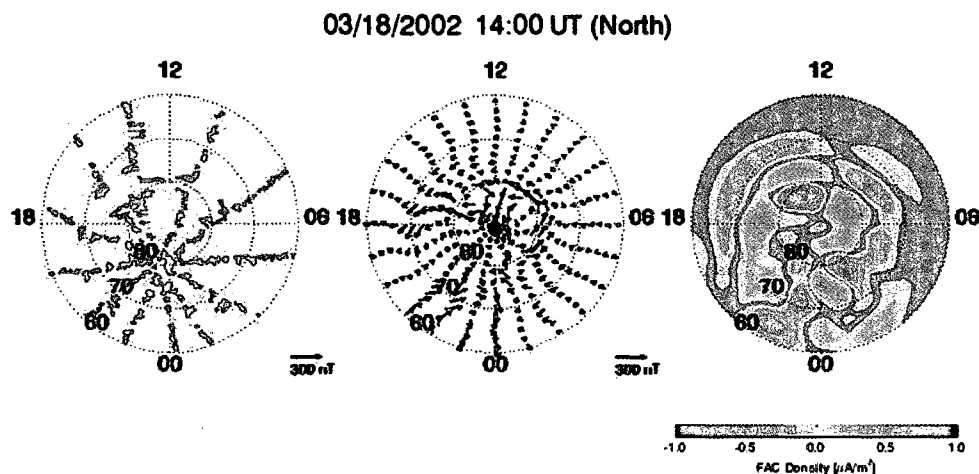
Figure 4.1. From left to right, the raw magnetic field data, the spherical harmonic fits to the magnetic field data, and the extrapolated FACs from the Iridium spacecraft for 14:00 UT.

4.2 Iridium and DMSP Observations

Figure 4.1 shows, from left to right, the raw Iridium magnetic field data, the spherical harmonic fits to the Iridium magnetic field data, and the extrapolated FACs in MLT for 14:00 UT, just prior to Cluster's magnetopause crossing. Reconnection is ongoing at this time, as observed by IMAGE [*Frey et al.,* 2003]. The location of the

magnetic shear is approximately 76° latitude and 1:30 MLT in altitude-adjusted corrected geomagnetic coordinates (AACGM). The location agrees well with the equatorward edge of the auroral spot observed by IMAGE at that time. The IMAGE data is in apex coordinates, but the difference between AACGM and apex coordinates at these latitudes and longitudes is always less than 1° in latitude and less than 2° in longitude, which is much smaller than the solid angle subtended by the spot. (The Appendix includes a discussion of the variety of coordinate systems that are relevant to this thesis.) There are similar but smaller shears at a few other dayside locations, less dramatic but perhaps clearer to the eye in the smoothed data. The magnetic shear signifies a corresponding current sheet. Indeed, the derived field-aligned current system to the far right has a downward FAC near the site of the reconnection auroral spot, and an accompanying upward FAC beside it. Such a current system corresponds to a northward four cell convection pattern with an IMF B_y component less than B_z [*Reiff and Burch*, 1985; *Burch and Reiff*, 1985; *Burke et al.*, 1979]. The four-cell pattern includes lobe cells that emerge from reconnection to a northward IMF and should contain polar cap sunward flows. We next look to DMSP data for polar cap convection flows.

Of the DMSP satellites, F13 makes a northern polar pass starting at about 15:12 UT, and F15 at about 14:30, and again at 16:12, UT. The ion drift meter data in corrected geomagnetic coordinates (Figures 4.2a-4.2c) show sunward flows in all three passes. The RPA measures corresponding polar cap potential drops of −16 kV, -15 kV, and −15 kV, respectively, in Figures 4.3a-4.3c. In these figures the time intervals corresponding to the sunward flows are marked by the dashed lines. In the coordinate system of the drift measurements, +y is horizontal and to the left relative to the spacecraft direction of

CROSS—TRACK PLASMA DRIFT DMSP F13
YEAR: 2002 DAY: 77 (March 18)

Northern Hemisphere
15:12 UT

Southern Hemisphere
16:01 UT

| = 1 km/sec

DATA QUALITY FLAGS:
CAUTION — POOR — UNDETERMINED

W. B. Hanson Center for Space Sciences, University of Texas at Dallas

CROSS—TRACK PLASMA DRIFT DMSP F15
YEAR: 2002 DAY: 77 (March 18)

Northern Hemisphere
14:30 UT

Southern Hemisphere
15:22 UT

| = 1 km/sec

DATA QUALITY FLAGS:
CAUTION — POOR — UNDETERMINED

W. B. Hanson Center for Space Sciences, University of Texas at Dallas

CROSS—TRACK PLASMA DRIFT DMSP F15
YEAR: 2002 DAY: 77 (March 18)

Northern Hemisphere
16:12 UT

Southern Hemisphere
17:03 UT

| = 1 km/sec

DATA QUALITY FLAGS:
CAUTION — POOR — UNDETERMINED

W. B. Hanson Center for Space Sciences, University of Texas at Dallas

Figure 4.2a-4.2c. The ion drift meter data shows sunward flows in all three DMSP northern (and southern) polar passes of this study.

motion, $+x$ is in the direction of spacecraft motion, and $+z$ is vertical (both F13 and F15 are moving from the dusk to dawn side of the northern polar cap). Sunward flows are also observed in the southern hemisphere.

DMSP-F13 Potential Northern Hemisphere Year = 2002 Day = 77

Potential maximum = 2.75 kV at magnetic latitude = 74.08 and MLT = 6.14 at 15:17:23 UT
Potential minimum = −24.19 kV at magnetic latitude = 85.84 and MLT = 7.14 at 15:14:03 UT
Offset potential = 0.74 kV
Center for Space Sciences −− University of Texas at Dallas

DMSP-F15 Potential Northern Hemisphere Year = 2002 Day = 77

Potential maximum = 0.04 kV at magnetic latitude = 59.19 and MLT = 20.32 at 14:21:26 UT
Potential minimum = −14.90 kV at magnetic latitude = 77.52 and MLT = 18.02 at 14:26:14 UT
Offset potential = 0.29 kV
Center for Space Sciences −− University of Texas at Dallas

DMSP-F15 Potential Northern Hemisphere Year = 2002 Day = 77

Potential maximum = 7.54 kV at magnetic latitude = 76.67 and MLT = 10.92 at 16:16:30 UT
Potential minimum = −39.86 kV at magnetic latitude = 82.98 and MLT = 13.23 at 16:13:50 UT
Offset potential = 13.37 kV
Center for Space Sciences −− University of Texas at Dallas

Figure 4.3a-4.3c. Corresponding to the sunward drifts observed in Figures 4.2a-4.2c, the RPA measures corresponding sunward-flow potential drops of about −16 kV, -15 kV, and –15 kV, respectively.

In both hemispheres, the convection is therefore consistent with a four-cell pattern. The pattern of downward and upward particle flows measured by the ion drift instrument is coherent with the downward FAC into the duskward cell and the upward FAC from the dawnward cell as predicted by models [*Burke et al.*, 1979; *Reiff and Burch*, 1985]. In the four-cell model the strong shear in the flows from sunward to anti-sunward, for example at about 86° latitude, 7 MLT and 15:14 UT in the F13 pass (Figures 4.2a and 4.3a), predict a FAC. The magnetometer data confirm the presence of a FAC at this location by way of a strong magnetic shear there (Figure 4.4). Similar structures are observed, though less dramatically, at the sunward-antisunward flow shears seen in all three passes. The DMSP data also corroborate the FAC pattern observed in the Iridium data, but lie somewhat poleward (about 86° latitude) of the auroral spot (about 80° latitude) observed by IMAGE. The difference between corrected geomagnetic coordinates and both AAGCM and apex coordinates at these latitudes and longitudes is always less than 4° in latitude and less than 1° in longitude. This discrepancy is small enough that the sunward flows are consistent with a position on the poleward side of the NBZ FAC observed by Iridium and also poleward of the auroral proton emission.

At this point we note that the IMF B_y varies during the time interval spanned by the three DMSP and the Cluster measurements [*Frey et al.*, 2003]. Though the IMF B_y varies it is small enough ($< B_z$) during the DMSP measurements that the work of *Burke et al.* [1979], *Reiff and Burch* [1985], and *Crooker* [1988] would predict a four-cell pattern. For a large enough B_y, *Crooker* [1988] predicts and *Heppner and Maynard* [1987] measure a distorted two-cell pattern.

F15 SSM 18 Mar 2002
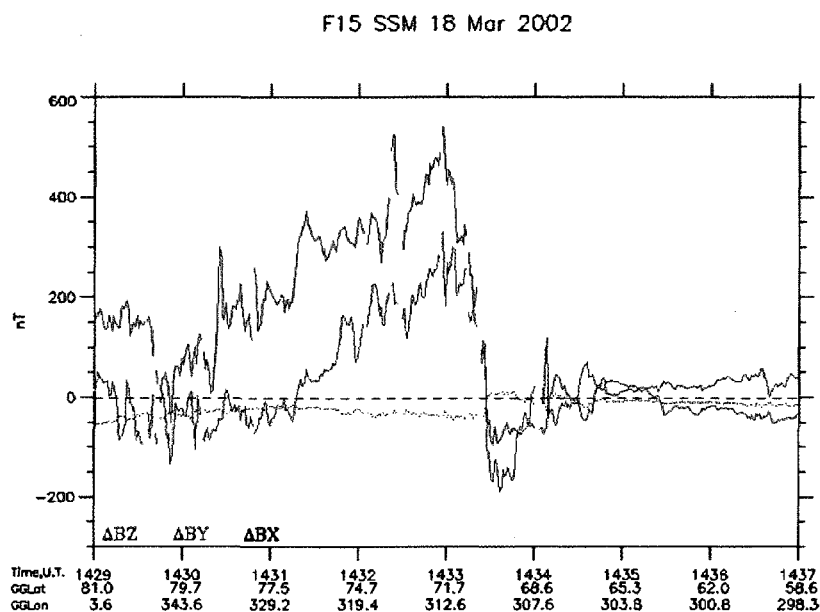
Figure 4.4. In the four-cell convection model, the strong shear in the flows from sunward to anti-sunward (as, for example, at about 88° magnetic latitude and 9 MLT in the F13 pass) predict a FAC. This figure shows that the magnetometer data confirm the presence of a FAC at this location by way of a strong magnetic shear there.

4.3 GGCM: Magnetic Nulls and Global Topology

The solar wind input parameters for the GGCM simulation are listed in Table 4.1. They are propagated from the actual solar wind data measured by the ACE satellite during the interval of this event. These parameters have important consequences for where and how reconnection occurs on the magnetopause. Open GGCM reads in the solar wind plasma and magnetic field data in GSM coordinates, which it then propagates from the solar wind satellite (ACE) to a simulation boundary box ($x = 24$ R_E). Unless otherwise noted, the inputs listed are the initial conditions at the start of the run. For this simulation we used a dipole tilt (9.4 ° in the GSE y-z and 18.2° in the GSE x-z plane)

Model	CCMC GGCM
Start time (UT)	2002/03/18 14:30
X-Z GSE dipole tilt (°)	9.4
Y-Z GSE dipole tilt (°)	18.2
Solar wind density (cm^{-3})	43
Solar wind temperature (K)	289755
Solar wind v_x (km/s, GSM)	-468
Solar wind v_y (km/s, GSM)	-4
Solar wind v_z (km/s, GSM)	11
IMF B_x (nT, GSM)	-10
IMF B_z (nT, GSM at 15:00 UT)	10
IMF magnitude (nT at 14:30 UT)	12.58
IMF clock angle (°, GSE at 15:00 UT)	15
IMF clock angle (°, GSE at 15:11 UT)	33
Ionospheric Conductance	auroral
Corotation velocity at inner boundary	no
Inflow Boundary Conditions	time-dependent
Anomalous resistivity model	current-dependent nonlinear

Table 4.1. This table summarizes the inputs to the GGCM MHD model. The inputs are the solar wind parameters as measured by ACE. Unless otherwise specified, the inputs listed are the initial conditions at the start of the simulation. The dipole tilt is fixed at the actual value corresponding to 15:00 UT, the time when Cluster crossed the current sheet.

corresponding to 15:00 UT, a time of interest when Cluster crossed the current sheet (the simulation does not update the dipole tilt in time). The simulation uses the average IMF B_x of -10 nT throughout the interval. During the hour preceding Cluster's magnetopause crossing at 15:00 UT, the IMF was mostly northward, ranging between 10 and 15 nT (GSE) on average, with a roughly -10 nT component in GSE x, and a IMF GSE B_y that varied between roughly -5 to 10 nT. At 15:00 UT, the IMF clock angle is about 15°, but by 15:11 UT, another time of interest for comparison to DMSP data, it has increased up to about 33°. As discussed by *Watanabe et al.* [2004], the greater the (nonzero) IMF clock angle is relative to the y-z dipolt tilt, the more the open field lines overdrape the flanks and slip across the top and bottom of the magnetopause. Also, the x-z dipole tilt and IMF B_x control overdraping and the timing of reconnection in the summer and winter hemispheres.

A comparison of crucial GGCM outputs along Cluster's trajectory to Cluster's actual measurements serves as a ground truth of the model validity at this time. As demonstrated in Figures 4.5a and 4.5b, the simulation places Cluster 1 in the magnetopause and crossing into the magnetosheath at very nearly the same time—only roughly 4-5 minutes later—as the observations. In the actual Cluster data, the magnetopause lies between about 14:54 and 15:03 UT. The coordinate system used in the figures is rotated from the GSE coordinate system so that it is aligned with the magnetic field direction on either side of the magnetopause, as measured several minutes before and after the magnetopause crossing. This direction is the new x direction, so that B_x and B_y are close to zero on either side of the magnetopause. The direction of the current sheet in this new coordinate system points approximately 20° tailward of the GSE $-y$ direction.

GGCM Cluster 1 Magnetic Field

Cluster Magnetic Field
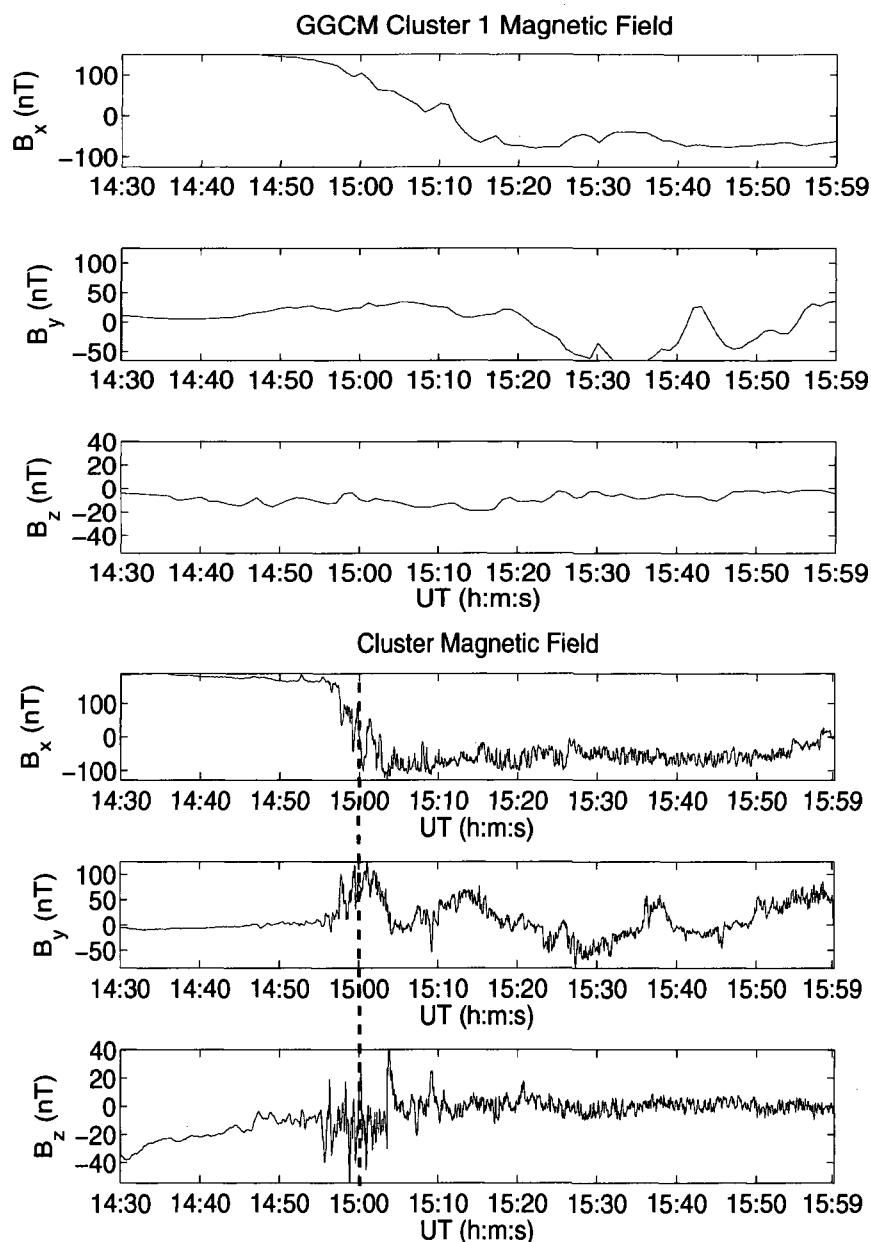
Figure 4.5a-4.5b. This figure compares the GGCM simulation magnetic field at the location of Cluster 1 (Figure 4.5a) to Cluster 1's magnetic field measurements (Figure 4.5b) over the interval of Cluster's magnetopause crossing. In the actual Cluster data, the magnetopause lies between about 14:54 and 15:03 UT. The coordinate system used in the figures is rotated from the GSE coordinate system so that it is aligned with the magnetic field direction on either side of the magnetopause, as measured several minutes before and after the magnetopause crossing.

The Cluster magnetic field measurements from the FGM instrument are shown at a spin-resolution sampling rate. The simulation's agreement with observed magnetic field magnitudes and signs is good. As expected, the gradients are sharper and steeper in the real data, which is exacerbated not only by the limits of the spatial resolution, but also the much lower time resolution (1 minute) of the simulation. Within the magnetopause, the magnetic field in the actual Cluster data develops a large bulge in the rotated y direction, while B_x and B_z simultaneously vanish and change sign (for example, at 15:00 UT, marked by the dashed line). This appears in the model's magnetic field, though it is smaller and more gradual. Likewise, while the actual Cluster data includes a 20 nT normal magnetic field at the magnetopause reconnection site (~ 15:00 UT), this feature is absent in the simulation, which, as we shall see, places the hyperbolic reconnecting components at somewhat higher latitudes than Cluster. Figure 4.6 plots the components of the current in the rotated coordinate system as calculated by the simulation for Cluster 1's position. The current sheets agree in location, again by a 4-5 minute delay, with a large amplitude current sheet in the negative y direction. However, the current estimated from the Cluster data is about -1.5 $\mu A/m^2$, more than an order of magnitude larger than the -.05 $\mu A/m^2$ the simulation produces at this location. This is because the simulation has a grid size that averages over the layer and misses the extrema in the current. Some discrepancies can be expected between the actual and predicted times and locations. Grid resolution Δr_g can also account for the timing difference Δt between the simulation and the observations: $\Delta t = \Delta r_g / v_{sc}$, where v_{sc} is the spacecraft velocity. For $\Delta r_g = .5$ R_E and v_{sc} = 3.5 km/s, Δt = 15 minutes.

GGCM Cluster 1 Current
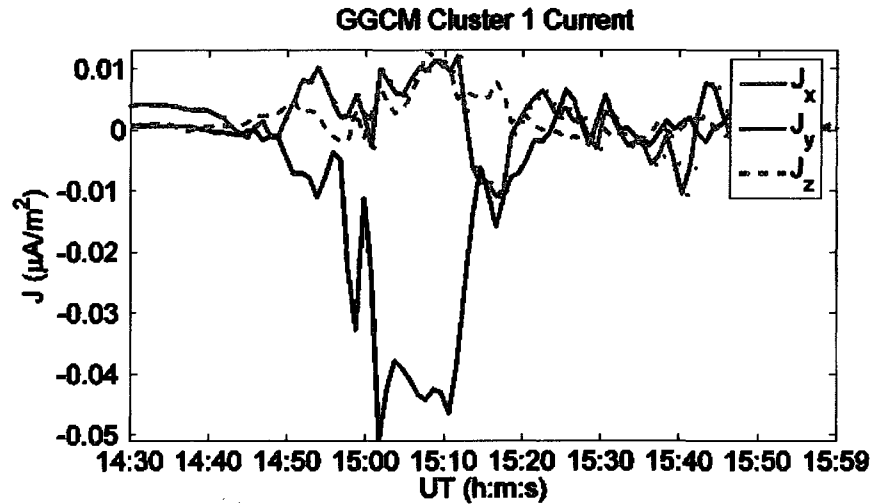
Figure 4.6 This figure provides further validation that the model accurately reflects Cluster's current sheet crossing.

4.4 Location of Reconnection

In this section we seek to answer two major questions: (1) what constraints the data and model place on where reconnection occurs, and whether they agree; (2) how reconnection is occurring, i.e., the global topology, location, length scale, and sequence of reconnection. The first step in this process is to derive the basic 3D magnetic skeleton ensuing from the reconnection, i.e., to locate the fan surfaces, the magnetic nulls, the separatrices, and the global separator. Our prerequisite for reconnection is the coincidence of a parallel electric field along a singular field line and a nearby perpendicular x-type magnetic merging topology, after *Priest and Forbes* [2000]. To disambiguate the length scale of merging, we will determine where the convection electric field in the solar wind couples to the ionosphere.

Figure 4.7, a view from the dayside dusk sector, illustrates the GGCM magnetic topology, revealing a pair of global nulls, a type A null (red) in the northern hemisphere
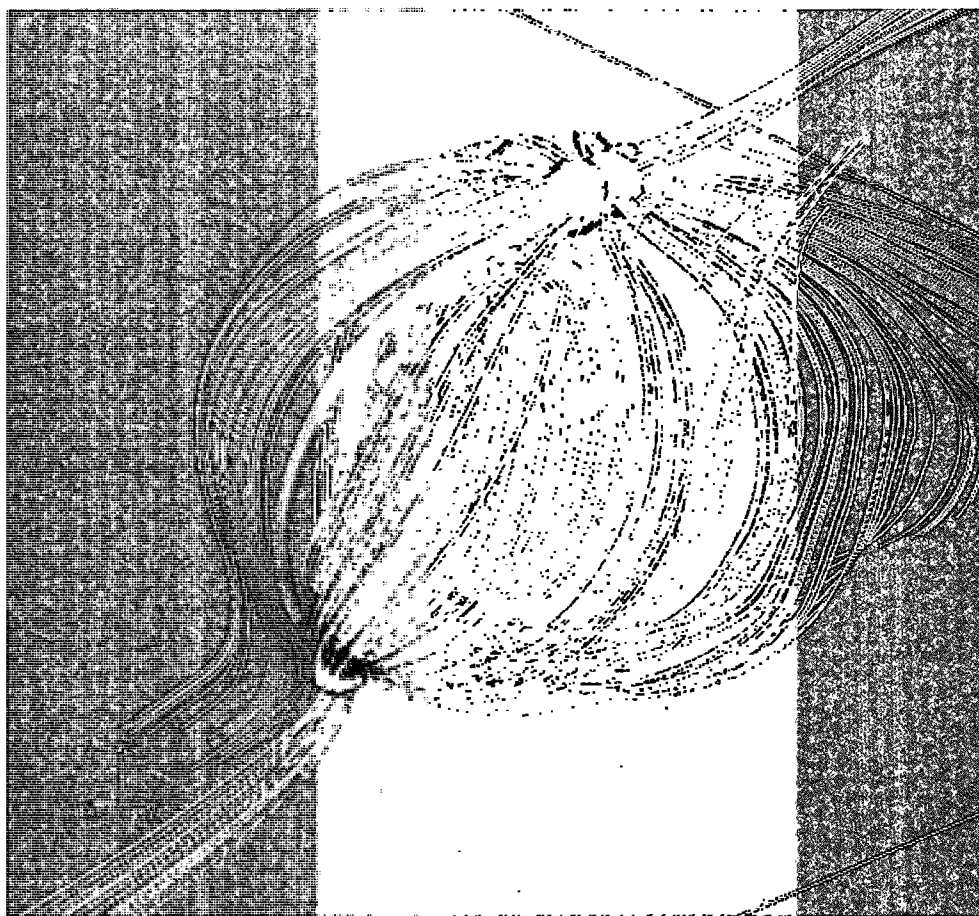
Figure 4.7. This figure, a view of the dusk dayside, renders the northern-reconnected field lines in white and the southern reconnected field lines in red, where the field lines were generated from 300 random seeds placed within 1.5 R_E from the northern and southern unpaired nulls. The surfaces that divide the open field lines from the solar wind field lines and from the closed earth lines intersect through a diagonal field line that lies across the dayside, through the subsolar point, from the northern cusp null to the southern. This field line is the global separator.

and a type B null (blue) in the southern. These two global nulls are accompanied by additional pairs of nulls corresponding to local reconnection (one extra pair in the southern hemisphere, and five extra pairs in the northern). The nulls in the tail region have not been included. The northern-reconnected field lines are rendered in white and the southern reconnected field lines in red, where the field lines are generated from 300 random seeds placed within 1.5 R_E from the northern and southern global nulls. The

surfaces that divide the open field lines from the solar wind field lines and from the closed earth lines intersect through a diagonal field line that lies across the dayside, through the subsolar point, from the northern cusp null to the southern. This field line is the global separator. A global separator (yellow field lines) extending across the dayside magnetopause joins this pair of nulls. Each hemisphere contains additional pairs of local nulls, each of which will in turn be joined by a local separator.

To compare this topology and the resulting current sheet to Cluster's location and inferred current sheet, Figure 4.8a shows the magnitude of the currents, the separator, the nulls, and the position of Cluster (the orange square). The black arrow with its foot at the position of Cluster represents the direction of the current sheet observed by Cluster as it passes through the magnetopause. The magnetic nulls are again the red and blue spheres and the approximate separator the yellow field line that joins the pair of nulls in each hemisphere. The surface consists of the current sheet that exceeds 0.02 μA/m^2 (which includes the ring current and auroral electrojets as well as the dayside current ribbon that joins the nulls in each hemisphere.) The surface color represents the value of the current component parallel to **B**, and clearly divides into regions where it is parallel and antiparallel to the field lines. The current sheet has the shape typical of the so-called *dayside sash*, as found by *Dorelli et al.* [2007] for the case of zero dipole tilt and uniform resistivity. Note that the separator's clock angle is somewhat smaller than that of the current sheet (the same as the IMF), replicating the results found by *Dorelli et al.* [2007]. However, as we will show, we believe this is because reconnection is occurring on the separatrix as well as the separator. The direction of the current observed by Cluster also matches the direction of the current sheet in the simulation.
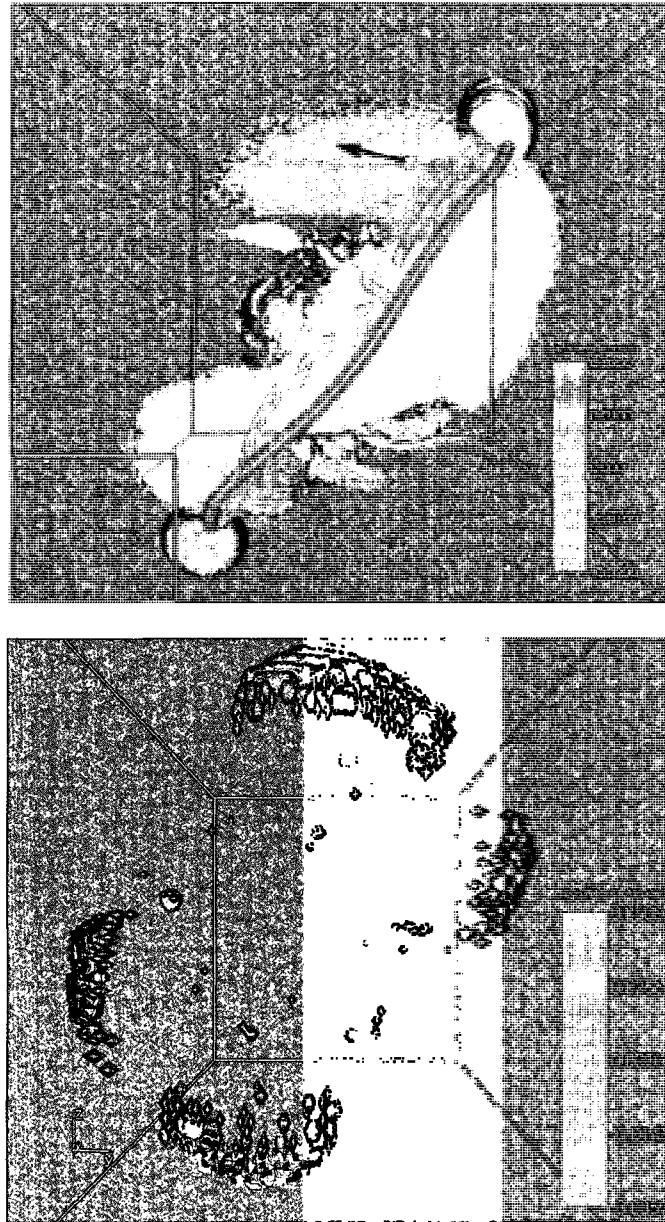
Figure 4.8a-4.8b. (a) Top: The surface contour in Figure 4.8a represents the magnitude of the currents that exceed 0.02 □A/m2 in the simulation, and its color represents the amplitude of the parallel current. The parallel current points in the GSE $-y$ direction in the northern and southern hemispheres and in the GSE $+y$ direction at the subsolar point. The yellow line is the closed field line corresponding to the dayside separator, and the blue and red spheres are nulls. Red spheres are type A nulls, and blue spheres are type B nulls. **(b) Bottom:** is a view from the sun of the isosurface of the dayside parallel electric field (all places where it exists). The color on the surface represents the magnitude of the parallel current.

However, we need to determine the distribution of the parallel electric field on the magnetopause. In contrast to *Dorelli et al* [2007], here the current-dependent anomalous resistivity varies spatially. Therefore a parallel electric field also requires a high resistivity and will not in general coincide with the large parallel currents. As demonstrated by the surface in Figure 4.8b, the parallel electric field on the dayside exists where the anomalous resistivity intersects the parallel currents. The surface represents the location of the parallel electric field, while the color signifies the value of parallel current. It exists in both hemispheres, but, owing to the IMF and dipole tilts, it is much stronger and covers a broader region in the northern hemisphere. There are isolated spots of parallel electric field on the dayside sash, as well as areas on the flanks that are probably viscous cells. However, what we have found is that the parallel electric field lies primarily on both the separatrix surfaces and on the separator at the cusps, where the Earth and solar magnetic fields are almost completely antiparallel. Cluster is not collocated with the nulls nor with the parallel electric field surface. The model's nearest parallel electric field is about 2.5 R_E away from Cluster. However, there are two points we can make about this. One point is that the reconnection is not limited to the nulls, but can occur on singular field lines passing through the nulls. The other point is that the resistivity model cannot be expected to exactly replicate real life conditions.

The parallel electric field along open magnetic field lines has to distribute itself in a way that forces the potential from many field lines to match at the null point. This is to avoid a singularity or discontinuity in the electric field at the null point. A potential drop, or electric field, between any two open field lines in the solar wind must be compensated for and removed once these two field lines meet at the null point if the electric field is to

remain finite there. To accomplish this, a parallel electric field develops along one or both of the field lines [*Siscoe et al.*, 2001]. All of the field lines feeding into the nulls, including the separator, are singular field lines that may have to modify their electric fields. The magnetopause becomes the fan plane. The nulls' fan planes do not need to be perpendicular--they can intersect at an arbitrary angle that determines the slope of the hyperbolic geometry. Figure 4.9 is a diagram of the fields that correspond to open field lines connected to nulls and fan out over the magnetopause at the Earth. The spines are in green, type A nulls in red, and type B nulls in blue. Potential singular field lines spread out over the fan plane are black, and the separator is yellow. The direction of the convection electric field E and of the parallel electric field $E_{\parallel}$ is shown by dashed orange lines. Figure 4.9a demonstrates why the potential drop between any two field lines with a foot in the solar wind and a foot in a null enforces a parallel electric field along those field lines so the potentials match at the null. The potential drop between two field lines with a foot in the solar wind and a foot in a null enforces a parallel electric field along those field lines so the potentials match at the null. If the potential at the northern null converges to some average φ_2, then $\varphi_1 - \varphi_2 < 0$ produces a downward parallel electric field as shown, and $\varphi_3 - \varphi_2 > 0$ produces an upward parallel electric field. In Figure 4.9b, local null pairs in a given hemisphere that are connected by a local separator also carry a parallel potential drop between nulls and along the separator. In this case, $E_{\parallel} = E$ when solar wind field lines merge into the null. The location of the field lines on the magnetopause that must develop a parallel electric field depends upon the particulars of the solar wind pressure, IMF and electric field, and on the Earth's dipole tilt. They may
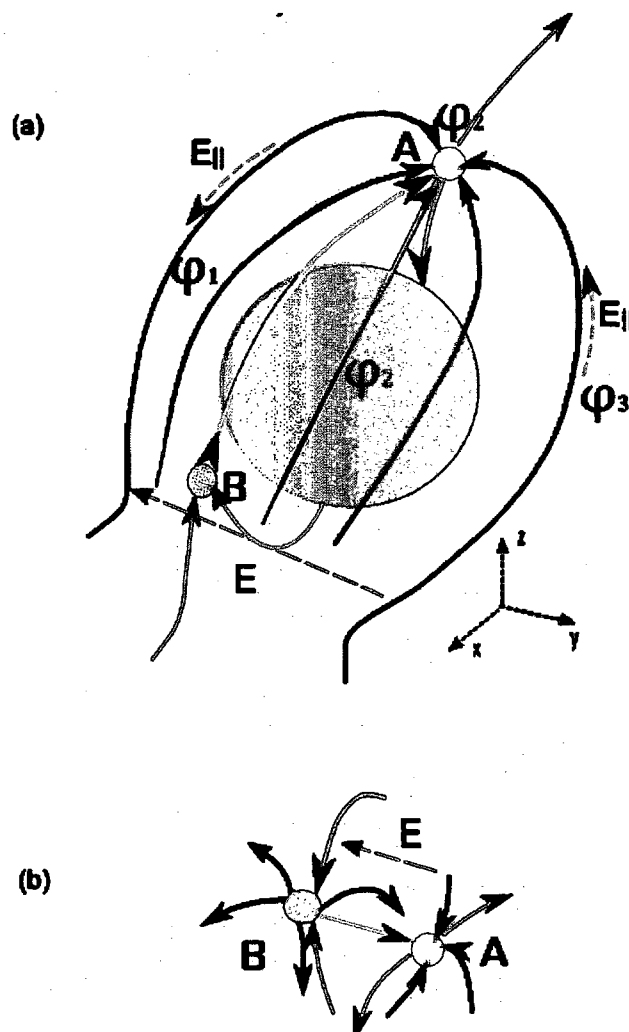
Figure 4.9 A diagram of the fields that correspond to separators, nulls, and singular field lines at the Earth. The spines are in green, type A nulls in red, and type B nulls in blue. Potential singular field lines on the fan plane are black, and the separator is yellow. The direction of the convection electric field E and the parallel electric field $E_{\parallel}$ is shown by dashed orange lines. **(a) Top:** The potential drop between two field lines with a foot in the solar wind and a foot in a null enforces a parallel electric field along those field lines so the potentials match at the null. If the potential at the northern null converges to some average φ_2, then $\varphi_1 - \varphi_2 < 0$ produces a downward parallel electric field as shown, and $\varphi_3 - \varphi_2 > 0$ produces an upward parallel electric field. **(b) Bottom:** Local null pairs in a given hemisphere that are connected by a local separator also carry a parallel potential drop between nulls along the separator. In this case, $E_{\parallel} = E$ when solar wind field lines merge into the null.
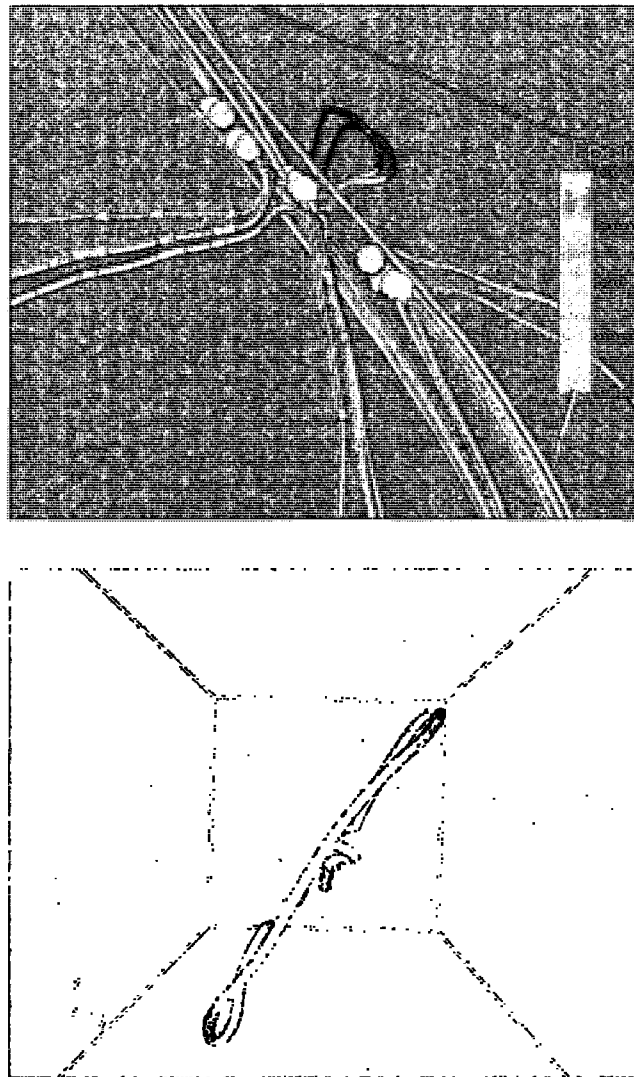
Figure 4.10a-4.10b **(a) Top:** View from the dawn side of the cusp with the sun to the right, shows the model field lines spanning the region in the northern cusp with the parallel electric field. The field lines are shaded by the relative magnitude of the parallel electric field. **(b) Bottom:** Illustration that there is a parallel electric field on the separator at the northern and southern cusp only.

or may not lie along the separator. We will need to determine their shape and location for our particular case.

The set of field lines carrying a parallel electric field that also thread nearby perpendicular fields forming an x-type topology are the set of field lines on which merging occurs. These are the singular field lines. We will show that reconnection

happens on a set of singular field lines that fan across the open/IMF separatrix as well as on the separator at the cusps. Figure 4.10a, a view from the dawn side of the cusp with the sun to the right, shows the field lines spanning the region in the northern cusp with the parallel electric field. The field lines are shaded by the relative magnitude of the parallel electric field. The field lines feed into one or another of the northern nulls and drape and fan out across the dayside and the flanks of the magnetopause. The parallel electric field is negative on the dawn side of the nulls, and positive on the dusk side, meaning that it lies roughly along the negative y direction across the cusp. Figure 4.10b demonstrates the parallel electric field on the separator. The separator by definition satisfies the requirements for reconnection where it possesses a parallel electric field. Figure 4.10b illustrates that there is a parallel electric field on the separator at the northern and southern cusp only. Thus antiparallel reconnection occurs on the same field line to form new closed field lines if that field line lies along the separator line of symmetry. Figure 4.11 shows the null region connected to the cusp field lines with the parallel electric field and the separator in finer detail, this time in a view from the dusk (with the sun to the left). Figure 4.11a shows that the nulls in the northern cusps belong to a tearing mode train. An o-line as well as hyperbolic fields are clearly apparent in this figure. The null-finding software used to distinguish type A from type B nulls does not find type A_s and type B_s nulls, but clearly they are present in the form of o-lines with fields spiraling into and out of them. Figure 4.11b reveals a very clear x within the tearing mode, whose field lines carry a strong parallel electric field and connect to a number of perpendicular singular field lines. These figures demonstrate that parallel electric field bearing singular field lines lying roughly along the GSE y direction thread a series of

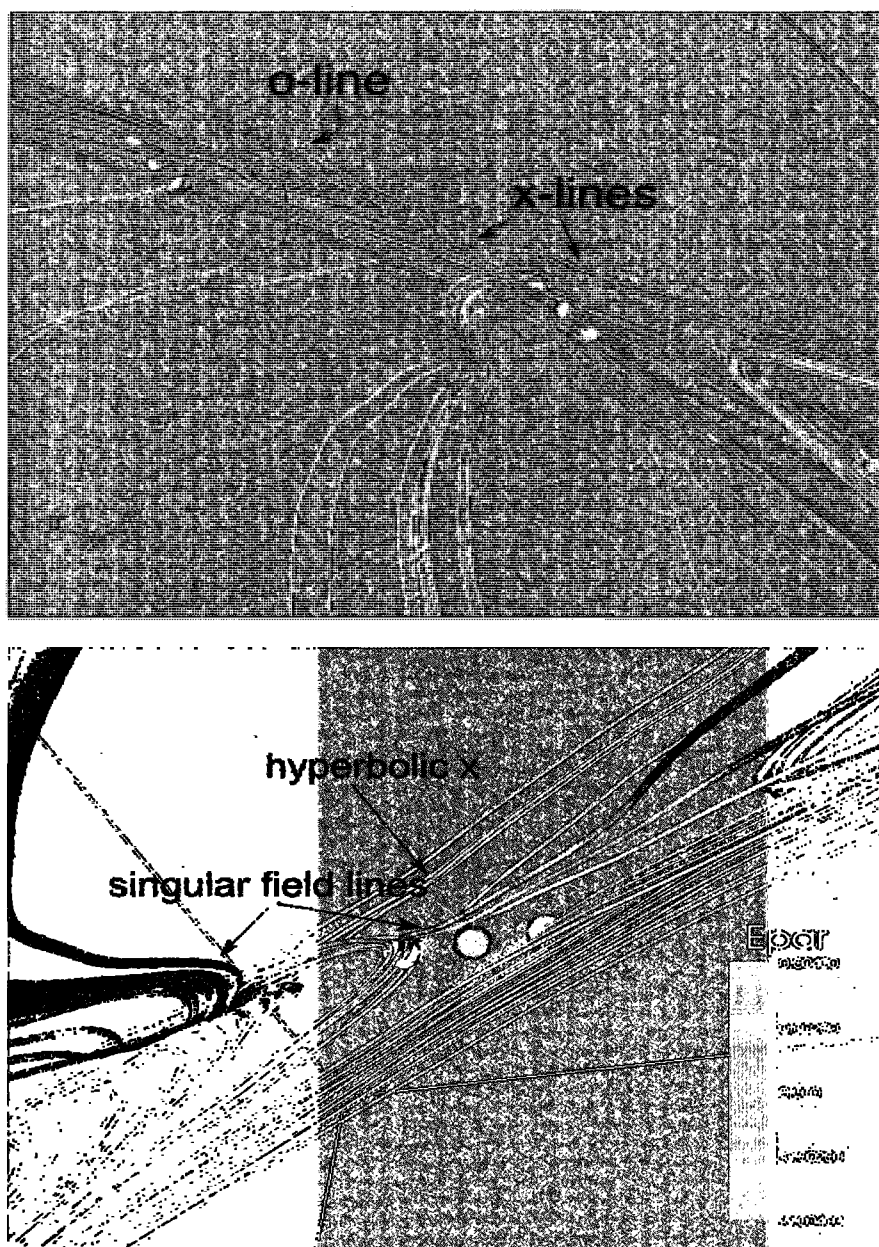**Figure 4.11a-4.11b** (a) **Top:** The nulls in the northern cusps belong to a tearing mode train. An o-line as well as hyperbolic fields are clearly apparent in this figure. (b) **Bottom:** A very clear x lies within the tearing mode, whose field lines carry a strong parallel electric field and connect to a number of perpendicular singular field lines. These figures are from the dusk side with the

perpendicular x's and o's near the nulls, and even develop braids and ropes. Thus these sets of field lines fanning out along the flanks of the magnetopause and carrying a parallel electric field satisfy the requirements for singular field lines reconnection on the separatrices and at the nulls.

Reconnection occurs near the nulls in the region of antiparallel magnetic fields, but it also occurs on the open/closed and the open/IMF separatrices. Figure 4.12 is the parallel electric field surface along with the separatrix surfaces and the magnetic nulls. Figure 4.12a includes the open/IMF separatrix surface (in orange) and Figure 4.12b the open/closed separatrix surface (in whit). The red surface is now the parallel electric field. The open/IMF separatrix includes the nulls and the area of parallel electric field dawnward of the nulls in the northern hemisphere. The open/closed separatrix includes the northern and southern global nulls and the parallel electric field region astride the nulls in the southern hemisphere. Reconnection in the narrow swath duskward of the northern nulls lies on the open/closed separatrix and occurs between IMF and closed field lines. Thus it is an extension of the separator, which seems to be a ribbon rather than a line. Thus the separatrix reconnection on the dawn side of the northern nulls is between open and IMF field lines, and the reconnection on the dawn and dusk sides of the southern nulls is between open and closed field lines. Along the separator line of symmetry at the nulls, the reconnection is between IMF and open field lines as well as IMF and closed field lines. We will show below that the topology of the field lines corroborates these conclusions.

In a coordinate system aligned with the tilt of the magnetopause and the orientation of the IMF, Cluster measures a component of the magnetic field that exists
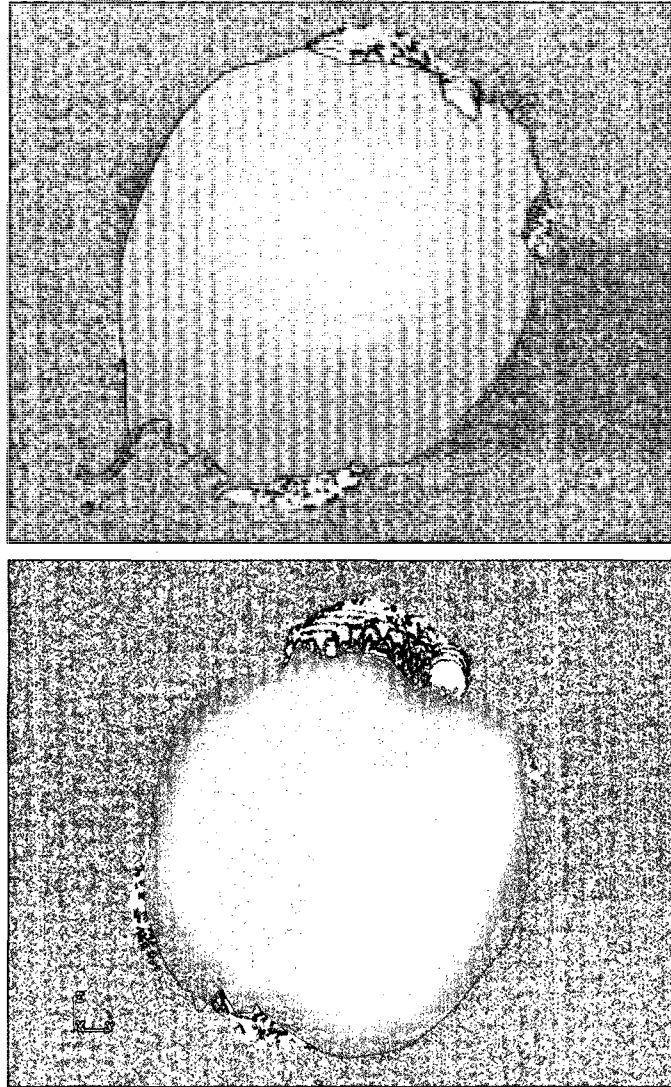
Figure 4.12a-4.12b The parallel electric field surface along with the separatrix surfaces and the magnetic nulls. **(a) Top:** includes the open/IMF separatrix surface (in orange) and **(b) Bottom:** the open/closed separatrix surface (in white). The red surface is the parallel electric field.

only within the magnetopause. We call this the y direction in this rotated coordinate system. In this system, the other two components of the magnetic field simultaneously vanish and change sign (see for example, around 15:00 UT, marked by the dashed line, in Figure 4.5b). The orientation of the reconnection current sheet in the actual Cluster observations also agrees with that in the simulation current in the vicinity of Cluster. In the GGCM simulation, Cluster is 4 R_E away from the global separator and 2.5 R_E away

from the nearest $E_\parallel$. Given expected discrepancies between the simulation and the physical data, it is possible Cluster's position is on a reconnecting singular field line. It is easy to interpret Cluster's magnetic field observations in terms of a position along a singular field line: positioned this way, one observes an out-of-plane positive B_y and hyperbolic reconnection fields in the x-z plane. Thus the reconnection topology of the model completely matches that observed in the Cluster data. The series of x's and o's would also provide a natural explanation for the O^+ flows and waves observed by Cluster in the magnetopause. The waves may belong to a traveling plasmoid or o-line. The length of the tearing mode region and the extent of the reconnecting singular field lines on the separatrix surface redounds to increase the likelihood of satellite encounters with reconnection.

Now we will try to address what forces contribute to this configuration of reconnection singular field lines for this particular case. Some of the reasons depend on changes in field line shape. The merging process might conserve flux in a global sense, as in returning flux from the dayside to the nightside by reclosure of opened field lines in conjugate hemisphere merging. But local changes in magnetic flux and in field line shape are a necessary part of reconnection. *Song and Lysak* [2006] have gone beyond the force balance of the generalized Ohm's law to derive the physical source of the parallel electric field. They prove that it lies in a twist or torque of the magnetic flux tube. They assume small perturbations to the background field and wavelengths smaller than the gradient length scales of the magnetic field. In a simplified geometry of a cyclindrical flux tube of radius R oriented along z, they derive a pair of coupled equations that express the

dynamic dependence of the parallel electric field on the parallel vorticity (e.g., equations 15 and 16 of *Song and Lysak* [2006]):

$$c\frac{\partial \Phi_B}{\partial t} = \frac{cB_{||}}{4\pi} \mathbb{O}_{||}|_0^{\Delta h}, \tag{4.1}$$

where $\mathbb{O} = \oiint(\nabla \times \mathbf{v})_{||}\, dS$, and

$$\frac{\partial \Phi_v}{\partial t} = \frac{c}{\varepsilon B_{||}} \mathbb{I}'|_0^{\Delta h}, \tag{4.2}$$

where $\mathbb{I}' = \oiint J'_{||}\, dS = \iint_0^R \frac{c}{4\pi r}\left[\frac{\partial(rB_\varphi)}{\partial r} - \frac{\partial B_r}{\partial \varphi}\right] r\, dr\, d\varphi = \frac{c}{4\pi}(\int rB_\varphi\,|_0^R\, d\varphi + \int B_r\,|_0^{2\pi}\, dr)$

and we use *cgs* units, following *Song and Lysak* [2006]. Here c is the speed of light, $B_{||}$ is the background magnetic field, ε the dielectric constant, dS the cross-sectional area element of the flux tube and Δh some length along $B_{||}$, and $\mathbb{O}$ is the parallel component of the vorticity integrated over dS. Φ_B is the azimuthal magnetic flux $\int_0^{\Delta h} dz \int_0^R B_\varphi\, dr$, where, in the chosen cylindrical geometry, $B_\varphi = \frac{2\pi r}{c}J'_{||}$. $J'_{||}$ is the total current, including the displacement current $\frac{1}{4\pi}\frac{\partial E_{||}}{\partial t}$. The relative importance of the $J'_{||}$ or $\frac{1}{4\pi}\frac{\partial E_{||}}{\partial t}$ contributions is determined by the density and the rate of change of $E_{||}$, the displacement current being larger for lower densities or large $\frac{\partial}{\partial t}$. Φ_u is the azimuthal velocity flux $\int_0^{\Delta h} dz \int_0^R v_\varphi\, dr$, where $v_\varphi = \omega_{||} 2\pi r\, dr$. Equation (4.1), derived from Faraday's and Ampere's law, says that a parallel electric field from an azimuthal magnetic flux in the flux tube is produced by a parallel shear in the parallel velocity (through the integral of the vorticity). Equation (4.2), which is derived from the curl of the MHD momentum equation, shows that the generation of vorticity, or azimuthal velocity flux, depends on a vertical magnetic shear in the components of **B** perpendicular to the ambient field $B_{||}$ (through the integral of $J'_{||}$).

The time-dependent terms in Maxwell's equations, i.e., the displacement current $\frac{\partial \mathbf{E}}{\partial t}$ and

the magnetic flux, $\frac{\partial \mathbf{B}}{\partial t}$, are necessary to derive the source of $E_{\parallel}$. Therefore, a change in

field line shape and consideration of dynamic conditions is crucial to the development of

the $E_{\parallel}$ necessary for reconnection to take place.

Magnetic draping thus contributes to the observed spatial distribution of magnetic

field lines carrying field aligned electric fields—i.e., to the observed spider web of

singular field lines. By producing a field line tension, draping is the mechanism that

allows reconnection at the magnetopause to get underway. In a study of the effects of

magnetic draping over a galactic core moving in a magnetized plasma, *Dursi and*

Pfrommer [2008] find a cause and effect relationship between the magnetic draping layer

and the growth of a vorticity layer in an initially vorticity-free plasma. They quantify this

by noting the equation of motion for the vorticity is related to the magnetic field line

tension. The momentum equation is

$$\frac{\rho d\mathbf{v}}{dt} = -\nabla p + \mathbf{j} \times \mathbf{B}. \tag{4.3}$$

Taking the curl of both sides and setting $\boldsymbol{\omega} = \nabla \times \mathbf{v}$ gives the equation of motion for the

vorticity:

$$\frac{d\boldsymbol{\omega}}{dt} = \frac{1}{\rho^2} \nabla \rho \times \left[\nabla p + \frac{\nabla B^2}{2\mu_0} - \frac{(\mathbf{B} \cdot \nabla)\mathbf{B}}{\mu_0} \right] + \frac{1}{\rho\mu_0} \nabla \times (\mathbf{B} \cdot \nabla)\mathbf{B} \tag{4.4}$$

This is derived from the same principles as equation (4.2), but is expressed in a way that

makes the role of field line tension from draping more transparent. The terms involving

$\frac{(\mathbf{B} \cdot \nabla)\mathbf{B}}{\mu_0}$ express the magnetic tension. The *Dursi and Pfrommer* [2008] simulation finds that

both of the magnetic tension terms play a role in the development of ω within the draping layer. The first tension term dominates where the density gradient misaligns with the magnetic tension, i.e., at the large density gradient where the field lines meet the obstacle. The latter rotational magnetic tension term dominates throughout the rest of the magnetic draping layer in the wake of the density gradient.

Thus there is a causal relationship starting with magnetic draping and ending with an $E_{\parallel}$. This is not to say that draping and vorticity are sufficient conditions for reconnection, but they are necessary. The magnetic draping produces a tension in the field line, which initiates a localized vorticity. Vorticity is necessary for a parallel electric field. It produces a parallel electric field when its flux parallel to a flux tube undergoes a shear along the flux tube. Figure 4.13 is an image of the velocity flow lines, seeded within a 5 R_E region at $x = 12$ R_E along the Sun-Earth line. The flow streamlines (roughly equivalent to particle paths for a quasi-steady solar wind flow) are shaded by the value of the vorticity. The vorticity occupies the same region as the draping of the magnetic field lines and overlaps the areas with $E_{\parallel}$ (Figure 4.8b).

Furthermore, good coupling of reconnected field lines to the ionosphere retains any initial twists in the flux tube, and can even enhance the twist, through line-tying. Line tying occurs when the ionospheric conductivity is high enough to produce strong ionospheric drag. Initially, a torque at the magnetosphere end of the magnetic flux tube produces a FAC, as in equation 4.1 above. This current closes through a current opposing the electric field in the magnetopause, acting as a generator, a Pedersen current in the ionosphere, and an oppositely directed FAC. Line-tying, a condition of low ionospheric dissipation, keeps these currents flowing, provided the magnetosphere maintains its

Figure 4.13 A view from the sun of the solar wind flow lines seeded at 12 R$_E$ along the Sun-Earth line. The shading along the flow lines represents the magnitude of the vorticity, which is greatest where draping occurs. The white surface is the parallel electric field.

torque on the field line. Once precipitating electrons make their way down to the ionosphere, they increase the conductivity there, and this can serve to enhance the twist that already exists on the field line by increasing the ionospheric drag from collisions [*Paschmann et al.*, 2003]. Without line tying, an $E_{||}$ develops along the flux tube between the magnetopause and the ionosphere that allows the footpoint of the flux tube to slip and decouple from the plasma. In any event, the drag of the plasma connected to the footpoint through line tying becomes a mechanical load that the dynamic coupling at the magnetopause must overcome. The drag will build the distortion of the field line. The electric field mapping to the ionosphere convects the ionospheric footpoints sunward,

while the **E×B** drift of the IMF points antisunward. Although this may first occur on an open field line, the feature persists even if the field line is newly-closed. Moreover, the draping, line-tying and convection would tend to produce this distortion only within the magnetopause, while the Earth and solar fields are essentially still antiparallel on either side of the magnetopause. The point is that only a portion of the already open field line needs to lie antiparallel to the IMF (i.e., the downward directed portion), while the draped portion may lie in a very different direction. The crucial mechanism behind this is the boundary condition of the ionosphere. (It would be interesting to test this kind of boundary condition applied to one end of one field line in a kinetic or hybrid reconnection simulation.) We know from the previous figures from the simulation that there is no parallel electric field along the portion of the reconnected field lines that lies between the magnetopause and the ionosphere. We will also show below that the Cluster data corroborates this. Thus we can say that the field line torque that results from good coupling applies to this event. In the next few paragraphs we will show that draping and field line tying help produce the shape of the singular field lines that reconnect.

The following figures will follow field lines to confirm where, and what types of, field lines reconnect. The field lines' topology confirms that IMF field lines reconnect to magnetic field lines already opened on the northern dawn side of the separator to form a new IMF field line and a new open field line. The magnetic topology stemming from various points near the northern nulls is shown in Figure 4.14a, a view from above the dawnside polar region. The field lines that have reconnected to the IMF (purple line) in the northern cusp dawn side of the separator symmetry line were initially open field lines (in orange). The open field lines were first overdraped lobe field lines (orange on
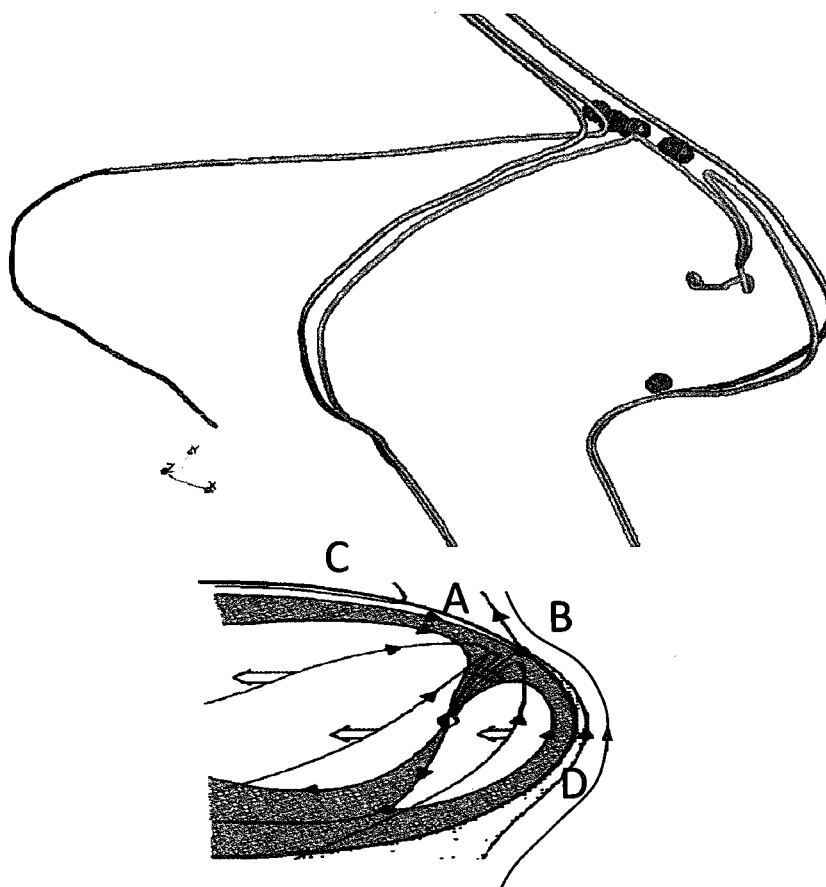
Figure 4.14a-4.14b. (a) **Top:** The GGCM field lines that have reconnected to the IMF in the northern cusp dawn side of the separator symmetry line were initially open. These field lines convected tailward along the dawn side, and subsequently reconnected with a new IMF field line in the northern cusp region. (b) **Bottom:** A diagram of the field lines before and after reconnection in the northern cusp. The field line A that has been opened on the dayside and convected tailwards reconnects with a new IMF field line (labeled B). The subsequent field lines are a new IMF field line (C) and a new open field line (D). The thick arrows indicate the direction of field line convection. From *Crooker* [1992].

dayside) that then convected tailwards along the dawn flank (presumably after first convecting sunward). While overdraping the flank (in orange), the field line reconnected again to an IMF field line to form a new overdraped field line and a new IMF field line (also in purple). The part of the field line connected to the Earth (sometimes called the *stemline*) lies antiparallel to a new draped IMF field line and reconnects with it, even though the IMF portion of the field line is not parallel to the new IMF field line. This is

essentially the topology of Figure 1.15e, but in our example the field lines are torqued and draping the flanks. Figure 4.14b is a diagram of the process. The drawing (from *Crooker* [1992]) shows the configuration after the overdraped dayside field line (segment A) has reconnected and convected tailward and a new, roughly antiparallel, IMF field line (segment B) drapes above it. Segment C is now a new IMF field line and segment D a new open field line, the IMF portion of which begins to convect tailward. The thick arrows indicate the direction of the IMF motion in this region. The point is that the open field line has convected and draped so that only part of the field line is actually antiparallel to the imposing IMF. The part of the field line below the magnetopause and connected to the Earth is antiparallel to the IMF, but the overdraped portion is not. The part of the open field line that is draped over the flank is torqued from a combination of draping and field line tying and becomes the singular field line. (We shall see that this type of reconnection also occurs in the southern hemisphere). On the dusk side of the separator, the component is also along the current sheet, but in the opposite sense. Note also that this mechanism produces an out-of-plane component only within the magnetopause—the field lines lying above and below are actually antiparallel. This kind of reconnection is quasi-steady, because the reconnection to open field lines occurs in only one hemisphere, and convection into the tail returns open flux from the dayside to the nightside. Thus there is no net flux change. However, as discussed previously, time–dependent effects from draping, line-tying, and sunward convection of tail field lines do change the shape of the field lines as they convect.

This occurs, however, only along the northern dawn side of the separator, not along the line of symmetry of the separator or on the northern dusk and or anywhere
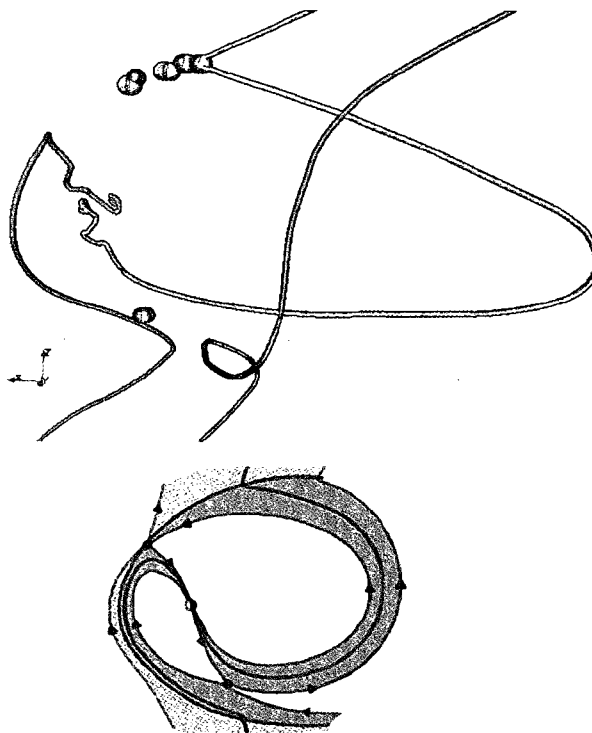
Figure 4.15 (a) Top: A view from dusk of merging of the IMF with closed field lines. The red field line was initially a closed tail field line that has reconnected to the IMF. The orange field line is the resulting overdraped dayside field line. This field line convects sunward, then tailward along the dusk flank. At the southern null, it reconnects with an open field line there to form a new closed dayside field line and a new IMF field line, such as the purple field line. **(b) Bottom:** Diagram from *Crooker* [1992] illustrating the fund fundamental process in 2D.

within the southern parallel electric field. In the latter regions, there are two types of steady state reconnection involving overdraping—i.e., the two models discovered by *Crooker* [1992] and by *Watanabe et al.* [2004]. Both of these result from the sunward dipole tilt. Figure 4.15, a view from dusk, shows the progression of field lines merging in the manner described by *Crooker* [1992]. The red field line was initially a closed lobe field line that has reconnected to the IMF at one of the northern null. The orange field line is the resulting overdraped dayside field line. This field line convects sunward, then tailward along the dusk flank. At the southern null, it reconnects with an open field line there to form a new closed field line and a new IMF field line, such as the purple field

line shown. Therefore, field lines that first reconnect with closed field lines in the north, overdrape, convect sunward, and then reclose at the southern null. These field lines thus follow the *Crooker* [1992] model of overdraped sunward convection and subsequent reclosure in the conjugate hemisphere. Her model includes a sunward dipole tilt and/or IMF x tilt, both of which are features of this event.

However, along the nulls and in the winter hemisphere we see yet another sequence of reconnection. In this case, the IMF reconnects first with an open field line in the northern (summer) hemisphere, convects sunward, and recloses with a closed tail lobe field line in the southern (winter) hemisphere. The latter reconnection forms a new dayside closed field line and a new open tail lobe field line. The process is demonstrated in Figure 4.16, where the overdraped field line convects sunward, then tailward over the flank, and reconnects with a closed field line near the southern null (as, for example, the closed blue tail field line). It forms a new closed field line (such as the closed orange field line in the flank) and a new open tail field line (in blue). This reclosure mechanism in the winter hemisphere (the southern hemisphere in our case) is in keeping with the *Watanabe et al.* [2005] expansion upon the *Crooker* [1992] model, i.e. that portrayed in Figure 1.16b. *Watanabe et al.* [2005] show that the resulting convection in the winter hemisphere involves a pair of cells that circulate outside the polar cap and are coupled to the cells of convection on open field lines in the summer ionosphere. An analysis of the ionospheric data for the location of the polar cap boundary would therefore comprise an interesting expansion of this study. The presence of both the *Watanabe et al* [2004] and the *Crooker* [1992] models of dayside reclosure in the winter hemisphere explain why the southern swath of parallel electric field lies on the open/closed separatrix.
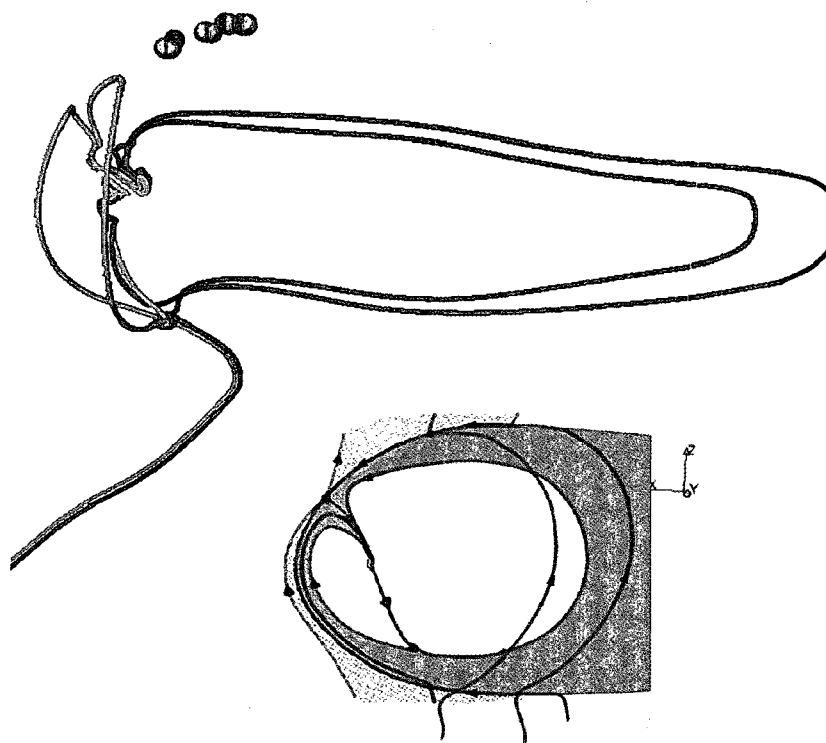
Figure 4.16 (a) Top: Merging of IMF to open field lines: the overdraped field line convects sunward, then tailward over the flank, and reconnects with a closed field line near the southern null (as, for example, the closed blue tail field line). It forms a new closed field line (such as the closed orange field line in the flank) and a new open tail field line (in blue). **(b) Bottom:** A diagram of the fundamental process.

Thus, the field line topology and evolution corroborate the inference we made based on the parallel electric fields of open/IMF separatrix reconnection and closed field line reconnection along the separator and the open/closed separatrix. The implications are significant for understanding the event and the Cluster data. For example, knowledge of the reconnecting field line's history—whether it is newly closed, newly open, or newly IMF—has bearing on what characteristics we should expect in the local particle populations. If the reconnecting field lines have already opened—but in the same hemisphere, for example, a solar wind population may be present, but particles reflected off the conjugate hemisphere will not. Although reconnection occurs on closed field lines and recloses on others, the above analysis shows that Cluster lies in a quadrant where

open field lines reopen. The fact that reconnection occurs on open field lines or on field lines that reclose subsequently—not simultaneously—in the winter hemisphere implies that the bidirectional electrons and the magnetosheath O^+ Cluster observes did not come from the conjugate hemisphere. It implies the source is a tearing mode x upstream of Cluster's magnetopause crossing. Furthermore, in terms of comparison to ionospheric DMSP data, it behooves us to know that quasisteady state magnetospheric convection is at work.

4.5 MI Coupling Width—Merging Width

In this section we will attempt to measure the width of the merging region in the northern hemisphere, for this is what matters for coupling to the ionosphere. The patch of parallel electric field forms a fairly broad band astride the nulls, especially in the northern hemisphere. One way of measuring the merging width is to look at where the solar wind convection electric field couples to the magnetopause and thence to the ionosphere. The model shows that there is an electric field that couples from the magnetosheath to lower altitudes inside the magnetopause. Figure 4.17a, a view from the sun of a slice at the x coordinate of the northern global null, is the local value of the GGCM dusk-to-dawn electric field for 15:11 UT. We present the conditions at 15:11 UT in Figures 4.17a and 4.17b because the results will be useful for a comparison to DMSP F13's data, while they are still otherwise illustrative of the other times of interest to this study. The red polygons mark the locations of the parallel electric field ηJ. As expected for northward IMF reconnection, a negative E_y spans the region of parallel electric field because reconnection is a dissipative process with $\mathbf{E} \cdot \mathbf{J} > 0$. However, it lies sandwiched between
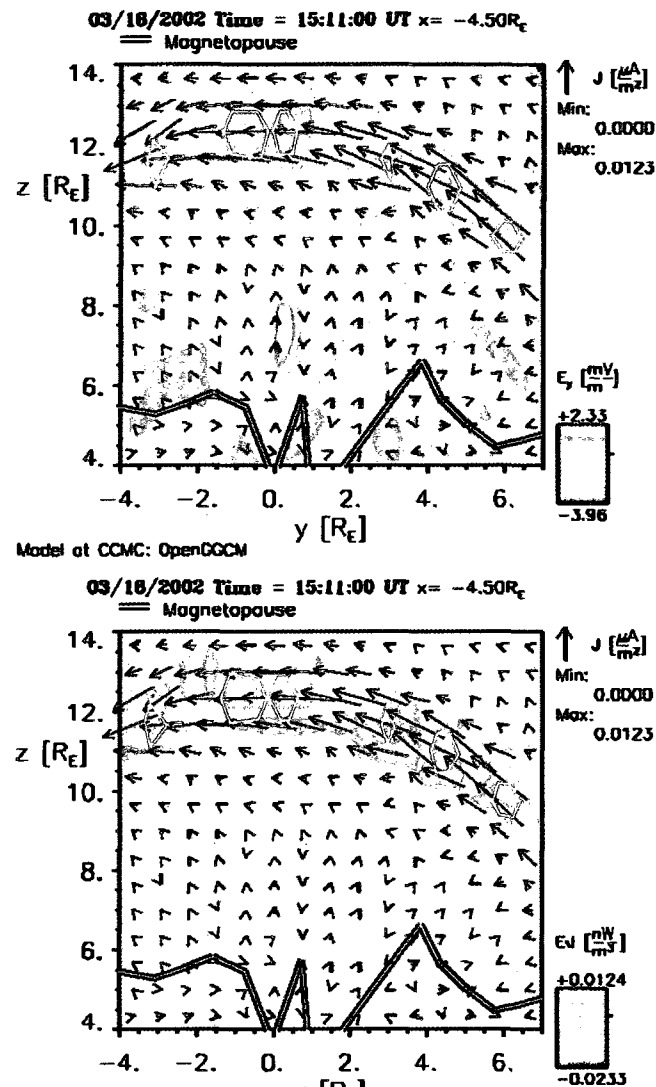
Figure 4.17a-4.17b. **(a) Top:** Large arrows manifest a strong current layer across the polar cap region. The locations of the strongest nonideal $E_{||}$ are denoted by the red polygons in the current layer. The power **E•J** forms layers of generation and dissipation within the current sheet. The red polygons are again the strongest patches of nonideal $E_{||}$. **(b) Bottom:** The negative (dusk-to-dawn) E_y corresponds to the layer of dissipation (**E•J** > 0).

sheets of positive E_y. This is because the magnetopause acts like a generator, with **E•J** < 0, in producing the FAC that couples to the load of the ionosphere. So, in this region, the magnetopause is both a load and a generator. The distribution of power dissipation and Poynting flux divergence supports the estimated cusp reconnection size. The dissipation

along the magnetopause is roughly the same in extent as the parallel electric field. As shown in Figure 4.17b, a view from the sun of a slice at the x coordinate of the northern global null, the electromagnetic power conversion $\mathbf{E} \cdot \mathbf{J}$ lies in layers of generation and dissipation within the current sheet, corresponding to layers of negative, positive, then negative E_y. (The red polygons are again the strongest patches of nonideal $E_{\parallel}$.) Figures 4.17a and 4.17b show the merging width is approximately 4 R_E at this x position—the location of the lowest latitude northern null. The value of E_y is somewhat spatially patchy, but on average is about -1.3 mV/m. The coupled electric field can be less than the solar wind electric field, because the parallel potential drop (i.e., the parallel electric field) along the field lines across the diffusion region lower the electric field. The peak value is about -2 mV/m, which is half that derived from Cluster data. Again, this order of discrepancy can be attributed to the simulation averaging spatial variations over the grid.

A reliable mapping of the sunward flows observed by DMSP will place additional observational constraints on the cross-polar cap width of the reconnection region at the magnetopause. Figure 4.18a shows a view from the sun of the Tsyganenko '04 (and GGCM) field line mappings from the edges of the reverse convection flows observed by DMSP. We include only the DMSP data from the F13 polar pass at 15:11 UT, since it is closer in time to the Cluster and simulation study time (15:00 UT) and because it takes a more direct path across the polar cap, measuring the most truly sunward flows. The white field lines in Figure 4.18 are traced from the edges of the sunward flows observed by F13 from 15:11 to 15:14 using the TS '04 model. The contoured surface is the location of the parallel electric field at 15:11 UT. All of the colored field lines lying along and between the two white field lines are GGCM field lines traced along a line that stretches between

the ends of the TS '04 field lines at a radial distance of 5 R_E. The GGCM field lines agree well with the TS '04 field lines at least up to the magnetopause, though there is some deviation at larger radii. The TS '04 model includes a term for modeling magnetic reconnection [*Tsyganenko and Sitnov*, 2005], but consistency with the best equivalent GGCM field lines supports it and any comparisons drawn between the two models. The DMSP region of sunward flows map onto tail field lines, consistent with the observation that these sunward flow measurements lie somewhat poleward of the reconnection auroral proton emission observed by IMAGE. Most of these field lines are open field lines that have reconnected in the winter (southern) hemisphere by way of the *Watanabe et al.* [2004] reclosure mechanism already discussed. The width of the region of mapped DMSP sunward flows in Figure 4.18 roughly matches the width of the GGCM dusk-to-dawn electric field sector. Since the convection is quasi-steady, we expect the potential drop of the sunward flowing tail to match the merging voltage of the southern hemisphere.

The model's potential drop across the reconnection width therefore supplies another test for consistency with the DMSP data. The first question is how well the potential drop in the ionosphere couples with a horizontal potential drop at the magnetopause. Assuming coupling is static, it can be modeled by a circuit that connects the ionosphere and magnetopause horizontal potential drops and a field-aligned potential drop on the resistive upward current leg [*Paschmann et al.*, 2003]. We can avail ourselves of Cluster's magnetopause measurements to calculate the actual coupling. Assuming static magnetopause-ionosphere coupling (i.e., $\partial\rho/\partial t + \nabla \cdot \mathbf{J} \approx \nabla \cdot \mathbf{J} = 0$)

03/18/2002 Time = 15:11:00 UT x= −4.52R$_E$
═══ Magnetopause

z [R$_E$]

y [R$_E$]

Model at CCMC: OpenGGCM
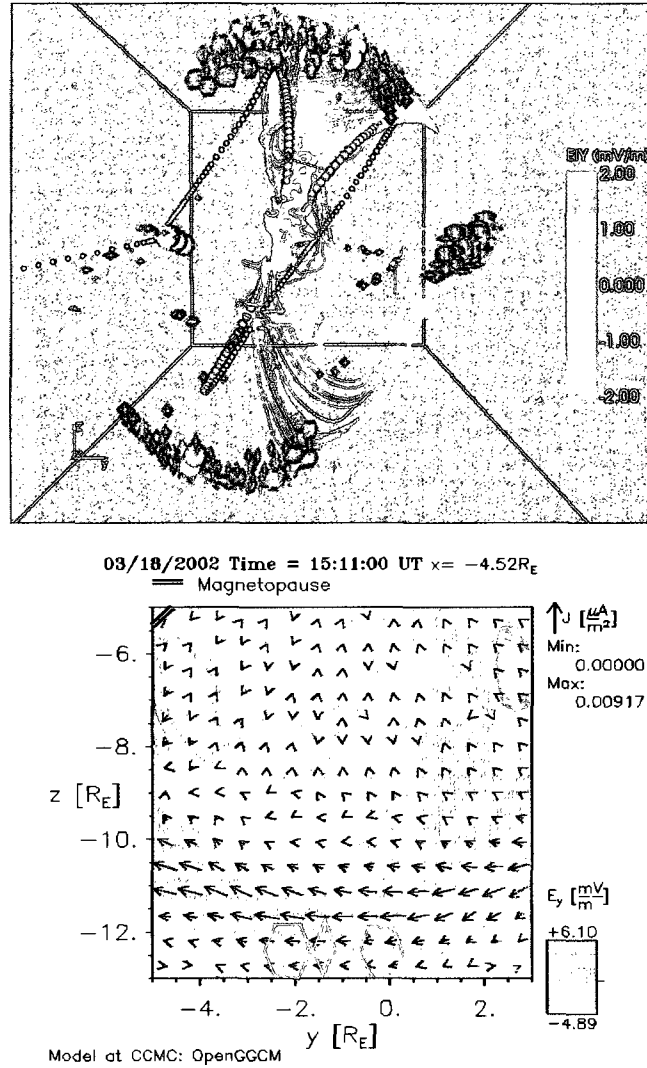
Figure 4.18 (a) Top: The DMSP TS '04 field lines traced (in white) from the edges of DMSP F13's sunward flows and the simulation's $E_{||}$ surface, in a view from the sun. All of the colored field lines lying along and between the two white field lines are GGCM field lines traced along a line that stretches between the ends of the TS '04 field lines at 5 R$_E$. Most of the field lines are open field lines that have reconnected in the southern hemisphere. **(b) Bottom:** A view from the sun of a slice of the E_y contours at the x of the southern nulls. At the southern hemisphere, the GGCM solar wind electric field couples to the magnetosphere over 2.5 R$_E$. The red polygons denote the location of the parallel electric field.

which is approximately true over coupling length scales, and applying Knight's relation and Kirchoff's law to the circuit, yields the relation

$$\Delta\varphi_{\perp\text{ion}} = \left(1 + \frac{\Sigma_p}{K}\frac{1}{l_{\perp\text{ion}}^2}\right)^{-1}\Delta\varphi_{\perp\text{mp}},\tag{4.5}$$

where Σ_p is the height-integrated Pedersen conductivity, $K = e^2 n_e/(2\pi m_e k_\text{B} T_e)^{1/2}$ is the Knight conductance, $\Delta\varphi_{\perp\text{ion}}$ the horizontal potential drop in the ionosphere, $\Delta\varphi_{\perp\text{mp}}$ the horizontal potential drop in the magnetopause, and $l_{\perp\text{ion}}$ the length of sunward flow in the ionosphere [Paschmann et al., 2003]. The Knight conductance is from the Knight relation $j_{\parallel\text{ion}} = K\Delta\varphi_\parallel$, with n_e and T_e the electron density and temperature in the magnetopause. Cluster provides measurements of the electron density and temperature ($n_e \approx 80/\text{cm}^3$ and $T_e \approx 9\times10^5$ K) at the magnetopause (GGCM provides these values as well for the fluid, not the electrons, i.e., $n \approx 50/\text{cm}^3$, and $T \approx 8\times10^6$ K, but even so these values don't differ from the Cluster values enough to make a measurable difference to the end results From the length of the F15 sunward flow path, $l_\perp \approx 860$ km, and we assume a typical value of 10 S for Σ_p. With these values, the second term in parentheses is on the order of 10^{-5}. Thus the ionosphere and magnetopause are well-coupled over this length scale and $\Delta\varphi_{\perp\text{ion}} \approx \Delta\varphi_{\perp\text{mp}}$. Figure 4.18b is a view from the sun of a slice of the GGCM E_y contours at the x of the southern nulls. The red polygons denote the location of the parallel electric field. Figure 4.18b shows that, from the spatial extent of the parallel electric field, the southern hemisphere magnetosphere couples with the solar wind electric field over about 2.5 R_E and that the coupled electric field is, as in the northern hemisphere, on average about -1.3 mV/m. The GGCM magnetopause electric field of roughly -1.3 mV/m and a coupling length of about 2.5 R_E gives a magnetopause potential drop of approximately -21 kV.
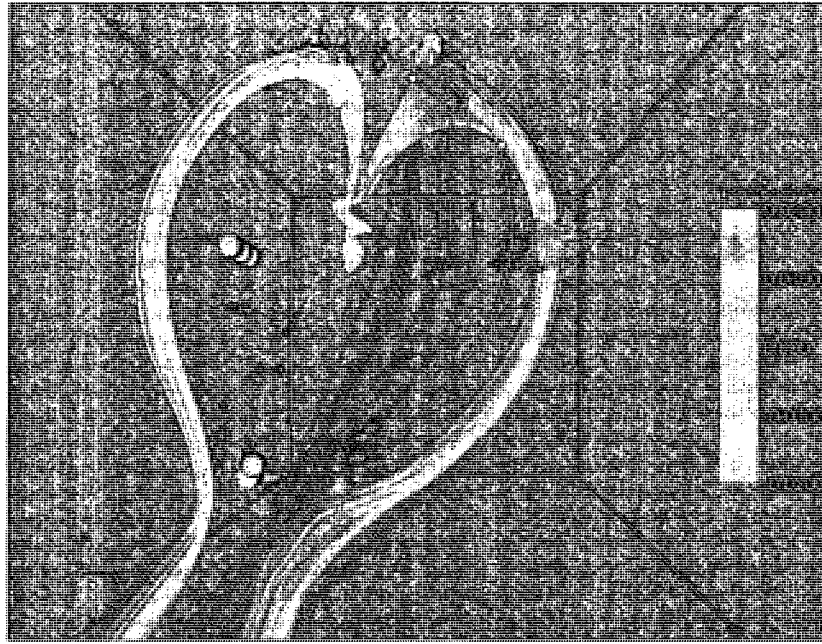
Figure 4.19. The CCMC GGCM model's FAC system into the northern polar cap, the color representing the value and sense of the FAC. The view is from the sun.

DMSP F13 measures a potential drop of about -16 kV. This order of agreement is acceptable, since the resistive MHD models typically somewhat overestimate the transpolar potential (for example, *Merkin et al.*, [2005]).

Figure 4.19, a view from the sun of the simulated magnetic fields colored by the parallel current, proves that the simulation is also consistent with the four cell electric field pattern. As predicted by models (*[Burke et al., 1979; Reiff and Burch, 1985]*), a FAC flows from the polar cap into the ionosphere on the dusk side, and upward from the polar cap on the dawn side. This completes the correspondence with the predicted and measured four-cell polar cap convection and the simulation data is consistent with the DMSP and Iridium data. These field aligned currents combined with the cusp electric field pattern prove that the global separator model couples electric fields from the solar wind to the ionosphere in a way that drives reverse convection. In Figure 4.20, a view
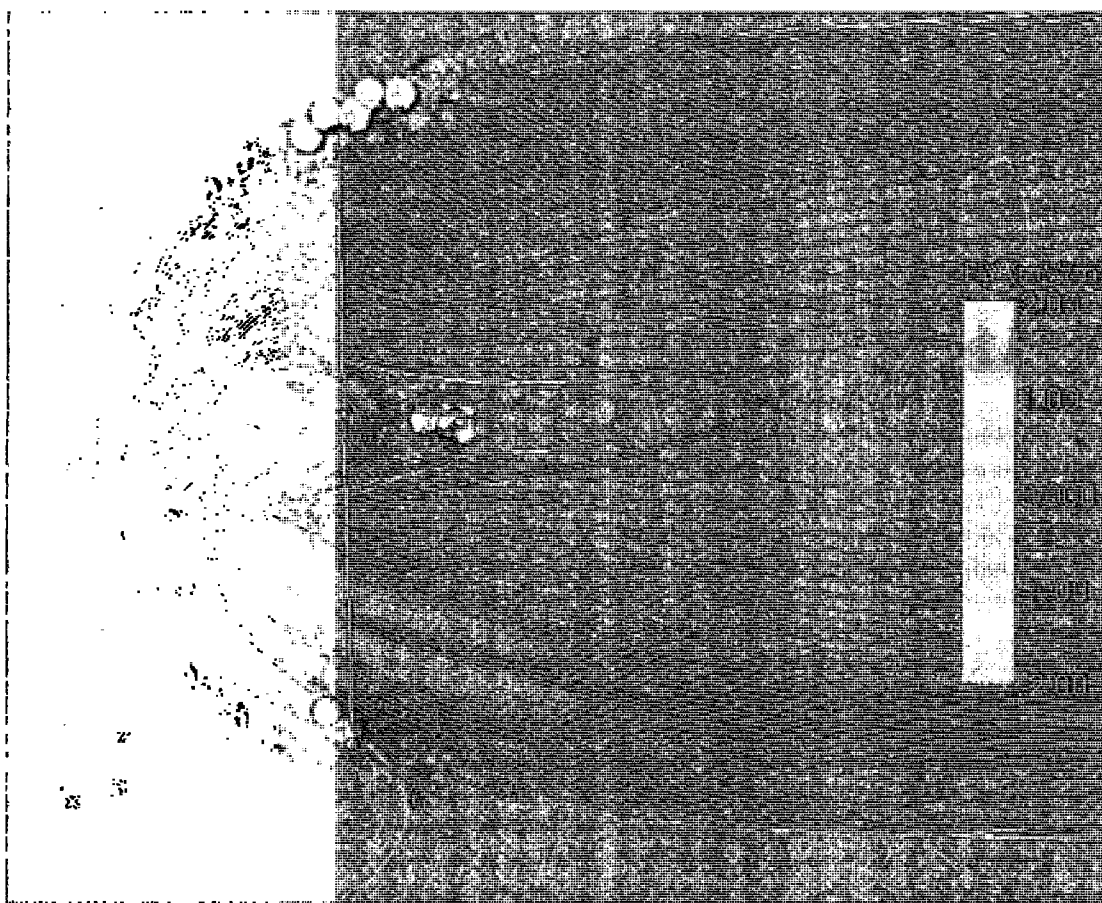
Figure 4.20 The progression of merging field lines around the polar cap. The field lines are seeded along a line connecting the nulls in both hemispheres that lies parallel to the separator line. The color of the field lines signifies the value of the cross-polar cap electric field, and thus whether flow is sunward or antisunward. Field lines that have merged in the north move equatorward, then, because of overdraping, merge in the south with closed field lines. From there field lines convect to the dusk and dawn, then toward the tail, from whence field lines move sunward to refill the polar cap flux, as evidenced by the dusk-to-dawn electric field on those field lines (blue signifies $E_y < 0$).

from dusk, we see the progression of merging field lines around the polar cap. The color of the field lines signifies the value of the cross-polar cap electric field, and thus whether flow is sunward or antisunward. Along this line of symmetry, field lines that have merged in the north move equatorward, then, because of overdraping, merge in the south. From there field lines convect to the dusk and dawn, then toward the tail, whence field lines

move sunward to refill the polar cap flux, as evidenced by the dusk-to-dawn electric field on those field lines (blue signifies $E_y < 0$) .

Chapter 5

CONCLUSIONS

In this work, we have investigated a northward IMF magnetopause reconnection event from both *in situ* and global perspectives. The simulated global and the measured local magnetic topology and parallel electric fields are consistent with one another. Our analysis also addresses whether the observed reconnection is steady-state or time dependent, antiparallel or component, and investigates the convection patterns and scale lengths of northward IMF reconnection at the magnetopause. This study also develops a collection of tools that are generally beneficial to the vetting of reconnection 'sightings' in spacecraft data. Most significantly, the reconnection field line topology and distribution of parallel electric fields observed in both the simulation and the data are characteristic of a general 3D merging topology known as singular field line reconnection. With this topology, a singular field line carrying a parallel electric field threads nearby perpendicular magnetic fields that vanish in an x-type geometry. Moverover, both local Cluster data and the global simulation reveal quasi-steady reconnection predominantly on antiparallel fields. The location of the reconnection site and the magnetospheric convection are generally steady, but time-dependent effects play a role in several ways: through waves, magnetic field line draping, and through the boundary conditions of field line tying in the ionosphere, all of which distort the shape of the reconnected field lines in the magnetopause and contribute to the singular field line topology. The Cluster analysis removes the motion of the separator to provide an

instantaneous thin current sheet of 30 km thickness embedded in a larger current sheet thickness of 130 km, and an ion diffusion region on the order of the ion Larmor radiius (up to 100 km for O^+). The reconnection electric field of -4 mV/m derived from the Cluster data agrees qualitatively with what is observed in the simulation. The electric field in the 3D reconnection topology of the simulation drives convection in the ionosphere that is consistent with ionospheric measurements. This in turn verifies earlier models of northward IMF convection based on two-dimensional antiparallel merging topologies.

In the microscale study, to summarize, we have,

- for the first time, exploited multiple spacecraft to instantaneously capture an active northward IMF, dayside x-line consistent with a singular field line topology;

- for the first time, applied a two-dimensional superposed epoch technique using multiple spacecraft to create an x-z mapping of particle and field parameters in the vicinity of an x-line;

- measured a nonideal electric field parallel to the singular field line

- captured a pattern of particle flows normal to the boundary layer near an x-line

- observed signatures consistent with a filamentary current sheet and a thin current sheet within a broader current sheet in the vicinity of the x-line.

With the Cluster satellites, we observe antiparallel reconnection with hyperbolic B_x, B_z fields, and an out-of-plane field B_y induced within the magnetopause, consistent with singular field line reconnection. An out-of-plane field B_y that exists only within the magnetopause overrides a quadrupolar signature. This is much more likely to be observed

for northward IMF and on the dayside magnetopause, which greatly complicates the merging topology. Null lines and quadrupolar magnetic fields are much more likely to be observed in the magnetotail or at the subsolar point for southward IMF reconnection. However, we have also detected signatures of a non-ideal electric field associated with a particle diffusion region, providing the final necessary and sufficient condition for reconnection in the absence of a magnetic null. Analysis of the magnetic and electric fields and the particle data infers a singular field line parallel electric field and in-plane non-ideal electric field. Measurements comparing components of the ion drift electric field to the measured electric field predict a separator electric field of -4 mV/m. A calculation from the estimated normal magnetic field component (20 nT) and an x-line length of 1 R_E also yields a reconnection electric field of about -4 mV/m. Again from the difference between ion and electron drift electric fields and the measured electric field, we also deduce a non-ideal electric field in the x-z reconnection plane of 5 to 15 mV/m. In the case of the electrons, this field consistently points away from the separator, which is consistent with the behavior of a pressure divergence electric field. The numerical simulation of this event also places Cluster adjacent to the region of a parallel electric field distributed on singular field lines. We also observe flows and a magnetic field component normal to the magnetopause.

We find, using spacecraft timing and position analysis, that the position of the separator oscillates about a steady location on the magnetopause. At one instance prior to the separator crossing, it is possible that a circular wave, surface wave, or an o-line structure sweeps past the spacecraft. A deeper analysis of this wave activity could form the basis for a subsequent study. Other than this episode, it appears that the separator

position is fairly steady. Resistance to tailward slippage at a cusp location adjacent to the magnetosheath is consistent with *Phan et al.*'s [2003] observation of a plasma depletion layer (PDL) at the same time and location. *Fuselier et al.* [2000] have found that a larger magnetic field and a lower density in a PDL produces sub-Alfvénic flow adjacent to the magnetopause, which is consistent with a relatively steady reconnection site position.

Aspects of the Cluster data imply proximity to multiple reconnection sites from a tearing mode. The magnetic oscillations may be the passage of large rotational and/or surface waves in the magnetic field. The flow pattern of the O^+ ions indicates exhaust from an adjacent sunward reconnection site, and the repeated appearance of B_x-B_z minima at various times during the magnetopause crossing probably represents the x-lines in a tearing mode structure. In support of this, the numerical simulation develops a train of x's and o's within a tearing mode along multiple nulls.

The Cluster particle moments and the electric and magnetic field data allow inferences about important length scales. The spacecraft have passed through at least the electron outflow and the ion diffusion regions, and within an ion Larmor radius of where electron agyrotropy is observed. The discrepancy between the $\mathbf{E} \times \mathbf{B}$ drift speeds and the particle perpendicular bulk speeds at the x-line indicate a breakdown of the frozen-in flux and $\mathbf{E} \cdot \mathbf{B} = 0$ assumptions and a reconnection electric field along the x-line of approximately -4 mV/m. Statistical fitting of the meso-scale magnetic field to a hyperbolic tangent yields a current sheet thickness estimate of approximately 130 km. We infer an ion diffusion region that is at least as large as roughly 270 km wide ($10d_i$) and on the order of an Oxygen Larmor radius (100 km) thick. However, it appears there may be a thinner current sheet embedded within this on the order of the proton Larmor

radius or the proton skin depth, 23 and 27 km, respectively. The off-diagonal pressure components also indicate proximity to an electron diffusion region. The pressure shear terms attain values about 25% of the diagonal pressure values near the reconnection site in the **B** field-aligned coordinate system. The non-ideal electric field estimated from comparison to electron drift fields has outward diverging values that exceed the noise floor by about 5 to 15 mV/m. However, it is not clear if the latter are significant, for these data points lie at distances greater than 100 km from the x-line.

Future data from the MMS mission will provide higher time-fidelity measurements at smaller inter-spacecraft distances, dramatically improving this kind of study. These advantages will lift many limitations imposed by the spatial and temporal resolution of the Cluster mission. Faster data rates will allow determination of more accurate electron moments and closer spacecraft distances will allow calculation of the pressure divergence and resolution of the electron diffusion region. Nevertheless, this technique is clearly applicable to many two and three-dimensional reconnection events discovered by current missions.

For the global analysis, we merge findings from the GGCM MHD simulation, from IMAGE and Cluster data, and from the DMSP and Iridium ionospheric observations. Like the IMAGE spacecraft, the DMSP and Iridium satellites observe ionospheric signatures of northward IMF reconnection on March 18, 2002. The GGCM resistive MHD simulation likewise replicates reconnection for the conditions of the event. While the Cluster flotilla observes magnetopause properties of the event, the DMSP and Iridium satellites extend the observations to the ionosphere. The GGCM global resistive

simulation encompasses the structure of the entire magnetopause, magnetosheath, and magnetosphere region, down to about 5 R_E.

The F13 and F15 DMSP satellites pass over the north pole a total of three times within just over an hour of the time of Cluster's magnetopause observation. In all passes, the satellites observe a region of sunward flows near the center of the northern polar cap, accompanied by a shear in the magnetic field at the edges of the sunward flow. The shear corresponds to a FAC flowing towards the ionosphere. The measured particle fluxes corroborate this. The Iridium spacecraft measure magnetic shears corresponding to the downward and upward current sheets and two clearly defined regions of upward and downward FAC. The pattern of FACs measured by Iridium and sunward flows measured by DMSP fit the four-cell convection pattern that *Burke et al.* [1979], *Reiff and Burch* [1985] and *Burch and Reiff* [1985] predicted for northward IMF reconnection with $B_y < B_z$.

Like many recent measurements, global MHD studies help address competing reconnection theories—specifically the relative importance of anti-parallel versus component reconnection. A null/separator analysis of the GGCM simulation with a current-dependent resistivity model reveals a pair of global nulls, one of each type in each hemisphere, connected by a global separator, as well pairs of local nulls in the northern and southern hemispheres. The three-dimensional spherical separator across the dayside overlaps part of the parallel current. In a uniform resistivity model (e.g., [*Dorelli et al.*, 2007]), the parallel current across the dayside is a proxy for the parallel electric field of nonideal MHD. For the current-dependent resistivity of the CCMC GGCM run, however, the parallel electric field lies in the cusps where the fields are antiparallel.

Where the parallel electric fields overlie the separator ribbon is where reconnection occurs. In GGCM models with uniform resistivity, the parallel electric field across the dayside demonstrates that component reconnection occurs at the subsolar point at the same time that anti-parallel merging occurs at the cusps [*Dorelli et al,* 2007]. This resolution of competing component and antiparallel merging theories confirms recent statistical data analyses by *Trattner et al.* [2004] and *Fuselier et al.* [200b] that both types of reconnection occur in different locations, depending on the magnetic shear and the solar wind compression. The dayside component merging is less obvious for the current-dependent GGCM resistivity model, though it possibly occurs on small scales.

Moreover, we have observed a distribution of singular field lines over the magnetopause that accounts for an out-of-plane component at the reconnection site, complicating a simple hyperbolic x-line geometry. Indeed, the magnetic field observed by Cluster includes a bulge along the current sheet direction within the magnetopause. The GGCM simulation spreads the field lines in just such a way over the magnetopause, so that an out-of-plane reconnection field component exists only upon the magnetopause. This structure enables reconnection upon the separatrices, not just the separator. The magnetic merging reoccurs on these field lines so long as only a portion—not necessarily the entire line—lies antiparallel to the IMF. One source of this type of distribution of singular field lines is magnetic field line draping. Another factor relates to the boundary conditions of the magnetosphere-ionosphere system. Field line-tying in the ionosphere coupled with magnetic field convection and field line draping over the magnetopause conspire to bend at least portions of the field line in the direction perpendicular to the plane of the hyperbolic kinks. This is also a time-dependent effect, for part of the field

line convects sunward, and part antisunward, changing the shape of the field line and involving a $\partial \mathbf{B}/\partial t$.

There have been a multitude of claims about what types of field lines merge in northward IMF reconnection—some proposing that it occurs on open field lines [*Maezawa*, 1976], others that it happens on closed field lines (e.g., [*Crooker*, 1985]). There is also the question as to whether it occurs only in the summer hemisphere, or in both. The simulation indicates reconnection occurs in multifarious ways in both hemispheres. On the open/IMF separatrix, IMF field lines merge with open field lines in the northern dawn. The resulting overdraped field lines convect tailward and reconnect again with the IMF field on the northern dusk side. Because of the Earth's dipole tilt, where reconnection occurs in both hemispheres, it happens first in the summer (northern) hemisphere. Field lines that reconnect in both hemispheres reconnect initially either on the separator or on the side of the northern separatrix. Along the separator at the nulls, some IMF field lines merge with closed magnetosphere field lines in the summer (northern) hemisphere, the resulting overdraped portion of which convects sunward. The overdraped field line then convects tailward over the flank and recloses on the dayside by merging with open tail lobe field lines at the winter (southern) nulls or on the open/closed separatrix. This forms a new closed and a new IMF field line. Other IMF field lines first reconnect with open field lines at the northern nulls or on the dusk side of the northern nulls. The resulting overdraped field lines convect sunward, then tailward. Subsequently they reclose in the winter hemisphere with closed tail lobe field lines on the separator or on the winter open/closed separatrix. All of the observed reconnection cycles are quasi-

steady. There is a symmetry to where these different types of field lines reconnect that follows the symmetry of the dayside current sash.

From the separatrix and separator reconnection, a cross polar cap electric field couples to the magnetosphere and thence to the ionosphere. The implication is that the component of the solar wind electric field across the width of the separator current ribbon and the separatrix plays the role that the electric field along the separator plays in 2D reconnection models. We were able to show that the simulation's cross-polar cap electric fields in the merging region and the corresponding FACs map to lower altitudes in a manner consistent with the observed ionospheric four-cell convection pattern and the Iridium data. The 4 R_E width of the coupling in the northern cusp in the GGCM model is determined by the width across which the $E_y < 0$ in the solar wind maps to the magnetosphere. The DMSP sunward flow region matches the width of sunward convecting flows in the GGCM model, and the corresponding GGCM field lines are sunward convecting tail field lines. This result is consistent with the observation that the DMSP ionospheric sunward flows lie somewhat poleward of the reconnection auroral proton emission observed on the ionosphere by IMAGE. The sunward convection occurs on tail field lines that have opened in the southern hemisphere and on overdraped tail lobe field lines on the dayside. The 2.5 R_E width and the -1.3 mV/m electric field coupled to the ionosphere from the southern hemisphere are consistent—to within known errors-- with the DMSP ionospheric sunward flow potential drop of -16 kV observed by F13.

Perhaps the most important implication of the three-dimensional global reconnection topology is that reconnection at the magnetopause does not necessarily require a null line, or even an x-line with a guide field. The topology may differ in

several ways from a simple two-dimensional hyperbolic geometry. Reconnection does not require a null—or even on a separator. So long as a parallel electric field is present along a field line perpendicular to which field components merge in an x, reconnection occurs. This means that reconnection can lie on a separatrix. The statistical likelihood of a spacecraft encounter with a reconnection diffusion region greatly intensifies. This conclusion calls to mind *Mozer et al.'s* [2005] recent assertions that spacecraft encounters with magnetopause diffusion regions are much more common than expected.

The global and local scale findings suggest a few avenues for future exploration that involve considerations of the time-dependence and spatial distribution of reconnection. One aspect of this is the type of reconnection cycle proposed by *Watanabe et al.,* [2004], in which field lines that have reconnected to open field lines and overdrape the dayside than reclose in the conjugate hemisphere onto closed tail field lines. It would be of interest to verify the boundary of the polar cap within the DMSP and Iridium data to determine if the predicted polar cap convection takes place: the resulting convection in the winter hemisphere involves a pair of cells that circulate outside the polar cap and are coupled to the cells of convection on open field lines in the summer ionosphere. Another aspect of this is the apparent wave motion observed by Cluster. Further work is required to distinguish between the signature of travelling waves and of a moving or stationary tearing mode formation. A wavevector and pressure data analysis exploiting the spacecraft multiplicity, for example, would help determine which of these was being observed. Another time-dependent feature that will affect spacecraft observations and should be considered in small-scale particle simulations of reconnection stems from the boundary condition of the ionosphere and the solar wind convection. The combination of

these factors introduces a change in shape of the magnetic flux tube that corresponds to a non-steady state. To our knowledge, these effects have not yet been included in small scale simulation studies. However, they present the inescapable reality that needs to be considered when interpreting spacecraft observations of reconnection on the magnetopause.

References

Baker, K. B. and S. Wing (1989), A new magnetic coordinate system for conjugate studies at high latitudes, *J. Geophys. Res., 94,* 9139-9143.

Balogh, A., M. W. Dunlop, S. W. H. Cowley, D. J. Southwood, J. G. Thomlinson, K. H. Glassmeier, G. Musmann, H. Lühr, S. Buchert, M. H. Acuna, D. H. Fairfield, J. A. Slavin, W. Riedler, K. Schwingenschuh, M. G. Kivelson, and the Cluster Magnetometer Team (1997), The Cluster Magnetic Field Investigation, in *The Cluster and Phoenix Missions,* edited by C. P. Escoubet, C. T. Russell, and R. Schmidt, pp. 65-92, Kluwer Academic Publishers,Dordrecht, The Netherlands.

Birn, J., J. F. Drake, M.A. Shay, B. N. Rogers, R. E. Denton, M. Hesse, M. Kuznetsova, Z. W. Ma, A. Bhattacharjee, A. Otto, and P. L. Pritchett (2001), Geospace environmental modeling (GEM) magnetic reconnection challenge, *J. Geophys. Res., 106,* 3715.

Birn, J., K. Schindler, and M. Hesse (2004), Thin electron current sheets and their relation to auroral potentials, *J. Geophys. Res., 109,* A02217.

Boozer, A. H., Reconnection and the ideal evolution of magnetic fields (2002), *Phys. Rev. Lett., 88,* 215,005.

Borg, A. L., M. Øieroset, T. D. Phan, F. S. Mozer, A. Pedersen, C.Mouikis, J. P. McFadden, C. Twitty, A. Balogh, and H. Rème (2005), Cluster encounter of a magnetic reconnection diffusion region in the near-Earth magnetotail on September 19, 2003, *Geophys. Res. Lett., 32,* L19105.

Burch, J. L., P. H. Reiff, J. D. Menietti, R. A. Heelis, W. B. Hanson, S. D. Shawhan, E. G. Shelley, M. Sugiura, D. R. Weimer, and J. D. Winningham (1985), IMF B_y-dependent plasma flow and Birkeland Currents in the Dayside Magnetosphere 1. Dynamics Explorer Observations, *J. Geophys. Res., 90,* 1577-1593.

Burke, W. J., M. C. Kelley, R. C. Sagalyn, M. Smiddy, and S. T. Lai (1979), Polar cap electric field structures with a northward interplanetary magnetic field, *Geophys. Res. Lett., 6, 21-24.*

Burlaga, L. F., and J. F. Lemaire (1978), Interplanetary magnetic holes—Theory, *J. Geophys. Res., 83,* 5157.

Chanteur, G. (1997), Spatial Interpolation for Four Spacecraft: Theory, in *Analysis Methods for Multi-Spacecraft Data,* edited by G. Paschmann and P. W. Daley, pp. 349-369, ESA Publications Division, Noordwijk.

Chanteur, G., and C. C. Harvey (1997), Spatial Interpolation for Four Spacecraft: Application to Magnetic Gradients, in *Analysis Methods for Multi-Spacecraft Data,* edited by G. Paschmann and P. W. Daley, pp. 371-393, ESA Publications Division, Noordwijk.

Cowley, S. W. H. (1973), A qualitative study of the reconnection between the earth's magnetic field and an interplanetary field of arbitrary orientation, *Radio Sci., 8,* 903–913.

Cowley, S. W. H. (1976), Comments on the merging of nonantiparallel magnetic fields, *J. Geophys. Res., 81,* 3455–3458.

Cowley, S. W. H. (1981), Magnetospheric and ionospheric flow and the interplanetary magnetic field, The Physical Basis of the Ionosphere in the Solar-Terrestrial System, AGARD Conf. Publ., AGARD-CP-295, 4/1-4/14, 1981.

Cowley, S. W. H. (1983), Interpretation of observed relations between solar wind characteristics and effects at ionospheric altitudes, in *High Latitude Space Plasma Physics,* edited by B. Hultqvist and T. Hagfors, pp. 225-249, Plenum, New York, 1983.

Craig, I. J. D., J. Heerikhuison, and P. G. Watson (2003), Hall current effects in dynamic magnetic reconnection solutions, *Phys. Plasmas,10,* 3120.

Credland, J., G. Mecke, and J. Ellwood (1997), The Cluster mission: ESA's spacefleet to the magnetosphere, in *The Cluster and Phoenix Missions,* edited by C. P. Escoubet, C. T. Russell, and R. Schmidt, pp. 33-64, Kluwer Academic Publishers, Dordrecht, The Netherlands.

Crooker, N. U. (1979), Dayside merging and cusp geometry, *J. Geophys. Res.,84,* 951–959.

Crooker, N. U. (1985), A split separator line merging model of the dayside magnetopause, *J. Geophys. Res.,90,* 12,104-12,110.

Crooker, N. U. (1986), An evolution of antiparallel merging, *Geophys. Res. Lett., 13,* 1063-1066.

Crooker, N. U. (1988), Mapping the merging potential from the magnetopause to the ionosphere through the dayside cusp, *J. Geophys. Res., 93,* 7338.

Crooker, N. U. (1992), Reverse Convection, *J. Geophys. Res., 97,* 19,363-19,372.

Crooker, N. U., J. G. Lyon, and J. A. Fedder (1998), Mhd model merging with imf by: Lobe cells, sunward polar cap convection, and overdraped lobes, *J. Geophys. Res., 103*, 9143– 9151.

Daughton, William, Jack Scudder, and Homa Karimabadi (2006), Fully knietic simulations of undriven magnetic reconnection with open boundary conditions, *Phys. Plasmas, 13*, 072101.

Dorelli, John C., Amitava Bhattacharjee, and Joachim Raeder (2007), Separator reconnection at Earth's dayside magnetopause under generic northward interplanetary magnetic field conditions, *J. Geophys. Res.,112*, A02202.

Dungey, J. W. (1961), Interplanetary magnetic field and the auroral zones, Phys. Rev. Lett., 6, 47–48.

Dungey, J. W. (1963) The structure of the exosphere, or adventures in velocity space, in Geophysics, The Earth's Environment, edited by C. DeWitt, J. Hieblot, and A. Lebeau, p. 505, Gordon and Breach, New York.

Dunlop, M. W., A. Balogh, K. –H. Glassmeier, and P. Robert (2002), Four-point Cluster application of magnetic field analysis tools: The Curlometer, *J. Geophys. Res., 107*, 1384.

Eastwood, J. P., T. –D. Phan, F. S. Mozer, M. A. Shay, M. Fujimoto, A. Retinò, M. Hesse, A. Balogh, E. A. Lucek, and I. Dandouras (2007), Multi-point observations of the Hall electromagnetic field and secondary island formation during magnetic reconnection, *J. Geophys. Res.,112,* A06235.

Engwall, E., A. I. Eriksson, M. André, I. Dandouras, G. Paschmann, J. Quinn, and K. Torkar (2006), Low-energy (order 10 eV) ion flow in the magnetotail lobes inferred from spacecraft wake observations, *Geophys. Res. Lett.*, *33*, L06110.

ESA/ESOC, Data Delivery Interface Document (2000), CL-ESC-ID-2001, Issue 3, ESA/ESOC technical report.

Fazakerley, Andrew N., Steven J. Schwartz, and Götz Paschmann (1997), Measurement of Plasma Velocity Distributions, in *Analysis Methods for Multi-Spacecraft Data*, edited by G. Paschmann and P. W. Daley, pp. 91-124, ESA Publications Division, Noordwijk.

Frey, H. U., T. D. Phan, S. A. Fuselier, and S. B. Mende (2003), Continuous magnetic reconnection at Earth's magnetopause, *Nature, 426,* 533.

Fuselier, S. A., S. M. Petrinec, and K. J. Trattner (2000a), Stability of the high-latitude reconnection site for steady northward IMF, *Geophys. Res. Lett.*, *27*, 473.

Fuselier, S. A., K. J. Trattner, and S. M. Petrinec (2000b), Cusp observations of high- and low-latitude reconnection for northward interplanetary magnetic field, *J. Geophys. Res., 105,* 255– 266.

Gosling, J. T., M. F. Thomsen, S. J. Bame, R. C. Elphic, and C. T. Russell (1990), Plasma flow reversals at the dayside magnetopause and the origin of asymmetric polar cap convection, *J. Geophys. Res., 95,* 8073– 8084.

Gosling, J. T., M. F. Thomsen, S. J. Bame, and R. C. Elphic (1991), Observations of reconnection of interplanetary and lobe magnetic field lines at the high latitude magnetopause, *J. Geophys. Res., 96,* 14,097–14,106.

Greene, J. (1992), Locating three-dimensional roots by a bisection method, *J. Comput. Phys., 98,* 194-198.

Gustafsson, G., R. Boström, B. Holback, G. Holmgren, A. Lundgren, F. S. Mozer, D. Pankow, P. Harvey, P. Berg, R. Ulrich, A. Pedersen, R. Schmidt, A. Butler, A. W. C. Fransen, D. Klinge, M. Thomsen, C. –G. Fälthammar, P. –A. Lindqvist, S. Christenson, J. Holtet, B. Lybekk, T. A. Sten, P. Tanskanen, K. Lappalainen, J. Wygant, The Electric Field and Wave Experiment for the Cluster mission, in *The Cluster and Phoenix Missions,* edited by C. P. Escoubet, C. T. Russell, and R. Schmidt, pp. 137-156, Kluwer Academic Publishers,Dordrecht, The Netherlands.

Harvey, C. C. (1997), Spatial Gradients and the Volumetric Tensor, in *Analysis Methods for Multi-Spacecraft Data,* edited by G. Paschmann and P. W. Daley, pp. 307-322, ESA Publications Division, Noordwijk.

Hausman, B. A., F. C. Michel, J. R. Espley, and P. A. Cloutier (2004), On determining the nature and orientation of magnetic directional discontinuities: Problems with the minimum variance method, *J. Geophys. Res.,109,* A11102.

Heppner, J. P. and N. C. Maynard (1987), Empirical high-latitude electric field models, *J. Geophys. Res., 92,* 4467-4489.

Hesse, M., and K. Schindler (1988), A theoretical foundation of general magnetic reconnection, *J. Geophys. Res., 93,* 5559– 5567.

Hesse, Michael, Karl Schindler, Joachim Birn, and Masha Kuznetsova (1999), The diffusion region in collisionless magnetic reconnection, *Phys. Plasmas, 6,* 1781.

Hesse, M., J. Birn, and M. Kuznetsova (2001), Collisionless magnetic reconnection: Electron processes and transport modeling, *J. Geophys. Res., 106,* 3721.

Hesse, Michael, Masha Kuznetsova, and Joachim Birn (2004), The role of electron heat flux in guide-field magnetic reconnection, *Phys. Plasmas, 11,* 5387.

Hill, T. W., Theoretical models of polar-cap convection under the influenceof a northward interplanetary magnetic field (1992), *J. Atmos. Terr. Phys.,* 56, 185-194.

Hultquist, B. and G. Gustafsson (1960), On the magnetic time dependence of auroral zone currents, *J. Atmos. Terr. Phys.,* 19, 246.

Johnstone, A. D., C. Alsop, S. Burge, P. J. Carter, A. J. Coates, A. J. Coker, A. N. Fazakerley, M. Grande, R. A. Gowen, C. Gurgiolo, B. K. Hancock, B. Narheim, A. Preece, P. H. Sheather, J. D. Winningham, R. D. Woodliffe (1997), PEACE: A Plasma and Electron Current Experiment, in *The Cluster and Phoenix Missions,* edited by C. P. Escoubet, C. T. Russell, and R. Schmidt, pp. 351-398, Kluwer Academic Publishers,Dordrecht, The Netherlands.

Kan, J. R. and W. J. Burke (1985), A theoretical model of polar cap auroral arcs, *J. Geophys. Res., 90,* 4171-4177.

Karimabadi, H. (2005), Antiparallel versus component merging at the magnetopause: Current bifurcation and intermittent reconnection, *J. Geophys. Res., 110,* A03213.

Kessel, R. L., S.-H. Chen, J. L. Green, S. F. Fung, S. A. Boardsen, L. C.Tan, T. E. Eastman, J. D. Craven, and L. A. Frank (1996), Evidence for high-latitude

reconnection during northward imf: Hawkeye observations, *Geophys. Res. Lett.*, *23*, 583–586.

Khrabrov, A. V. and Bengt U. Ö. Sonnerup (1998), DeHoffmann-Teller Analysis, in *Analysis Methods for Multi-Spacecraft Data*, edited by G. Paschmann and P. W. Daley, pp. 221-248, ESA Publications Division, Noordwijk.

Kronecker, L. (1869), Ueber systeme von funktionen mehrerer variabeln, *Monatsber. Berlin Akad.*, 159-193, 688-698.

Laitinen, T. V., P. Janhunen, T. I. Pulkkinen, M. Palmroth, H. E. J. Koskinen (2006), On the characterization of magnetic reconnection in global MHD simulations, *Ann. Geophys.*, *24*, 3059-3069.

Landau, L. D., and E. M. Lifshitz (1960), *Electrodynamics of Continuous Media*, Addison-Wesley Publishing, Reading, Mass..

Lavraud, B., M. F. Thomsen, M. G. G. T. Taylor, Y. L. Wang, T. D. Phan, S. J. Schwartz, R. C. Elphic, A. Fazakerley, H. Rème, A. Balogh (2005), Characteristics of the magnetosheath electron boundary layer under northward interplanetary magnetic field: Implications for high-latitude reconnection, *J. Geophys. Res.*, *110*, A06209.

Longcope, D. W., and I. Klapper (2002), A general theory of connectivity and current sheets in coronal magnetic fields anchored to discrete sources, *Astrophys. J.* 579, 468-481.

Maezawa, K. (1976), Magnetospheric convection induced by the positive and negative Z components of the interplanetary magnetic field - Quantitative analysis using polar cap magnetic records, *J. Geophys. Res., 81*, 2289-2303.

Mende, S. B., H. U. Frey, T. J. Immel, J. –C. Gérard, B. Hubert, S. Habraken, J. Spann, G. R. Gladstone, D. V. Bisikalo, and V. I. Shematovich (2003), Summary of Quantitative Interpretation of Image Far Ultraviolet Auroral Data, in *Magnetoshpheric Imaging: The IMAGE Prime Mission,* edited by J. L. Burch, pp. 211-254, Kluwer Academic Publishers, Dordrecht, The Netherlands.

Merkin, V. G., G. Milikh, K. Papadopoulos, J. Lyon, Y. S. Dimant, A. S. Sharma, C. Goodrich, and M. Wiltberger (2005), Effect of anomalous electron heating on the transpolar potential in the LFM global MHD model, *Geophys. Res. Lett., 32*, L22101.

Mozer, F. S., S. D. Bale, and T.D. Phan (2002), Evidence of diffusion regions at a subsolar magnetopause crossing, *Phys. Rev. Lett., 89*, 1.

Mozer, F. S., S. D. Bale, J. P. McFadden, and R. B. Torbert (2005), New features of electron diffusion regions observed at subsolar magnetic field reconnection sites, *Geophys. Res. Lett., 32*, L24102.

Onsager, T. G., and S. A. Fuselier (1994), The location of magnetic reconnection for northward and southward interplanetary magnetic field, in *Solar System Plasmas in Space and Time, Geophys. Monogr. Ser.*, vol. 84, edited by J. L. Burch and J. H. Waite Jr., p. 183, AGU, Washington, D. C.

Onsager, T. G., J. D. Scudder, M. Lockwood, and C. T. Russell (2001), Reconnection at the high-latitude magnetopause during northward interplanetary magnetic field conditions, *J. Geophys. Res.*, *106*, 25,467.

Paschmann, G., W. Baumjohann, N. Sckopke, T.-D. Phan, and H. Lühr (1993), Structure of the dayside magnetopause for low magnetic shear, *J. Geophys. Res.*, *98*, 13,409.

Paschmann, G., A. N. Fazakerley, and S. J. Schwartz (1997), Moments of Plasma Velocity Distributions, in *Analysis Methods for Multi-Spacecraft Data*, edited by G. Paschmann and P. W. Daley, pp. 371-393, ESA Publications Division, Noordwijk.

Paschmann, G., S. Haaland, and R. Treumann (eds) (2003), *Auroral Plasma Physics*, Kluwer Academic Publishers, Dordrecht, The Netherlands.

Phan, T. D., H. U. Frey, S. Frey, L. Peticolas, S. Fuselier, C. Carlson, H. Rème, J. –M. Bosqued, A. Balogh, M. Dunlop, L. Kistler, C. Mouikis, I. Dandouras, J. –A. Sauvaud, S. Mende, J. McFadden, G. Parks, E. Moebius, B. Klecker, G. Paschmann, M. Fujimoto, S. Petrinec, M. F. Marcucci, A. Korth, and R. Lundin (2003), Simultaneous Cluster and IMAGE observations of cusp reconnection and auroral proton spot for northward IMF, *Geophys. Res. Lett.*, *30*, 1509.

Phan T. D., H. Hasegawa, M. Fujimoto, M. Oieroset, T. Mukai, R. P. Lin, W. R. Paterson (2006), Simultaneous Geotail and Wind observations of reconnection at the subsolar and tail flank magnetopause, *Geophys. Res. Lett.*, *33*, L09104.

Pitout, F. J. –M. Bosqued, D. Alcaydé, W. F. Denig, H. Rème, Observations of the cusp region during northward IMF (2001), *Ann. Geophys., 19,* 1641.

Pontin, D. I., and A. Bhattacharjee (2007), Current sheet formation and nonideal behavior at three-dimensional magnetic null points, *Phys. Plasmas,14,* 052106.

Potemra, T. A., L. J. Zanetti, P. F. Bythrow, and A. T. Y. Lui (1984), B_y-Dependent convection patterns during northward interplanetary magnetic field. *J. Geophys. Res.,89,* 9753-9760.

Priest, E. R. and T. G. Forbes (1989), Steady magnetic reconnection in three dimensions, *Solar Phys. 119,* 211-214.

Priest, E. R. and T. G. Forbes (2000), *Magnetic Reconnection: MHD Theory and Applications,* Cambridge University Press, Cambridge.

Priest, E. R., G. Hornig, and D. I. Pontin (2003), On the nature of three-dimensional magnetic reconnection, *J. Geophys. Res.,* 108, A7, SSH6-1-8.

Pritchett, P. L. (2001), Geospace Environment Modeling magnetic reconnection challenge: Simulations with a full particle electromagnetic code, *J. Geophys. Res., 106,* 3783.

Quest, K. B., and F. V. Coroniti (1981), Tearing at the dayside magnetopause, *J. Geophys. Res., 86,* 3289– 3298.

Raeder, J., J. Berchem, and M. Ahsour-Abdalla (1996), The importance of small scale processes in MHD simulations: Some numerical experiments, in *The Physics of Space Plasmas,* edited by T. Chang and J. R. Jasperse, v. 14, p. 403, MIT Cent. for Theoret. Geo/Cosmo Plasma Phys., Cambridge, Mass.

Raeder, J., J. Berchem, and M. Ashour-Abdalla (1998), The geospace environment grand challenge: Results from a global geospace circulation model, *J. Geophys. Res*, *103*, 14787.

Raeder, J. (2001), Global simulation of the geospace environment modeling substorm challenge event, *J. Geophys. Res., 106*, 381.

Raeder, J. (2003), Global geospace modeling: Tutorial and review, in: *Space Plasma Simulation, Lecture Notes in Physics, vol. 615*, Springer Verlag, Heidelberg.

Reiff, P. H., and J. L. Burch (1985), IMF B_y-dependent plasma flow and birkeland currents in the dayside magnetosphere 2. Global model for northward and southward IMF, *J. Geophys. Res., 90*, 1595.

Rème, H., J. M. Bosqued, J. A. Sauvaud, A. Cros, J. Dandouras, C. Aoustin, J. Bouyssou, Th. Camus, J. Cuvilo, C. Martz, J. L. Médale, H. Perrier, D. Romefort, J. Rouzaud, C. d'Uston, E. Möbius, K. Crocker, M. Granoff, L. M. Kistler, M. Popecki, C. W. Carlson, D. W. Curtis, R. P. Lin, J. P. McFadden, V. Formisano, E. Amata, M. B. Bavassano-Cattaneo, P. Baldetti, G. Belluci, R. Bruno, G. Chionchio, A. di Lellis, E. G. Shelley, A. G. Ghielmetti, W. Lennartsson, A. Korth, H. Rosenbauer, R. Lundin, S. Olsen, G. K. Parks, M. McCarthy, and H. Balsiger (1997), The Cluster Ion Spectrometry (CIS) Experiment, in *The Cluster and Phoenix Missions,* edited by C. P. Escoubet, C. T. Russell, and R. Schmidt, pp. 303-350, Kluwer Academic Publishers,Dordrecht, The Netherlands.

Ricci, Paulo, J. U. Brackbill, W. Daughton, and Giovanni Lapenta (2004), Collisionless magnetic reconnection in the presence of a guide field, , *Phys. Plasmas, 11*, 4102.

Robert, P., M. W. Dunlop, A. Roux, and G. Chanteur, Accuracy of Current Density Determination (1998), in *Analysis Methods for Multi-Spacecraft Data*, edited by G. Paschmann and P. W. Daley, pp. 395-418, ESA Publications Division, Noordwijk.

Robert, P., A. Roux, C. Harvey, M. W. Dunlop, P. W. Daley, and K.-H. Glassmeier (1998), Tetrahedron Geometric Factors, in *Analysis Methods for Multi-Spacecraft Data*, edited by G. Paschmann and P. W. Daley, pp. 323-348, ESA Publications Division, Noordwijk, p. 323.

Rogers, B. N., R. E. Denton, and J. F. Drake (2003), Signatures of collisionless magnetic reconnection, *J. Geophys. Res.,108,* 1111.

Runov, A., V. A. Sergeev, R. Nakamura, W. Baumjohann, S. Apatenkov, Y. Asano, T. Takada, M. Volwerk, Z. Vörös, T. L. Zhang, J.-A. Sauvaud, H. Rème, and A. Balogh (2006), Local structure of the magnetotail current sheet: 2001 Cluster observations, *Ann. Geophys., 24,* 247.

Runov, A., R. Nakamura, W. Baumjohann, R. A. Treumann, T. L. Zhang, M. Volwerk, Z. Vörös, A. Balogh, K.-H. Glaßmeier, B. Klecker, H. Rème, and L. Kistler (2003), Current sheet structure near magnetic x-line observed by Cluster, *Geophys. Res. Lett., 30,* 1579.

Russell, C. T. (1972), The configuration of the magnetosphere, in *Critical Problems of Magnetospheric Physics,* edited by E. R. Dyer, p. 1-16, IUCSTP Secretariat, Washington D. C..

Russell, C. T., J. Fedder, S. Slinker, X.-W. Zhou, G. Le, J. Luhmann, F. Fenrich, M. Chandler, T. Moore, and S. Fuselier (1998), Entry of the polar spacecraft into the polar cusp under northward imf conditions, *Geophys. Res. Lett., 25,* 3015–3018.

Russell, C. T. (2008), http://www-ssc.igpp.ucla.edu/personnel/russell/ESS265/Ch6.

Schindler, K., and M. Hesse (1988), General magnetic reconnection, parallel electric fields, and helicity, *J. Geophys. Res., 93,* 5547– 5557.

Scudder, J.D., F. S. Mozer, N.C. Maynard, and C. T. Russell (2002), Fingerprints of collisionless reconnection at the separator, I, Ambipolar-Hall signatures, *J. Geophys. Res., 107,* 1294.

Shay, M. A. (1998), The dynamics of collisionless magnetic reconnection, PhD thesis, University of Maryland at College Park, College Park, MD.

Shay, M. A., J. F. Drake, and B. N. Rogers (1999), The scaling of collisionless, magnetic reconnection for large systems, *Geophys. Res. Lett., 26,* 2163.

Singh, N. C. Deverapalli, and G. Khazanov (2006), Electrodynamics in a very thin current sheet leading to magnetic reconnection, *Nonlinear Processes in Geophys., 13,* 509.

Siscoe, G. L., G. M. Erickson, B. U. O. Sonnerup, N. C. Maynard, K. D. Siebert, D. R. Weimer, and W. W. White (2001), Global role of $e_\parallel$ in magnetopause reconnection: An explicit demonstration, *J. Geophys. Res., 106,* 13,015– 13,022.

Sitnov, M. I., P. N. Guzdar, and M. Swisdak (2003), A model of the bifurcated current sheet, *Geophys. Res. Lett., 30,* 1712.

Song, P., D. L. DeZeeuw, T. I. Gombosi, C. P. T. Groth (1999), A numerical study of solar wind-magnetosphere interaction for northward interplanetary magnetic field, *J. Geophys. Res.*, *104*, 28,361.

Song, Y. and R. L. Lysak (2006), Displacement current and the generation of parallel electric fields, *Phys. Rev. Lett.,96*, 145002.

Sonnerup, B. U. O. and L. J. Cahill (1968), Explorer 12 Observations of the Magnetopause Current Layer, *J. Geophys. Res., 73*, 1757.

Sonnerup, B. U. O. (1974), The magnetopause reconnection rate, *J. Geophys. Res., 79*, 1546–1549.

Sonnerup, B. U. Ö. and M. Scheible (1998), Minimum and Maximum Variance Analysis, in *Analysis Methods for Multi-Spacecraft Data*, edited by G. Paschmann and P. W. Daley, pp. 185-220, ESA Publications Division, Noordwijk.

Swisdak, M., B. N. Rogers, J. F. Drake, and M. A. Shay (2003), Diamagnetic suppression of component magnetic reconnection at the magnetopause, *J. Geophys. Res., 108(A5)*, 1218.

Trattner, K. J., S. A. Fuselier, and S. M. Fuselier (2004), Location of the reconnection line for northward interplanetary magnetic field, *J. Geophys. Res.*, 109, A03219.

Trattner, K.J., S. M. Petrinec, W. K. Peterson, S. A. Fuselier, and H. Rème (2006), Tracing the location of the reconnection site from the northern and southern cusps, *J. Geophys. Res.,111*, A11211.

Trattner K. J., J. S. Mulcock, S. M. Petrinec, S. A. Fuselier (2007), Probing the boundary between antiparallel and component reconnection during southward interplanetary magnetic field conditions, *J. Geophys. Res., 112*, A08210.

Tsyganenko, N. A. (1995), Modeling the Earth's magnetospheric magnetic field confined within a realistic magnetopause, *J. Geophys. Res., 100*, 5599-5612.

Tsyganenko, N. A. (1996), Effects of the solar wind conditions on the global magnetospheric configuration as deduced from data-based field models, *Proc. Third Internat. Conf. on Substorms (ICS-3)*, ESA SP-389.

Tsyganenko, N. A. and M. I. Sitnov (2005), Modeling the dynamics of the inner magnetosphere during strong geomagnetic storms. *J. Geophys. Res., 110*.

Vaivads, A. Y. Khotyaintsev, M. André, A. Retinò, S. C. Buchert, B. N. Rogers, P.Décréau, G. Paschmann, T. D. Phan (2004), Structure of the magnetic reconnection diffusion region from four-spacecraft observations, *Phys. Rev. Lett., 93*.

Van Zandt, T. E. W. L. Clark, and J. M. Warnock (1972), Magnetic Apex Coordiantes: A magnetic coordinate system for the ionospheric F_2 layer, *J. Geophys. Res., 77*, 2406-2411.

Vasyliunas, V. M. (1975), Theoretical models of magnetic field line merging, 1, *Rev. Geophys. and Space Phys., 13*, 303.

Vasyliunas, V. M. (1988), Electrodynamics of the ionosphere/magnetosphere/solar wind system at high latitudes, in *Proc. NATO Adv. Studies Inst.*, Lillehammer.

Vontrac-Reberac, A., J. M. Bosqued, M. G. G. T. Taylor, B. Lavraud, D. Fontaine, M. W. Dunlop, H. Laakso, N. Cornilleau-Werhlin, P. Canu, and A. Fazakerley (2003), Cluster observations of the high-altitude cusp for northward interplanetary field: A case study, *J. Geophys. Res., 108,* 1346.

Watanabe, M., K. Kabin, G. J. Sofko, R. Rankin, T. I. Gombosi, A. J. Ridley, C. R. Clauer (2005), Internal reconnection for northward interplanetary magnetic field, *J. Geophys. Res.,110,* A06210.

Watanabe, M., George J. Sofko, and Dieter A. André (2004), Polar cap bifurcation during stead-state northward interplanetary magnetic field with $|B_y| \sim B_z$, *J. Geophys. Res.,109,* A01215.

Wiegelmann, T. and J. Buchner (2001), Evolution of magnetic helicity in the course of kinetic magnetic reconnection, *Nonlinear Processes in Geophys. ,8,* 127.

Wygant, J.R., C. A. Catell, R. Lysak, Y. Song, J. Dombeck, J. McFadden, F. S. Mozer, C. W. Carlson, G. Parks, E. A. Lucek, A. Balogh, M. Andre, H. Reme, M. Hesse, and C. Mouikis (2005), Cluster observations of an intense normal component of the electric field at a thin reconnection current sheet in the tail and its role in the shock-like acceleration of the ion fluid into the separatrix region, *J. Geophys. Res.,110,* A09206.

Xie, H., and Y. Lin (2000), Two-dimensional hybrid simulation of the dayside reconnection layer and associated ion transport, *J. Geophys. Res, 105,* 25,171.

Yin, L. D. Winske, S. P. Gary, and J. Birn (2001), Hybrid and Hall-MHD simulations of

collisionless reconnection: Dynamics of the electron pressure tensor, *J. Geophys.*

Res., 106, 10,761.

Appendix

A.1 The deHoffmann-Teller frame and the Walén Relation

If the electric field measured in the instrument frame is **E**, then the deHoffmann-Teller (HT) frame, assuming such a frame exists, is defined as the frame in which

$$\mathbf{E}' = \mathbf{E} + \mathbf{v} \times \mathbf{B} = 0, \qquad\qquad \text{(A.1)}$$

where **v** is the plasma bulk velocity. Faraday's law in the HT frame then gives $\nabla \times \mathbf{E}' = -(\partial \mathbf{B}/\partial t)' = 0$. The existence of the HT frame therefore implies that the magnetic field in the bulk plasma frame is time-stationary. (The converse is not necessarily true: there are time-independent structures for which no reference frame with $\mathbf{E}' \equiv 0$ exists.)

The Walén test invokes the relationship between the plasma velocities in the HT frame and the local Alfvén speed [*Khrabov et al.*, 1998]. The slope of these two quantities plotted against one another over a data interval reveals how the particle speeds in the HT frame scale with the Alfvén speed. With the Alfvén speed along the horizontal axis, a rotational discontinuity associated with a shock or reconnection will yield a slope in the range of 0.8 to 1.0 If the slope is smaller than this, however, the data fails the Walén test in that the particles are generally moving at speeds well enough below the Alfvén speed that the magnetic and velocity structure is inconsistent with a rotational discontinuity. Such a boundary layer would be typical of a tangential discontinuity. One source that discusses the experimental determination of the HT frame and the Walén test is *Khrabrov et al.* [1998].

A.2 Minimum Variance Analysis

The Minimum Variance Analysis (MVA) is a method to determine the normal direction to a magnetic discontinuity from a least squares minimization. The normal **n** is found from minimizing

$$\sigma^2 = \frac{1}{M} \sum_{m=1}^{M} |(\mathbf{B}^m - \langle \mathbf{B} \rangle) \cdot \mathbf{n}|^2 \tag{A.2}$$

where m is the measurement and M the total number of measurements. Minimization leads to an eigenvalue equation

$$\mathbf{M} \cdot \mathbf{n} = \lambda \mathbf{n} \tag{A.3}$$

where $M_{\mu\nu} = \langle B_\mu B_\nu \rangle - \langle B_\mu \rangle \langle B_\nu \rangle$ and the eigenvalues correspond to the directions of minimum, intermediate, and maximum variance of **B** across the discontinuity,

To test the validity of the MVA, we first perform standard error analysis on the results. The standard methods are demonstrated by *Sonnerup and Scheible* [1998], culminating in their equation 8.23, and involve the number of data points and the three eigenvalues. The resulting errors $|\Delta\varphi_{ij}| = |\Delta\varphi_{ji}|$ represent the angle by which eigenvector *j* deviates toward or away from eigenvector *i*. To test the stability of the MVA over time, we also apply the MVA to averages over a range of time interval sizes in the magnetopause. Specifically, for a magnetopause crossing of 16139 data points, we average over $Q = 1, 2, 4, \ldots, 2^k$ sequential data points, where we take *k* up to 10. Setting *k* = 10 corresponds to averaging over the longest period variation observed in the data. We
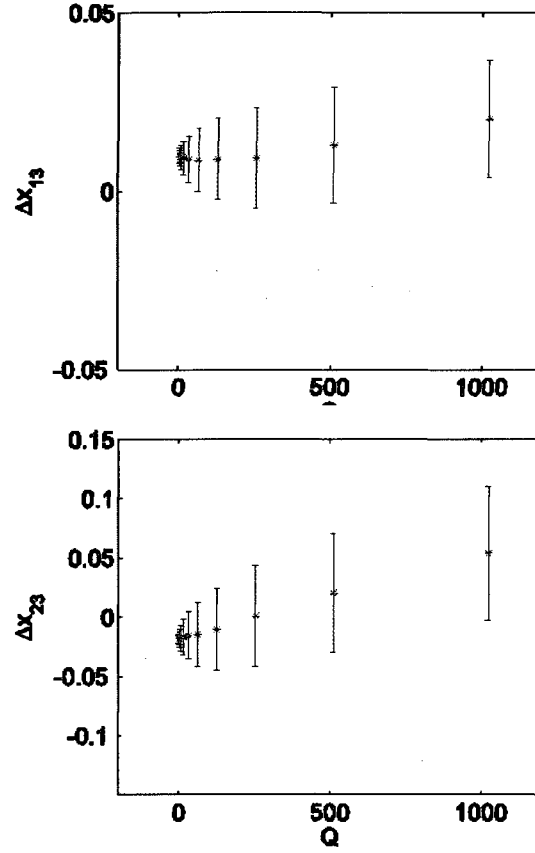
Figure A1a - A1b. (a) Top: The x and **(b) Bottom:** the y component of the normal vector as a function of the averaging length Q. The error bars in the upper and lower panels are the values of the angular deviations of the normal eigenvector toward the direction of the other two eigenvectors. The error bars $\Delta\varphi_{13}$ and $\Delta\varphi_{23}$, shown in radians, are also a function of Q.

then apply the MVA to the resulting 11 data sets of length $16139/2^k$. The scatter in the answers gives a measure of robustness of the results. In Figures A1a and A1b, we plot the deviations into the x and y directions (upper and lower panels respectively) of the normal vector x_3 as a function of Q. The error bars in the upper and lower panels are the values of $\pm\Delta\varphi_{13}$ and $\pm\Delta\varphi_{23}$, respectively. The error bars $\Delta\varphi_{13}$ and $\Delta\varphi_{23}$, shown in radians, are also a function of Q. The results have small component values (less than 0.05) perpendicular to the normal, for all Q, and demonstrate sturdiness over data length and

over averages up to the length of the slowest variations. The error bars are contained within $\Delta\varphi_{13} \cong \pm 0.02$, and $\Delta\varphi_{23} \cong \pm 0.07$. Furthermore, the eigenvalues are not degenerate. For $k=10$, for example, the eigenvalue in the x direction is 9305, in the y direction it is 850, and in the z direction, 32.

A.3 Linear Least Squares Estimates and the Curlometer Method

The four Cluster spacecraft provide a grid on which to estimate spatial gradients with scale lengths greater than the inter-spacecraft spacing. The algorithm is a linear least squares fit using the measurements and positions of all four spacecraft. The gradient of a scalar, i.e.,

$$k_l = \frac{\partial x}{\partial r_l}, \tag{A.4}$$

where r_l is the l-th spacecraft's position relative to the mesocenter, defined by

$$\sum_{\alpha=1}^{N} r_\alpha = 0 \tag{A.5}$$

can be estimated by minimizing

$$S = \sum_{\alpha=1}^{N} \sum_{\beta=1}^{N} [k \cdot (r_\alpha - r_\beta) - (x_\alpha - x_\beta)]^2. \tag{A.6}$$

To find the spatial gradients of a vector, i.e.,

$$x_{nl} = \frac{\partial x_n}{\partial r_l}, \tag{A.7}$$

for N spacecraft. The quantity to be minimized is

$$S = \sum_{n=1}^{3} \sum_{\alpha=1}^{N} \sum_{\beta=1}^{N} [x_{nm}(r_{\alpha m} - r_{\beta m}) - (x_{\alpha n} - x_{\beta n})]^2. \tag{A.8}$$

Differentiating and setting this to zero gives

$$x_{nl} = \frac{1}{N^2} [\sum_{\alpha \neq \beta} (x_{\alpha n} - x_{\beta n})(r_{\alpha k} - r_{\beta k})] R_{kl}^{-1} \tag{A.9}$$

where

$$R_{jk} = \frac{1}{N} \sum_{\alpha=1}^{N} r_{\alpha j} r_{\alpha k}. \tag{A.10}$$

This expression can be improved for a solenoidal vector, such as the magnetic field, by including a Lagrange multiplier to constrain the derivatives to $\nabla \cdot \mathbf{B} = 0$:

$$x_{nl} - \lambda R_{nl}^{-1} = \frac{1}{N^2} [\sum_{\alpha \neq \beta}(x_{\alpha n} - x_{\beta n})(r_{\alpha k} - r_{\beta k}) - \lambda \delta_{nk}] R_{kl}^{-1}, \tag{A.11}$$

where the Lagrange multiplier λ is defined by

$$\lambda = \frac{\sum_n x_{nn}}{\sum_n R_{nn}^{-1}}. \tag{A.12}$$

When the magnetic field spatial derivatives are used to calculate the current, the technique is referred to as the *curlometer method* [*Harvey*, 1998].

It is possible to extend this method to an approximate quadratic least squares estimate by interpolating between the spacecraft positions. This is done by using the spacecraft velocity to estimate a point midway along each axis separating any two spacecraft. Measurements at these 'points' provides the six more independent measurements required for a quadratic estimate [*Chanteur*, 1998].

The quadratic estimator of a spatial gradient requires reciprocal vectors. Reciprocal vectors $\mathbf{k}_1, \ldots \mathbf{k}_4$ are defined from

$$\mathbf{k}_4 = \mathbf{r}_{12} \times \mathbf{r}_{13} / \mathbf{r}_{14} \cdot (\mathbf{r}_{12} \times \mathbf{r}_{13}), \tag{A.13}$$

where $\mathbf{r}_{\alpha\beta} = \mathbf{r}_\alpha - \mathbf{r}_\beta$, $\mathbf{r}_\alpha$ and $\mathbf{r}_\beta$ are the positions of spacecrafts α and β, respectively. The reciprocal vector $\mathbf{k}_\alpha$ is normal to the face of the tetrahedron that lies opposite to spacecraft α and is proportional to the area of that tetrahedral face and inversely proportional to the volume of the tetrahedron [*Chanteur*, 1998]. The quadratic estimate of a spatial gradient of a vector $\mathbf{v}$ in terms of reciprocal vectors is found from

$$L_2[\mathbf{v}] = \sum_{\alpha=1}^{4}\sum_{\beta>\alpha}(\mathbf{k}_\alpha + \mathbf{k}_\beta)\mathbf{v}_{\alpha\beta}^{T} \qquad \textbf{(A.14)}$$

where $\mathbf{v}_{\alpha\beta}$ is the measurement of $\mathbf{v}$ at the midpoint between the two spacecraft denoted by α and β.

One could estimate the midpoint samples at the expense of time resolution by averaging measurements from nearest vertical neighbors on the Cluster tetrahedron at supplementary positions. But since that results in midpoint and vertical samples from different times, it is necessary to average this mean value over Cluster measurements at two different positions of the tetrahedron, one retarded and the other advanced with respect to the central position. Because one tetrahedron position yields two independent midpoint samples on opposite edges of the tetrahedron, three pairs of retarded/advanced measurements suffice to estimate the six midpoint samples, as from the following scheme:

$$\mathbf{v}_{23}(t) = 1/4(\mathbf{v}_2(t - 2dt) + \mathbf{v}_3(t - 2dt) + \mathbf{v}_2(t + 2dt) + \mathbf{v}_3(t + 2dt))$$

$$\mathbf{v}_{14}(t) = 1/4(\mathbf{v}_1(t - 2dt) + \mathbf{v}_4(t - 2dt) + \mathbf{v}_1(t + 2dt) + \mathbf{v}_4(t + 2dt)). \qquad \textbf{(A.15)}$$

The time interval dt should be both small enough to preserve accuracy and large enough to guarantee independence of successive filtered data samples [*Chanteur*, 1998].

The x-line is a region where we expect a significant current density $J_y < 0$, $\partial B_z/\partial x < 0$ (but $> \partial B_x/\partial z$ to guarantee $J_y < 0$), $\partial B_x/\partial z < 0$, a minimum or near-minimum in B_x and
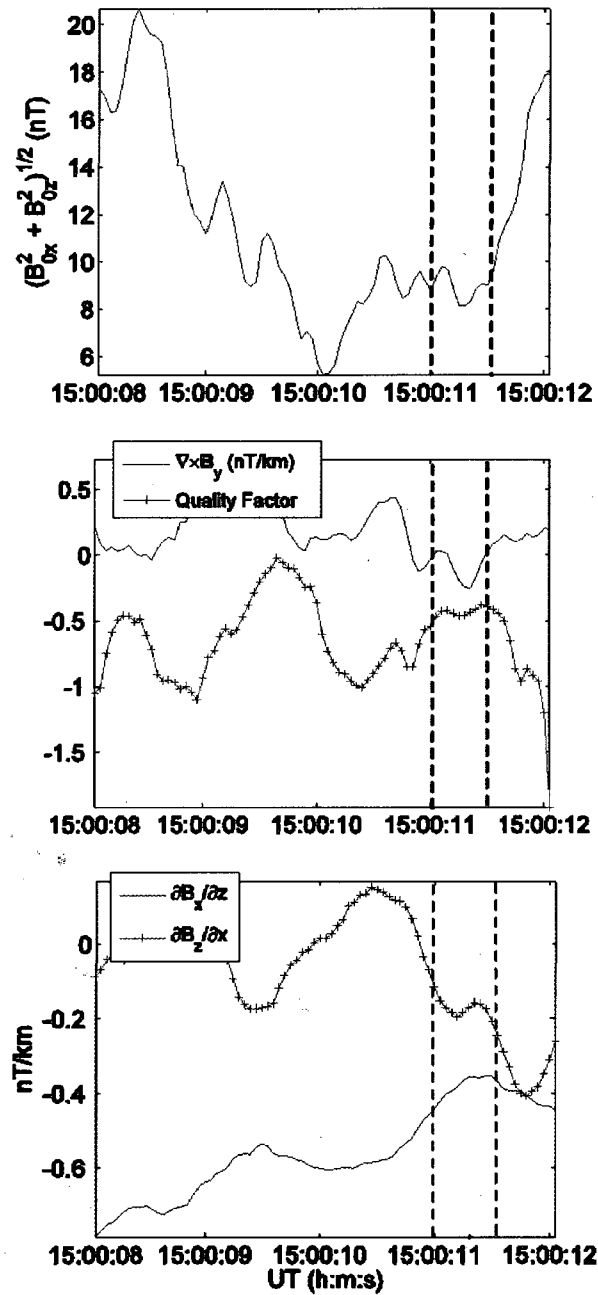
Figure A2a - A2c (a) Top: The magnitude $(B_x^2+B_z^2)^{1/2}$ measured at the centroid, in a region near the x-line. We seek the spatial gradients where the value of $(B_x^2+B_z^2)^{1/2}$ has minima. **(b) Middle:** The quality factor $\nabla \cdot B / |\nabla \times B|$ used to estimate the quality of the quadratic interpolated spatial gradients. The reconnection site derivatives (next figure) are taken at the dotted line where $(B_x^2+B_z^2)^{1/2}$ has a minimum. **(c) Bottom:** The spatial gradients $\partial B_x/\partial z$ and $\partial B_z/\partial x$ near reconnection at 15:00 UT.

B_z, and a low value for the quality factor. We would also expect the derivatives $\partial B_x/\partial x$

and $\partial B_z/\partial z$ to be relatively small for a symmetric geometry. A region that satisfies all

these criteria fairly well lies between the two dotted lines in Figures A2a –A2c. At the

time of the smallest $\sqrt{B_x^2 + B_z^2}$ observed at the centroid, shown in Figure A2a, the value

of the quality factor is poor (Figure A2c), but the region between the dotted lines still has

a very small $\sqrt{B_x^2 + B_z^2}$ and a much better quality factor—one that lies below the worst

case for a potato/pancake tetrahedron. In this region, $\partial B_x/\partial z$ lies between approximately -

0.4 and -0.5nT/km and $\partial B_z/\partial x$ between approximately -0.1 and -0.2 nT/km, as shown in

Figure A2b. Furthermore, at these locations, the values of $\partial B_x/\partial x$ and $\partial B_z/\partial z$ are small in

comparison (both between ± 0.05 nT/km).

A.4 Propagation of Errors in the Calculation of Magnetic Spatial gradients

The propagation of errors in the estimates for the spatial gradients arise from the

relative errors in the spacecraft positions and in the magnetic field measurements. The

absolute errors are negligible in comparison. The error in inter-spacecraft distances is 10

km for separations less than 1000 km, and the relative error in magnetic field

measurements is on the order of 0.5 nT. The resulting errors in the estimates for $\partial B_x/\partial z$

and $\partial B_z/\partial x$ vary, but in the current sheet the rms error for $\partial B_x/\partial z$ lies between about 0.02

and 0.09 nT/km, and the rms error for $\partial B_z/\partial x$ ranges between 0.02 and 0.08 nT/km. In

calculating the rms errors, we have assumed a general tetrahedral geometry and equal

relative errors for all three magnetic and spatial components. Figure A3 plots the

spacecraft centroid position uncertainties in the superposed epoch coordinate system that

result from the propagation of relative position and magnetic spatial gradient
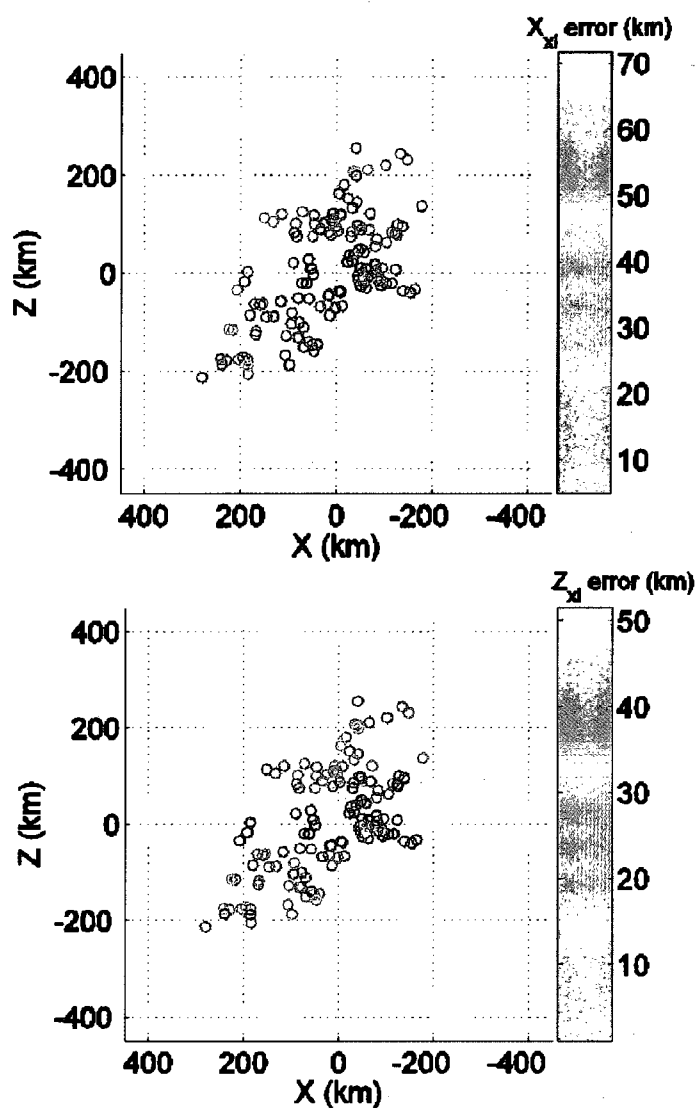
Figure A3a - A3b. The error sizes of the x (top) and z (bottom) coordinates of the x-line at the positions of the centroid throughout the layer. Brighter colors signify greater errors in position. Position errors are small within roughly 50 km above and below the x-line.

uncertainties. Figure A3a shows the uncertainty in the x, and Figure A3b in the z, component. Warmer colors signify greater errors in position. Position errors are small (less than 10 km) within roughly 50 km above and below the x-line and 200 km on either side of the x-line. The largest error in the x position is about 70 km, and the largest in the z position about 50 km.
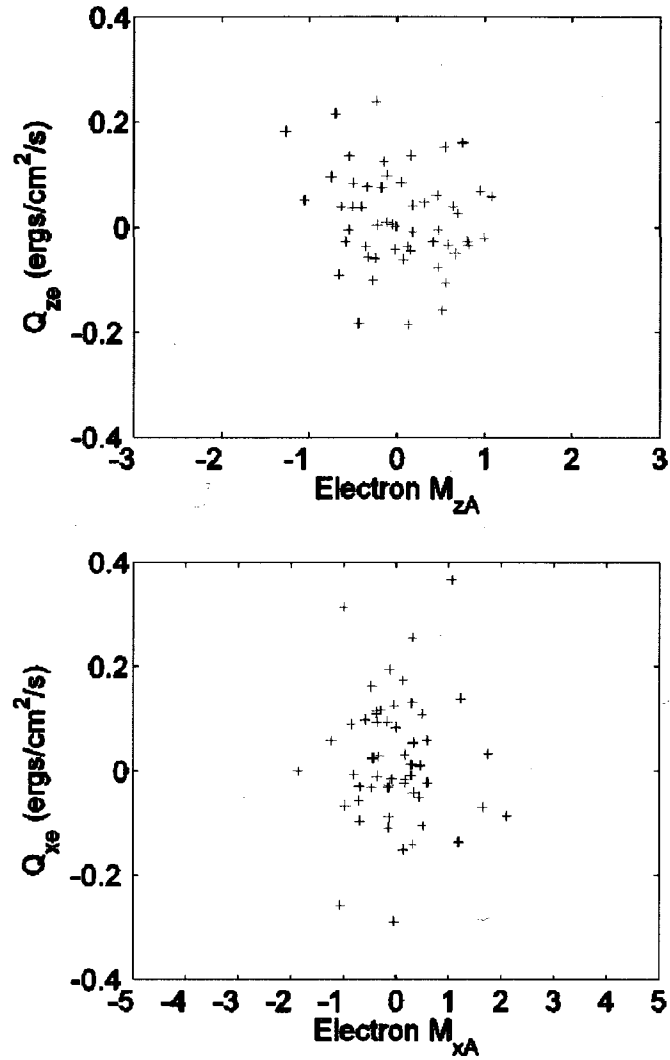
Figure A4a - A4b. (a) Top: The horizontal (x) component of the electron heat flux Q_x and the x component of the electron Alfvén Mach number M_{Ae} do not present strong off-diagonal correlations. **(b) Bottom:** The same applies for the vertical (z) components. The four shades in the figure simply indicate different spacecraft.

A.5 Heat Flux and Electron Moments

Figures A4a and A4b compare the x and z components of the electron heat flux to the electron M_{Ae} in the x and z directions, respectively (where the four shades correspond to different spacecraft). The highest values of M_{Ae} and the largest heat fluxes tend to lie

on lines along the horizontal and vertical axes, respectively, which indicates that the at least the highest flows are usually not seriously aliased. Correlations between the quantities being compared would tend to form lines at angles to the axes and might suggest that passage through different temperature regions during a spin are misinterpreted as flows by the moments analysis.

A.6 Calculation of Electron Pressure Divergence

In order to calculate the pressure divergence contribution to the reconnection electric field, we exploit the Cluster tetrahedron to estimate linear spatial pressure tensor gradients by way of the same least squares estimation used to uncover the magnetic field spatial gradients. The math is the same, only we replace the magnetic field vector components with pressure tensor components in the minimization formula. In many cases, this method provides an excellent approach to determining the reconnection electric field. However, for this spacecraft tetrahedral geometry, the error in the pressure divergence that propagates from pressure and relative position measurement errors is large. The error exceeds the value obtained for E_y (~-0.12 mV/m) from the y component of the pressure divergence calculated using this method. Moreover, the interspacecraft spacing on the order of at most 180 km may lack the resolution necessary to measure the dissipation region on the electron scales: at best it yields a lower limit to the measurement. Because we cannot accurately calculate the y component of the pressure divergence, we do not use the pressure divergence to find the nonideal electric field at the reconnection site.

A.7 Agyrotropy Tests

To estimate the influence of the magnetic field motion during high-shear spins, we start with the equation for a pressure tensor, which we assume to be gyrotropic, in terms of its components $p_\perp$ and $p_{/\!/}$ perpendicular and parallel to $\mathbf{B}$, respectively, i. e.,

$$\mathbf{P} = p_\perp \mathbf{I} + (p_{\|} - p_\perp)\frac{\mathbf{B}\mathbf{B}^T}{B^2} \tag{A.16}$$

The extent to which rapid fluctuations in the magnetic field $\mathbf{B}$ would engender false off-diagonal terms in the pressure during a spin interval would come into the second term. For each spin of apparent agyrotropy, we measure the mean value of the highest (0.04 s) resolution $\mathbf{B}$ during one spin, since this value is used as the direction of $\mathbf{B}$ for the onboard calculation of the components of the moments during a spin. We then use this mean value of $\mathbf{B}$ to set the direction of $\mathbf{B}$ during a spin, and rotate the highest resolution $\mathbf{B}$ field vectors to lie along this direction during a spin. This gives us $\mathbf{B}\mathbf{B}^T/B^2$ in equation A.13, setting the components of $\mathbf{P}$ during a spin. We then calculate the amount of deviation of the resulting off-diagonal terms $(p_{\|}-p_\perp)\mathbf{B}\mathbf{B}^T/B^2$ during a spin by taking the standard deviation of $\mathbf{B}\mathbf{B}^T/B^2$ during a spin. This tells us by how much the direction of $\mathbf{B}$ calculated from the spin mean value of the direction of $\mathbf{B}$ differs from the actual value of the direction of $\mathbf{B}$ during a spin. The result reveals how much the corresponding off-diagonal terms in $\mathbf{P}$ result from this direction error rather than from a real shear. Finally, we divide by the actual off-diagonal pressure term (e.g. P_{xy}) to get what percentage of it is just due to the direction error. For the spin corresponding to the first largest peak in P_{xy} between the dashed lines in Figure 3.27b, the biggest shear term is P_{xy}, and it's error is 5.9%. The P_{zx} term, much smaller, has an error of 26%, and the P_{yz} term an error of 7.4%. For the second largest peak between the dashed lines, the biggest shear term is P_{xy} and its

error is 1.7%. The P_{yz} term's error is less than 1%, and the P_{zx} term error is 1.1%. Thus we can rule out that the largest observed agyrotropy merely represents the magnetic field fluctuations.

A.8 Electron distributions

The smoothing method applied to the angular electron distributions in Figures 3.22, 3.23 and 3.28 enhances poorly visible features (C. Gurgiolo, personal communication, 2008). The data are first placed unsmoothed in a two dimensional N×M grid corresponding to N elevations and M azimuths, where N and M are determined by the instrument. The grid size is increased from MxN to M*SxN*S for a given smoothing factor S. This results in S blank rows and columns between the filled ones. The outer rows and columns are filled and anchored. Finally, a 2D least squares fit fills in the unfilled cells in the grid. Except near the edges, the program makes sure that there is at least one filled cell in each of the 4 quadrants surrounding the empty cell. To prevent instabilities, the fit is constrained so that it cannot create data larger than the maximum or less than the minimum data used in the fit.

A.9 Coordinate Systems

There are several coordinate systems in use in this work. The Cluster data, before we apply any rotations, and the GGCM simulation output are in the commonly used GSE (Geocentric Solar Ecliptic) coordinate system. In this coordinate system, the positive x-axis points toward the sun and lies parallel to the Earth-sun line on the ecliptic plane. The positive z-axis is perpendicular to the ecliptic plane and points along the north ecliptic
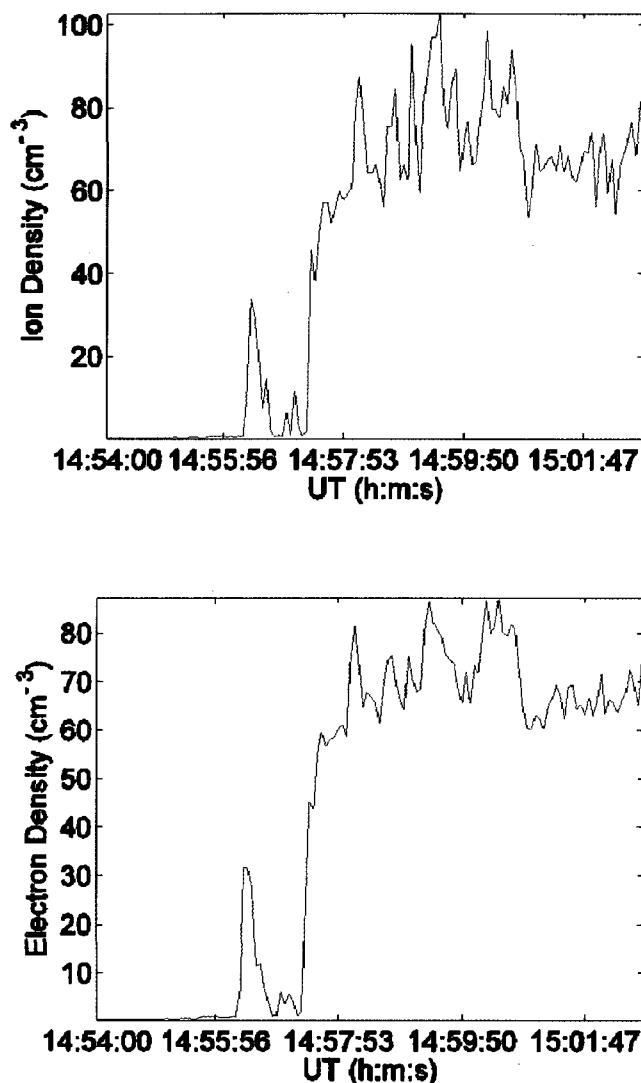
Figure A5a - A5b. The Cluster 1 ion (top) and the electron (bottom) particle densities in the magnetopause. Cluster 1 enters the magnetopause at about 14:57.

pole. The positive *y*-axis completes the right-handed coordinate system by pointing perpendicular to both of these axes toward dusk in the ecliptic plane. Thus this coordinate system does not move in time and does not rotate with the Earth. The GGCM input is in the GSM coordinate system, which rocks about the *x*-axis in time. Like the GSE coordinate system, the *x*-axis points toward the sun on the ecliptic plane, but the *z*-axis is

defined as the axis perpendicular to the x-axis that lies in a plane defined by the x-axis and the Earth's dipole axis. The y-axis completes the right-handed coordinate system, but will rock back and forth about the x-axis in time as the Earth's dipole rotates. The location of the dipole axis is based on an empirical model known as the International Geomagnetic Reference Field (IGRF). The IGRF, last updated in 2005, is calculated from an order 13 spherical harmonic dipole expansion

The IMAGE, DMSP, and Iridium data are all in some variant version of geomagnetic field based coordinates. These types of coordinate systems allow tracing of satellite data along field lines so that they can be organized and presented based on an underlying physical principle. Corrected Geomagnetic Coodinates (CGM), as used in DMSP data, trace along magnetic field lines from the satellite to the footprint in the ionosphere using the IGRF and Tsyganenko 1987 models [*Hultquist and Gustafsson*, 1960]. The coordinates of the footprint are then traced back to a point p in the dipole equatorial plane using the IGRF at radii up to 8 R_E and using the dipole field further out. Finally, the coordinates in CGM are determined from point p. The longitude and magnetic local time of the measured data equals the dipole longitude and magnetic local time of p, and the latitude of the data point is $(\frac{1}{L})^{\frac{1}{2}}$, where L is the distance from the Earth to the point p.

The Iridium data is available in Altitude Adjusted Geomagnetic Coordinates, which is adapted to coverage at high and low latitudes [*Baker and Wing*, 1989]. These are based on corrected geomagnetic coordinates, but the final tracing goes all the way to the ground in the conjugate hemisphere instead of stopping in the dipole equator. This means all points on a field line have the same latitude and longitude. The function that converts

from geographic latitude and longitude is expressed as a spherical harmonic expansion. Each desired data point coordinate X, Y, Z has a separate set of expansion coefficients, which are a function of altitude. The expansion coefficients are determined by requiring X, Y, Z to equal X_m, Y_m, Z_m, the magnetic coordinates, at a set of grid points. The spherical harmonics are functions of the geographic colatitude and longitude.

The IMAGE data is organized in Apex Geomagnetic Coordinates. The Apex coordinate system is similar to the CGM, but it provides coverage at lower latitudes. It is defined in terms of the apex of a field line over the geoid of the Earth and magnetic shells based on their apex coordinates. The apex radius A is defined as $(1 + \frac{h_A}{r_E})$, where h_A is the height of the apex of the field line above the geoid and r_E is the semi-major axis of the geoid. The apex longitude labels a given field line in a given apex shell, and the third apex coordinate is the height of the apex above the geoid [*VanZandt et al.,* 1972].